



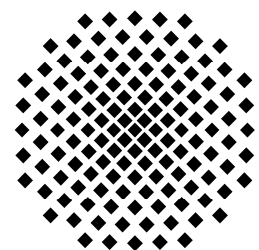
Max-Planck-Institut für Festkörperforschung
Stuttgart

**The Relativistic Effect in Intermetallic Phases
of Gold, Platinum and Thallium**

Vyacheslav Saltykov

Dissertation an der Universität Stuttgart

Stuttgart, 2011



The Relativistic Effect in Intermetallic Phases of Gold, Platinum and Thallium

Von der Fakultät Chemie der Universität Stuttgart
zur Erlangung der Würde eines
Doktors der Naturwissenschaften (Dr. rer. nat.)
genehmigte Abhandlung

Vorgelegt von

Vyacheslav Saltykov

aus Konotop, Ukraine

Hauptberichter:	Prof. Dr. Martin Jansen
Mitberichter:	Prof. Dr. Robert E. Dinnebier
Prüfungsvorsitzender:	Prof. Dr. Thomas Schleid

Tag der mündlichen Prüfung:	02.03.2011
-----------------------------	------------

Max-Planck-Institut für Festkörperforschung, Stuttgart

2011

*To my brother and
the whole family*

Contents

Part I. Introduction	1
1. Introduction	3
1.1. Theory of Relativity and Its Effects on the Chemistry of the Heavy Elements	3
1.2. Aims of the Present Work	14
Part II. General Part	17
2. Apparatus and Experimental Conditions	19
2.1. Handling of Air-sensitive Materials	19
2.1.1. Vacuum Line Setup	19
2.1.2. Glove Box	22
2.2. Reaction Vessels	22
2.3. Handling of the Alkali Metals	24
2.4. Preparation of Single Crystals for X-Ray Analyses	25
2.5. High-Temperature Facilities	26
3. Analysis Techniques	27
3.1. Chemical Analysis	27
3.2. Energy Dispersive X-ray Spectroscopy	27
3.3. Powder X-ray Analysis and Details about the Refinement of Lattice Parameters	28
3.4. X-ray Diffraction on Single Crystals	29
3.5. Thermal analysis	31

3.6. Measurements of Electrical Resistivity	31
3.7. Magnetic Susceptibility Measurements	32
3.8. Electron Spectroscopy for Chemical Analysis	33
4. Theoretical calculations	35
4.1. Density Functional Theory	35
4.2. Extended Hückel Method	36
4.3. Selection of Functionals and Basis Sets	37
4.4. Addressing Relativistic Effects	39
4.5. Topological Analysis of the Electron Density	40
5. Starting materials	44
5.1. Alkali and Alkaline-Earth Metals	44
5.1.1. Potassium	44
5.1.2. Cesium	44
5.1.3. Barium, Calcium, Strontium	45
5.2. Cesium Oxide	46
5.3. Tetrel Metal Dioxides	46
5.4. Platinum, Gold, Thallium, Indium, Tin (IV) and Tin (II) Oxides .	49
 Part III. Special Part	 53
 6. Alkaline-Earth Metal Auride Platinides	 55
6.1. Quasi Binary System BaAu-BaPt	55
6.1.1. Synthesis, Powder XRD and Thermal Stability	56
6.1.2. Crystal Structure Analysis	57
6.1.2.1. Single Crystal X-ray Structure Analysis of BaAu _{0.5} Pt _{0.5} and BaAu	57
6.1.2.2. Powder Diffraction X-ray Analysis of BaAu–BaPt System . . .	62
6.1.3. Electrical Resistivity Measurements	63
6.1.4. Magnetic Susceptibility Measurements	64
6.1.5. ESCA	65
6.2. SrAu_{0.5}Pt_{0.5} and CaAu_{0.5}Pt_{0.5} – Featuring Purely Intermetallic Behaviour	 67

6.2.1. Synthesis, Powder XRD and Thermal Stability	68
6.2.2. Crystal Structure Analysis	69
6.2.3. Electrical Resistivity Measurements	73
6.2.4. Magnetic Susceptibility Measurements	74
6.2.5. ESCA	75
6.3. Conclusions	76
7. Ternary Alkali Metal Oxide Thallides	78
7.1. Distorted $[\text{Tl}_8]^{6-}$ Clusteranion in $\text{Cs}_{18}\text{Tl}_8\text{O}_6$	79
7.1.1. Synthesis, Powder XRD and Thermal Stability	79
7.1.2. Crystal Structure Analysis	81
7.1.3. Electrical Resistivity Measurements	88
7.1.4. Magnetic Susceptibility Measurements	89
7.1.5. Electron Balance of the $[\text{Tl}_8]^{6-}$ Clusteranion	90
7.1.6. Electronic Structure Calculations and Quantum Chemical Analysis	91
7.2. Regular $[\text{Tl}_6]^{6-}$ Cluster in $\text{Cs}_4\text{Tl}_2\text{O}$	101
7.2.1. Synthesis, Powder XRD and Thermal Stability	101
7.2.2. Crystal Structure Analysis	102
7.2.3. Magnetic Susceptibility Measurements	107
7.2.4. Electron Balance of the $[\text{Tl}_6]^{6-}$ Clusteranion	108
7.2.5. Electronic Structure Calculations and Quantum Chemical Analysis	108
7.3. Two Different Tl_{11} Clusteranions in $\text{K}_{21}\text{Tl}_{22}\text{O}_2$	111
7.3.1. Synthesis, Powder XRD and Thermal Stability	111
7.3.2. Crystal Structure Analysis	112
7.3.3. Magnetic Susceptibility Measurements	119
7.3.4. Electron Balance of the $[\text{Tl}_{11}]$ Clusteranions	120
7.4. Conclusions	121
8. Cesium Oxotetrelate-Thallides: $\text{Cs}_{10}\text{Tl}_6\text{SiO}_4$, $\text{Cs}_{10}\text{Tl}_6\text{GeO}_4$ and $\text{Cs}_{10}\text{Tl}_6\text{SnO}_3$	124
8.1. Synthesis, Powder XRD and Thermal Stability	125
8.2. Crystal Structure Analysis	127

8.3. Electron Balance of the $[\text{Tl}_6]^{6-}$ Clusteranion	136
8.4. Electrical Resistivity Measurements	137
8.5. Magnetic Susceptibility Measurements	138
8.6. Conclusions	139
9. Cesium Silicate Indide: $\text{Cs}_{22}\text{In}_6(\text{SiO}_4)_4$	140
9.1. Synthesis, Powder XRD and Thermal Stability	141
9.2. Crystal Structure Analysis	142
9.3. Electrical Resistivity Measurements	150
9.4. Conclusions	151
10. General Conclusions	152
Part IV. Summary	155
11. Abstract	157
11.1. Alkaline-Earth Metal Auride Platinides	157
11.2. Ternary Alkali Metal Oxothallides	158
11.3. Cesium Oxotetrelate-Thallides	160
11.4. Cesium Oxosilicate-Indide	161
Part V. Zusammenfassung	163
12. Zusammenfassung	165
12.1. Erdalkalimetall-Auridplatinide	165
12.2. Ternäre Alkalimetalloxothallide	166
12.3. Cäsium Oxotetrelat-Thallide	168
12.4. Cäsium Oxosilikat-Indid.	169
13. Literature	171
Part VI. Appendix A	183
Part VII. Appendix B	197

14. Acknowledgements	199
15. Curriculum Vitae	201
16. Publications	202

List of Figures

1.1 The relativistic contraction of the 6s orbital for the elements with Z from 55 to 100 based on calculations by Desclaux [19].	7
1.2 Electron affinity of halogens (red), chalcogens (cyan) as well as gold (orange) and platinum (blue).	8
1.3 First ionisation potentials of the elements of 2 nd (diamonds), 5 th (circles) and 6 th (squares) period (reproduced from [11]).	14
2.1 Vacuum line setup.	20
2.2 Schematic representation of argon cleaning installation.	21
2.3 Schlenk apparatus (upper joint has size 29; the rest joints have size 14.5; a – ampoule for storing the substance; b – glass capillary for X-ray analysis).	21
2.4 Drying tube (Length ca. 40 cm, diameter ca. 3 cm).	22
2.5 Arc welder for sealing tantalum ampoules.	23
2.6 Apparatus: a) for dividing the alkali metals into desired amount; b) for weighing the alkali metals in tantalum ampoules.	24
2.7 Single crystal mounting apparatus.	25
5.1 Measured (<i>above</i>) and theoretically calculated (<i>below</i>) [159] powder diffraction patterns of the Cs ₂ O ($\lambda = 0.7093 \text{ \AA}$).	47
5.2 Measured (<i>above</i>) and theoretically calculated (<i>below</i>) [160] powder diffraction patterns of the SiO ₂ ($\lambda = 1.5406 \text{ \AA}$).	47
5.3 Measured (<i>above</i>) and theoretically calculated (<i>below</i>) [161] powder diffraction patterns of the GeO ₂ ($\lambda = 1.5406 \text{ \AA}$).	48
5.4 Measured (<i>above</i>) and theoretically calculated (<i>below</i>) [162] powder diffraction patterns of the SnO ₂ ($\lambda = 0.7093 \text{ \AA}$).	48
5.5 Measured (<i>above</i>) and theoretically calculated (<i>below</i>) [163] powder	

diffraction patterns of the Au ($\lambda = 0.7093 \text{ \AA}$)	49
5.6 Measured (<i>above</i>) and theoretically calculated (<i>below</i>) [164] powder diffraction patterns of the SnO ($\lambda = 0.7093 \text{ \AA}$)	50
6.1 Measured (<i>above</i>) and theoretically calculated (<i>below</i>) powder diffraction patterns of BaAu _{0.5} Pt _{0.5} ($\lambda = 0.7093 \text{ \AA}$)	56
6.2 Measured (<i>top</i>) and theoretically calculated (<i>bottom</i>) powder diffraction patterns of BaAu ($\lambda = 0.7093 \text{ \AA}$)	57
6.3 Perspective representations of the crystal structures of BaAu _{0.5} Pt _{0.5} (<i>a</i>) and BaAu (<i>b</i>)	61
6.4 Concentration dependencies (red lines) of the unit cell volume (<i>a</i>) and lattice parameters (<i>b</i>) in the solid solution BaAu _{1-x} Pt _x ($x = 0.15 - 0.9$) region, green lines are demarking the ranges of experimental errors.	63
6.5 Temperature-dependent resistivity data of BaAu _{0.5} Pt _{0.5}	64
6.6 Field-dependent magnetic susceptibility data of BaAu _{0.5} Pt _{0.5} at 300 K.	65
6.7 Temperature-dependent magnetic susceptibility data of BaAu at 1T (black squares) and 3T (white circles).	65
6.8 Pt (<i>4f</i>) and Au (<i>4f</i>) region of ESCA spectra of the BaAu _{0.5} Pt _{0.5} and BaAu.	67
6.9 Measured (<i>above</i>) and theoretically calculated (<i>below</i>) powder diffraction patterns of SrAu _{0.5} Pt _{0.5} ($\lambda = 1.5406 \text{ \AA}$)	68
6.10 Measured (<i>above</i>) and theoretically calculated (<i>below</i>) powder diffraction patterns of CaAu _{0.5} Pt _{0.5} ($\lambda = 1.5406 \text{ \AA}$)	69
6.11 Temperature – dependent resistivity data of SrAu _{0.5} Pt _{0.5} and CaAu _{0.5} Pt _{0.5}	73
6.12 Temperature-dependent magnetic susceptibility data of SrAu _{0.5} Pt _{0.5} at 3T (black squares), 5T (red circles) and 7T (blue triangles).	74
6.13 Temperature-dependent magnetic susceptibility data of CaAu _{0.5} Pt _{0.5} at 3T (black squares), 5T (red circles) and 7T (blue triangles).	74
6.14 Pt (<i>4f</i>) and Au (<i>4f</i>) region of ESCA spectra of the BaAu _{0.5} Pt _{0.5} [171], SrAu _{0.5} Pt _{0.5} and CaAu _{0.5} Pt _{0.5} intermetallics.	76
7.1 Measured (<i>above</i>) and theoretically calculated (<i>below</i>) powder diffraction patterns of CsTl ($\lambda = 0.7093 \text{ \AA}$)	80
7.2 Measured (black) as well as theoretically calculated (blue) of the	

Cs ₁₈ Tl ₈ O ₆ powder diffraction patterns, stars (*) are indicating the impurity of Cs ₄ Tl ₂ O (see Chapter 7.2) and Cs ₈ Tl ₁₁ [178] ($\lambda = 0.7093 \text{ \AA}$).	81
7.3 Graphical presentation of the crystal structure of Cs ₁₈ Tl ₈ O ₆ (<i>a</i> , Tl ₈ clusters emphasized as blue polyhedra, OCS ₆ octahedra in red), and of KSbO ₃ (<i>b</i> , SbO ₆ octahedra in red, the K atoms are depicted as a corner-connected array of K ₈ stellae quadrangulae). Green lines mark the unit cell edges.	84
7.4 Representation of the cubic γ -brass (<i>a</i> , light blue spheres – Zn atoms, red spheres – Cu atoms, white spheres – voids located in 24-fold sites symmetry) and Cs ₁₈ Tl ₈ O ₆ (<i>b</i> , blue spheres – thallium atoms, green spheres – cesium atoms, red spheres – oxygen atoms) structures in the form of 26-atom cluster. Green lines mark the unit cell edges.	85
7.5 Group-subgroup relation between the Cu ₅ Zn ₈ and Cs ₁₈ Tl ₈ O ₆ crystal structures, including the site transformations.	86
7.6 Comparison between the Tl ₈ tetrahedral star (<i>a</i>) and ideal Tl ₈ cube (<i>b</i>). Interatomic distances in (\AA) and angles in ($^\circ$). T1–T1: $3.3816(6) \times 4$, T1–T2: $3.1113(4) \times 12$, T11–T12–T11: $65.84(1) \times 12$, T12–T11–T12: $109.548(8) \times 12$	86
7.7 Temperature – dependent resistivity data of Cs ₁₈ Tl ₈ O ₆	88
7.8 Temperature – dependent magnetic susceptibility data of Cs ₁₈ Tl ₈ O ₆ at 0.1T (black squares), 1T (red circles) and 3T (blue triangles).	89
7.9 Graphical presentation of the crystal structure of Cs ₈ Tl ₈ O [104]: Tl ₈ clusters emphasized as blue polyhedra, Cs ₈ polyhedra in red, centered by oxygen.	90
7.10 Optimized structures of Cs ₆ Tl ₈ -Clusters. The shapes of the Tl ₈ -units conform to the polyhedra found in Cs ₁₈ Tl ₈ O ₆ (left, tetrahedral star) and in Cs ₈ Tl ₈ O (right, parallelepiped). The symmetry-unique computed (two component relativistic, PBE, def2-TZVP) Tl-Tl distances are given in \AA . The corresponding experimental values found for the crystal are added in parenthesis.	92
7.11 Total densities of states (DOS) near the Fermi level of Cs ₁₈ Tl ₈ O ₆ (<i>a</i> and <i>b</i>), hypothetical Cs ₁₈ Tl ₈ O ₆ with cubic Tl ₈ -unit (<i>c</i>) and Cs ₈ Tl ₈ O (<i>d</i>)	

and <i>e</i>). Grey: without spin–orbit coupling (<i>a</i> and <i>e</i>); black: including spin–orbit coupling (<i>b</i> , <i>c</i> and <i>d</i>).	93
7.12 Atom-projected non-spin-polarized density of states for Cs ₁₈ Tl ₈ O ₆ , spin-orbit coupling is considered.	95
7.13 Atom-projected non-spin-polarized density of states for Cs ₈ Tl ₈ O, spin–orbit coupling is considered.	96
7.14 Density of states (DOS) of the crystals and MO diagrams of the Cs ₆ Tl ₈ clusters. Left side: Cs ₁₈ Tl ₈ O ₆ and tetrahedral star; right side: Cs ₈ Tl ₈ O and parallelepiped. The diagrams show scalar relativistic MOs (majority spin, column 3 and 5; occupied: black; partially occupied: grey; unoccupied: red), fully relativistic spinors (column 2 and 6) and DOS including spin-orbit coupling (column 1 and 7; total DOS: grey; Tl-projected DOS: black). E _F and ε _{HOMO} are shifted to 0 eV.	98
7.15 Domains (isosurfaces) of the ELF (<i>left</i>), Cs semi-core omitted as well as ELF distribution on selected planes (<i>right</i>) for Cs ₆ Tl ₈ molecule in form of tetrahedral star (<i>a</i>), parallelepiped (<i>b</i>) and cube (<i>c</i>).	100
7.16 Le Bail refinement of Cs ₄ Tl ₂ O (measured curve (blue line), theoretically calculated curve (red line), difference curve (grey line), Bragg reflections (blue ticks)) (λ = 0.7093 Å).	102
7.17 Perspective representation of the crystal structure of Cs ₄ Tl ₂ O (green line marks the unit cell edges, blue spheres – Tl atoms, green spheres – Cs atoms, red spheres – oxygen atoms).	105
7.18 The [Tl ₆] ⁶⁻ clusters in Cs ₄ Tl ₂ O (<i>a</i>) and Rb ₁₀ Tl ₆ O ₂ [105] (<i>b</i>).	106
7.19 Temperature – dependent magnetic susceptibility data of Cs ₄ Tl ₂ O at 0.1T (black squares), 1T (red circles) and 3T (blue triangles).	107
7.20 Total (grey) and atom-projected densities (colored, see legend) of states of Cs ₄ Tl ₂ O, from a relativistic DFT calculation including spin–orbit coupling. The Fermi level is shifted to 0 eV.	109
7.21 Total density of states (DOS) near the Fermi level without (<i>above</i>) and with (<i>below</i>) spin-orbit coupling of Cs ₄ Tl ₂ O (<i>a</i>) and Rb ₁₀ Tl ₆ O ₂ (<i>b</i>). E _F is shifted to 0 eV.	110
7.22 Respective graphical presentation of the crystal structure of K ₂₁ Tl ₂₂ O ₂	

<p>(a) and the projection of latter on (001) (b): Tl_{11} clusters emphasized as blue polyhedra, OK_6 octahedra in red, green spheres – K atoms. Green lines mark the unit cell edges, orange lines mark borders of $2 \times 2 \times 2$ supercell.</p>	116
<p>7.23 $[Tl_{11}]$ clusters presented in $K_{21}Tl_{22}O_2$. Red lines are displaying arrangement of Tl atoms in the shape of trigonal bipyramid. Interatomic distances in Å. The corresponding distances are presented in Table 7.13.</p>	118
<p>7.24 Graphical presentation of the crystal structure of $K_{21}Tl_{22}O_2$: Tl_{11} clusters emphasized as blue polyhedra (only central bipyramids are shown), red spheres – O atoms, green spheres – K atoms. Blue parallelepipeds emphasizing octahedral voids, red triangles – tetrahedral voids. Green lines mark the unit cell edges.</p>	119
<p>7.25 Temperature – dependent magnetic susceptibility data of $K_{21}Tl_{22}O_2$ at 0.1T (black squares), 1T (red circles) and 3T (blue triangles).</p>	120
<p>8.1 Le Bail refinement of $Cs_{10}Tl_6SiO_4$ (measured curve (blue line), theoretically calculated curve (red line), difference curve (grey line), Bragg reflections (blue ticks)) ($\lambda = 0.7093$ Å).</p>	126
<p>8.2 Le Bail refinement of $Cs_{10}Tl_6GeO_4$ (measured curve (blue line), theoretically calculated curve (red line), difference curve (grey line), Bragg reflections (blue ticks)) ($\lambda = 0.7093$ Å).</p>	126
<p>8.3 Le Bail refinement of $Cs_{10}Tl_6SnO_3$ (measured curve (blue line), theoretically calculated curve (red line), difference curve (grey line), Bragg reflections (blue ticks)) ($\lambda = 0.7093$ Å).</p>	127
<p>8.4 Group-subgroup relation between the $Cs_{10}Tl_6SnO_3$ and $Cs_{10}Tl_6SiO_4$ crystal structures, including the site transformations.</p>	128
<p>8.5 Perspective representations of the crystal structures of $Cs_{10}Tl_6TtO_4$ (Tt = Si and Ge) (a) and $Cs_{10}Tl_6SnO_3$ (b) (green lines mark the unit cell edges, blue spheres – Tl atoms, green spheres – Cs atoms, grey spheres – Si, Ge or Sn atoms, red spheres – oxygen atoms); vertical black lines at the bottom emphasize the intergrowth type of structure, consisting of Cs_6Tl_6 and Cs_4TtO_4 (Tt = Si and Ge) or Cs_4SnO_3 slabs. . .</p>	132
<p>8.6 The $[Tl_6]^{6-}$ clusters in $Cs_{10}Tl_6TtO_4$ (Tt = Si and Ge) (a) and</p>	

Cs ₁₀ Tl ₆ SnO ₃ (<i>c</i>). The tetrahedral arrangement of oxygen around Si and Ge (<i>b</i>) in Cs ₁₀ Tl ₆ TtO ₄ (Tt = Si and Ge) as well as triple-coordinated Sn by oxygen (<i>d</i>) in Cs ₁₀ Tl ₆ SnO ₃ compound. Dotted lines emphasize the compressed diagonals of the clusters, Table 8.5.	133
8.7 MO diagrams (qualitative sketch) of the [Tl ₆] ⁸⁻ (<i>O_h</i>) and [Tl ₆] ⁶⁻ (<i>D_{4h}</i>) clusters [182].	136
8.8 Temperature – dependent resistivity data of Cs ₁₀ Tl ₆ SiO ₄	137
8.9 Temperature – dependent magnetic susceptibility data of Cs ₁₀ Tl ₆ SiO ₄ (black squares), Cs ₁₀ Tl ₆ GeO ₄ (red circles) and Cs ₁₀ Tl ₆ SnO ₃ (blue triangles) at field strength 3T.	138
9.1 Le Bail refinement of Cs ₂₂ In ₆ (SiO ₄) ₄ (measured curve (blue line), theoretically calculated curve (red line), difference curve (grey line), Bragg reflections (blue ticks)) ($\lambda = 0.7093 \text{ \AA}$).	142
9.2 Perspective representations of the crystal structures of Cs ₂₂ In ₆ (SiO ₄) ₄ (<i>a</i>) and Rb ₂ In ₃ (<i>b</i>) (green lines mark the unit cell edges, blue spheres – In atoms, green spheres – Cs or Rb atoms, grey spheres – Si atoms, red spheres – oxygen atoms); horizontal black lines at the right hand side emphasize the intergrowth type of structure, consisting of Cs ₆ In ₆ and 4 × Cs ₄ SiO ₄ slabs; solid blue lines represent bonding interactions between the indium atoms forming quasi-finite square planar sheets. . .	144
9.3 The [In ₆] ⁶⁻ (<i>a</i>) and [In ₆] ⁴⁻ (<i>b</i>) clusters in Cs ₂₂ In ₆ (SiO ₄) ₄ and Rb ₂ In ₃ , respectively. Dotted line emphasizes the In–In distance, which is much too long as to be assigned to a homoatomic bond, Table 9.5.	149
9.4 Temperature – dependent resistivity data of Cs ₂₂ In ₆ (SiO ₄) ₄	150
A2.1 Curie-Weiss fitting (red curve) of the magnetic susceptibility data of Cs ₁₈ Tl ₈ O ₆ at 1T (black circles).	188
A2.2 Curie-Weiss fitting (red curve) of the magnetic susceptibility data of Cs ₁₈ Tl ₈ O ₆ at 3T (black circles).	189
A2.3 Curie-Weiss fitting (red curve) of the magnetic susceptibility data of Cs ₁₈ Tl ₈ O ₆ at 5T (black circles).	189
A2.4 Curie-Weiss fitting (red curve) of the magnetic susceptibility data of Cs ₁₈ Tl ₈ O ₆ at 7T (black circles).	190
A2.5 Curie-Weiss fitting (red curve) of the magnetic susceptibility data of	

Cs ₄ Tl ₂ O at 1T (black circles)	190
A2.6 Curie-Weiss fitting (red curve) of the magnetic susceptibility data of Cs ₄ Tl ₂ O at 3T (black circles)	191
A2.7 Curie-Weiss fitting (red curve) of the magnetic susceptibility data of Cs ₄ Tl ₂ O at 5T (black circles)	191
A2.8 Curie-Weiss fitting (red curve) of the magnetic susceptibility data of Cs ₄ Tl ₂ O at 7T (black circles)	192
A2.9 Curie-Weiss fitting (red curve) of the magnetic susceptibility data of K ₂₁ Tl ₂₂ O ₂ at 1T (black circles)	192
A2.10 Curie-Weiss fitting (red curve) of the magnetic susceptibility data of K ₂₁ Tl ₂₂ O ₂ at 3T (black circles)	193
A2.11 Curie-Weiss fitting (red curve) of the magnetic susceptibility data of K ₂₁ Tl ₂₂ O ₂ at 5T (black circles)	193
A2.12 Curie-Weiss fitting (red curve) of the magnetic susceptibility data of K ₂₁ Tl ₂₂ O ₂ at 7T (black circles)	194
A2.13 Curie-Weiss fitting (red curve) of the magnetic susceptibility data of Cs ₁₀ Tl ₆ SnO ₃ at 1T (black circles)	194
A2.14 Curie-Weiss fitting (red curve) of the magnetic susceptibility data of Cs ₁₀ Tl ₆ SnO ₃ at 3T (black circles)	195
A2.15 Curie-Weiss fitting (red curve) of the magnetic susceptibility data of Cs ₁₀ Tl ₆ SnO ₃ at 5T (black circles)	195
A2.16 Curie-Weiss fitting (red curve) of the magnetic susceptibility data of Cs ₁₀ Tl ₆ SnO ₃ at 7T (black circles)	196

List of Tables

6.1	Crystal and structure refinement data of BaAu _{0.5} Pt _{0.5} and BaAu.	59
6.2	Atomic coordinates and equivalent isotropic displacement parameter $U_{eq} / \text{\AA}^2$ of BaAu _{0.5} Pt _{0.5} and BaAu.	60
6.3	Atomic displacement parameters $U_{ij} / \text{\AA}^2$ for BaAu _{0.5} Pt _{0.5} and BaAu . . .	60
6.4	Selected bond distances / \AA^2 and angle / $^\circ$ of BaAu, BaAu _{0.5} Pt _{0.5} and BaPt [96]	62
6.5	Binding energies of the Pt (4 <i>f</i>) and Au (4 <i>f</i>) levels of BaAu, BaAu _{0.5} Pt _{0.5} and BaPt [96]	66
6.6	The crystallographic and structure refinement data for SrAu _{0.5} Pt _{0.5} and CaAu _{0.5} Pt _{0.5}	70
6.7	Atomic coordinates and equivalent isotropic displacement parameter $U_{eq} / \text{\AA}^2$ for SrAu _{0.5} Pt _{0.5} and CaAu _{0.5} Pt _{0.5}	71
6.8	Atomic displacement parameters $U_{ij} / \text{\AA}^2$ for SrAu _{0.5} Pt _{0.5} and CaAu _{0.5} Pt _{0.5}	71
6.9	Selected bond distances / \AA^2 and angle / $^\circ$ of BaAu _{0.5} Pt _{0.5} , SrAu _{0.5} Pt _{0.5} and CaAu _{0.5} Pt _{0.5}	72
6.10	Binding energies of the Pt (4 <i>f</i>) and Au (4 <i>f</i>) levels of BaAu _{0.5} Pt _{0.5} , SrAu _{0.5} Pt _{0.5} and CaAu _{0.5} Pt _{0.5}	75
7.1	The crystallographic and structure refinement data for Cs ₁₈ Tl ₈ O ₆	82
7.2	Atomic coordinates and equivalent isotropic displacement parameter $U_{eq} / \text{\AA}^2$ for Cs ₁₈ Tl ₈ O ₆ and Hf ₁₀ Ta ₃ S ₃	83
7.3	Atomic displacement parameters $U_{ij} / \text{\AA}^2$ for Cs ₁₈ Tl ₈ O ₆	83
7.4	Selected bond distances / \AA^2 and angle / $^\circ$ of Cs ₁₈ Tl ₈ O ₆	87
7.5	The ELF distribution η in Cs ₆ Tl ₈ neutral molecule.	101
7.6	The crystallographic and structure refinement data for Cs ₄ Tl ₂ O.	103

7.7 Atomic coordinates and equivalent isotropic displacement parameter $U_{eq} / \text{\AA}^2$ for $\text{Cs}_4\text{Tl}_2\text{O}$	104
7.8 Atomic displacement parameters $U_{ij} / \text{\AA}^2$ for $\text{Cs}_4\text{Tl}_2\text{O}$	104
7.9 Bond distances [\AA] of $[\text{Tl}_6]^{6-}$ clusters in various compounds.	106
7.10 The crystallographic and structure refinement data for $\text{K}_{21}\text{Tl}_{22}\text{O}_2$	113
7.11 Atomic coordinates and equivalent isotropic displacement parameter $U_{eq} / \text{\AA}^2$ for $\text{K}_{21}\text{Tl}_{22}\text{O}_2$	114
7.12 Atomic displacement parameters $U_{ij} / \text{\AA}^2$ for $\text{K}_{21}\text{Tl}_{22}\text{O}_2$	115
7.13 Selected bond distances / \AA^2 in $\text{K}_{21}\text{Tl}_{22}\text{O}_2$	117
8.1 The crystallographic and structure refinement data for $\text{Cs}_{10}\text{Tl}_6\text{SiO}_4$, $\text{Cs}_{10}\text{Tl}_6\text{GeO}_4$ and $\text{Cs}_{10}\text{Tl}_6\text{SnO}_3$	129
8.2 Atomic coordinates and equivalent isotropic displacement parameter $U_{eq} / \text{\AA}^2$ of $\text{Cs}_{10}\text{Tl}_6\text{SiO}_4$ and $\text{Cs}_{10}\text{Tl}_6\text{GeO}_4(*)$	130
8.3 Atomic coordinates and equivalent isotropic displacement parameter $U_{eq} / \text{\AA}^2$ of $\text{Cs}_{10}\text{Tl}_6\text{SnO}_3$	131
8.4 Selected bond distances / \AA^2 and angles / $^\circ$ of $\text{Cs}_{10}\text{Tl}_6\text{TtO}_4$ (Tt = Si, Ge) and $\text{Cs}_{10}\text{Tl}_6\text{SnO}_3$	134
8.5 Lengths of the space diagonals (Tl–Tl) of $[\text{Tl}_6]^{6-}$ octahedra / \AA in various compounds.	135
9.1 The crystallographic and structure refinement data for $\text{Cs}_{22}\text{In}_6(\text{SiO}_4)_4$	143
9.2 Atomic coordinates and equivalent isotropic displacement parameter $U_{eq} / \text{\AA}^2$ for $\text{Cs}_{22}\text{In}_6(\text{SiO}_4)_4$	145
9.3 Atomic displacement parameters $U_{ij} / \text{\AA}^2$ for $\text{Cs}_{22}\text{In}_6(\text{SiO}_4)_4$	147
9.4 Selected bond distances / \AA^2 and angles / $^\circ$ of $\text{Cs}_{22}\text{In}_6(\text{SiO}_4)_4$	148
9.5 Bond distances of $[\text{In}_6]^{6-}$ octahedra / \AA in various compounds.	150
A1.1 Scalar relativistic (column 5 non-relativistic) unrestricted open shell Kohn-Sham calculations of the Cs_6Tl_8 cluster (PBE+functional).	185
A1.2 Two-component relativistic DFT calculations of the Cs_6Tl_8 cluster, applying the PBE and the B3LYP functional.	186
A1.3 Scalar relativistic unrestricted open shell Kohn-Sham calculations of the Cs_6Tl_8 cluster, applying the B3LYP hybrid functional.	187

Part I.

Introduction

1. Introduction

1.1. Theory of Relativity and Its Effects on the Chemistry of Heavy Elements

Significant peculiarities of chemical and physical properties of heavy elements cannot be described without taking into account the relativistic effects. The anomalously small size of the sixth-row transition elements and many other irregular features in chemistry and physics of these elements are usually explained in two ways: (i) the *lanthanide contraction*, i.e. the diminished shielding of the nucleus due to the inclusion of the 4*f* electrons (*f*-shell effect) causing a contraction of the valence shells and (ii) the large *relativistic effects*, which occur due to the high speed of electrons when they move near a heavy nucleus.

In 1905 Albert Einstein published his paper about the special theory of relativity and showed that the mass of any moving object increases with its speed. However, in 1926 Erwin Schrödinger [1] formulated his famous equation disregarding the dependence of electron mass on its velocity. Nevertheless, 10 years earlier Sommerfeld taking into account relativistic effects had already explained the fine-structure of hydrogen [2, 3]. Finally, in 1928 Dirac achieved the synthesis between quantum mechanics and relativity [4-6]. He showed spin-orbit coupling to be a purely relativistic effect and that all electrons, including *s* electrons, have *angular* momentum, consisting of a “*sum*” of “*orbital*” and “*spin*” angular momentum.

In the context of electronic structure calculations, the difference between non-relativistic (Schrödinger) and relativistic (Dirac) quantum mechanics treatments is denoted as “relativistic effects”, where are distinguishes three aspects:

1. Direct effect: A *contraction of s and p orbitals* occurs due to the relativistic mass increase together with the decrease of the Bohr radius.

$$a_0 = \frac{4\pi\epsilon_0\hbar^2}{mZe^2} \quad (1.1)$$

2. Direct effect: The *spin-orbit splitting* in the relativistic treatment become relevant, and instead of the orbital angular momentum \vec{l} and the spin angular momentum \vec{s} their vector sum $\vec{j} = \vec{l} + \vec{s}$ must be used.
3. Indirect effect: An *expansion of d and f orbitals* occurs because the *s* and *p* atomic orbitals, both inside and outside the *d* and *f* atomic orbitals, have contracted screening the nuclear attraction experienced by electrons in the latter orbitals.

When discussing the first effect in more detail it is necessary to emphasize that the mass of a particle increases as its speed approaches the speed of light. It is the *s* electron with no orbital angular momentum that approaches the nucleus most closely and therefore gains the highest velocity. For the heavy atoms (Z very large, a_0 very small) the inner $1s$ and $2s$ electrons have speeds close enough to that of light to experience a substantial increase in mass. As a result, a_0 is further reduced and these electrons spend even more time near the nucleus, leading to contracted mean radii and lower orbital energies. With this contraction of the inner *s* shells, the outer *s* electrons also can get closer to the nucleus and are affected similarly. The effect on *p* orbitals shows a similar but smaller trend. Furthermore, a treatment according to Dirac shows that the degeneracy of *p* orbitals is lifted, splitting them into two sets, $p_{1/2}$ and $p_{3/2}$. The magnitude of the contraction of the $p_{1/2}$ subshell is comparable to that of $s_{1/2}$, while the $p_{3/2}$ subshell contracts much less. Therefore, the relativistic effects are one of the reasons for a substantial stabilization of the *s* and *p* shells. Another reason is classical shell-structure effects of *d*- and *f*-shells contraction simultaneously, which experience the elements of the sixth row of the periodic table, in particular gold, platinum and mercury. Such, a nuclear charge drastically enhanced by 24, which is only weakly screened by respectively added *d*- and *f*-electrons.

The spin-orbit coupling, being the second relativistic effect, is the interaction of the electron spin with the angular momentum due to the orbital motion of the electron. Its strength is proportional to the electric field gradient in the atom. This

spin-orbit energy, which is often observed by the splitting of spectral lines, becomes large for the heavy elements. Indeed, it is convenient to take this spin-orbit energy as a measure of the need to use relativistic theory for describing chemical phenomena. As it was already mentioned before, except for the *s* orbitals, where there is no orbital angular momentum, the spin-orbit interaction divides a shell of a given *l* into subshells with total angular momentum $j = l - \frac{1}{2}$ and $j = l + \frac{1}{2}$. For example, the case with $l = 1$ and $j = \frac{1}{2}$ is called $p_{1/2}$. In this case the magnetic quantum number m_j (or the component of j along a given direction) may assume two possible values $+\frac{1}{2}$ and $-\frac{1}{2}$. Therefore, the $p_{1/2}$ shell may accommodate two electrons. Similarly the $p_{3/2}$ shell may receive up to four electrons with m_j equal to $+\frac{3}{2}$, $+\frac{1}{2}$, $-\frac{1}{2}$, or $-\frac{3}{2}$. Due to spin-orbit splitting the $p_{1/2}$ shell lies below the corresponding $p_{3/2}$ shell and is therefore filled first. The spin-orbit interaction can also be treated as a magnetic interaction, but with the magnetic field generated by the orbital motion of an electron within the atom itself. The relativistic effect on *p* bonding should be most prominent for thallium, where the atom has a single $p_{1/2}$ valence electron.

The shells with higher angular momentum, *d* and *f*, experience mostly an "indirect" relativistic effect, which is brought about by the relativistic relaxation of the other shells. In particular, the contraction of the *s* and *p* semicore (e.g., the *s* and *p* shells with the same quantum numbers and about the same spatial extent as the *d/f* shell in under consideration, albeit with much different energy) will lead to a more effective shielding of the *d* and *f* orbitals and thus to an energetic destabilization.

Both effects, the *4f* shell orbital contraction and the relativistic contraction of *s/p* shells, are of the same general magnitude, with the latter becoming more important for the elements substantially heavier than the lanthanides [7, 8]. In the case of the *5d* orbitals, however, the relativistic effect is in the opposite direction: the filled *4f* shell contracts the *5d* orbital, but the relativistic effects expand it. Nevertheless, one can regard the superposition of relativistic and the particularly strong orbital effects encountered by platinum, gold and mercury as responsible for the peculiarities observed for these elements.

The consequences of relativistic effects for the chemical properties of elements in the periodic table have been widely discussed by Grant [9], Pyykkö and Desclaux [10], and recently by Jansen [11, 12]. In particular, P. Pyykkö in

series of reviews [13-18] has expanded the realm of possibilities regarding experimental results. M. Jansen, in his turn, has shown the influence of relativistic effects especially on the chemistry of gold and platinum based on experimental evidence [11, 12]. The first theoretical relativistic calculations of atomic structures by I. P. Grant [9] and, more comprehensive, by J. P. Desclaux [19] provided a first quantitative basis for studying the significance of the relativistic motion for the chemical and physical properties of the elements. Since then a number of thorough review essays [8, 20-24] and monographs [25-30] have been published over the last decades featuring the achievements of theory. Moreover, the whole bibliography of this particular field is unusually well documented by P. Pyykkö in the up-to-date version of the bibliography being available on-line in the world-wide web [31]. But the essential conclusion, that can be derived, is that calculations based on the Schrödinger equation are not adequate for a discussion of the chemical properties of the heavy atoms and that these can only be described by the Dirac equation, or some approximations to it.

Qualitatively, the effects resulting from taking the dependence of the electron mass on its velocity into account can be estimated from the results of Grant [9] and Desclaux [19]. An illustrative graph of the 6s orbital contraction as function of atomic number has been published by Pyykkö and Desclaux [10] (Fig. 1.1), demonstrating that gold and platinum show a conspicuously large relativistic 6s orbital contraction.

The relativistic effects on the orbital energies and thus on the excitation energies, ionization potentials and electron affinities, are very noticeable in many chemically relevant data, in particular the electronegativity. The relativistic effects on the size of an atom are reflected in the polarizability of the element [32, 33], and thus also in the bonding properties. Simple explanations of relativistic effects on molecular properties that would cover all cases are difficult to give [34], because many opposing effects of higher order (e.g. the relativistic change of the force constant, the relativistic second-order change of the slope of the potential curve, or the effect of differential electron correlation) have to be considered. But in many simple cases, in particular when the bonding mainly involves the outer *s* and *p* electrons, we experience a relativistic bond length contraction.

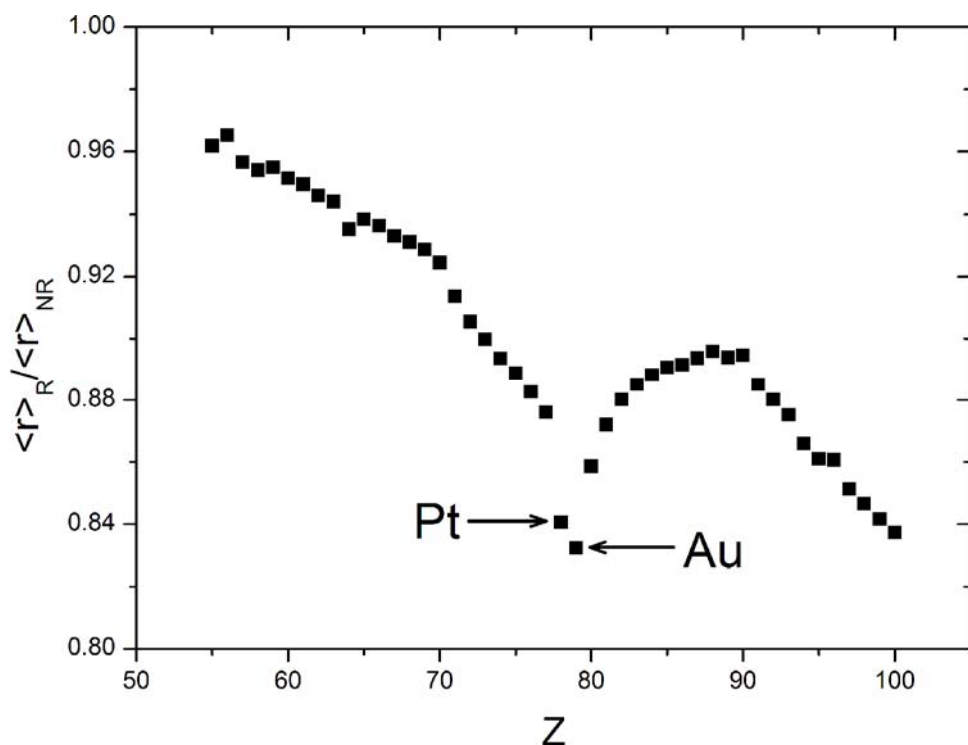


Figure 1.1. The relativistic contraction of the 6s orbital for the elements with Z from 55 to 100 based on calculations by Desclaux [19].

Already the data presented in Fig. 1.1 direct one's attention to the element *gold*. The exceptional position of gold is reflected by several other atomic and structural quantities also showing exceptional behaviour, e.g. the ionisation energy of gold is the highest among all elements of the same period (Au – 9.23 eV, e.g. Pt – 9.0 eV, Tl – 6.11 eV and Pb – 7.42 eV) [35]. Another, very conspicuous feature of gold is its highest electron affinity (2.31 eV) among all metals [36] (Fig. 1.2), approaching the values found for the halogens (e.g. iodine – 3.06 eV [36]). The lattice parameters of gold ($a = 4.078 \text{ \AA}$ [37]) are smaller than of the isostructural silver ($a = 4.086$ [37]). This all demonstrates the effect of relativistic stabilization of the 6s orbital of gold.

A classical example of the existence of gold as a monovalent anion is the formation of the salt-like compound CsAu. This compound was synthesized for the first time by W. Biltz and F. Weibke in 1938 in the form of orange-red crystals [38] during the investigation of the volume shrinkage when reacting gold with cesium and other alkaline metals. Later, the composition was confirmed by A. Sommer by distilling cesium on gold until saturation, indicating the formation of an alloy with the formula CsAu [39]. It was found that the compound

crystallizes in the CsCl type of structure [40-42]. The semiconducting properties such as a band gap of 2.6 eV have been determined from optical absorption spectra [41], X-ray photoemission [43-46] as well as photoelectron spectra [47]. The ionic bonding character of this compound with one extra localized electron on the gold atom, such forming a negatively charged auride ion, has been validated by means of ESCA [48], Mößbauer [47, 49, 50] and XANES [51, 52].

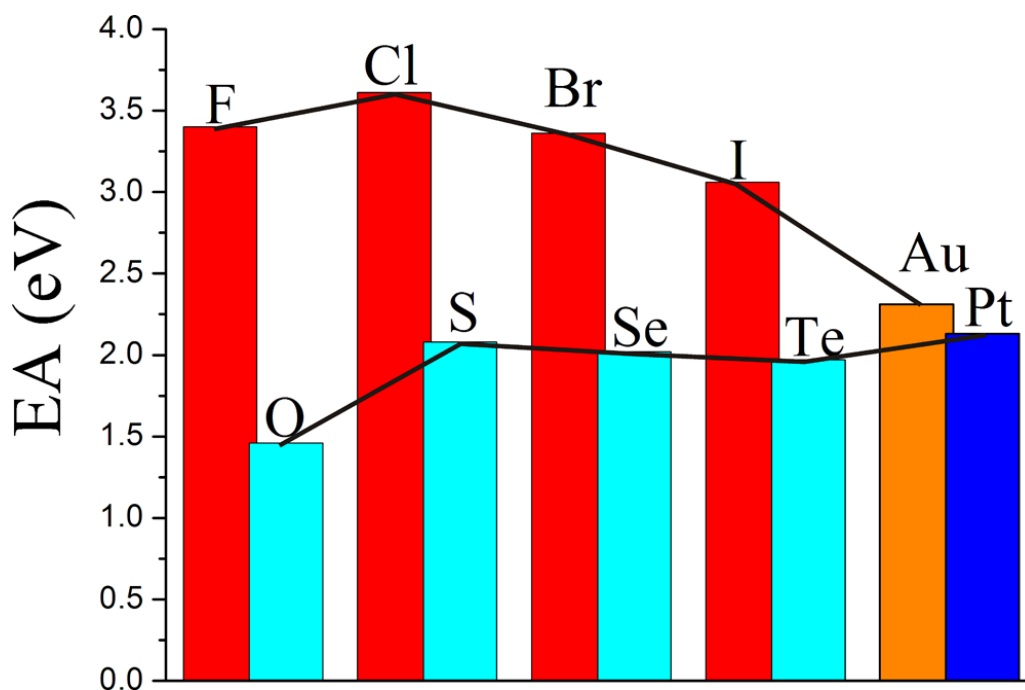


Figure 1.2. Electron affinity of halogens (red), chalcogens (cyan) as well as gold (orange) and platinum (blue).

The results of ^{133}Cs -NMR spectroscopy on the existence of localized electrons were pointed out to be in agreement with the ionic character of CsAu [53-55]. In accordance with the experimental results, band structure calculations showed a clear band gap, thus confirming the charge transfer from cesium to gold, independent from the method of calculation [56-65]. However, according to calculations without taking into account the relativistic contraction of 6s orbitals the compound would exhibit metallic properties, instead of semiconducting ones [61]. The ionic behaviour of bonding of CsAu has been observed also in the molten state [53, 54, 66-70]. Finally, the unusually high binding energy of CsAu molecules in the gas phase was attributed to the ionic character of Cs–Au bonds. Unfortunately, the ideal picture of pure ionic crystals has been significantly

disturbed by several reports. For example, it has been claimed that a significant amount of mutual replacement of Cs and Au is present [40], that the colour of a single crystal is black [42] and that a high absolute value or positive temperature coefficient of electrical conductivity is observed [41, 68, 71, 72].

The only way that unambiguously helps to prove the existence of gold anions as integral entities is by interdiffusion reactions that require transport of the intact anion over a long distance. Thus, the reactions between binary alkaline metal aurides and the corresponding alkaline metal oxides were investigated at temperatures significantly below the decomposition or melting temperatures of both reactants [51, 52, 73]. As a result, Cs₃AuO with an ideal hexagonal perovskite type of structure and in the form of transparent yellow-orange colour crystals has been formed in quantitative yields [51]. Since the acceptor levels available for accommodating an electron are associated with either Cs⁺ or O²⁻ states, and thus lie rather high, any alternative transport mechanism assuming decoupled diffusion of Au⁰ and e⁻ can be excluded. Other doubts were resolved by considering the formation of an insulating (ionic) or semiconducting compound with band gap 2.35 eV [74] from another two semiconducting compounds CsAu and Cs₂O (with band gaps of 2.6 eV [40] and 1.9 eV [75], respectively) and, thus, providing evidence for all valence electrons being localized. The analogous compounds Rb₃AuO and K₃AuO have been synthesized by similar routes [73, 76]. However, in contrast to the cesium compound, rubidium and potassium compounds are shiny black and opaque, and crystallize in the ideal cubic perovskite type of structure. In addition, the electronic structures of A₃AuO (A = Cs, Rb, K) have been characterized by optical absorption spectroscopy [74], Au L_{III} and L_I XANES [52, 76], magnetic susceptibility [73] and conductivity measurements [73]. The position of the absorption edges, as measured by XANES, correlates with the valence state and provides further justification to assign a valence of 1- to gold in A⁺₃Au⁻O²⁻ (A = Cs, Rb, K) [52]. Also it was shown that gold is similar to halogens not only by its electron affinity approaching the values proper for the halogens but also by featuring a similar chemistry [77-81]. Such ternary alkaline metal halogenide oxides M₃XO (M = K, Rb, Cs; X = Br, I) crystallize in the same type of structure showing pronounced similarity of crystal chemistry of auride, bromide as well as iodide [78]. The structural equivalence of halides and aurides, as seen in the isostructural CsAu, CsI, CsBr and CsCl, was demonstrated by forming solid

solutions (e.g. CsAu/CsBr) in the whole concentration range [77, 81]. The next similarity to halogens can be noticed from the ability of elemental gold to disproportionate in an alkaline environment by a redox process into Au^+ and Au^- [79, 80]. The synthesized auride aurates(I), $\text{Rb}_5\text{Au}_3\text{O}_2$, $\text{Rb}_7\text{Au}_5\text{O}_2$ and $\text{Cs}_7\text{Au}_5\text{O}_2$, represent the first members of a homologues series of general composition $[\text{MAu}]_m[\text{M}_3\text{AuO}_2]$, as can be deduced from their crystal structure. The presence of gold in these compounds in two different oxidation states was confirmed by Mößbauer spectroscopy and is supported by various band structure calculations [80, 82].

The mobility of auride ions has been investigated also in polar electrolytes. Lagowski *et al.* showed the existence of Au^- in a chemical environment by reacting gold and dissolved cesium in liquid ammonia [83, 84] and in ethylenediamine [85]. The auride ion was characterized by electrochemistry [84] and spectroscopy [83], but could not be isolated from the solution. In reaction with ligands, such as 2,2,2-crypt, in the liquid ammonia environment the precipitation of $(2,2,2\text{-crypt-M}^+)\text{Au}^-$ ($\text{M} = \text{Cs, Rb}$) has been formed [49]. The materials were measured by ^{197}Au -Mößbauer spectroscopy showing the chemical shifts and thus indicating the presence of anionic gold [49]. Also bulk CsAu easily dissolves in liquid ammonia forming transparent and very pale yellow colour solution [86]. The stability of Au^- perform the opportunity to execute metathesis reaction as well as to form a solid solvate. Such $[\text{NMe}_4]\text{Au}$ forms through metathesis reaction by substitution of Cs^+ cations by $[\text{NMe}_4]^+$ cations in the solution of CsAu in liquid ammonia. Thus, the resulting compound crystallizes in the form of colourless transparent crystals showing all prototypical properties of a salt-like solid [87] and being isostructural to the analogous bromide.

During slow evaporation of the solvent ammonia from a clear solution of CsAu, the crystals of auride are not precipitating directly, but a deep blue crystalline product of $\text{CsAu}\cdot\text{NH}_3$ forms first [82, 86]. The characteristic blue colour, which is reminiscent as the colour of electrons solvated by ammonia, is clearly indicating changes in the bonding situation. Mößbauer spectroscopy measurements showed that gold in $\text{CsAu}\cdot\text{NH}_3$ is in a less negative state than in CsAu, where it has a value of $1-$ [82]. This finding was confirmed by ^{133}Cs solid state NMR spectroscopy [88]. The measured signal shows inhomogeneous line broadening, and the nuclei display a frequency-shift-dependent spin-lattice

relaxation rate. Such behaviour can be explained by a partial charge transfer from gold to cesium, whether latter one is coordinated by ammonia.

In another and rather new field of auride chemistry, reactions with crown ethers [89, 90], gold(-I) can function as an acceptor in a hydrogen bond, $\text{N-H}\cdots\text{Au}$ [90]. Thus, the $\text{N-H}\cdots\text{Au}^-$ interaction satisfies both models equally, Au^- as a pseudohalide and Au^- as an electron-rich transition-metal centre.

All these experimental findings show that the main effects at the atomic orbital level are the energetic stabilization and the radial contraction of the $6s$ shell and the accompanying destabilization and expansion of the $5d$ shell. Thus, the relativistic (mainly) and orbital effects without any doubts influence the properties of gold itself and its compound.

After gold, *platinum* exhibits the second highest electron affinity among all metals (Fig. 1.2). While gold is the best compared to the halogens which also need one more electron to achieve a closed shell situation, for platinum the best group reference are the chalcogens which need two electrons for a closed shell. When comparing with the chalcogens, the electron affinity of platinum (2.13 eV [36]) even exceeds the corresponding value of sulphur (2.08 eV [36]), which is the highest among all chalcogens and as a typical non-metal readily forms divalent anions. Despite of that fact that all divalent anions are known to be intrinsically unstable with respect to the loss of an electron, recently several compounds have been synthesized, featuring platinum as separate anion Pt^{2-} [91-94].

The most conclusive approach has been to alloy platinum with the most known electropositive element, which is cesium. Following the synthesis route mentioned above Cs_2Pt has been obtained at a unexpectedly high temperature of 700 °C [91]. The compound adopts the Ni_2In type of structure and crystallizes in the form of red transparent crystals, and is very sensitive towards oxidation and hydrolysis. The charge distribution in Cs_2Pt cannot be derived from structural arguments and, therefore, band-structure calculations have been performed. Depending on the method of calculation, a well-pronounced band gap of 1.3–2.1 eV has been found, and the stabilization of the $6s$ orbital has been confirmed [91]. Experimentally the charge transfer from cesium to platinum has been confirmed by XPS investigations [95]. XPS spectra clearly show a significant shift of Pt photopeaks to lower energies, which correspond to a formal oxidation charge of -1.6 .

The evidence of the existence of platinum anions as integral entities in a solid state compound was strengthened by the synthesis of a series of barium-platinum compounds [92, 96, 97] as well. Barium is another electropositive metal, showing a low first ionisation potential, and therefore might stabilize platinides. By reacting the elements in equimolar ratio [96], BaPt, which had been earlier mentioned as possibly capable of existence [98], has been realized recently. The compound crystallizes in the NiAs structure type with an anomalously low c/a ratio of 1.15 and very short Pt—Pt bonds (2.7 Å). Again, an analysis of the band structure leads to a deeper understanding of the bonding, by representing BaPt as a first example of a Zintl phase where the polyanionic structure is established by a transition element. Bader and ELF analyses yield an approximate charge transfer of one electron per barium atom from barium to platinum [96]. Enriching the barium content, the Ba₃Pt₂ compound formed adopting the Er₃Ni₂ structure type [97]. In this compound platinum gained more valence electron from barium, thus approaching the closed shell situation of 5d¹⁰6s². A partial charge of (−1) can be assigned to platinum in both BaPt and Ba₃Pt₂, featuring Pt—Pt bonds [96, 97]. The platinide richest in barium Ba₂Pt is the first example of an intermetallic compound that adopts the CdCl₂ type of structure. The structural peculiarities (the Ba—Pt distance of 3.15 Å is in a good agreement with the sum of the ionic radii of 3.03 Å) as well as band structure calculations (Pt 5d and 6s bands are narrow and below the Fermi level) justify an assignment of charges according to (Ba²⁺)₂Pt^{2−}·2e[−] [92]. The structural increments of “negative platinum” in these barium compounds range from isolated atoms (Ba₂Pt), through dumbbells (Ba₃Pt₂), to chains (BaPt) [92, 96, 97]. Moreover, the negative oxidation state of these platinides was experimentally proved by ESCA (Electron Spectroscopy for Chemical Analysis) leading to a consistent formal description [Ba²⁺·e[−]]Pt[−], [(Ba²⁺)_{1.5}·1.5e[−]]Pt^{1.5−}, and (Ba²⁺·2e[−])₂Pt^{2−} [99].

Also the presence of platinum anions has been reported in more complex cluster compounds Pt₂In₁₄Ga₃O₈F₁₅ [94] and PtIn₇F₁₃ [93]. However, the oxidation state (2−) of Pt in the second compound has only been suggested and is based on structural and electronic peculiarities of the investigated compound. A more thorough analysis, including structural and electronic investigations, has been performed for the first compound Pt₂In₁₄Ga₃O₈F₁₅. The presence of platinum anion has been deduced on the basis of an MO diagram and the electron count for the Pt

atom. In this way, supposing covalent bonding in $[\text{PtIn}_6]^{10+}$, the 12 electrons can be assigned to Pt, suggesting the oxidation state (-2) [94]. Some hints from band structure calculations for a negatively charged Pt were found for CaPtIn_2 [100].

All these, up to now, not very numerous results show that relativistic effects without any doubts play a significant role for the structure and properties of platinum containing compounds. However, the relativistic contraction of the platinum 6s orbital is smaller than that for gold [10] and thus it becomes more difficult to achieve a closed shell situation.

However, these conspicuous experimental findings on gold and platinum and their compounds cannot be straightforwardly attributed to the “relativistic effects”, since both elements are unique in that they are the first elements that have experienced the *d* and *f* contractions at the same time. Thus, conventional orbital and relativistic effects are superimposed, and are difficult to separate. In contrast, spin-orbit coupling and its enhancement with growing nuclear charge, as already has been discussed, is of relativistic origin, exclusively [4, 5].

Due to the strong relativistic spin-orbit coupling, the degeneracy of the Russel-Saunders ground state of a $6p^2$ configuration is lifted and a diamagnetic ground state $6p_{1/2}^2$ (Dirac's notation) results. The concomitant lowering in energy is impressively reflected by the first ionization potential of lead exceeding the one of bismuth, which has a half filled p-shell (Fig. 1.3). For all corresponding pairs of lighter elements the reverse sequence in ionization potentials is observed. Thus compounds containing Tl^- should be good candidates to possess a closed shell $6p_{1/2}^2$ configuration in a chemical compound, whose being diamagnetic can only be understood in terms of relativistic quantum mechanics.

A number of alkali thallides featuring novel and interesting structural properties have been previously synthesized [101, 102]. However, no evidence for the existence of “isolated” thallium(-I) was obtained. With the objective of realizing solids containing isolated Tl^- anions, recently the systems Rb/Tl/O and Cs/Tl/O have been investigated [103-105]. The introducing of oxygen in binary alkali metal-thallium systems creates an additional degree of freedom as well as additional opportunities to form appropriate compositions and atom packings. Thus, the oxide thallides A_8Tl_8O ($A = \text{Cs, Rb}$) have been characterized structurally, featuring the formation of a $[Tl_8]^{6-}$ cluster anion in the shape of a bicapped

octahedron; in addition Extended-Hückel calculations have been performed [103, 104].

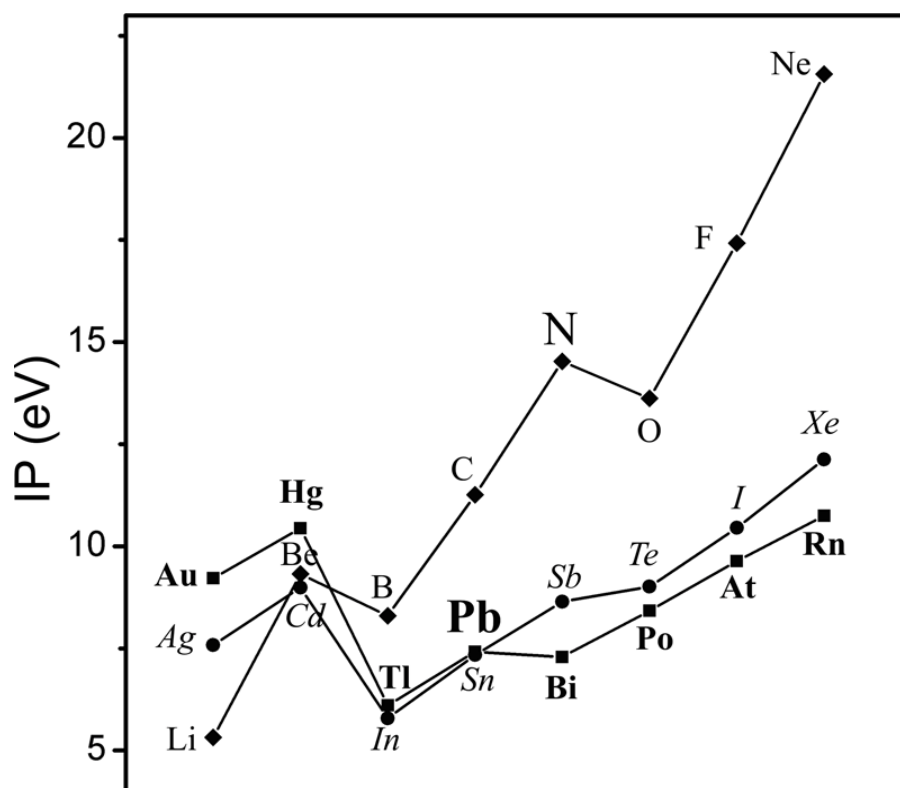


Figure 1.3. First ionisation potentials of the elements of 2nd (diamonds), 5th (circles) and 6th (squares) period (reproduced from [11]).

The closed shell character of the $[\text{Tl}_8]^{6-}$ cluster has been confirmed by reflectance spectroscopy, resistivity, magnetic measurements and by calculations. Other oxide thallides with the general formula $\text{A}_{10}\text{Tl}_6\text{O}_2$ ($\text{A} = \text{Rb}, \text{K}$) contain hypoelectronic $[\text{Tl}_6]^{6-}$ clusters, which are strongly compressed along one of their originally 4-fold axis [105]. The stability of such clusters-anions can be understood in the terms of the Jahn–Teller theorem.

1.2. Aims of the Present Work

The development of new solid state materials demands more and more understanding of properties as they relate to structure. Thus, the present work comprises the synthesis and characterization of new compounds containing

negatively charged gold, platinum and thallium. The intrinsic properties of these compounds should reveal new experimental evidence for the effects theoretically predicted for gold, platinum and thallium. Thus, the structures of the newly synthesized compounds have to be solved and the bonding situation needs to be analysed by band structure calculations. Also the physical properties of the investigated compounds should comply with the calculated electronic structures, thus providing further background for using theoretical tools for describing a complex structure of new compounds.

In 1939 Eduard Zintl developed the concept [106], which was named after him later, and which was subsequently generalized by Wilhelm Klemm [107, 108]. The classical formulation assumes that in a compound of elements with quite different electronegativities, the more electropositive element (metal) transfers all valence electrons to the more electronegative elements (nonmetal). Among all transition metals, gold and platinum possess the highest electron affinities which are 2.31 eV and 2.13 eV [36], respectively. Thus, these elements might be good candidates to realize the Zintl–Klemm concept in compounds as the electronegative species. The most suitable electropositive species are alkali and alkaline-earth elements. One of them is cesium, which is the most electropositive metal available in the Periodic Table. Barium is another electropositive metal showing a low first ionization potential. It is known that gold and platinum are mutually soluble elements which form a continuous solid solution in the liquid and the solid state over the whole concentration range [109]. Thus, the systematic study of ternary Ba–Au–Pt, or the quasibinary system BaAu–BaPt is required when aiming at the formation and characterization of $\text{Ba}^+_2\text{Au}^-\text{Pt}^{2-}$, where the transition of charge from electropositive barium to electronegative gold and platinum takes place.

In accordance with the general motivation of the present work, the formation of a closed shell $p_{1/2}^2$ configuration in a chemical compound is required. Such configuration being diamagnetic can only be understood in terms of relativistic quantum mechanics. Thus, such species as TT^- anions should be good candidates to achieve such an electronic state.

Our approach to generate new thallium ions, in particular the elusive monoatomic anion, includes increasing the compositional and structural degrees of freedom by introducing additional anionic species. Thus oxygen as well as other

anions (e.g. SiO_4^{4-}) can be used for generating additional degrees of freedom. This offers opportunities to realize an isolated Tl^- as well as other stable and structurally new anionic thallium species.

Thus, following such specific ideas, which are in accordance with the general motivation of the present work, mainly $A\text{-Au-Pt}$ ($A = \text{Ba}, \text{Sr}, \text{Ca}$), Cs-Tl-O and Cs-Tl-Tt-O ($\text{Tt} = \text{Si}, \text{Ge}, \text{Sn}$) systems were investigated. In addition, initial explorations of K-Tl-O and Cs-In-Si-O systems show a unique chemistry of both thallium and indium metals.

Part II.

General Part

2. Apparatus and Experimental Conditions

2.1. Handling of Air-Sensitive Materials

Due to relying on the extremely air- and moisture sensitive character of alkali-, alkaline earth metals, alkali metal oxides as well as products presented in the present work, all experimental stages have to take place under very good inert conditions. Thus the mentioned substances were handled with the help of the Schlenk technique together with a vacuum line setup, or in a glove box.

2.1.1. Vacuum Line Setup

The Vacuum Line Setup consists of a vacuum line, a protective gas line filled with argon, and several connectors to connect the reaction vessels.

The vacuum line is made from Duran glass and is presented in Fig. 2.1. At one side a two-stage rotary vane vacuum pump (type TRIVAC D8B, LEYBOLD VACUUM GmbH) is connected, creating an end vacuum of 2×10^{-3} mbar. The vacuum was constantly controlled by a Pirani manometer (Thermovac TM 20, LEYBOLD VACUUM GmbH) in the $10^{-3} - 10^3$ mbar measurement range. A high-frequency vacuum analyzer (VP 201, G. Lauer GmbH) was applied to check the leakage of joints as well as glass vessels. The reaction vessels that are connected to one of the connectors through the glass spirals and glass bends could be evacuated or filled with a protective gas, which was cleaned in the gas cleaning installation (Fig. 2.2). To isolate the system, the joints were treated with high-vacuum grease (APIEZON PRODUCTS M&I MATERIALS LTD). Before use the requested

vessels were heated several times by a gas flame of an earth-gas-burner, where at the same time the whole system was evacuated. Between heating steps the vessels were filled with argon.

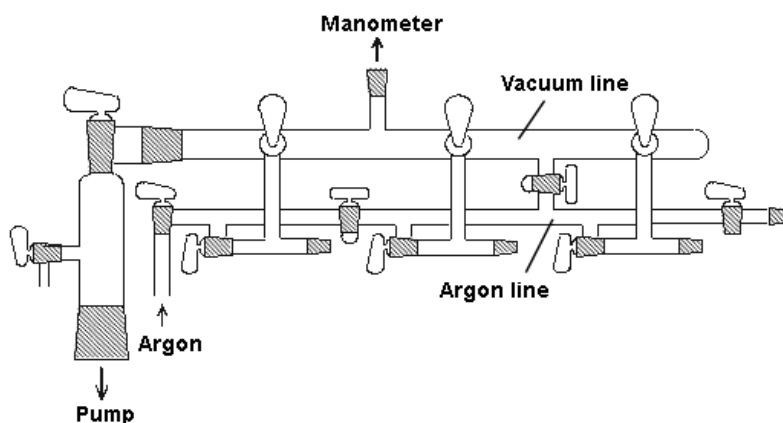


Figure 2.1. Vacuum line setup.

As a protective gas, within the scope of the present work, argon was used, because of higher density in comparison to air created protection for open vessels in the gas stream. Pure argon (5.0, provided by Low-Temperature Service Group, Max Planck Institute Stuttgart) is additionally let through the copper pipes to a specially constructed cleaning setup (Fig. 2.2), where the traces of oxygen and humidity have been completely removed. Firstly the argon passing through the bubble counter filled with paraffin oil (1) to control the gas stream, and subsequently to four drying tubes. The first drying tube (2) is filled with a blue gel and used for preliminary drying. Afterwards the argon passes through the second drying tube (3), which contains potassium hydroxide and absorbs oxygen containing gases (especially carbon dioxide). The molecular sieve (3 Å) in the next drying tube (4) absorbs moisture and carbon hydrides. To remove the remaining moisture traces the last drying tube (5) is filled with phosphor pentoxide (sicapent). After passing through all drying tubes (made from Duran glass) the argon reaches the drying tube (Quartz) (7) filled with a titanium sponge and heated up to 750 °C by a tube oven, where the rest of oxygen as well as nitrogen were removed. The manometer (8) filled with paraffin oil is used to protect the whole setup from overpressure. Afterwards, the dried argon enters the protective gas line part of the whole vacuum line setup.

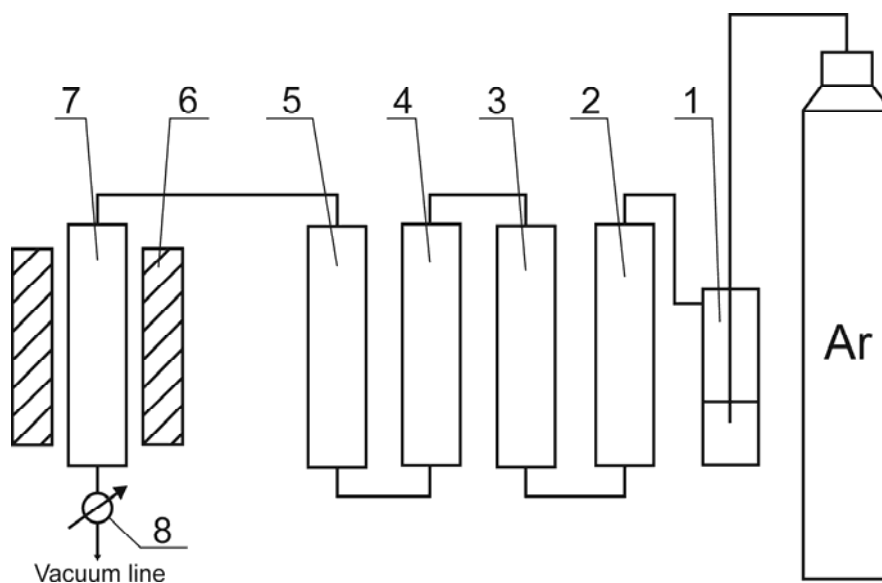


Figure 2.2. Schematic representation of argon cleaning installation.

All important operations under inert conditions were accomplished by use of the standard apparatus (Fig. 2.3) or a drying tube (Fig. 2.4), which are based on the technology developed by Schlenk [110] for handling air sensitive substances.

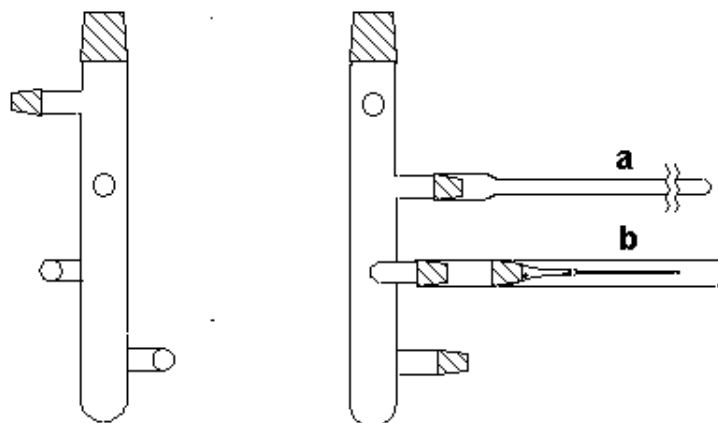


Figure 2.3. Schlenk apparatus (upper joint has size 29; the rest joints have size 14.5; a – ampoule for storing the substance; b – glass capillary for X-ray analysis).

These apparatuses provide possibilities for substance homogenization using a dried glass rod as well as dividing a sample into smaller amounts by sealing smaller peaces into glass ampoules (5–10 mm in diameter) (see Fig. 2.3). Also it is

possible to fill capillaries for X-ray analysis with the help of the Schlenk apparatus shown in Fig. 2.3. For open apparatuses all operations were performed under the flow of dried argon. The drying tube (Fig. 2.4) was used for drying the educts before reaction.

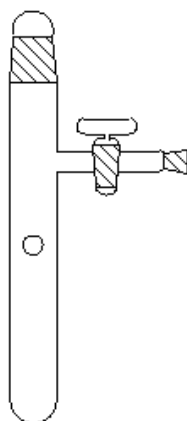


Figure 2.4. Drying tube (Length ca. 40 cm, diameter ca. 3 cm).

2.1.2. Glove Box

The operations, which could not be performed using the vacuum line setup (e.g. weighing of air sensitive substances or pressing the pellets), were performed in a Glove Box. The argon filled glove box MB 150B-G-II (M. Braun GmbH, Munich, Germany) was used during experimental work. The inert gas was sent through the molecular sieve and copper contact for cleaning from humidity as well as oxygen. The atmosphere inside the glove box was controlled by the gas analyzers and achieved H₂O and O₂ levels less than 0.1 ppm. Apparatus and samples can be taken inside and outside the glove box through a special airtight chamber, which can be evacuated.

2.2. Reaction Vessels

The Duran glass does not react with the alkali metals up to 400 °C and therefore Duran glass tubes can be used to store material for a long time. The

reaction and transporting vessels were always heated with the flame of a burner in a dynamic vacuum (2×10^{-3} mbar) before use.

Tantalum (Plansee SE, Reutte, Austria) does not react with alkali metals up to approximately 850 °C and with alkali-earth metals up to 1200 °C. Firstly, a long tube was cut into smaller pieces, which were sealed at one side. Before use, the tantalum vessels (latter ampoules) were treated as follows: the ampoules were put into diluted HF acid (5%) for 2-3 hours and then thoroughly washed with water. Afterwards the ampoules were heated at 1100 °C for 12 h in a dynamic high vacuum ($\sim 10^{-5}$ mbar) and stored the whole time under argon. The in this way handled tantalum ampoules were filled with the reaction mixture and tightly sealed under argon at the open side with the help of a special arc welder (Fig. 2.5). In order to prevent oxidation, the tantalum tubes were encapsulated under inert gas (e.g. argon) in Duran (for reaction temperatures < 500 °C) or silica jackets (for reaction temperatures > 500 °C).

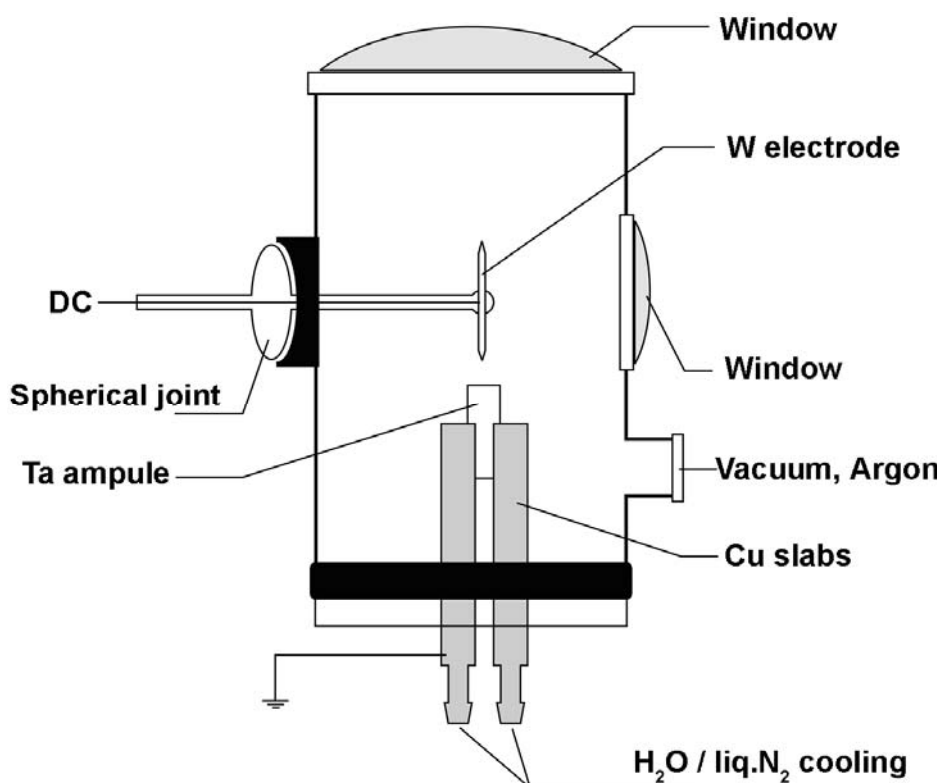


Figure 2.5. Arc welder for sealing tantalum ampoules.

2.3. Handling of the Alkali Metals

The extremely air sensitive character of alkali metals, their high ductility and their particularly low melting temperatures required special working techniques. Firstly, the relatively big quantity of alkali metal (2-3 g) from one ampoule was divided into four smaller ones using a special Schlenk apparatus (later Schlenk), which is shown in Fig. 2.6a. The ampoule with the alkali metal was wrapped with a copper wire, which had a loop on the upper end. The ampoule was opened in the argon stream, put inside a vessel together with the copper wire, and the upper end of the wire was hung to the hook of the joint cap. After flushing with argon the cap was placed on top and the whole apparatus was evacuated. Afterwards the apparatus was filled with argon, and the alkali metal was uniformly melted from top to bottom by fanning with a blue earth gas burner flame. Then the whole system was carefully evacuated, such that the alkali metal was slowly squeezed into the Schlenk due to the expanded inert gas in the ampoule. Afterwards, the empty ampoule was removed under the argon flow. The alkali metal in the Schlenk was heated with an earth gas burner flame until it became liquid, and then was divided among four ampoules with the desired amounts. Then the ampoules were sealed off from the apparatus one after another under argon flow.

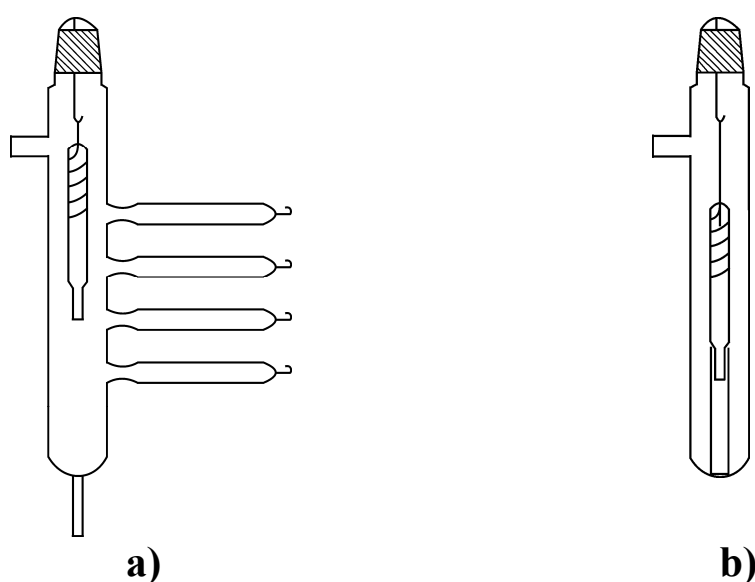


Figure 2.6. Apparatus: a) for dividing the alkali metals into desired amount; b) for weighing the alkali metals in tantalum ampoules.

The as described prepared ampoules containing alkali metal were directly used for weighing the metals for reactions using apparatus shown in Fig. 2.6*b*. The general experimental procedure was similar to the one described above. The difference was that the alkali metals were squeezed into Ta ampoules.

2.4. Preparation of Single Crystals for X-Ray Analyses

Preparation of the single crystals of the extremely air sensitive substances (e.g. $\text{Cs}_{18}\text{Tl}_8\text{O}_6$) for X-ray analysis was performed in the apparatus shown in Fig. 2.7 that has been specially constructed for searching and mounting single crystals into the capillaries using modified Schlenk technique. It consists of one long tube for separating the crystals and two rows, with a 90° angle in between, of three capillary holders for mounting the crystals.

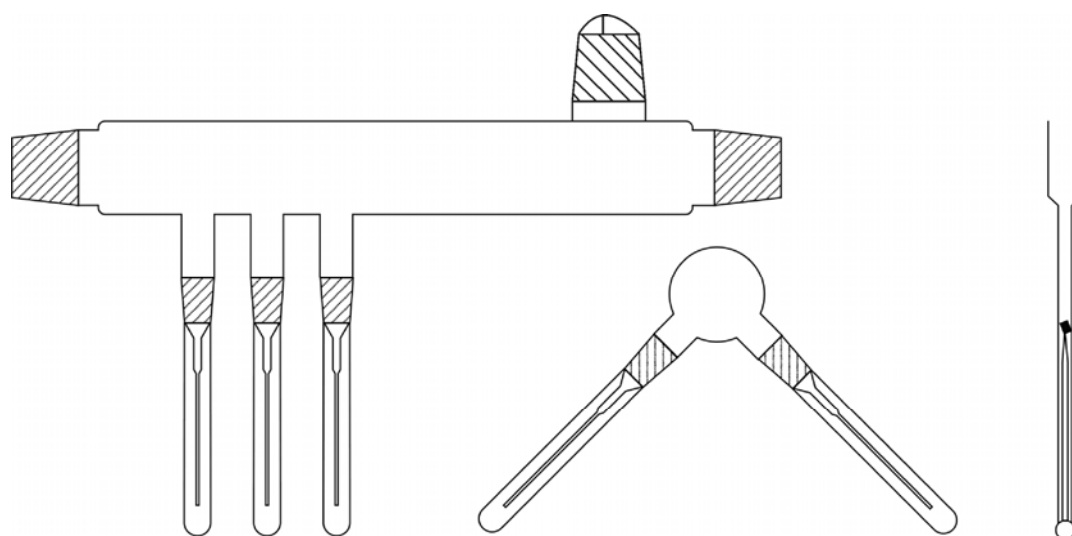


Figure 2.7. Single crystal mounting apparatus.

The long tube is filled with the substance under investigation through the upper joint: the ampoule with crystals was broken under argon stream and the substance was transferred into the apparatus. The suitable crystals were selected using a stereomicroscope, picked with a micro-needle and transported to one of the cones of the capillary holder. The Lindemann capillaries (Hildenberg, Malsfeld)

were fixed by Parafilm (PARAFILM®M) on the capillary holders after washing in hydrochloric acid, water, ethanol and heating at 120 °C overnight in dynamic vacuum. For better jamming a crystal at fixed position, a thin pulled-out capillary ($\varnothing_{OD} = 0.1$ mm) was inserted into a second thicker capillary ($\varnothing_{OD} = 0.2$ mm), and both were sealed together at the end (Fig. 2.7 *right*). After mounting the crystals, the capillaries were sealed under argon by a small hand burner after removing the protective jacket.

The preparation of crystals for the single crystal X-ray analysis was also possible in a glove box with the equipped stereomicroscope. According to this procedure, the suitable crystals were selected and transferred into Lindemann capillaries (described above and presented in Fig. 2.7 *right*) with the help of a micro-needle. The filled capillaries were sealed directly inside the glove box by a resistively heated platinum wire.

2.5. High-Temperature Facilities

The high temperature treatment of samples was performed in electrical resistance tube ovens with a FeCrAl heat conductor winding (Reetz GmbH, Germany), which can be used up to 1200 °C. The ovens were controlled by controller elements (Eurotherm GmbH, Limburg, Germany) while the temperature was monitored by Ni-CrNi thermoelements.

3. Analysis Techniques

3.1. Chemical Analysis

Chemical compositions of the samples (quantitative analysis) were determined using an Inductive Coupled Plasma - Optical Emission Spectrometer (ICP-OES; Vista Pro, Varian, Darmstadt, Germany). Firstly, the samples were weighed in nickel crucibles (ca. 10–15 mg) under inert atmosphere in a glove box. Afterwards the substance was dissolved in a HCl/HNO₃ mixture at 700 °C in a Teflon bomb together with the nickel container, and the solution was injected in the form of aerosol with argon, as a carrier gas, in a plasma torch.

3.2. Energy Dispersive X-ray Spectroscopy

The chemical composition was determined using a scanning electron microscope (XL30 TMP, Philips, Holland, tungsten electrode, 25 kV), equipped with an integrated EDAX-EDX system (EDX = Energy Dispersive X-Ray Analysis; EDAX, Wiesbaden, Germany) and with a S-UTW-Si(Li)-detector (S-UTW = Super Ultra Thin Window, polymer window, active detector surface 10 mm²). The self-absorption of this detector allows the detection of elements with an atomic number Z of more than 5, which corresponds to Bor. The qualitative as well as quantitative analysis of the energy spectra (resolution < 135 eV for Mn-K α /1000 cps and 65 eV for C) was carried out with the program system Phoenix (EDAX, Wiesbaden, Germany). The air sensitive samples were prepared in a glove box and transferred under argon to the electron microscope using special a transfer chamber.

3.3. Powder X-ray Analysis and Details about the Refinement of Lattice Parameters

All samples were examined by X-Ray powder diffraction using an automatic powder diffractometer (STADI-P, Stoe & Cie GmbH, Darmstadt, Germany) and D8 Advance (Bruker AXS GmbH, Karlsruhe, Germany) diffractometer. The two diffractometers are equipped with a molybdenum anode ($\text{MoK}\alpha_1$ radiation, $\lambda = 0.70930 \text{ \AA}$) for measuring samples, which contain strongly beam absorbing elements (e.g. barium and cesium). The samples were measured using the Debye-Scherrer geometry. In addition, for detecting low absorbing elements, a D8 Advance diffractometer equipped with a copper anode ($\text{CuK}\alpha_1$ radiation, $\lambda = 1.54060 \text{ \AA}$) was used.

The STADI-P diffractometer is equipped with a linear PSD (Position-Sensitive Detector) with a focused Ge single crystal monochromator. Powder patterns were collected at the $4 < 2\theta < 40$ degrees range in steps of $0.01 \text{ } 2\theta$ degree).

The D8 Advance diffractometer is equipped with a LynxEye – Super Speed Detector, which allows to perform extremely fast measurements ($1/200^{\text{th}}$ of the time required using a point detector) with the same resolution. Powder patterns were collected over the $4 < 2\theta < 40$ degrees range and a time period of at least 20 hours using this diffractometer.

The data were calibrated with respect to an external Si-standard, regarding 2θ zero points. Recording and analysis of the powder pattern was carried out with the help of the Stoe STADI-P software [111]. The identification of the measured substances was accomplished by comparing them with known substances, the crystallographic data of which were already stored in databases (e.g. PCPDFWIN [112]) or had been manually calculated according to known literature data using the Stoe STADI-P software [111].

The air sensitive samples were firstly filled into and afterwards sealed in the glass Lindemann capillaries ($\varnothing_{\text{OD}} = 0.2 \text{ mm}$, glass Nr. 14, Hilgenberg GmbH) under argon.

Scattering of the powder samples gives one-dimensional projections of the reciprocal space. As a consequence of the limited resolution of the detectors during recording of powder diffraction patterns, the information of single reflection intensity can be lost due to the overlap of closely located reflections. In addition, the overlap of symmetrically non-equivalent reflections occurs for compounds (structures) with low symmetry or with large lattice parameters. Thus, the methods of structure refinement, which depend on the calculation of structure factors based on powder data intensities, are usually not used for the solution of complex structures. However, the problem of overlapping of reflections can be avoided using a method developed by Rietveld [113, 114] for a known or postulated structural model. This procedure is also suitable for laboratory X-ray powder diffraction data. According to this method, the single data points of the measurement are used in the calculations instead of integrated intensities.

The other category of approaches is referred to as whole-powder pattern decomposition methods, in which the reflection positions are also determined from the space group and initial unit cell parameters, but the reflection intensities are treated as arbitrary unknowns. The Le Bail method [115] has been used in the present work to calculate and refine lattice parameters, profile parameters as well as background coefficients. Le Bail fitting was performed using the *TOPAS-Academic* software [116]. The programs Diamond [117] and Atoms [118] were used for graphical representation of the obtained structural information.

3.4. X-ray Diffraction on Single Crystals

The experimental single crystal data sets were collected with a SMART-APEX-I-diffractometer (Bruker AXS GmbH, Karlsruhe, Germany) and a dual wavelength three circle single crystal diffractometer – SMART-APEX-II (Bruker AXS GmbH, Karlsruhe, Germany) equipped with a CCD-detector. Both diffractometers are equipped with a graphite monochromator and molybdenum anode (MoK α_1 radiation, $\lambda = 0.7073 \text{ \AA}$). ω -scans were always performed. The cooling was provided by a Cryostream 700 plus system (Oxford Cryosystems, Oxford, United Kingdom) in the 80-500 K temperature range. The collection and reduction of data was carried out with the Bruker Suite software package [119].

Semiempirical absorption correction (SADABS [120]) was applied to correct the intensities for absorption effects. The structures were solved by direct methods and refined using the full-matrix least squares method from the SHELXTL program package [121].

The structure refinement includes the refinement of such parameters as: the atomic coordinates, the atomic displacement parameters (temperature parameter) as well as scale, weighting and extinction factors. The quality of the calculated structure model was evaluated according to the residual values R_1 (unweighted factor) and wR_2 (weighted factor). Both values are calculated according to equations:

$$R_1 = \frac{\sum \left| |F_0| - |F_c| \right|}{\sum |F_0|}, \quad (3.1)$$

$$wR_2 = \sqrt{\frac{\sum w (F_0^2 - F_c^2)^2}{\sum w (F_0^2)^2}}. \quad (3.2)$$

The goodness-of-fit is calculated by equation:

$$GooF = \sqrt{\frac{\sum w (F_0^2 - F_c^2)^2}{n - p}}, \quad (3.3)$$

where $w = (\sigma^2 F_0^2 + a^2 P^2 + b^2 P^2)^{-1}$ – weighting factor,

a and b – variables, $P = \frac{1}{3} F_0^2 + \frac{2}{3} F_c^2$;

n – number of independent reflections;

p – number of refined parameters;

F_0 – measured structure amplitude;

F_c – calculated structure amplitude.

During refinement the residual values should be as small as possible while the goodness-of-fit factor should only deviate slightly from “one”.

Before the accurate X-ray single-crystal structure analysis, the crystals were tested on a precession camera. A crystal has to be initially fixed and then adjusted

on the precession camera goniometer in such a way that a reciprocal crystal axis is oriented parallel to the rotation axis of the camera. A constant orientation of a crystal with respect to the film plane during the precession around the X-Ray beam is achieved by a mechanical coupling. In such a way an undistorted image of the reciprocal lattice could be obtained. Metric, type of lattice (integral extinction) and diffraction symbol (serial and zone extinction) of a measured compound could be definitely determined by taking several layers into account.

3.5. Thermal Analysis

The thermal analysis comprises the methods, which allow to measure the physical and/or chemical properties of a substance as a function of temperature. Thermogravimetry (TG), Differential Thermal Analysis (DTA) and Differential Scanning Calorimetry (DSC) were applied in the present work for distinguishing the thermal behaviour of the samples. The registration of thermal activities using DTA and TG were performed simultaneously on the STA 429 thermal analysis device (Netzsch GmbH, Selb, Germany). Differential Scanning Calorimetry (DSC) was performed with a computed-controlled DSC sensor (DSC 404 C Pegasus, Netzsch GmbH, Selb, Germany) equipped with a Pt10%Rh-Pt thermoelement (type S). As a sample holder the cylindrical form corundum (DTA-TG: $\varnothing_{OD} = 8$ mm, $l = 16$ mm; DSC: $\varnothing_{OD} = 7$ mm, $l = 4$ mm) or tantalum (DSC, $\varnothing_{OD} = 7$ mm, $l = 4$ mm) crucibles with lids were used. The samples were weighed in a glove box and transported in Schlenk apparatuses directly to the one of the thermal devices. The whole process took place under argon.

3.6. Measurements of Electrical Resistivity

Temperature – dependent resistivity measurements were performed using the *van der Pauw* method [122, 123]. The sample was ground into a powder and subsequently pressed into 1 mm thick disc-shaped pellet of 6 mm diameter. The pellet was then connected to four contacts of the resistivity measurement apparatus. A current of 10 mA (Keithley 2400 current source) was applied, and the voltage

was measured with a Hewlett Packard 34420 nanovoltmeter in a temperature range of 5–290 K at 5 K interval.

The evaluation of the activation energy E_A from resistivity measurements of powder samples is subjected to certain errors (influence of grain sizes; for air-sensitive materials there exists the danger of surface oxidation). Hence, the synthesized substances were classified only qualitatively as insulators, semiconductors, or metals.

3.7. Magnetic Susceptibility Measurements

The temperature – dependent magnetic susceptibility of the samples was measured using a SQUID magnetometer (Superconducting Quantum Interference Device, MPMS 5.5, Fa., Quantum Design, USA). The magnetometer allows to perform investigations in the temperature range 1.7 – 300 K in a homogeneous magnetic field up to 7 T. The specimen that had been ground into a powder was put into a gelatin capsule or sealed in a high purity synthetic fused silica (SUPRASIL®) tube under helium. The magnetization was corrected for the holder contribution.

The values of diamagnetic core corrections [124] were evaluated for all compounds. Also a diamagnetic correction for the Larmor precession of the electron pairs in the cluster orbitals of each cluster (χ_L , emu/mol-cluster) [125, 126] was calculated for cluster compounds investigated in the present work (e.g. $\text{Cs}_{18}\text{Tl}_8\text{O}_6$):

$$\chi_L = -0.79 Z_i \times 10^{-6} (r_{\text{av}}/a_0)^2, \quad (3.4)$$

where Z_i – number of skeletal electrons in the cluster;

r_{av} – average radius of orbitals (Å);

$a_0 = 0.529$ Å.

The *Curie-Weiss law* was applied to determine the amount of paramagnetic impurities for those diamagnetic compounds, which showed steep increase in susceptibility at very low temperatures, indicating the presence of paramagnetic species (Curie-tail):

$$\chi_{mol} = \frac{C}{T - \Theta}, \quad (3.5)$$

where χ_{mol} – magnetic susceptibility of the compound;

C – material specific Curie constant;

T – absolute temperature (K);

Θ – Weiss constant (K);

Curie constant can be described according to the expression:

$$C = \frac{\mu_0 N_a \mu^2}{3k_B}, \quad (3.6)$$

where μ_0 – magnetic constant ($\mu_0 = 1$ in CGS unit system);

N_a – the Avogadro constant;

k_B – Boltzmann's constant;

μ – magnetic moment, which is equal $1.73\mu_B$ for a single electron with spin quantum number $S = 1/2$;

μ_B – Bohr magneton.

Thus, calculating the amount of substance N using expression

$$N = \frac{3Ck_B}{\mu_0 \mu^2}, \quad (3.7)$$

and comparing it with the number of elementary entities per mole of substance (N/N_a), the amount of paramagnetic impurities in the investigated compounds was determined.

The program Origin [56] was used for the presentation of the measured results in a graphic form and for correlating them with different models.

3.8. Electron Spectroscopy for Chemical Analysis

ESCA (Electron Spectroscopy for Chemical Analysis) was applied to analyze valence states or partial charges of elements in synthesized compounds. For investigation the sample was ground into a powder and directly fixed on a conducting tape. The sample was prepared in a glove box and transferred to the

electron spectrometer AXIS ULTRA (Kratos, UK) using a special transfer chamber. ESCA spectra were recorded by using monochromatized AlK_{α} radiation (1486.58 eV). The vacuum during the measurements was kept at *ca.* $4 \cdot 10^{-9}$ mbar. To account for charging, the spectra were calibrated with respect to an internal C(1s) line, assuming its invariance for the investigated sample (binding energy of 285.0 eV). The peak profile was fitted with a Voigt function. Besides the strongest peak corresponding to the binding energy, one additional peak was admitted in each case, in order to account for the asymmetric shape.

4. Theoretical calculations

The quantum chemical calculations establish the basics to understand and describe the fundamental behaviour of matter at the molecular scale. The calculations can in some cases predict and explain hitherto unobserved chemical phenomena as a complement to the information obtained by chemical experiments.

In quantum chemistry, the system is described by a wavefunction which can be found by solving the Schrödinger equation. This equation relates the stationary states of the system and their energies to the Hamilton operator, which can be viewed as the recipe for obtaining the energy associated with a wavefunction describing the positions of the nuclei and electrons in the system. In practice the Schrödinger equation cannot be solved exactly and approximations have to be made. The approach is called “*ab initio*” when it makes no use of empirical information, except for the fundamental constants of nature such as the mass of the electron, Planck’s constant etc. that are required to arrive at numerical predictions. In spite of the necessary approximations, *ab initio* theory has the conceptual advantage of generality, and the practical advantage that (with experience) its successes and failures are more or less predictable.

The major disadvantage of “*ab initio*” quantum chemistry is the heavy demand on computer power. Therefore, further approximations have been applied for a long time, where empirical parameters are introduced into the theoretical model. This has led to a number of semi-empirical quantum chemical methods, which can be applied to larger systems, and give reasonable electronic wavefunctions so that electronic properties can be predicted.

4.1. Density Functional Theory

According to DFT (Density Functional Theory) the properties of a many-electron system can be determined by using functionals (function of a function) of the electron density instead of a complicated many-electron wavefunction, like in

Hartree-Fock (HF) theory. DFT is based on the Hohenberg and Kohn theorem [127] for non-degenerate ground states in the absence of a magnetic field. A practical application of this theory was developed by Kohn and Sham [128]. Within the framework of the Kohn-Sham approach, which is very popular nowadays, the total electron density is expressed as a sum of one electron densities of non-interacting electrons that generate the same density as any given system of interacting ones. The sum of the orbital energies is related to the total energy and includes the following terms: the kinetic energy of non-interacting electrons, the external potential acting on the interacting system (e.g. electron-nuclei interaction for a molecular system) and the interaction between the electrons, including coulomb, exchange and correlation parts. The advantage of using the electron density is that for the calculation of the electron-electron interaction, only three-centre integrals are involved, in contrast to HF, where four-centre integrals are needed.

4.2. Extended Hückel Method

The Extended Hückel Method (EHM) belongs to a group of semi-empirical methods of calculation in quantum chemistry. It was developed by Roald Hoffmann in 1963 for describing the hydrocarbons [129] and boron-nitrogen compounds [130]. It based on the Hückel method including the contribution not only π electrons (original method) but also σ electrons (extended method). The following approximations are used in EHM:

- 1) the molecular orbitals are considered as linear combination of atomic orbitals;
- 2) the Hamiltonian is given as the sum of one electron terms;
- 3) the total energy is calculated as the sum of one electron terms of the occupied molecular orbitals.

The method can be used for determining the molecular orbitals as well as the relative energy of different geometrical configurations and for computing band structures with reasonable CPU time requirements.

4.3. Selection of Functionals and Basis Sets

The major problem with DFT is that the exact functionals for the exchange and correlation are not known except for the free electron gas. Therefore, the local density approximation (LDA) was introduced, first formulated by Kohn and Sham in 1965 [128], in which the exchange-correlation energy is simply an integral over all space with the exchange-correlation energy density at each point, to be the same as in a homogeneous electron gas with that density. For spin-polarized systems this corresponds to the local spin density approximation (LSDA).

In general, the most popular functionals have a form appropriate for slowly varying densities: the local density approximation (LDA) and the generalized gradient approximation (GGA), the latter depending not only on the density but also on its gradient. In comparison with LDA, GGA's tend to improve total energies [131, 132], atomization energies [131-133], energy barriers and structural energy differences [134, 135].

Semiempirical GGA's can be remarkably successful for small molecules, but fail for delocalized electrons in the uniform gas and thus for simple metals. A first-principles numerical GGA can be constructed [136] by starting from the second-order density-gradient expansion for the exchange-correlation hole surrounding the electron in a system of slowly varying density, then cutting off its spurious long-range parts to satisfy sum rules on the exact hole. The Perdew-Wang 1991 (PW91) [137] functional is an analytic fit to this numerical GGA, designed to satisfy several further exact conditions [136]. PW91 incorporates some inhomogeneity effects while retaining many of the best features of LDA, but has its own problems. One of the problems appears because PW91 reduces to the second-order gradient expansion for density variations that are either slowly varying or small, and, thus, describes the linear response of the density of a uniform electron gas less satisfactorily than does LDA.

In contrast to the construction of the PW91 functional, which was designed to satisfy as many exact conditions as possible, a simple derivation of a simple GGA, also known as the PBE-functional [138], satisfies only those which are energetically significant. The problems present in PW91 are solved in PBE with a straightforward derivation of a simple new GGA functional in which all parameters

(other than those in LDA) are fundamental constants. Although the derivation depends only on the most general features of the real-space construction behind PW91, the resulting functional is close to numerical GGA. The PBE functional retains correct features of LDA, and combines them with the most energetically important features of gradient-corrected nonlocality. Although PBE and PW91 are very close-related, the first one is simpler and makes it easier to understand as well as apply. According to test calculations [138] DFT with PBE gives quite satisfactory results for solid state calculations in comparison to experimental data.

In quantum chemistry, the *basis set* usually refers to the combinations of mathematical functions used to represent the molecular orbitals, which are expanded as a linear combination of atomic orbitals and also described by such functions. Nowadays, Gaussian functions or linear combinations of them are used as the basis functions. To improve the variational degree of freedom of minimal (one basis function for each atomic orbital in the atom) basis sets further functions (double-zeta, triple-zeta) as well as polarization functions are added, which describe the distortion of the atomic orbitals in a molecular environment and are important for reproducing chemical bonding.

To simplify the complicated effects of the motion of the core electrons of atoms, effective core potentials (ECP) or pseudopotentials (PP) have been developed. In general, the pseudopotential is an effective potential constructed to replace the atomic all-electron potential such that core states are eliminated and the valence electrons are described by nodeless pseudo-wavefunctions. In this approach only the chemically active valence electrons are dealt with explicitly, while the core electrons are “frozen”, being considered together with the nuclei as rigid non-polarizable ion cores. Thus, the advantages of using PP are the reduction of basis set size and the ability to handle with a big number of electrons. Also, it is very easy to incorporate relativistic effects into ECP, which are important in describing heavier atoms.

The second particular-well suited set of basis functions, which helps to solve the resulting single-particle Kohn-Sham equations for extended systems like crystalline solids, is the plane wave (PW) basis set. The use of a PW basis set offers a number of advantages, including the simplicity of the basis functions, which make no a bias assumptions regarding the form of the solution, the absence of basis set superposition error, and the ability to efficiently calculate the forces on

atoms. These basis sets are used in calculations involving periodic boundary conditions. Different computational methods based on plane wave basis sets have been developed. Many of them use the Muffin-Tin (MT) approximation, which has been proposed by Slater in 1937 [139] to minimize the size of the basis set. According to the MT approximation the unit cell can be divided into non-overlapping spheres that are centered on the atomic positions and the remaining interstitial region. In the interstitial region the single electron wave functions can be expanded in terms of plane waves. In the atom-centered regions, the wave functions can be expanded in terms of spherical harmonics and the eigenfunctions of a radial Schrödinger equation. Such a use of functions other than plane waves as basis functions is termed the augmented plane-wave approach (APW). The problem of this approach is the dependence of the radial part of the eigenfunctions on the eigenenergy E , which is originally unknown. This makes the method inflexible and quite cumbersome. The linearized form of APW (LAPW) presented by Andersen [140] replaced the functions of the APW basis set by a linear combination of the functions and their energy derivatives (Taylor series). Due to the additional functions, the LAPW basis functions are flexible enough to represent all eigenstates in an energy region around the energy, for which the functions are evaluated. Recently, an alternative approach was proposed by Sjöstedt et al. [141], namely the APW+lo (local orbitals) method. Here the augmentation is similar to the original APW scheme but each radial wave function is computed at fixed linearization energy to avoid the non-linear eigenvalue problem that complicated the APW method. Thus only the condition of continuity needs to be fulfilled and the basis functions may contain a kink at the sphere boundary. The missing variational freedom of the radial wave functions can be recovered by adding another type of local orbitals containing a function and its derivative term.

4.4. Addressing Relativistic Effects

Relativistic effects are most accurately described within the four-component Dirac theory generalized to many-electron systems [29]. For practical applications this approach is not well suited for two reasons. On the one hand it is very costly, on the other hand it involves the charge-conjugated degrees of freedom for the

electrons, which is not necessary, as they have negligible influence on the stability and structure of chemical compounds.

From a practical point of view it is reasonable to account for relativistic effects by modeling the inner electrons of atoms with effective core potentials (ECPs) that are fitted to the results of relativistic all-electron calculations. This has become the standard way for inclusion of relativistic effects in self-consistent field (SCF) procedures. However, in most program systems this facility is restricted to scalar relativistic effects that include the effect of relativistic mass/velocity and the Darwin-shift, but omit spin-orbit coupling (SOC). The latter effect can efficiently be included by a second variational treatment [142] in the WIEN2k program [143], allowing to calculate SOC for periodic systems. In this approach the spin orbit term is set up in a subspace spanned by the scalar relativistic solution with about twice the number of the occupied orbitals but much less than the full basis. The proper treatment of SOC may require an improved basis set, in particular for semi-core states of heavy elements. Spin polarized calculations can provide both spin and orbital moments in magnetic materials [144].

Another treatment for molecular structures was realized within the TURBOMOLE program package [145, 146]. Matters are different when using ECPs covering also SO effects in SCF procedures: for this purpose the one-component formalism operating with orbitals has to be extended to a two-component formalism with complex orbitals (spinors). The program mentioned employs such a formalism, which accounts for spin-orbit effects (as well as for scalar relativistic effects) in a self-consistent manner by the use of effective core potentials. The resolution-of-the-identity approximation (RI) was applied for the Coulomb operator, which leads to significant savings for larger basis sets, such as the one used in the present work def2-TZVP (2-improved Default Valence Triple-Zeta plus Polarization).

4.5. Topological Analysis of the Electron Density

In the many-body system, the description of the complex electronic interaction between atoms in molecules and in the solid state is complicated. One powerful

technique for doing this is to decompose properties of the molecule or material into contributions from the individual atoms. Bader suggested an elegant way to do this partitioning [147]. The Quantum Theory of Atoms in Molecules (QTAIM) introduced by Bader approach is a quantum chemical model that characterizes the chemical bonding of a system based on the topology of the quantum charge density. In QTAIM an atom is defined as a proper open system, i.e. a system that can share energy and electron density, which is localized in the three dimensional space. Each atom acts as a local attractor of the electron density, and therefore it can be defined in terms of the local curvatures of the electron density. Bader's idea allows to divide charge density space within molecular and periodic systems into atomic (Bader) volumes. Each Bader volume contains a single charge density maximum, and is separated from other volumes by surfaces (also called zero-flux surfaces) on which the charge density is a minimum normal to the surface. This Bader partitioning has an advantage over other partitioning schemes (e.g. Mulliken population analysis) in that it is based upon the charge density, which is an observable quantity that can be measured experimentally or calculated. Furthermore, in a converged electronic structure calculation, the charge density is rather insensitive to the basis set used. In this regard, the Bader analysis is more robust than wavefunction-based population analysis methods.

Most current implementations of Bader's analysis are based upon a grid of charge density values [148-150]. This is particularly important for plane-wave-based DFT calculations, because it allows for the analysis of condensed phase systems with many atoms. In general the improved algorithm can be described as one, in which ascent trajectories along the charge density were followed between grid points to determine the Bader volumes. The constraint of ascent trajectories to the grid means that each point need be considered only once. The method is highly efficient, scales linearly with system size, and is robust with respect to the complex bonding topology found in condensed systems.

Analysis of the chemical bonding and electronic structure of the solid bodies have become an inseparable part of the system description. Besides QTAIM, the second most frequently used investigative tool is the ELF (Electron Localization Function). The ELF is based on the probability of finding an electron in the neighborhood space of a reference electron located at a given point and with the same spin. The analysis of ELF provides information about chemical attributes,

such as shell structure of the atoms, covalent bonding, multicentered bonding and lone pairs, etc. [151]. Thus, the ELF is often used for visualization and discussion of bonding properties in atoms and molecules [152, 153].

The ELF was introduced by Becke and Edgecombe as a derivative of the pair density for electrons of equal spin. The original formula is based on the Taylor expansion of the spherically averaged conditional same-spin pair probability density to find an electron close to a reference electron with the same-spin. The main aspect of this formulation is that the ELF in this way is a *property of the same-spin pair density*. Based on Hartree-Fock or Kohn-Sham orbitals, the probability density can be calculated as:

$$C(\vec{r}) = \frac{1}{2} \sum_i n_i |\nabla \varphi_i|^2 - \frac{1}{8} \frac{|\nabla \rho|^2}{\rho}, \quad (4.1)$$

where r – coordinates of position;

φ – orbital function;

ρ – electron density; $\rho = \sum_i n_i |\varphi_i|^2$.

After normalization on the values of the homogeneous electron gas with the same density and scaling the function between 0 and 1, the ELF can be defined as

$$ELF = \left\{ 1 + \left[\frac{C(\vec{r})}{C_h(\rho(\vec{r}))} \right]^2 \right\}^{-1}. \quad (4.2)$$

In density functional theory the pair density is not explicitly defined. Thus, the original formulation of ELF derived from the pair density is not applicable. Savin et al. [154] utilized the observation that the Kohn-Sham orbital representation of the Pauli kinetic energy density has the same formal structure as the expression $C(\vec{r})$ of Becke and Edgecombe. Thus, the equation for ELF can be represented as:

$$ELF = \left\{ 1 + \left[\frac{t_p(\vec{r})}{t_{p,h}(\rho(\vec{r}))} \right]^2 \right\}^{-1}, \quad (4.3)$$

where t_p – three-dimensional density of kinetic energy by Pauli;

$t_{p,h}$ – the kinetic energy density of a uniform electron gas of the same electron density.

In this case the pair density is not necessary for the derivation of ELF and the ground state energy of a system can be calculated on the basis of Kohn and Sham's approximation DFT using the electron density, because the kinetic energy of the electrons can be represented as a functional of the electron density.

Where the electrons are alone, or form pairs of antiparallel spins, the Pauli principle has little influence on their behaviour and the excess local kinetic energy has a low value. Therefore, the ELF is close to 1, whereas at the boundaries between such regions the probability of finding parallel spin electrons close together is rather high. Thus, the excess local kinetic energy has a large value and the ELF is small.

The topological analysis of ELF [155] provides information to classify the chemical bonds, allowing an absolute characterization of covalency versus ionicity to be obtained from the electron density. It complements and augments the theory of Bader [147].

5. Starting materials

5.1. Alkali and Alkaline-Earth Metals

5.1.1. Potassium

The commercial quality potassium metal (Sigma-Aldrich Chemie GmbH, Steinheim, Germany) was purified from coarse impurities by the liquating process. After removing the mineral oils by washing with petroleum ether, the piece of metal was put into vertical Schlenk apparatus with ampoules connected to it (Fig. 2.6a). After heating and melting with a Bunsen burner the liquid metal was divided into the desired amounts among the connected ampoules while the oxidized crust stayed in the main tube. The ampoules filled with potassium were sealed off under argon. Afterwards the purified potassium metal was additionally distilled two times in a dynamic vacuum.

5.1.2. Cesium

Cesium was synthesized from cesium chloride by reduction with Ca and distilled twice in vacuum [156]:



Firstly, cesium chloride (99%, Sigma-Aldrich Chemie GmbH, Steinheim, Germany) was pulverized in an agate bowl and filled, in alternating numerous layers, in an iron crucible together with calcium granulate (99.99 % Sigma-Aldrich Chemie GmbH, Steinheim, Germany), in the ration $\text{CsCl} : \text{Ca} = 2 : 1$. The highest layer was covered with a glass wool. The iron crucible had been connected to a

special Schlenk apparatus with already connected ampoules (similar to the presented in Fig. 2.6a) for collecting and two round flasks for purifying pure metal. The whole system had been evacuated, heated up to 450 °C at a rate of 50 °C/h and stayed at constant temperature for 8 hours. Then the reaction mixture was heated up to 850 °C at the same rate of 50 °C/h and annealed at this temperature for 2 hours. At about 600 °C elemental cesium was formed and could be distilled under vacuum out of the crucible. Immediately after the reaction was completed the whole apparatus was filled with argon and sealed off from the iron crucible. The cesium formed still contained impurities of calcium, which were removed by a second distillation. The yield of reaction is 90–95%.

5.1.3. Barium, Calcium, Strontium

Barium (99.99 %, Sigma-Aldrich Chemie GmbH, Steinheim, Germany), which was delivered already under argon could be used without further purification. Nevertheless, it could still contain 1-3 at.-% of hydrogen. Therefore, barium was additionally purified in tightly sealed Ta ampoules under argon. The ampoule with barium inside was heated stepwise up to 1100 °C in a quartz tube under dynamic high vacuum (12 h at 400 °C, 12 h at 750 °C and finally at 1100 °C until a final vacuum of $\sim 1-2 \times 10^{-5}$ mbar is reached). During heating at temperatures about 550 °C the hydrogen was released from the metal and started to diffuse through the walls of the Ta ampoules [157]. After cooling, the ampoule was opened in a glove box and the barium was divided into smaller portions and stored under argon in glass ampoules outside the glove box.

Strontium and calcium (99.99 %, Sigma-Aldrich Chemie GmbH, Steinheim, Germany) were distilled in special steel-distilling apparatus in dynamic high vacuum ($\sim 10^{-5}$ mbar) at 800 °C (stepwise heating, annealing firstly 12 h at 550 °C and finally 12 h at 800 °C) to remove the remaining hydrogen as well as other impurities. At the same time the pure appropriate alkaline earth metal has been condensed on water cooled copper finger. The heating in vacuum at 550 °C is important in order to remove hydrogen. Otherwise, the direct heating above the melting temperature of the alkaline earth metal leads to further hydrogen absorption.

5.2. Cesium Oxide

The preparation of cesium oxide Cs₂O was performed by reacting elementary alkali metals with stoichiometric amount of oxygen [158]:



Firstly, cesium metal was weighed by the difference method and put into the reaction vessel which had been connected to the vacuum line through gas dosimeter. Afterwards, the whole setup was evacuated and the required amount of oxygen introduced in small portions through the gas dosimeter in the system. However, initially the reaction product consisted of a mixture of not reacted cesium metal, cesium oxide, peroxide and hyperoxide. Therefore, to homogenise the end product and to produce the cesium oxide as a single phase the system was heated up to 120 °C during 24 h several times. Each time the resultant bulk material was crushed and mixed with the help of a warm brass rod. Finally, the excess alkali metal was distilled off. The purity of cesium oxide was controlled by the X-ray powder diffraction method (Fig. 5.1).

5.3. Tetrel Metal Dioxides

The commercially produced silicon dioxide SiO₂ (99%, Sigma-Aldrich, Riedel-de-Haën), germanium dioxide GeO₂ (99.999%, ChemPur, Jülich, Germany) and tin dioxide SnO₂ (99.999%, ChemPur, Jülich, Germany) in form of very fine powders were dried before use at 120 °C in dynamic vacuum at 10⁻³ mbar for 12 h and afterwards stored the whole time under argon to prevent the condensation of humidity on the surface. The purity of the tetrel metal dioxides used was controlled by the X-ray powder diffraction method (Figs. 5.2-5.4).

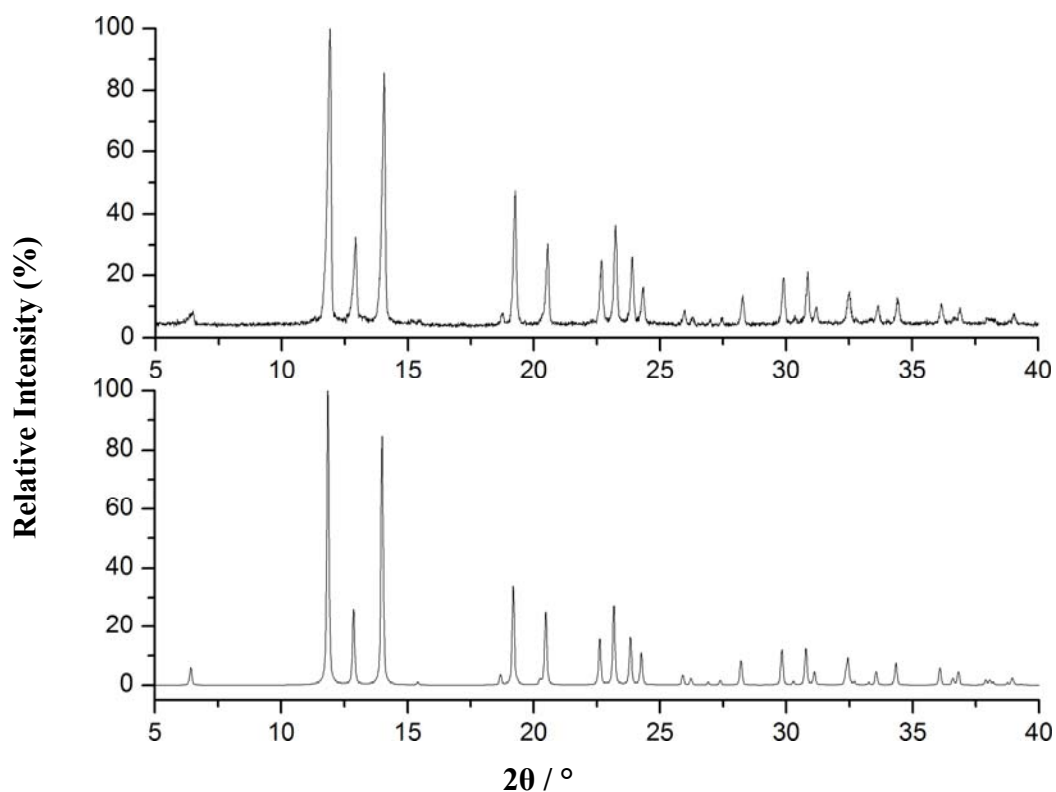


Figure 5.1. Measured (*above*) and theoretically calculated (*below*) [159] powder diffraction patterns of the Cs_2O ($\lambda = 0.7093 \text{ \AA}$).

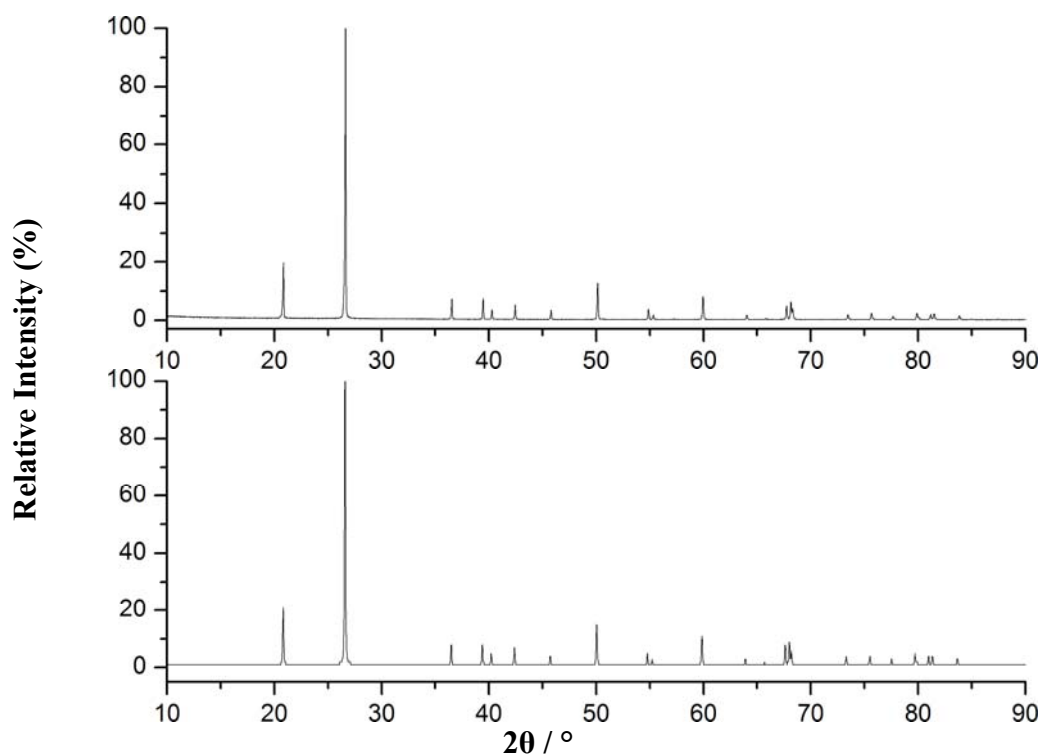


Figure 5.2. Measured (*above*) and theoretically calculated (*below*) [160] powder diffraction patterns of the SiO_2 ($\lambda = 1.5406 \text{ \AA}$).

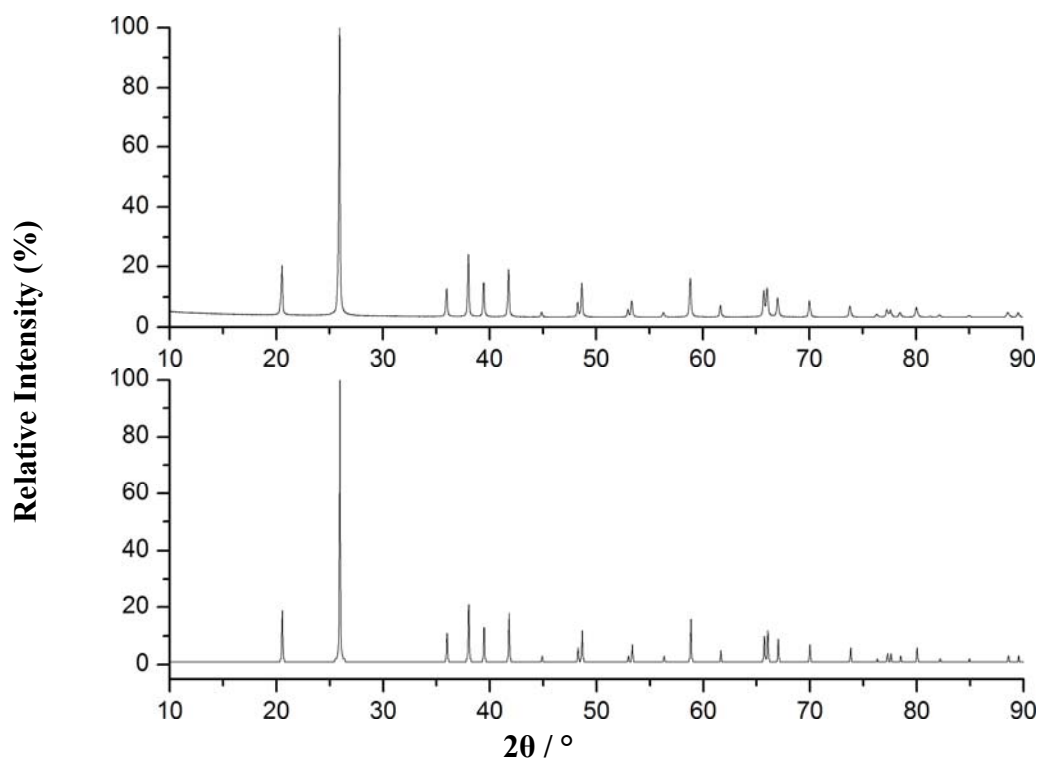


Figure 5.3. Measured (*above*) and theoretically calculated (*below*) [161] powder diffraction patterns of the GeO₂ (λ = 1.5406 Å).

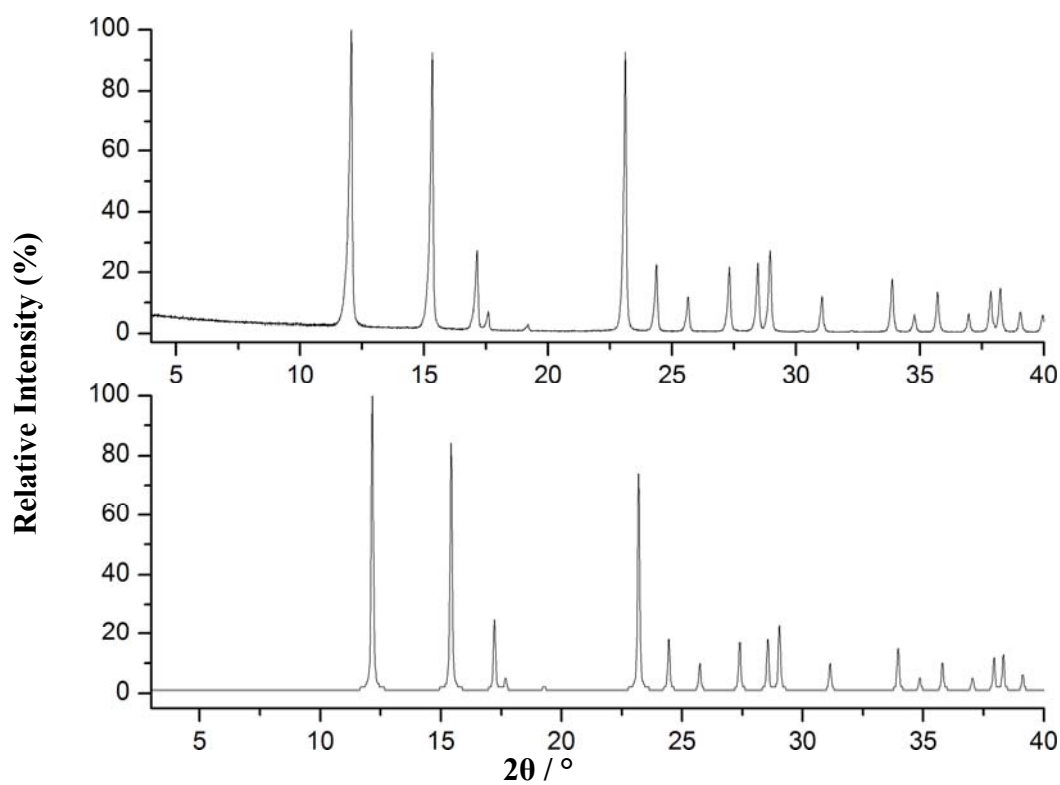


Figure 5.4. Measured (*above*) and theoretically calculated (*below*) [161, 162] powder diffraction patterns of the SnO₂ (λ = 0.7093 Å).

5.4. Platinum, Gold, Thallium, Indium, Tin (IV) and Tin (II) Oxides

Before being used, the Pt sponge (99.9 %, MaTeck GmbH, Jülich, Germany) was dried and degassed at 400 °C in a dynamic vacuum of 10^{-5} mbar.

Gold powder was prepared by the following procedure: firstly, the small amount of gold was dissolved in nitrohydrochloric acid (36 % hydrochloric acid, Merck, Darmstadt, Germany; 65 % nitric acid, Sigma-Aldrich Chemie GmbH), subsequently excess nitric acid as well as concentrated hydrochloric acid were completely fumed off. A saturated solution of sodium oxalate (Merck, Darmstadt, Germany) was added after cooling of the hydrochloric acid solution until completion of the gold precipitation. The obtained highly dispersed deposited gold was filtered through a glass frit (pore size G4) and was then heated up to boiling in hydrochloric acid several times until the virtually yellow solution coloring was no longer noticeable. Furthermore, the gold precipitate obtained was repeatedly boiled

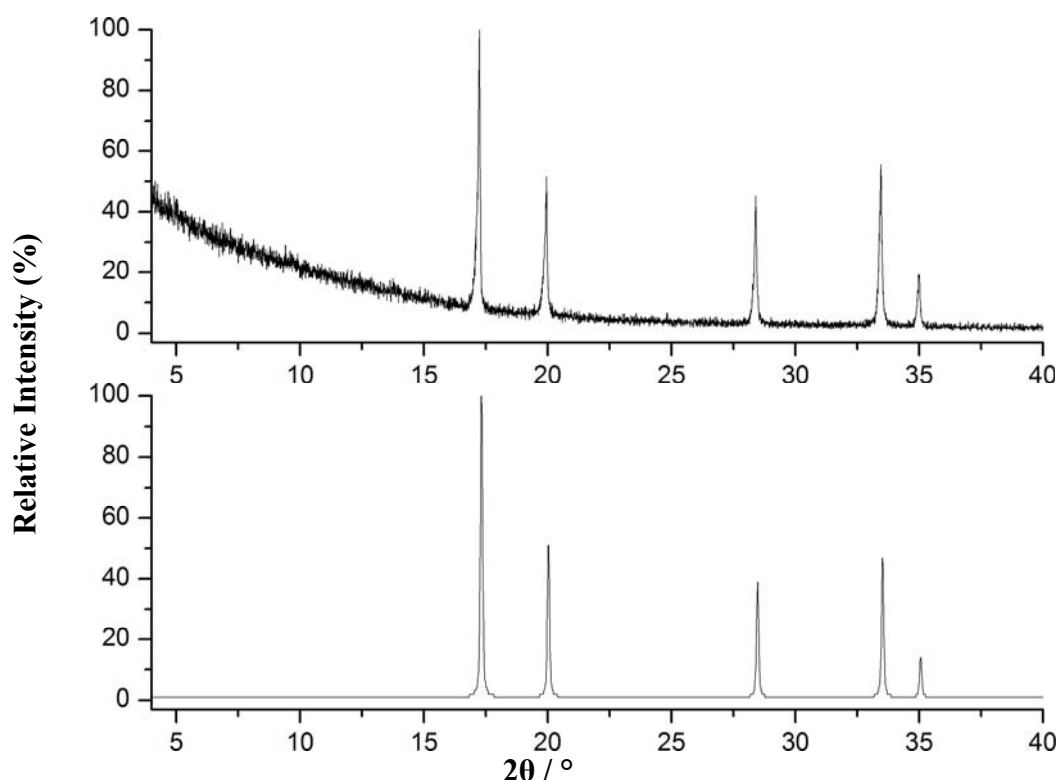


Figure 5.5. Measured (*above*) and theoretically calculated (*below*) [163] powder diffraction patterns of the Au ($\lambda = 0.7093$ Å).

in distilled water until the latter showed a neutral reaction. After two repetitions of the described above procedure the gold was finally dried at 150 °C for 12 h in a dynamic vacuum at 10^{-3} mbar. The purity of the gold powder was controlled by X-ray powder diffraction method (Fig. 5.5).

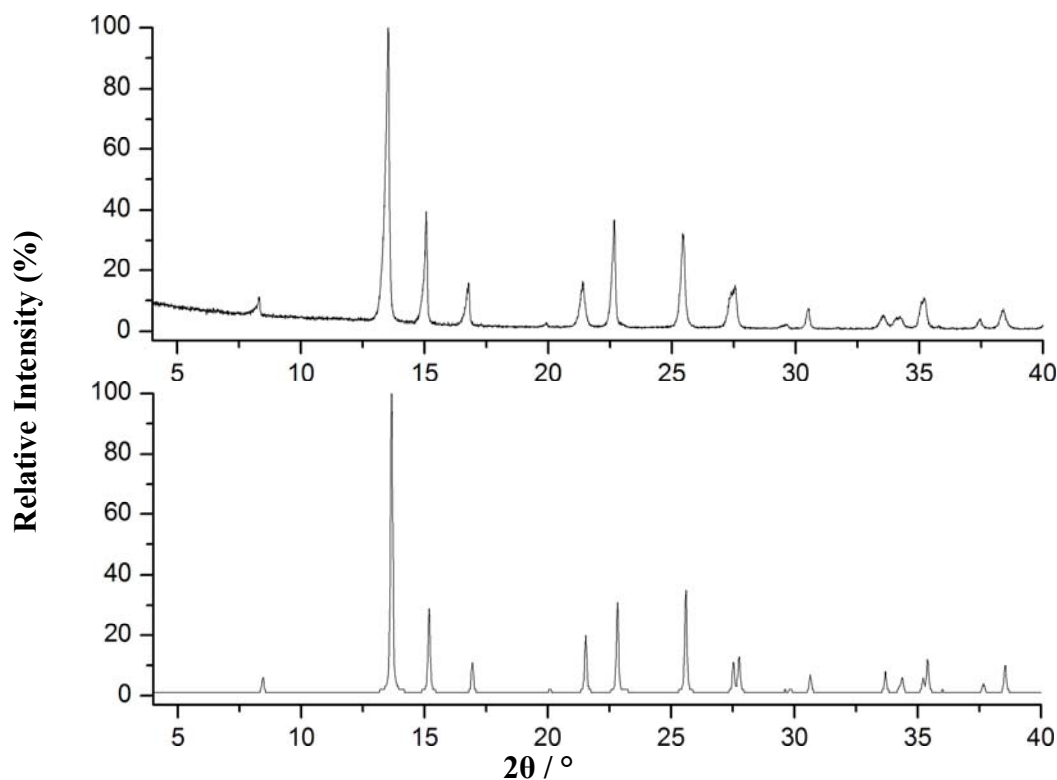


Figure 5.6. Measured (*above*) and theoretically calculated (*below*) [164] powder diffraction patterns of the SnO ($\lambda = 0.7093$ Å).

The commercially available granulated thallium (99.999%, ChemPur, Jülich, Germany, granules packed under water) was dried at 150 °C in a dynamic vacuum of 10^{-3} mbar and such separately stored the whole time under argon atmosphere. The matt grey surface of the granules was carefully removed and each granule itself was cut into smaller pieces before use.

Indium tear drops (99.999%, ChemPur, Jülich, Germany) were dried at 120 °C for 12 h in a dynamic vacuum of 10^{-3} mbar and then stored the whole time under argon atmosphere. Each drop was cut into smaller pieces before being placed into a Ta ampoule.

Tin (99.8%, Alfa Aesar GmbH & Co KG, Karlsruhe, Germany, shot), tin (II) oxide (99.99%, Sigma-Aldrich Chemie GmbH, crystalline powder) and tin (IV)

oxide (99.999%, Chempur, Jülich, Germany, powder) were used in the reaction after have been dried at 120 °C in a dynamic vacuum at 10^{-3} mbar for 12 h. Tin pieces also were cut into the smaller ones directly before use. The purity of the SnO and SnO₂ was controlled using the X-ray powder diffraction method (Figs. 5.6 and 5.4, respectively).

Part III.

Special Part

6. Alkaline-Earth Metal Auride Platinides

With respect to their positions in the Periodic System of the Elements, platinum, gold and mercury are unique, inasmuch as these are the first elements that experience both f- and d-contractions in superposition. The resulting orbital contractions are particularly strong for the 6s-orbital, which in a synergetic way are reinforced by relativistic effects [11, 12, 14, 19]. As one of the consequences, the electron affinities of gold and platinum are the highest and second highest, respectively, for all metals [36]. The peculiarities of the electronic structures of the gold and platinum atoms are mirrored by some striking chemical properties. Gold is able to exhibit an ionic charge of -1 in electrolytes [12, 83, 86, 87, 89, 90] and during transport processes in ionic solids [51, 73], numerous compounds exist containing negatively charged gold [80], and the chemistry of gold ($-I$) is very much reminiscent of the halide chemistry. Platinum has been shown recently to adopt the anionic charge of -2 in Cs_2Pt [91] and in Ba_2Pt [92], while structural properties and electron count for $BaPt$ are indicative for platinum ($-I$), featuring Pt—Pt bonds [96, 97].

6.1. Quasi Binary System BaAu-BaPt

In continuation to the projects on the chemistry of anionic gold and platinum, the possibilities of realizing such species in one compound have been explored in the present work, e.g. targeting Ba_2AuPt . Therefore in the present work a systematic study of the quasi binary system BaAu — BaPt has been undertaken. Since exact crystallographic information for BaAu was missing [165], this compound has also been synthesized and examined.

6.1.1. Synthesis, Powder XRD and Thermal Stability

All operations were performed under dried argon (Schlenk technique or glovebox). The elemental barium, gold and platinum were weighed out in the ratios $\text{BaAu}_{1-x}\text{Pt}_x$ ($x = 0.05\text{--}0.95$) at 5 at-% intervals in an argon-filled glovebox, placed into tantalum tubes which were sealed under argon with an arc welder. In order to prevent oxidation, the tantalum tubes were encapsulated in silica jackets, under argon. The reaction mixtures were heated at a rate of 50 K/h to 1223 K, annealed at this temperature for 2 days, and then cooled to room temperature at a rate of 10 K/h. In the case of BaAu, the mixture was heated to 1193 K at a rate of 50 K/h, annealed at this temperature for 2 days, then slowly cooled to 1153 K, annealed at this temperature for 1 week, and then cooled to room temperature at a rate of 10 K/h. The products were isolated and handled under strictly inert conditions (Schlenk technique or glovebox).

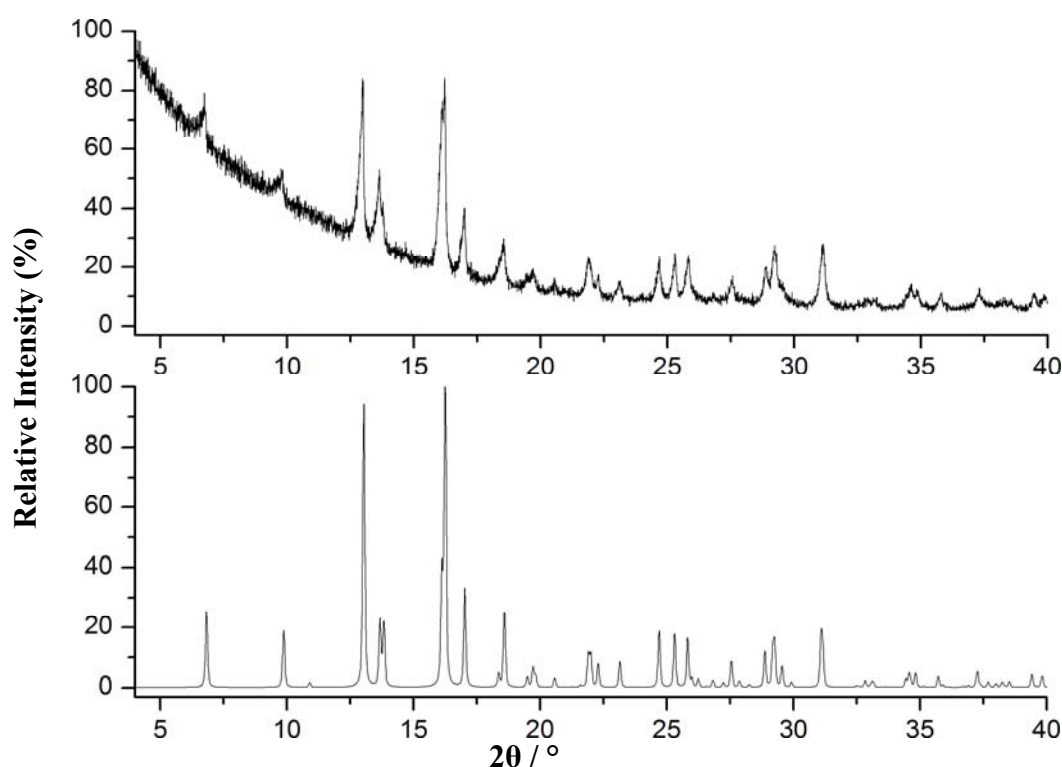


Figure 6.1. Measured (*above*) and theoretically calculated (*below*) powder diffraction patterns of $\text{BaAu}_{0.5}\text{Pt}_{0.5}$ ($\lambda = 0.7093 \text{ \AA}$).

According to the powder diffraction X-ray patterns, the products obtained are single phases. Measured as well as theoretically calculated X-ray powder patterns of one from solid solution region compound $\text{BaAu}_{0.5}\text{Pt}_{0.5}$ and BaAu are presented in Figs. 6.1 and 6.2, respectively. The chemical compositions were confirmed by EDX analysis, and no impurity elements were detected. According to DSC measurements, the melting point of $\text{BaAu}_{0.5}\text{Pt}_{0.5}$ is 1208 ± 5 K and BaAu melts incongruently in the temperature range of 1013–1093 K. Because of the air-sensitive character of investigated samples the thermal stability experiments were performed in an argon atmosphere.

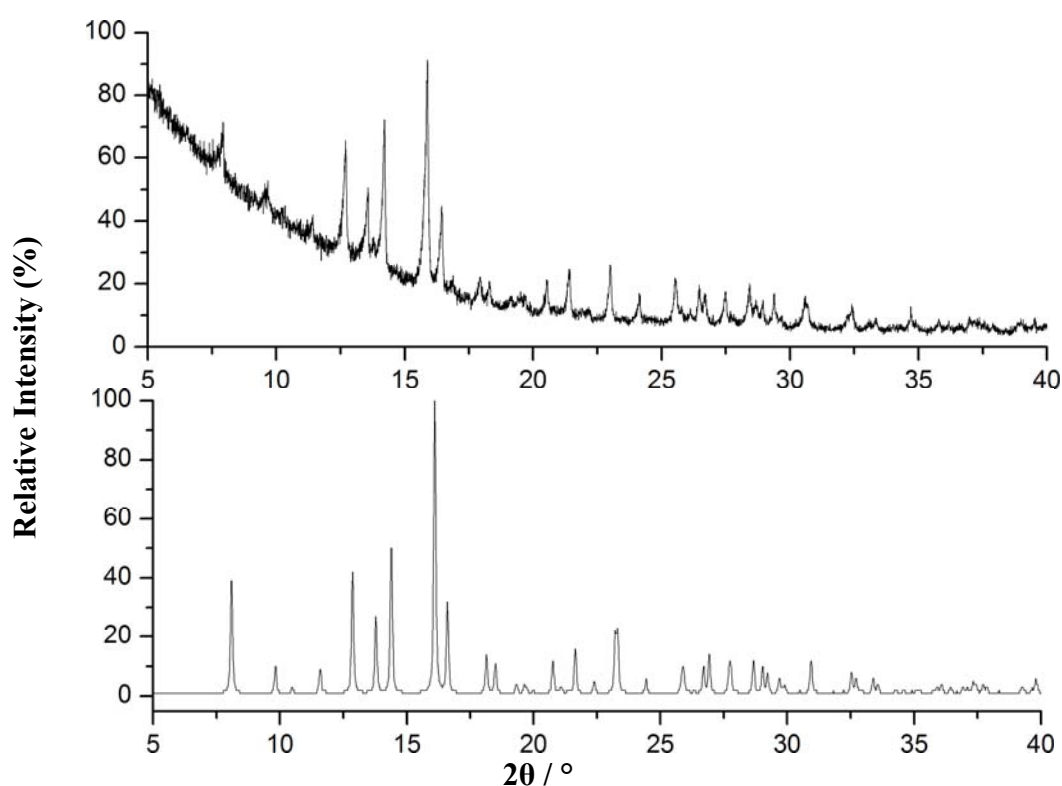


Figure 6.2. Measured (*above*) and theoretically calculated (*below*) powder diffraction patterns of BaAu ($\lambda = 0.7093 \text{ \AA}$).

6.1.2. Crystal Structure Analysis

6.1.2.1. Single Crystal X-ray Structure Analysis of $\text{BaAu}_{0.5}\text{Pt}_{0.5}$ and BaAu

Single crystal X-ray structure analyses of single crystals of $\text{BaAu}_{0.5}\text{Pt}_{0.5}$ and BaAu were performed at room temperature. Crystallographic data, atomic coordinates and anisotropic parameters are summarized in Tables 6.1, 6.2 and 6.3, respectively.

$\text{BaAu}_{0.5}\text{Pt}_{0.5}$ crystallizes in the CrB type of structure with the Ba atoms occupying the Cr position while both, Au and Pt are randomly distributed on the boron site. Due to the virtually equivalent X-ray structure factors of gold and platinum it is not possible to distinguish between them. Therefore the transition metal site was refined assuming an occupation of 50% Au and 50% Pt, in agreement with the EDX analysis (fixed site occupation factors, constrained atomic coordinates and displacement parameters; see tables 6.2 and 6.3). $\text{BaAu}_{0.5}\text{Pt}_{0.5}$ forming the CrB type of structure is unexpected at first sight, because of the fact that BaAu crystallizes in the FeB type [165], and BaPt in the NiAs type of structure [96]. The surprising observation of three structure types to occur in the quasi-binary system $\text{BaAu} - \text{BaPt}$ has prompted a closer inspection.

Both structures, BaAu and $\text{BaAu}_{0.5}\text{Pt}_{0.5}$, are characterized by trigonal prisms of Ba atoms which share their rectangular faces in such a manner that infinite rows of prisms result which are centered by transition metal atoms, forming a zigzag chain. The two structures differ only in the manner these $\frac{1}{\infty}$ building units are arranged with respect to each other (Fig. 6.3). In $\text{BaAu}_{0.5}\text{Pt}_{0.5}$ the rows are condensed such that infinite layers of trigonal prisms result. The structure can also be derived from the AlB_2 type of structure by vacating half the prisms and allowing the empty ones to collapse, in such a way, that square pyramidal voids are formed instead (shearing along a , vector $[1/2 \ 0 \ 0]$). Each transition metal atom is in 6+1 coordination by Ba, with monocapped trigonal prisms.

In the case of BaAu , however, the rows are connected by corners and edges of the trigonal prisms forming a three-dimensional network. The coordination number of Au is the same as the one of the transition metal elements in $\text{BaAu}_{0.5}\text{Pt}_{0.5}$. The relation between the CrB and FeB types of structures can also be interpreted in terms of a periodic unit cell twinning of closed packed structures [166, 167]. There is no obvious reason detectable for the switch in the structure type when substituting Pt for Au.

Table 6.1. Crystal and structure refinement data of BaAu_{0.5}Pt_{0.5} and BaAu.

	BaAu _{0.5} Pt _{0.5}	BaAu
Space group (no.); <i>Z</i>	<i>Cmcm</i> (63); 4	<i>Pnma</i> (62); 4
Cell parameters / Å	<i>a</i> = 4.3915(5); <i>b</i> = 11.915(1); <i>c</i> = 4.7920(5)	<i>a</i> = 8.3310(16); <i>b</i> = 4.9309(9); <i>c</i> = 6.3928(12)
Volume / Å ³	250.74(5)	262.61(9)
Molar weight / g·mol ⁻¹	333.37	334.31
Density (calculated) / g·cm ⁻³	8.831	8.456
Crystal form, color	Block, metallic black	Block, metallic black
Crystal size / mm ³	0.30 × 0.20 × 0.15	0.16 × 0.10 × 0.08
Diffractometer	Bruker AXS, APEX SMART CCD	
Monochromator	Graphite	
X-Ray radiation, λ / Å	Mo-Kα, 0.71073	
θ range, °	3.42 to 36.85	4.02 to 34.93
Index range	-7 ≤ <i>h</i> ≤ 7, -19 ≤ <i>k</i> ≤ 20, -8 ≤ <i>l</i> ≤ 8	-13 ≤ <i>h</i> ≤ 12, -7 ≤ <i>k</i> ≤ 7, -9 ≤ <i>l</i> ≤ 10
Absorption correction	SADABS [120]	
Total no. reflections <i>N</i> _{all}	2984	3812
Independent reflections <i>N</i>	376	614
Reflections with <i>I</i> > 2σ(<i>I</i>)	342	461
<i>N'</i>		
Absorption coefficient, μ / mm ⁻¹	72.267	70.294
Extinction coefficient	0.0030(15)	—
F(000)	538	540
Refinement method	Full-matrix least-squares on <i>F</i> ²	
Weighting scheme	$w = 1/[\sigma^2(F_o^2) + (0.1445P)^2 + 0P]$, $P = (F_o^2 + 2F_c^2) / 3$	$w = 1/[\sigma^2(F_o^2) + (0.0513P)^2 + 0.38P]$, $P = (F_o^2 + 2F_c^2) / 3$
Number of free parameters	10	13
Goodness-on-fit on <i>F</i> ²	1.317	1.174
<i>R</i> ₁ (<i>N'</i> ; <i>N</i>)	0.0674; 0.0716	0.0407; 0.0495
<i>wR</i> ₂ (<i>N'</i> ; <i>N</i>)	0.1808; 0.1836	0.0977; 0.1024
Deposition no. [168]	CSD – 419560	CSD – 419559

Table 6.2. Atomic coordinates and equivalent isotropic displacement parameter $U_{eq} / \text{\AA}^2$ of $\text{BaAu}_{0.5}\text{Pt}_{0.5}$ and BaAu .

Atom	Site	S.O.F	x	y	z	U_{eq}
$\text{BaAu}_{0.5}\text{Pt}_{0.5}$						
Au	4c	0.5	0	0.5763(1)	1/4	0.024(1)
Pt	4c	0.5	$x(\text{Au})$	$y(\text{Au})$	$z(\text{Au})$	$U_{eq}(\text{Au})$
Ba	4c	1	0	0.8633(1)	1/4	0.025(1)
BaAu						
Au	4c	1	0.0374(1)	1/4	0.1338(1)	0.021(1)
Ba	4c	1	0.1838(1)	1/4	0.6376(1)	0.018(1)

Table 6.3. Atomic displacement parameters $U_{ij} / \text{\AA}^2$ for $\text{BaAu}_{0.5}\text{Pt}_{0.5}$ and BaAu .

Atom	U_{11}	U_{22}	U_{33}	$U_{12} = U_{23}$	U_{13}
$\text{BaAu}_{0.5}\text{Pt}_{0.5}$					
Au	0.024(1)	0.024(1)	0.024(1)	0	0
Pt	$U_{11}(\text{Au})$	$U_{22}(\text{Au})$	$U_{33}(\text{Au})$	$U_{12}(\text{Au}) = U_{23}(\text{Au})$	$U_{13}(\text{Au})$
Ba	0.025(1)	0.022(1)	0.029(1)	0	0
BaAu					
Au	0.020(1)	0.021(1)	0.023(1)	0	0
Ba	0.018(1)	0.018(1)	0.018(1)	0	0

In contrast, in BaPt , which crystallizes in the NiAs structure type, the Pt atoms are coordinated octahedrally by six Ba atoms. Due to the very small c/a ratio, pronounced, infinite linear chains of Pt atoms are formed [96]. The formation of infinite chains of transition elements is a prominent feature of all three structures. Therefore, coordination numbers for Pt and/or Au, including the transition elements as well as barium, are 2+6+1 for BaAu and $\text{BaAu}_{0.5}\text{Pt}_{0.5}$, and 2+6 for BaPt , respectively. The latter displays the shortest distances between the transition elements, in all examples discussed. For better comparison, selected bond distances as well as the angles between atoms in the zigzag chains of the BaAu , $\text{BaAu}_{0.5}\text{Pt}_{0.5}$ and BaPt compounds are summarized in Table 6.4. From these data it is obvious that partial substitution of gold atoms by platinum in BaAu leads to a shortening of

not only the distances between transition metal atoms but also between transition metal and barium.

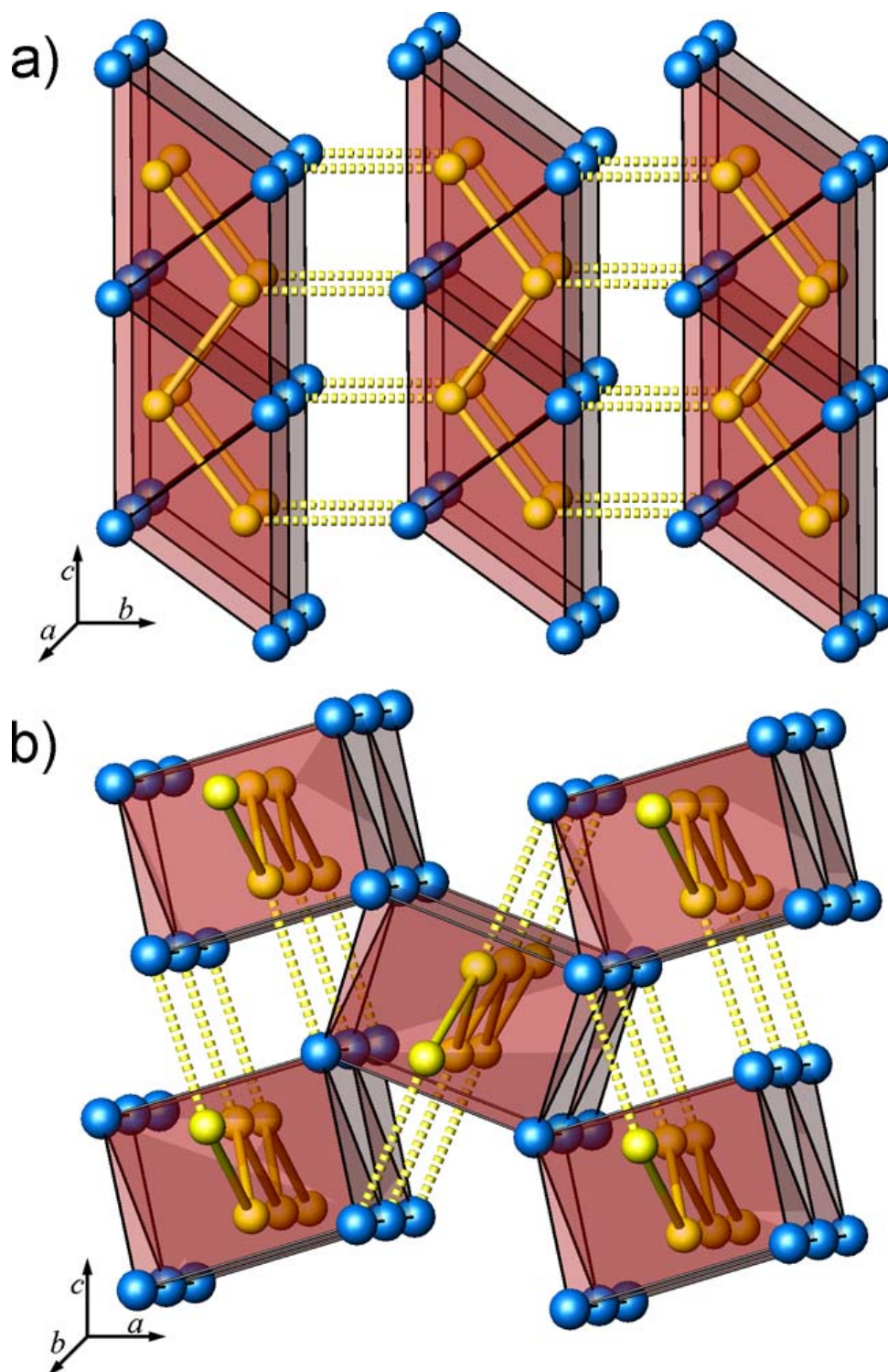


Figure 6.3. Perspective representations of the crystal structures of $\text{BaAu}_{0.5}\text{Pt}_{0.5}$ (a) and BaAu (b).

Table 6.4. Selected bond distances / Å² and angle / ° of BaAu, BaAu_{0.5}Pt_{0.5} and BaPt [96].

	BaAu	BaAu _{0.5} Pt _{0.5}	BaPt [96]
Ba-M ^{a)}	3.3878(7) × 2	3.3287(5) × 4	3.219(1) × 6
	3.3986(10)	3.3557(16) × 2	
	3.4068(7) × 2		
	3.4189(10)		
M-Ba ^{a)}	3.3878(7) × 2	3.3287(5) × 4	3.219(1) × 6
	3.3986(10)	3.3557(16) × 2	
	3.4068(7) × 2	3.420(2)	
	3.4189(10)		
	3.4439(11)		
M-M ^{a)}	3.0649(7) × 2	3.0075(12) × 2	2.710(2) × 2
M-M-M ^{a)}	107.11(3)	105.63(6)	180

^{a)} M – transition metal (gold or platinum) as well as mixture of two transition metals (gold and platinum).

6.1.2.2. Powder Diffraction X-ray Analysis of BaAu–BaPt System

Powder diffraction X-Ray analysis was applied to determine the homogeneity range of the solid solution BaAu_{1-x}Pt_x (x = 0.05–0.95) as well as to examine the boundary compositions at which crystal structure changes occur from hexagonal (BaPt) to the orthorhombic one with CrB structure type (BaAu_{0.5}Pt_{0.5}) and from the latter one to the orthorhombic FeB structure (BaAu). At the Pt rich side of the phase diagram the change from the NiAs type (BaPt) to the CrB type of structure appears in the BaPt_{0.95}Au_{0.05}—BaPt_{0.90}Au_{0.10} region, while at the Au rich side the crystal structure transition from the CrB type to FeB type (BaAu) occurs in the BaPt_{0.10}Au_{0.90}—BaPt_{0.15}Au_{0.85} region. There is an extended region of solid solution (BaPt_{0.15}Au_{0.85}—BaPt_{0.90}Au_{0.10}) with CrB type of structure, where all three lattice parameters decrease linearly with increasing amount of platinum (Fig. 6.4) in

agreement with *Vegard's law* [169, 170], and the formation of the FeB and NiAs types of structures is limited to the border phases BaAu and BaPt.

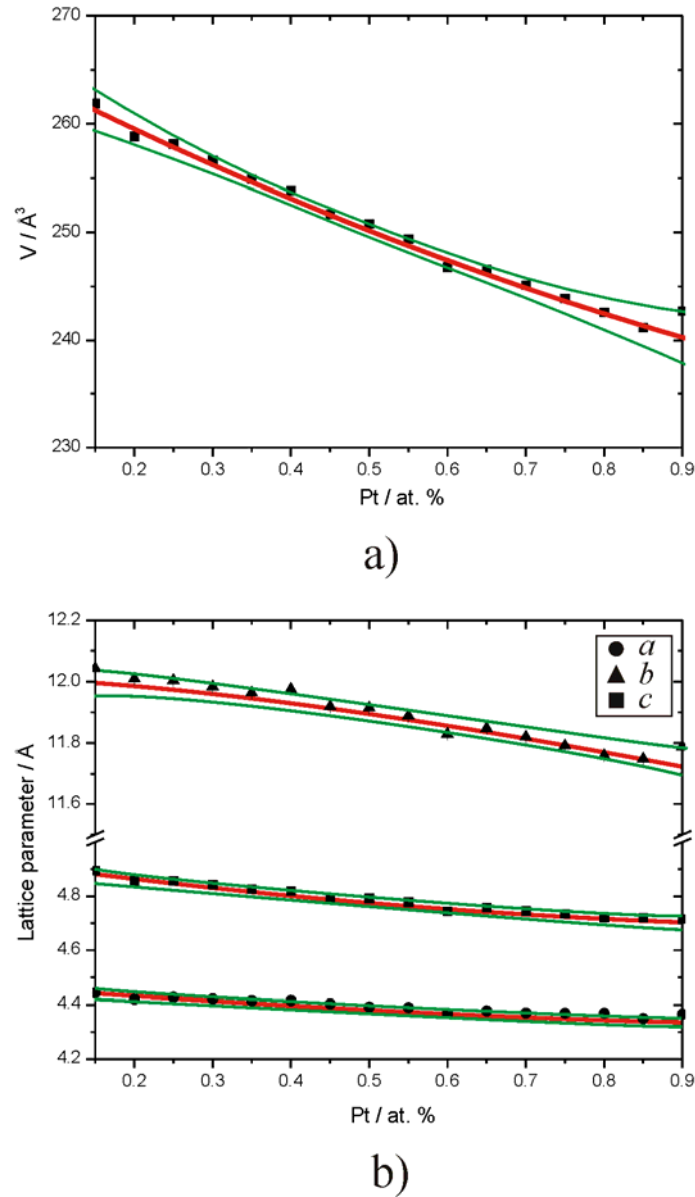


Figure 6.4. Concentration dependencies (red lines) of the unit cell volume (a) and lattice parameters (b) in the solid solution $\text{BaAu}_{1-x}\text{Pt}_x$ ($x = 0.15 - 0.9$) region. Green lines are demarking the ranges of experimental errors.

6.1.3. Electrical Resistivity Measurements

The result of a temperature – dependent resistivity measurement of $\text{BaAu}_{0.5}\text{Pt}_{0.5}$ is displayed in Fig. 6.5. The specific electrical resistivity increases

linearly from 1.07 mΩ·cm at 5 K to 1.5 mΩ·cm at 300 K. This corresponds to a moderate metallic conductor.

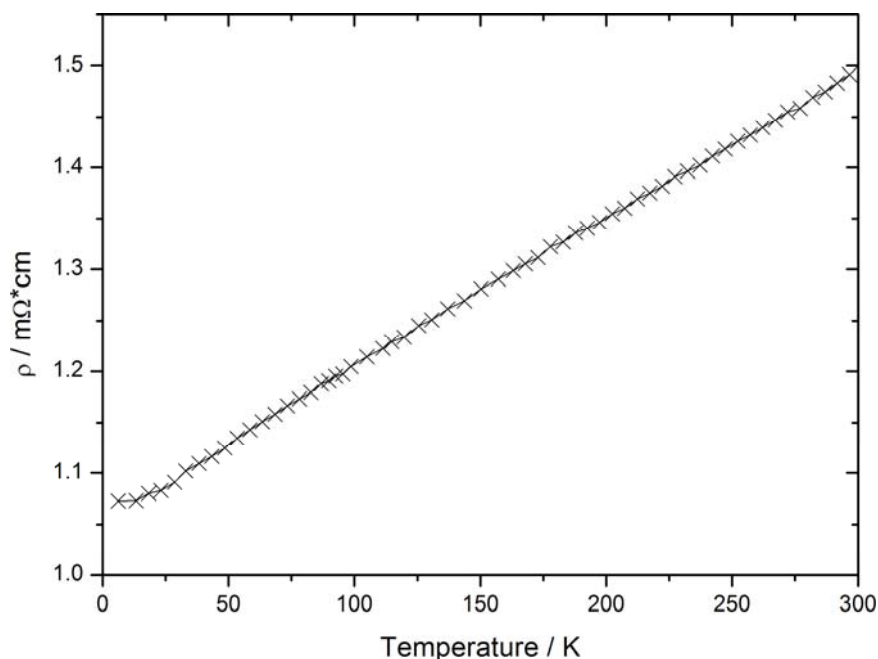


Figure 6.5. Temperature – dependent resistivity data of BaAu_{0.5}Pt_{0.5}.

6.1.4. Magnetic Susceptibility Measurements

Magnetizations of BaAu_{0.5}Pt_{0.5} and BaAu were measured in a gelatin capsule (0.1463 g and 0.1288 g, respectively) using a SQUID magnetometer in the temperature range 2–300 K at $H = 0.001, 0.1, 1, 3, 5$ and 7 T. The field-dependent magnetic susceptibility of BaAu_{0.5}Pt_{0.5} is presented in Fig. 6.6 showing the diamagnetic properties of the compound ($\chi(300\text{K}) = -3.5 \times 10^{-5}$ emu/mol at field strength 1.5–7 T). According to the temperature dependent measurements, the magnetic susceptibility for BaAu is independent of temperature in the region 20–300 K and is $\chi_{\text{mol}} = -1.5 \times 10^{-5} \pm 2.5\%$ / $-1.86 \times 10^{-5} \pm 2.5\%$ emu/mol at fields strength 1T / 3T, respectively (Fig. 6.7).

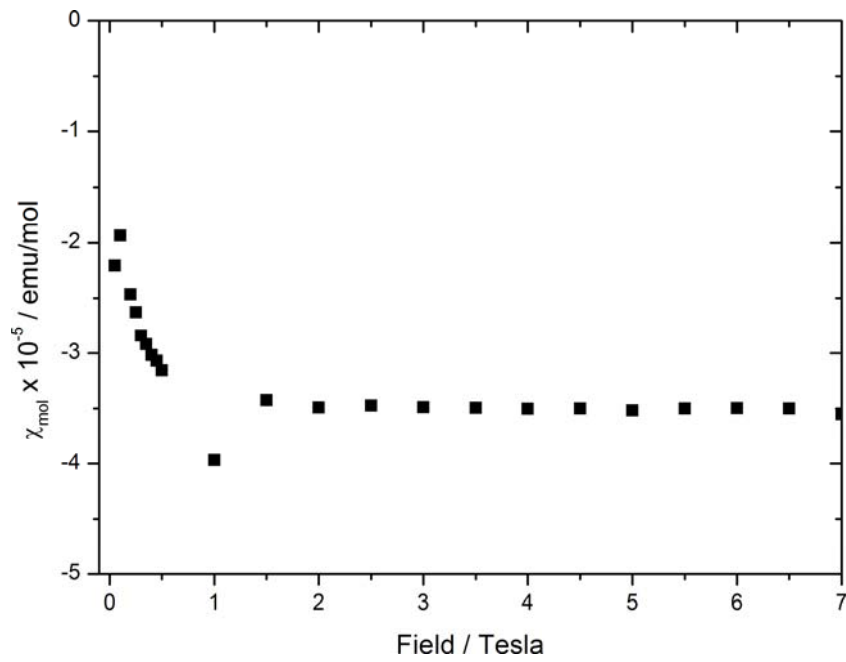


Figure 6.6. Field –dependent magnetic susceptibility data of BaAu_{0.5}Pt_{0.5} at 300 K.

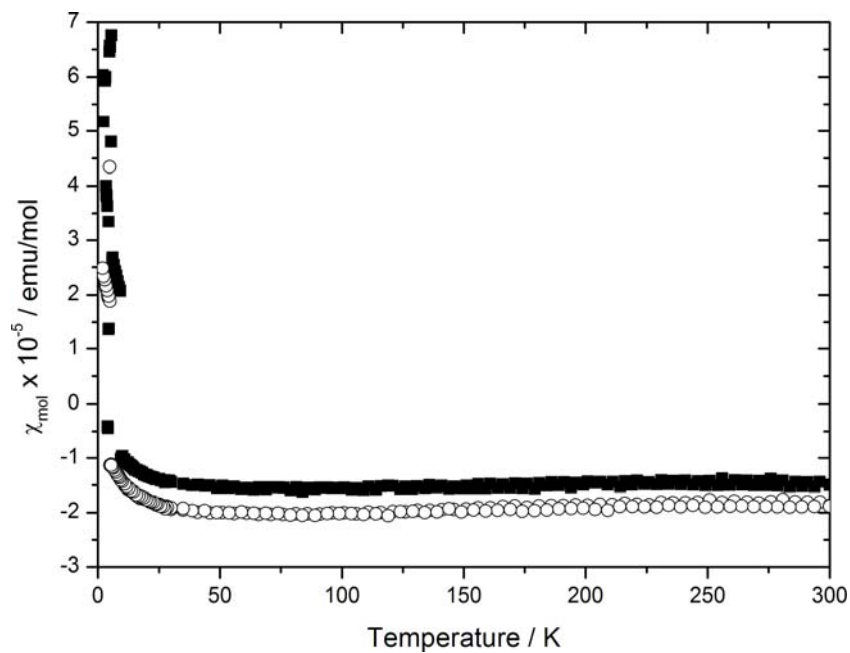


Figure 6.7. Temperature – dependent magnetic susceptibility data of BaAu at 1T (black squares) and 3T (white circles).

6.1.5. ESCA

ESCA spectra of the BaAu_{0.5}Pt_{0.5}, BaAu as well as pure gold and platinum are shown in Fig. 6.8. The resulting binding energies for the Au(4f_{7/2}) and Pt(4f_{7/2})

levels of elemental gold and platinum were 84.0 eV and 71.5 eV, respectively. The ESCA spectrum recorded for the studied compounds displayed a shift of the binding energy of the Au($4f_{7/2}$) as well as Pt($4f_{7/2}$) level to lower energies (the maximum of the Au($4f_{7/2}$) peak was found at 82.7 eV and for the Pt($4f_{7/2}$) peak at 69.8 eV in BaAu_{0.5}Pt_{0.5}; the maximum peak for Au($4f_{7/2}$) in BaAu corresponds to 82.7 eV). This indicates an elevated electron density on the gold and platinum atoms compared to elemental gold and platinum, thus demonstrating a negative oxidation state for both, gold and platinum. In order to quantitatively assign a valence state to gold and platinum, the linear correlations between shifting of the binding energies of the Au($4f_{7/2}$) [48] and Pt($4f_{7/2}$) [99] levels and the oxidation state of elements in compounds were used. According to the correlations mentioned, the “partial oxidation state” of gold and platinum in BaAu and BaAu_{0.5}Pt_{0.5} can be easily deduced: –1 for Au in BaAu (the difference between binding energies of the Au($4f_{7/2}$) level in the compound and the pure element is 1.3 eV), –1 for Au and –1.8 for Pt in BaAu_{0.5}Pt_{0.5} (the difference between binding energies of the Au($4f_{7/2}$) level in the compound and pure gold is –1.3 eV, in the case of platinum the difference between binding energies of the Pt($4f_{7/2}$) level in the compound and pure platinum is –1.7 eV). Thus in BaAu_{0.5}Pt_{0.5} and BaAu, gold and platinum exhibit a negative oxidation state. For better comparison, the binding energies of the Pt ($4f$) and Au ($4f$) levels of BaAu, BaAu_{0.5}Pt_{0.5} and BaPt are summarized in Table 6.5. According to the ESCA results, it is possible to formally describe the compounds mentioned as $[\text{Ba}^{2+} \cdot 0.5e^-] \cdot \text{Au}^-_{0.5} \cdot \text{Pt}^{2-}_{0.5}$ and $[\text{Ba}^{2+} \cdot e^-] \cdot \text{Au}^-$.

Table 6.5. Binding energies of the Pt ($4f$) and Au ($4f$) levels of BaAu, BaAu_{0.5}Pt_{0.5} and BaPt [96].

	Au($4f_{5/2}$)	Au($4f_{7/2}$)	Pt($4f_{5/2}$)	Pt($4f_{7/2}$)
Au	87.7	84.0	–	–
Pt	–	–	74.8	71.5
BaAu	86.4	82.7	–	–
BaPt [96]	–	–	73.5	70.2
BaAu _{0.5} Pt _{0.5}	86.4	82.7	73.1	69.8

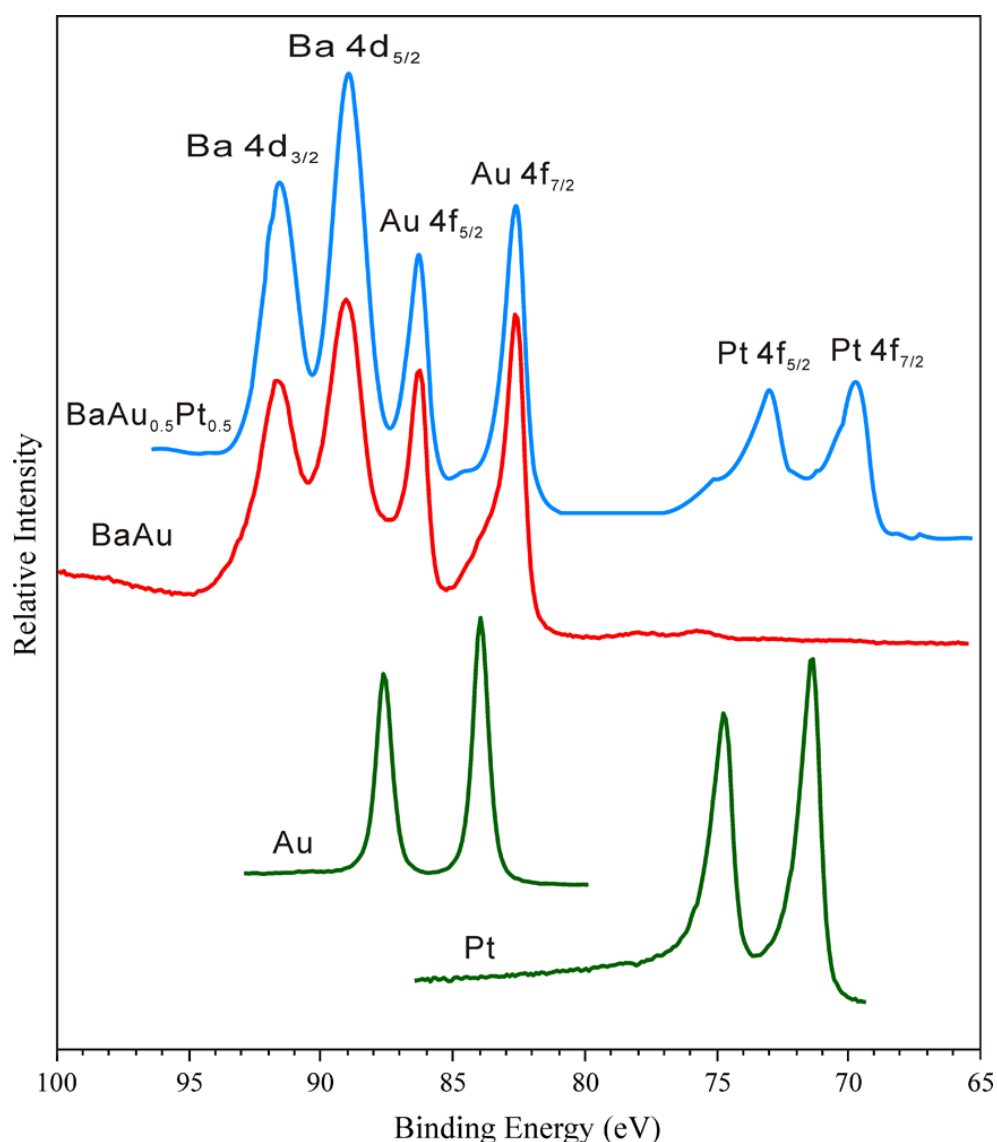


Figure 6.8. Pt (4f) and Au (4f) region of ESCA spectra of the BaAu_{0.5}Pt_{0.5} and BaAu.

6.2. SrAu_{0.5}Pt_{0.5} and CaAu_{0.5}Pt_{0.5} – Featuring Purely Intermetallic Behaviour

Following the success of realizing such species as Au⁻ and Pt²⁻ in one compound (BaAu_{0.5}Pt_{0.5} [171]); the results are discussed in the preceding Chapter 6.1, another two analogous alkaline earth metal auride platinides, CaAu_{0.5}Pt_{0.5} and SrAu_{0.5}Pt_{0.5}, were synthesized and characterized for the first time. The compounds are isostructural to BaAu_{0.5}Pt_{0.5} but with a different type of chemical bonding.

6.2.1. Synthesis, Powder XRD and Thermal Stability

For the synthesis of strontium or calcium auride platinides the corresponding alkaline earth metal was reacted with a platinum sponge as well as gold powder. The elemental strontium or calcium, gold and platinum were weighed out in the required ratios (Sr or Ca) : Au : Pt = 2 : 1 : 1 in an argon-filled glovebox, and placed into a tantalum tube, which was sealed under argon with an arc welder. In order to prevent oxidation, the tantalum tube was encapsulated in silica jackets, under argon. The reaction mixtures were heated at a rate of 50 K/h up to 1223 K, annealed at this temperature for 2 days followed by quenching in an ice-water cooling bath. In order to avoid admixtures of Sr_3Pt_2 and Ca_3Pt_2 in the product, quenching of the reaction vessel proved to be indispensable. The products were isolated and handled under strictly inert conditions (Schlenk technique or glovebox).

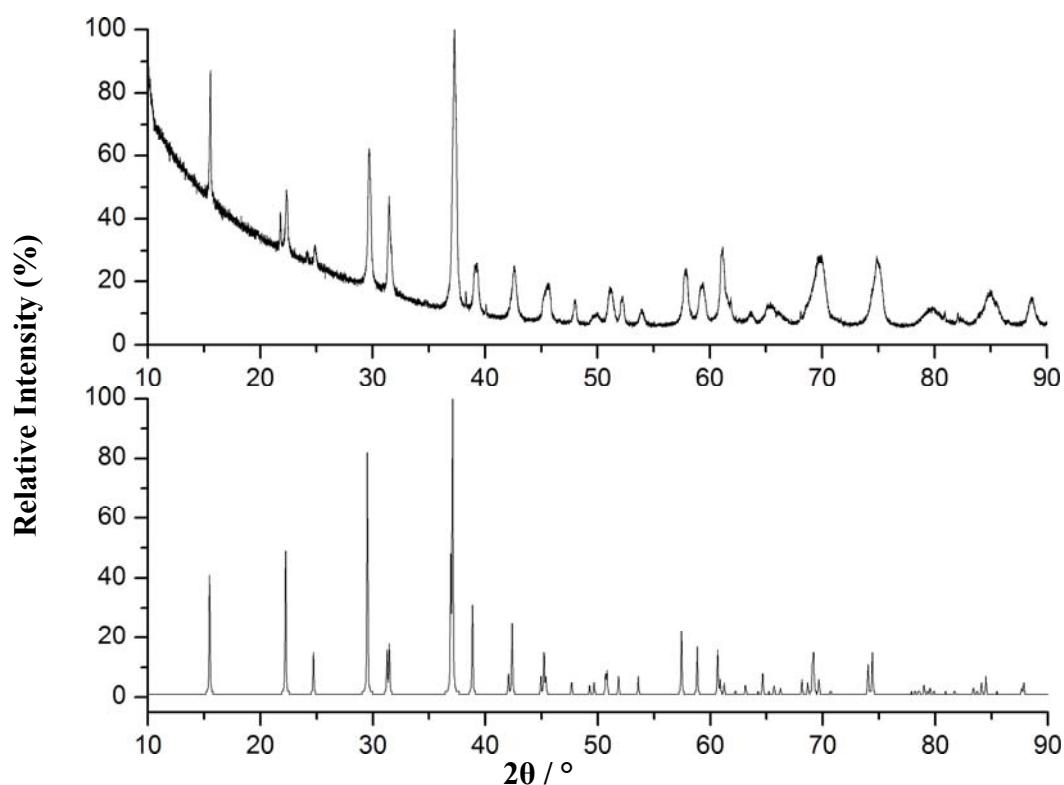


Figure 6.9. Measured (*above*) and theoretically calculated (*below*) powder diffraction patterns of $\text{SrAu}_{0.5}\text{Pt}_{0.5}$ ($\lambda = 1.5406 \text{ \AA}$).

According to the powder diffraction X-ray patterns, the products obtained are single phases. Measured as well as theoretically calculated X-ray powder patterns of $\text{SrAu}_{0.5}\text{Pt}_{0.5}$ and $\text{CaAu}_{0.5}\text{Pt}_{0.5}$ are presented in Figs. 6.9 and 6.10, respectively. The chemical compositions were confirmed by EDX analysis, and no impurity elements were detected.

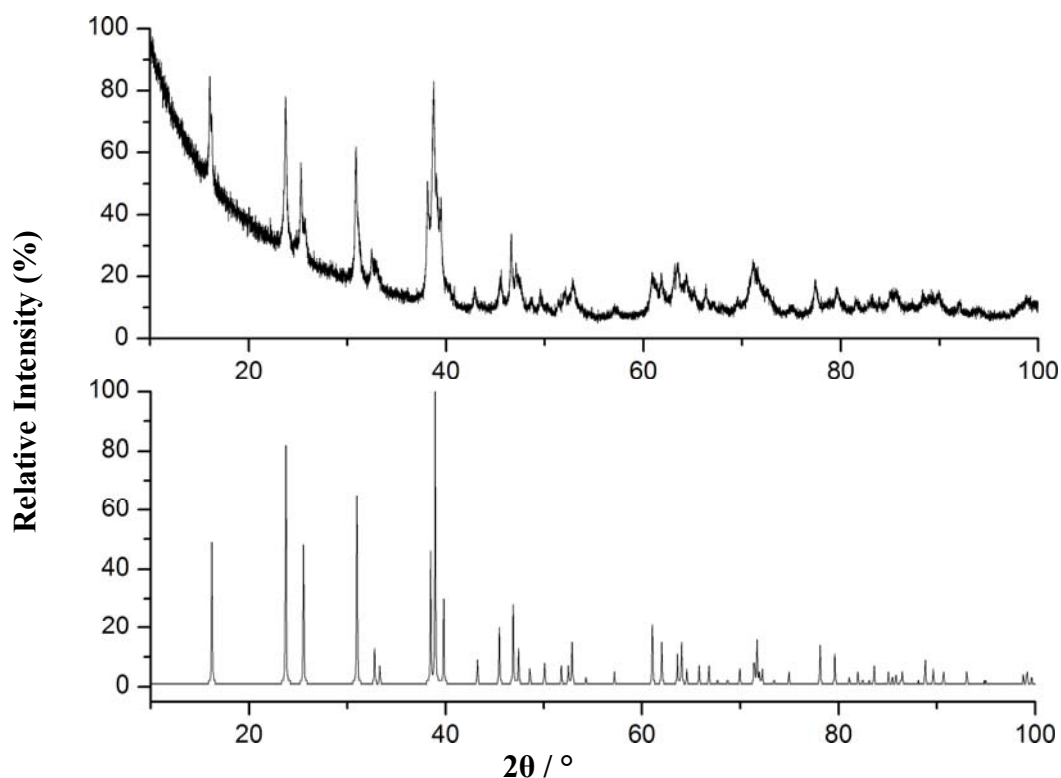


Figure 6.10. Measured (*above*) and theoretically calculated (*below*) powder diffraction patterns of $\text{CaAu}_{0.5}\text{Pt}_{0.5}$ ($\lambda = 1.5406 \text{ \AA}$).

According to DSC measurements, $\text{SrAu}_{0.5}\text{Pt}_{0.5}$ melts incongruently at $1323 \pm 5 \text{ K}$, and decomposition of $\text{CaAu}_{0.5}\text{Pt}_{0.5}$ occurs before melting in the temperature range of $1148\text{--}1178 \text{ K}$. Because of the air-sensitive character of investigated samples the thermal stability experiments were done in the argon atmosphere.

6.2.2. Crystal Structure Analysis

Single crystal X-ray structure analyses of $\text{SrAu}_{0.5}\text{Pt}_{0.5}$ and $\text{CaAu}_{0.5}\text{Pt}_{0.5}$ were performed at room temperature. Crystallographic data, atomic coordinates and

Table 6.6. The crystallographic and structure refinement data for SrAu_{0.5}Pt_{0.5} and CaAu_{0.5}Pt_{0.5}.

	SrAu _{0.5} Pt _{0.5}	CaAu _{0.5} Pt _{0.5}
Space group (no.); <i>Z</i>	<i>Cmcm</i> (63); 4	<i>Cmcm</i> (63); 4
Cell parameters / Å	<i>a</i> = 4.262(1); <i>b</i> = 11.435(3); <i>c</i> = 4.632(1)	<i>a</i> = 3.9858(4); <i>b</i> = 10.920(1); <i>c</i> = 4.5249(5)
Volume / Å ³	225.77(9)	196.95(4)
Molar weight / g·mol ⁻¹	283.65	236.11
Density (calculated) / g·cm ⁻³	8.35	7.96
Crystal form, color	Block, metallic black	Block, metallic black
Crystal size / mm ³	0.15 × 0.08 × 0.05	0.10 × 0.12 × 0.15
Diffractometer	Bruker AXS, APEX SMART CCD	
Monochromator	Graphite	
X-ray radiation, λ / Å	Mo-Kα, 0.71073	
θ range, °	3.56 to 34.88	3.73 to 34.55
Index range	-6 ≤ <i>h</i> ≤ 6, -17 ≤ <i>k</i> ≤ 17, -7 ≤ <i>l</i> ≤ 7	-6 ≤ <i>h</i> ≤ 6, -17 ≤ <i>k</i> ≤ 17, -7 ≤ <i>l</i> ≤ 7
Absorption correction	SADABS [120]	
Total no. reflections <i>N</i> _{all}	1721	1560
Independent reflections <i>N</i>	290	257
Reflections with <i>I</i> > 2σ(<i>I</i>) <i>N'</i>	288	253
Absorption coefficient, μ / mm ⁻¹	86.5	75.0
Extinction coefficient	—	0.0078(4)
<i>F</i> (000)	466	394
Refinement method	Full-matrix least-squares on <i>F</i> ²	
Weighting scheme	$w = 1/[\sigma^2(F_o^2) + (0.0196P)^2 + 1.7372P]$, where $P = (F_o^2 + 2F_c^2) / 3$	$w = 1/[\sigma^2(F_o^2) + (0.0231P)^2 + 0P]$, where $P = (F_o^2 + 2F_c^2) / 3$
Number of free parameters	9	10
Goodness-on-fit on <i>F</i> ²	1.091	1.118
<i>R</i> ₁ (<i>N'</i> ; <i>N</i> _{all})	0.0175; 0.0176	0.0170; 0.0174
<i>wR</i> ₂ (<i>N'</i> ; <i>N</i> _{all})	0.0389; 0.0389	0.0394; 0.0396
Δρ _{min} ; Δρ _{max} / e·Å ⁻³	-1.55 / 2.52	-1.49 / 2.81
Deposition no. [168]	CSD – 421651	CSD – 421650

Table 6.7. Atomic coordinates and equivalent isotropic displacement parameter $U_{eq} / \text{\AA}^2$ for $\text{SrAu}_{0.5}\text{Pt}_{0.5}$ and $\text{CaAu}_{0.5}\text{Pt}_{0.5}$.

Atom	Site	S.O.F	x	y	z	U_{eq}
$\text{SrAu}_{0.5}\text{Pt}_{0.5}$						
Au	4c	0.5	0	0.57491(2)	1/4	0.018(1)
Pt	4c	0.5	$x(\text{Au})$	$y(\text{Au})$	$z(\text{Au})$	$U_{eq}(\text{Au})$
Sr	4c	1	0	0.86125(6)	1/4	0.018(1)
$\text{CaAu}_{0.5}\text{Pt}_{0.5}$						
Au	4c	0.5	0	0.57823(2)	1/4	0.013(1)
Pt	4c	0.5	$x(\text{Au})$	$y(\text{Au})$	$z(\text{Au})$	$U_{eq}(\text{Au})$
Ca	4c	1	0	0.8593(1)	1/4	0.014(3)

Table 6.8. Atomic displacement parameters $U_{ij} / \text{\AA}^2$ for $\text{SrAu}_{0.5}\text{Pt}_{0.5}$ and $\text{CaAu}_{0.5}\text{Pt}_{0.5}$.

Atom	U_{11}	U_{22}	U_{33}	$U_{12} = U_{23}$	U_{13}
$\text{SrAu}_{0.5}\text{Pt}_{0.5}$					
Au	0.0191(1)	0.0171(1)	0.0178(2)	0	0
Pt	$U_{11}(\text{Au})$	$U_{22}(\text{Au})$	$U_{33}(\text{Au})$	$U_{12}(\text{Au}) = U_{23}(\text{Au})$	$U_{13}(\text{Au})$
Ba	0.0178(3)	0.0155(3)	0.0210(3)	0	0
$\text{CaAu}_{0.5}\text{Pt}_{0.5}$					
Au	0.0165(2)	0.0112(2)	0.0103(2)	0	0
Pt	$U_{11}(\text{Au})$	$U_{22}(\text{Au})$	$U_{33}(\text{Au})$	$U_{12}(\text{Au}) = U_{23}(\text{Au})$	$U_{13}(\text{Au})$
Ca	0.0134(6)	0.0117(6)	0.0169(6)	0	0

isotropic displacement parameters for the strontium as well as the calcium auride platinide are summarized in Tables 6.6 – 6.8, respectively.

The compounds $\text{SrAu}_{0.5}\text{Pt}_{0.5}$ and $\text{CaAu}_{0.5}\text{Pt}_{0.5}$ are isotypic with the corresponding barium compound [171], all of them crystallizing in the CrB type of structure with the alkaline earth metal atoms occupying the Cr position while both Au and Pt are randomly distributed on the boron site. Due to the virtually equivalent X-ray scattering factors of gold and platinum it is not possible to distinguish between them. Therefore the transition metal site (T) was fixed assuming an occupation of 50% Au and 50% Pt, in agreement with the EDX

analysis (fixed site occupation factors, constrained atomic coordinates and displacement parameters; see tables 6.7 and 6.8). The structure of both isostructural compounds, $AAu_{0.5}Pt_{0.5}$ ($A = Sr$ or Ca) can be described in the same way as for $BaAu_{0.5}Pt_{0.5}$ (see Chapter 6.1).

The coordination numbers for Pt and/or Au, including neighboring transition elements as well as the respective A metal are 2+6+1 for $AAu_{0.5}Pt_{0.5}$ ($A = Ca, Sr$ or Ba). For better comparison, selected bond distances as well as the angles between atoms in the zigzag chains of the discussed compounds are summarized in Table 6.9. From these data it is obvious that changing the alkaline earth metal cations significantly influences the distances between alkaline earth and transition metals as well as between the transition metals in the zigzag chain. The shortening of distances is a result of a decrease of the alkaline earth metal ionic radius in the period Ba to Ca. The angle between the transition metals in the chain $\angle T-T-T$ is not influenced by the size of the alkaline earth metal cations (Table 6.9).

Table 6.9. Selected bond distances / \AA^2 and angle / $^\circ$ of $BaAu_{0.5}Pt_{0.5}$, $SrAu_{0.5}Pt_{0.5}$ and $CaAu_{0.5}Pt_{0.5}$.

	$BaAu_{0.5}Pt_{0.5}$	$SrAu_{0.5}Pt_{0.5}$	$CaAu_{0.5}Pt_{0.5}$
$A-M^a$	$3.3287(5) \times 4$	$3.2309(5) \times 4$	$3.0914(4) \times 4$
	$3.356(2) \times 2$	$3.2421(8) \times 2$	$3.113(1) \times 2$
$M-A$	$3.3287(5) \times 4$	$3.2309(5) \times 4$	$3.0914(4) \times 4$
	$3.356(2) \times 2$	$3.2421(8) \times 2$	$3.113(1) \times 2$
	$3.420(2)$	$3.274(1)$	$3.069(2)$
$M-M$	$3.008(1) \times 2$	$2.8810(6) \times 2$	$2.8350(4) \times 2$
$M-M-M$	$105.63(6)$	$107.02(2)$	$105.89(2)$

^{a)} A – alkaline earth metal; M – transition metal (gold or platinum) as well as mixture of two transition metals (gold and platinum).

The binary gold phases crystallize in three different types of structures, namely CrB and FeB for CaAu [172] and BaAu [171], respectively, and a stacking variant of the CrB-FeB type for SrAu [165]. The relation between both types of structures can also be interpreted in terms of periodic unit cell twinning of closed packed structures [166, 167]. This is most illustratively demonstrated by the

structure of SrAu, which can be described as a stacking variant between both types, CrB and FeB [165]. This stacking phenomenon was also intensively investigated in the CaAg-SrAg-BaAg system, where several kind of stacking variants between CrB and FeB occur [173]. From the binary platinum phases only BaPt (NiAs type of structure [96]) is known, while CaPt and SrPt are missing, up to now. In contrast to the pronounced structural diversity of the binary compounds, all mixed alkaline earth metal gold platinides $AAu_{0.5}Pt_{0.5}$ ($A = Ca, Sr, Ba$) crystallize in the CrB structure type. It can be assumed, that Ca and Sr compounds also show a broad phase width (solid solution), which is discussed in detail in Chapter 6.1.2.2 for $BaAu_{1-x}Pt_x$ ($0.15 \leq x \leq 0.90$) [171].

6.2.3. Electrical Resistivity Measurements

Temperature-dependent resistivity measurements of $SrAu_{0.5}Pt_{0.5}$ and $CaAu_{0.5}Pt_{0.5}$ were performed according to the general procedure of the *van der Pauw* method, see Fig. 6.11. The specific electrical resistivity changes from $0.90 \text{ m}\Omega\cdot\text{cm}$ at 5 K to $0.95 \text{ m}\Omega\cdot\text{cm}$ at 300 K for $SrAu_{0.5}Pt_{0.5}$ and from $3.62 \text{ m}\Omega\cdot\text{cm}$ at 5 K to $3.93 \text{ m}\Omega\cdot\text{cm}$ at 300 K for $CaAu_{0.5}Pt_{0.5}$, which is typical for a moderate metallic conductor.

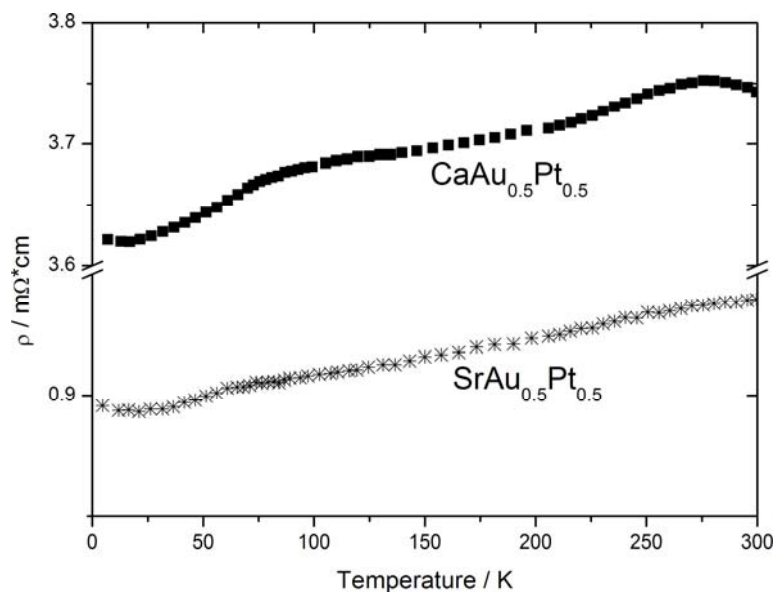


Figure 6.11. Temperature – dependent resistivity data of $SrAu_{0.5}Pt_{0.5}$ and $CaAu_{0.5}Pt_{0.5}$.

6.2.4. Magnetic Susceptibility Measurements

The magnetization of $\text{SrAu}_{0.5}\text{Pt}_{0.5}$ and $\text{CaAu}_{0.5}\text{Pt}_{0.5}$ was measured using a SQUID magnetometer in the temperature range 2–300 K at $H = 0.001, 0.1, 1, 3, 5$ and 7 T.

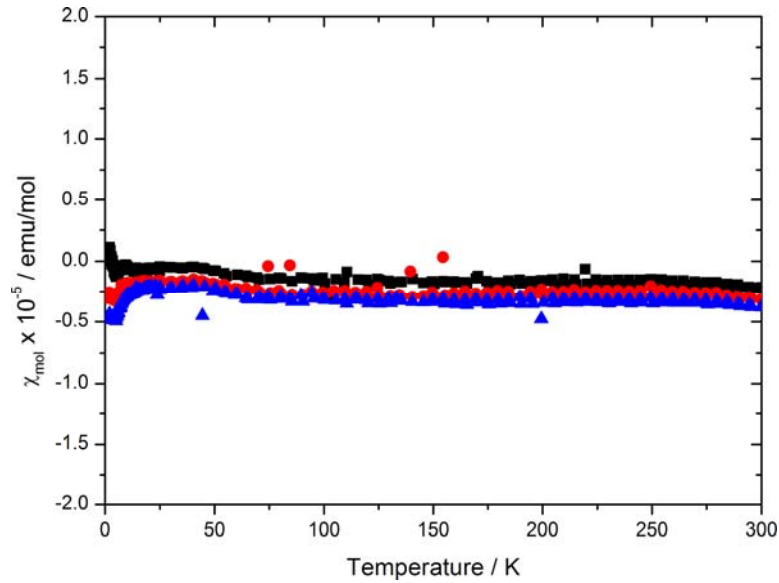


Figure 6.12. Temperature – dependent magnetic susceptibility data of $\text{SrAu}_{0.5}\text{Pt}_{0.5}$ at 3T (black squares), 5T (red circles) and 7T (blue triangles).

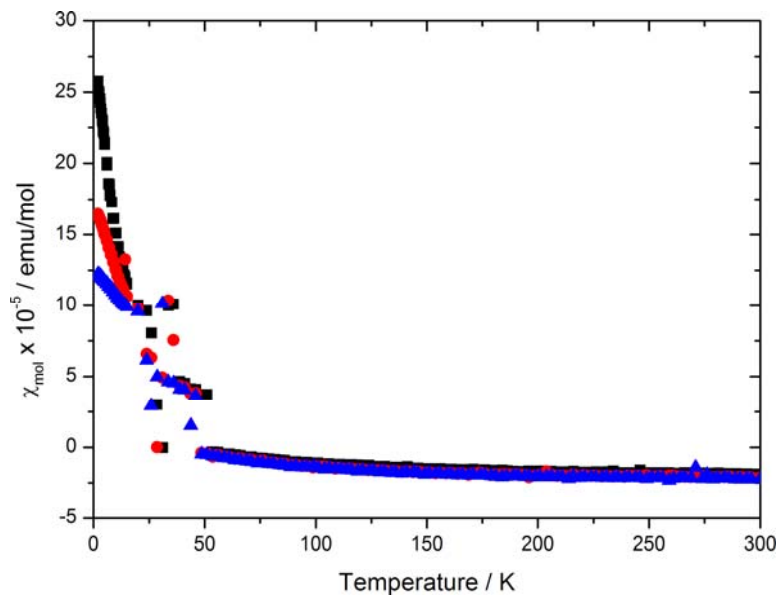


Figure 6.13. Temperature – dependent magnetic susceptibility data of $\text{CaAu}_{0.5}\text{Pt}_{0.5}$ at 3T (black squares), 5T (red circles) and 7T (blue triangles).

Both compounds show diamagnetic behaviour at field strengths of 3 to 7 T with temperature independent magnetic susceptibilities of $-1.7 \times 10^{-6} \pm 2.5\%$ emu/mole in the whole measured temperature range for $\text{SrAu}_{0.5}\text{Pt}_{0.5}$ and $-16 \times 10^{-6} \pm 2.5\%$ emu/mole at 25–300 K for $\text{CaAu}_{0.5}\text{Pt}_{0.5}$. The corresponding χ_{mol} vs. temperature dependencies are presented in Figs. 6.12 and 6.13. The increase of magnetic susceptibility of $\text{CaAu}_{0.5}\text{Pt}_{0.5}$ at the temperature range of 2 to 25 K is attributed to the presence of paramagnetic impurities in the investigated sample.

6.2.5. ESCA

The corresponding ESCA spectra of $A\text{Au}_{0.5}\text{Pt}_{0.5}$ ($A = \text{Ca}, \text{Sr}, \text{Ba}$) as well as pure gold and platinum are displayed in Fig. 6.14. The resulting binding energies for the $\text{Au}(4f_{7/2})$ and $\text{Pt}(4f_{7/2})$ levels of elemental gold and platinum were taken as 84.0 eV and 71.5 eV, respectively. The ESCA spectra recorded for $\text{SrAu}_{0.5}\text{Pt}_{0.5}$ and $\text{CaAu}_{0.5}\text{Pt}_{0.5}$ show a very small shift of the binding energy of the $\text{Au}(4f_{7/2})$ to higher values, and a small shift of the $\text{Pt}(4f_{7/2})$ level to lower binding energies, indicating slightly positively polarized gold and slightly negatively polarized platinum. The maximum of the $\text{Au}(4f_{7/2})$ peak was found at 84.1 eV / 84.2 eV and for the $\text{Pt}(4f_{7/2})$ peak at 71.0 eV / 70.9 eV in $\text{SrAu}_{0.5}\text{Pt}_{0.5}$ / $\text{CaAu}_{0.5}\text{Pt}_{0.5}$, respectively. This is in contrast to $\text{BaAu}_{0.5}\text{Pt}_{0.5}$, where both gold and platinum are significantly negatively polarized [25], exhibiting a pronounced anionic character. For better comparison, the binding energies of the Pt (4f) and Au (4f) levels of $\text{BaAu}_{0.5}\text{Pt}_{0.5}$, $\text{SrAu}_{0.5}\text{Pt}_{0.5}$ and $\text{CaAu}_{0.5}\text{Pt}_{0.5}$ are summarized in Table 6.10.

Table 6.10. Binding energies of the Pt (4f) and Au (4f) levels of $\text{BaAu}_{0.5}\text{Pt}_{0.5}$, $\text{SrAu}_{0.5}\text{Pt}_{0.5}$ and $\text{CaAu}_{0.5}\text{Pt}_{0.5}$.

	$\text{Au}(4f_{5/2})$	$\text{Au}(4f_{7/2})$	$\text{Pt}(4f_{5/2})$	$\text{Pt}(4f_{7/2})$
Au	87.7	84.0	–	–
Pt	–	–	74.8	71.5
$\text{BaAu}_{0.5}\text{Pt}_{0.5}$	86.4	82.7	73.1	69.8
$\text{SrAu}_{0.5}\text{Pt}_{0.5}$	87.8	84.1	74.3	71.0
$\text{CaAu}_{0.5}\text{Pt}_{0.5}$	87.8	84.2	74.2	70.9

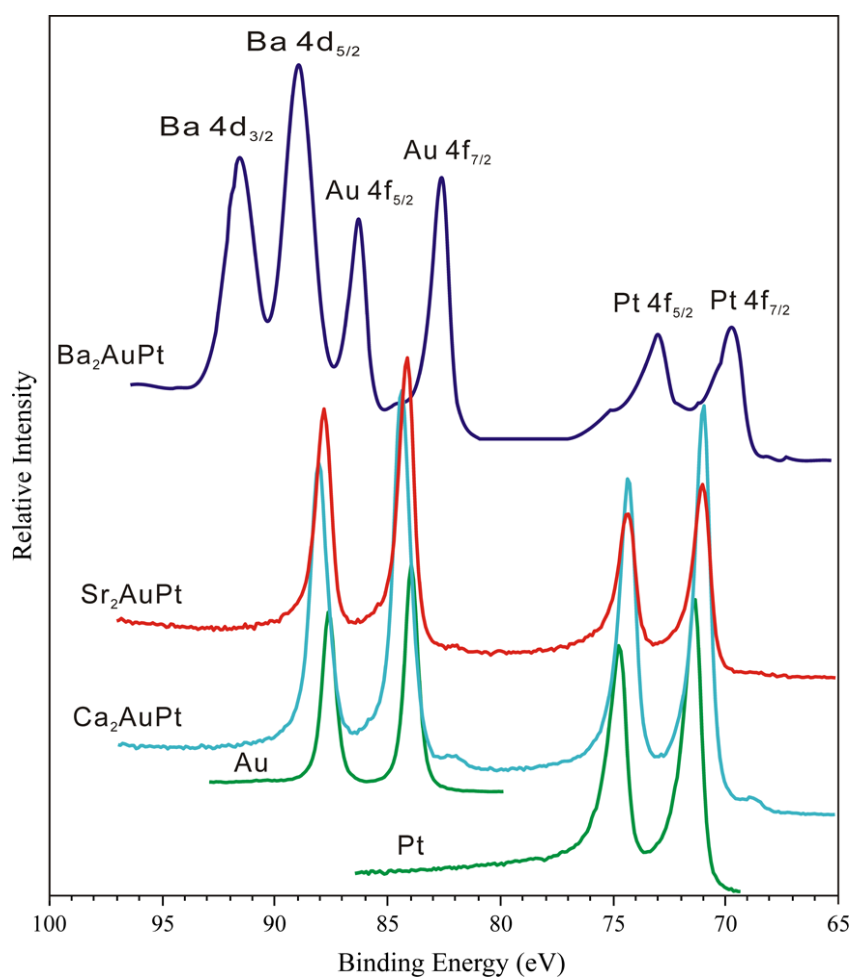


Figure 6.14. Pt (4f) and Au (4f) region of ESCA spectra of the BaAu_{0.5}Pt_{0.5} [171], SrAu_{0.5}Pt_{0.5} and CaAu_{0.5}Pt_{0.5} intermetallics.

6.3. Conclusions

Phase equilibria in the system BaAu—BaPt have been monitored by X-ray powder diffraction. Depending on composition, three structure types occur, the FeB type for BaAu, and NiAs for BaPt, while the CrB type of structure is adopted in between. The homogeneity range for the CrB type of structure was established to extend from BaPt_{0.15}Au_{0.85} to BaPt_{0.90}Au_{0.10}. The respective lattice parameters vary linearly, in accordance with *Vegard's law*. Single crystal X-ray diffraction analysis was applied for the characterization at the example of BaAu_{0.5}Pt_{0.5}. Two analogous alkaline earth metal auride platinides, CaAu_{0.5}Pt_{0.5} and SrAu_{0.5}Pt_{0.5}, were also synthesized and characterized for the first time. The new intermetallics

$AAu_{0.5}Pt_{0.5}$ ($A = Ba, Sr, Ca$) crystallize with the CrB type structure, where the noble metals are randomly distributed over the centers of trigonal prisms formed by the alkaline earth metal. According to ESCA measurements, $BaAu_{0.5}Pt_{0.5}$ and $BaAu$ can be formulated as $[Ba^{2+} \cdot 0.5e^{-}] [Au^{-}_{0.5} \cdot Pt^{2-}_{0.5}]$ and $[Ba^{2+} \cdot e^{-}] [Au^{-}]$, respectively, while $SrAu_{0.5}Pt_{0.5}$ and $CaAu_{0.5}Pt_{0.5}$ both can be formulated as having intermetallic character, showing a negligible electron transfer from alkaline earth metals to the noble metals. The investigated intermetallics are poor metallic conductors and exhibit diamagnetic behaviour of magnetic susceptibility.

7. Ternary Alkali Metal Oxide Thallides

Spin-orbit coupling and its enhancement with growing nuclear charge is exclusively of relativistic origin [4, 5], in contrast to the orbital contraction and expansion effects (see “Introduction”). Due to strong relativistic spin-orbit coupling, the degeneracy of the Russel-Saunders ground state of a $6p^2$ configuration is lifted and a diamagnetic ground state $(6p_{1/2}^2)_0$ results. Thus Tl^- is a good candidate to possess a closed shell $(6p_{1/2}^2)_0$ configuration in a solid state compound. For example a still hypothetic solid like Cs_3TlO being diamagnetic could only be understood in terms of relativistic quantum mechanics.

On the other side, thallium can form a great variety of isolated cluster anions in compounds with the electropositive alkali metals as well as in the presence of oxygen, which can introduce a further degree of freedom. With the objective of realizing solids containing isolated Tl^- anions, the systems $Rb-Tl-O$ and $Cs-Tl-O$ were investigated. A number of compounds featuring novel and interesting structural properties have been obtained from these combinations of elements [104, 105]; however, no evidence for the existence of “isolated” thallium(-I) was gained. Instead, in each case thallium cluster ions were observed, corroborating the well-known propensity of thallium in negative oxidation states to form homoatomic clusters [101, 102, 174-183]. All previously found thallium cluster can be classified as follows: $(Tl^-)_n$ can be described according to the Zintl-Klemm concept, while *nido*- $[Tl_4]^{8-}$ [174], *closo*- $[Tl_5]^{7-}$ [175] and *closo*- $[Tl_6]^{8-}$ [183] are examples of the classic Wade's rule, in analogy to the boranes. However, $[Tl_{11}]^{7-}$ [176, 178, 184], $[Tl_7]^{7-}$ [179, 180] and some examples of Jahn-Teller type distorted clusters $[Tl_6]^{6-}$ [105, 181, 182], $[Tl_9]^{9-}$ [175], $[Tl_{13}]^{10-}$ [177], $[Tl_{13}]^{11-}$ [177] are electron deficient with respect to any known classification system and, therefore, were denoted as hypoelectronic [102, 185]. Other experimental studies

have yielded new eight-vertex anionic cluster $[\text{Tl}_8]^{6-}$ [104], the valence electron concentration of which can be only explained by applying the extended Wade-Mingos condensation concept. All these clusters belong to closed-shell species with diamagnetic behaviour.

Following the aims of the present work, further investigations of Cs–Tl–O system have led to the discovery of a new $\text{Cs}_{18}\text{Tl}_8\text{O}_6$ containing a homocubane-like $[\text{Tl}_8]^{6-}$ clusteranion, not found before in compounds with covalently bonded homoatomic clusters, as well as $\text{Cs}_4\text{Tl}_2\text{O}$ containing hypoelectronic $[\text{Tl}_6]^{6-}$ in the shape of nearly *regular*-octahedra, different from previously known compounds (e.g. $\text{Rb}_{10}\text{Tl}_6\text{O}_2$ [105] and CsTl [182]). The $\text{K}_{21}\text{Tl}_{22}\text{O}_2$ compound contains two differently shaped isolated $[\text{Tl}_{11}]$ anionic units, the structure of one of them has not been observed before.

7.1. Distorted $[\text{Tl}_8]^{6-}$ Clusteranion in

$\text{Cs}_{18}\text{Tl}_8\text{O}_6$

7.1.1. Synthesis, Powder XRD and Thermal Stability

Because both, educts and products, are very sensitive to air and moisture, all operations were performed under dried argon (Schlenk technique or glovebox). $\text{Cs}_{18}\text{Tl}_8\text{O}_6$ was prepared by reaction of the binary compounds CsTl and Cs_2O . Cesium thallide was produced by reaction of cesium with thallium in the molar ratio 2 : 1 (total amount of 2 – 3 g) in a tantalum tube which was sealed under argon with an arc-welder. In order to prevent oxidation, the tantalum tubes were encapsulated in silica jackets, under argon. The reaction mixture was heated at a rate of 50 K/h up to 773 K, annealed at this temperature for 2 days, and then cooled to room temperature at a rate of 5 K/h. The excess of cesium was distilled off at 373 K in a dynamic vacuum of 10^{-3} mbar. The purity of the CsTl phase was determined by powder diffraction X-ray analysis (Fig. 7.1).

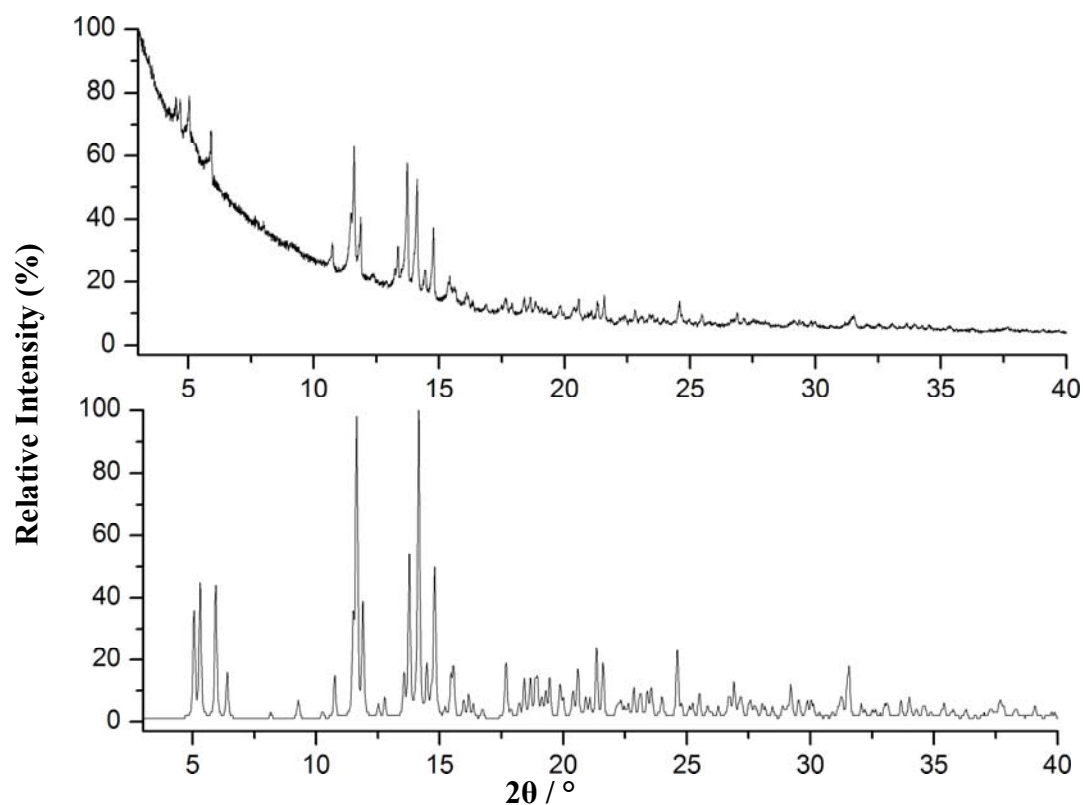


Figure 7.1. Measured (*above*) and theoretically calculated (*below*) powder diffraction patterns of CsTl ($\lambda = 0.7093 \text{ \AA}$).

The mixture of CsTl and Cs₂O in the molar ratio 1 : 1 (total amount of 0.5 – 1 g) was placed into a tantalum tube following the packing procedure described above. The reaction mixture was heated up to 573 K at a rate of 50 K/h, annealed at this temperature for one week, and then cooled to room temperature at a rate of 5 K/h. The as-synthesized products were pure, sometimes containing a small amount of Cs₄Tl₂O (see Chapter 7.2) and Cs₈Tl₁₁ [178] (1 – 4 wt.%), according to X-ray powder diffraction (Fig. 7.2). The purity of the product sensitively depends on purity, handling and composition of the starting mixtures, as well as on the precise control of the reaction conditions. The atom ratio of the heavy elements in the product was additionally confirmed by EDX analysis, and no impurity elements were detected.

The thermal stability was studied using Differential Scanning Calorimetry. The specimen (0.0184 g) was placed in an Al crucible with a lid, cold-sealed to prevent access of air and heated to 673 K at a rate of 2 K/min, and then cooled down to room temperature with the same rate. Cs₁₈Tl₈O₆ is extremely sensitive to moisture and air, and is stable up to 573 K in an argon atmosphere.

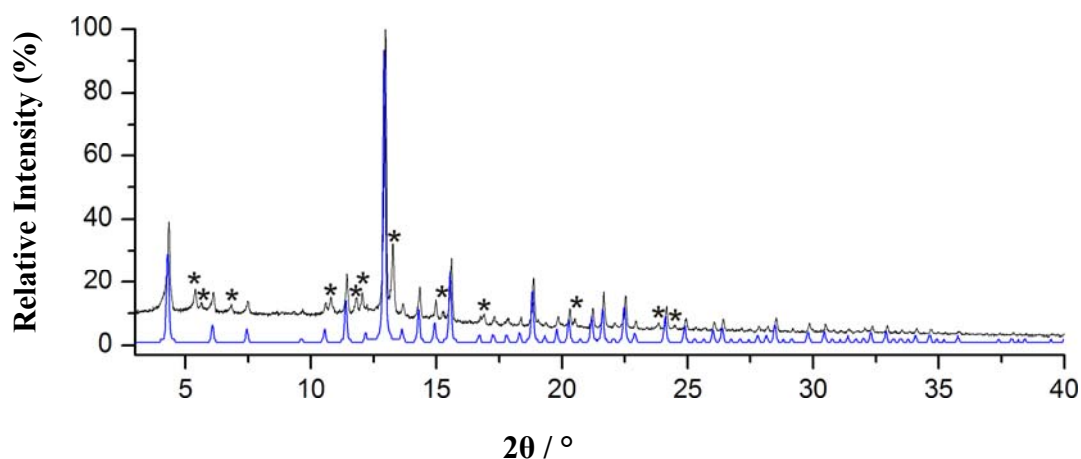


Figure 7.2. Measured (black) as well as theoretically calculated (blue) of the $\text{Cs}_{18}\text{Tl}_8\text{O}_6$ powder diffraction patterns, stars (*) are indicating the impurity of $\text{Cs}_4\text{Tl}_2\text{O}$ (see Chapter 7.2) and $\text{Cs}_8\text{Tl}_{11}$ [178] ($\lambda = 0.7093 \text{ \AA}$).

7.1.2. Crystal Structure Analysis

The single crystal X-ray structure analysis of $\text{Cs}_{18}\text{Tl}_8\text{O}_6$ was performed at room temperature. Crystallographic data, atomic coordinates and anisotropic parameters are summarized in Tables 7.1, 7.2, and 7.3, respectively.

$\text{Cs}_{18}\text{Tl}_8\text{O}_6$ crystallizes in a novel structure type (Fig. 7.3a) displaying isolated $[\text{Tl}_8]^{6-}$ units with the shape of a tetrahedral star, a so-called *stella quadrangula* [186]. $[\text{Tl}_8]^{6-}$ is the first example of a covalently bonded, homoatomic cluster with such an arrangement. The oxygen atoms are surrounded by six cesium atoms in the shape of a distorted octahedron. The Cs–O distances of 2.936 Å (4×) and 2.862 Å (2×) comply well with those in Cs_2O (2.87 Å) [159], which is indicative for a full ionization of the Cs atoms. On the other hand, these values are shorter than the sums of the tabulated ionic radii for CN = 6 [187]: $r(\text{O}^{2-}) + r(\text{Cs}^+) = 3.07 \text{ \AA}$, which is due to the increase in the surrounding electrostatic potential. The electrons, which are released from the Cs/O partial structure are accommodated by the isolated $[\text{Tl}_8]^{6-}$ groups. Cesium and oxygen constitute a three-dimensional network of corner and edge sharing octahedra $\infty^3[\text{OCs}_6]^{+}$ (Fig. 7.3a). The resulting framework contains voids, sufficient in number and size, to accommodate the Tl_8 clusters.

Table 7.1. The crystallographic and structure refinement data for Cs₁₈Tl₈O₆.

	Cs ₁₈ Tl ₈ O ₆
Space group (no.); <i>Z</i>	<i>I</i> 23 (197); 2
Cell parameters / Å	<i>a</i> = 13.3724(3)
Volume / Å ³	2391.27(9)
Molar weight / g·mol ⁻¹	4123.34
Density (calculated) / g·cm ⁻³	5.727
Crystal form, color	Block, silver black metallic
Crystal size / mm ³	0.18 × 0.08 × 0.06
Diffractometer	Bruker AXS, APEX SMART CCD
Monochromator	Graphite
X-ray radiation, λ / Å	Mo-Kα, 0.71073
θ range, °	2.15 to 34.92
Index range	-21 ≤ <i>h</i> ≤ 21, -20 ≤ <i>k</i> ≤ 21, -21 ≤ <i>l</i> ≤ 21
Absorption correction	SADABS [120]
Total no. reflections N _{all}	18656
Independent reflections N	1718
Reflections with <i>I</i> > 2σ(<i>I</i>) N'	1570
Absorption coefficient, μ / mm ⁻¹	40.366
Extinction coefficient	–
F(000)	3372
Refinement method	Full-matrix least-squares on F ²
Weighting scheme	$w = 1/[\sigma^2(F_o^2) + (0.0158P)^2 + 10.7273P]$, $P = (F_o^2 + 2F_c^2) / 3$
Number of free parameters	26
Goodness-on-fit on F ²	1.098
R ₁ (N'; N _{all})	0.0248; 0.0299
wR ₂ (N'; N _{all})	0.0519; 0.0536
Δρ _{min} ; Δρ _{max} / e·Å ⁻³	- 1.174 / 1.253
Deposition no. [168]	CSD – 421376

A similar three-dimensional topology is realized in the KSbO_3 [188] structure type (Fig. 7.3*b*), where the Sb atoms are surrounded by six O atoms. Also $\text{Cs}_{18}\text{Tl}_8\text{O}_6$ crystallizes in a structure type, which is isopointal to $\text{Hf}_{10}\text{Ta}_3\text{S}_3$ [189], in a broader sense, but with a different distribution of cations and anions. Such an idealized stoichiometry “ $\text{Hf}_9\text{Ta}_4\text{S}_3$ ” of $\text{Hf}_{10}\text{Ta}_3\text{S}_3$ would be similar to $\text{Cs}_9\text{Tl}_4\text{O}_3$ ($2\times$), but, in spite of similar positions of the atoms (Table 7.2), the mixed Ta/Hf occupancy leads to the formation of two new different structures and the experimentally determined stoichiometry of $\text{Hf}_{10}\text{Ta}_3\text{S}_3$.

Table 7.2. Atomic coordinates and equivalent isotropic displacement parameter $U_{eq} / \text{\AA}^2$ for $\text{Cs}_{18}\text{Tl}_8\text{O}_6$ and $\text{Hf}_{10}\text{Ta}_3\text{S}_3$.

Atom	Site	S.O.F	x	y	z	U_{eq}
$\text{Cs}_{18}\text{Tl}_8\text{O}_6$						
Tl1	8 <i>c</i>	1	0.91059(2)	x	x	0.03406(9)
Tl2	8 <i>c</i>	1	0.13439(2)	x	x	0.03625(9)
Cs1	12 <i>d</i>	1	0.36483(5)	0	0	0.0521(2)
Cs2	24 <i>f</i>	1	0.21363(3)	0.44826(4)	0.17401(3)	0.0426(1)
O1	12 <i>e</i>	1	0.3270(5)	$\frac{1}{2}$	0	0.0404(1)
$\text{Hf}_{10}\text{Ta}_3\text{S}_3$						
Ta1	8 <i>c</i>	1	0.9029(2)	x	x	
Hf1	8 <i>c</i>	0.55	0.1601(3)	x	x	
Ta2	8 <i>c</i>	0.45	0.1601(3)	x	x	
Hf2	12 <i>d</i>	1	0.3368(3)	0	0	
Hf3	24 <i>f</i>	1	0.2964(2)	0.2816(2)	0.0671(2)	
S1	12 <i>e</i>	1	0.327(2)	$\frac{1}{2}$	0	

Table 7.3. Atomic displacement parameters $U_{ij} / \text{\AA}^2$ for $\text{Cs}_{18}\text{Tl}_8\text{O}_6$.

Atom	U_{11}	U_{22}	U_{33}	U_{23}	U_{13}	U_{12}
Tl1	0.03406(9)	U_{11}	U_{11}	-0.00193(8)	U_{23}	U_{23}
Tl2	0.03625(9)	U_{11}	U_{11}	-0.00158(9)	U_{23}	U_{23}
Cs1	0.0311(2)	0.0377(3)	0.0874(5)	-0.0124(3)	0	0
Cs2	0.03559(8)	0.0526(2)	0.0395(2)	-0.0003(2)	-0.0003(2)	-0.0006(2)
O1	0.044(3)	0.042(3)	0.035(3)	0.001(3)	0	0

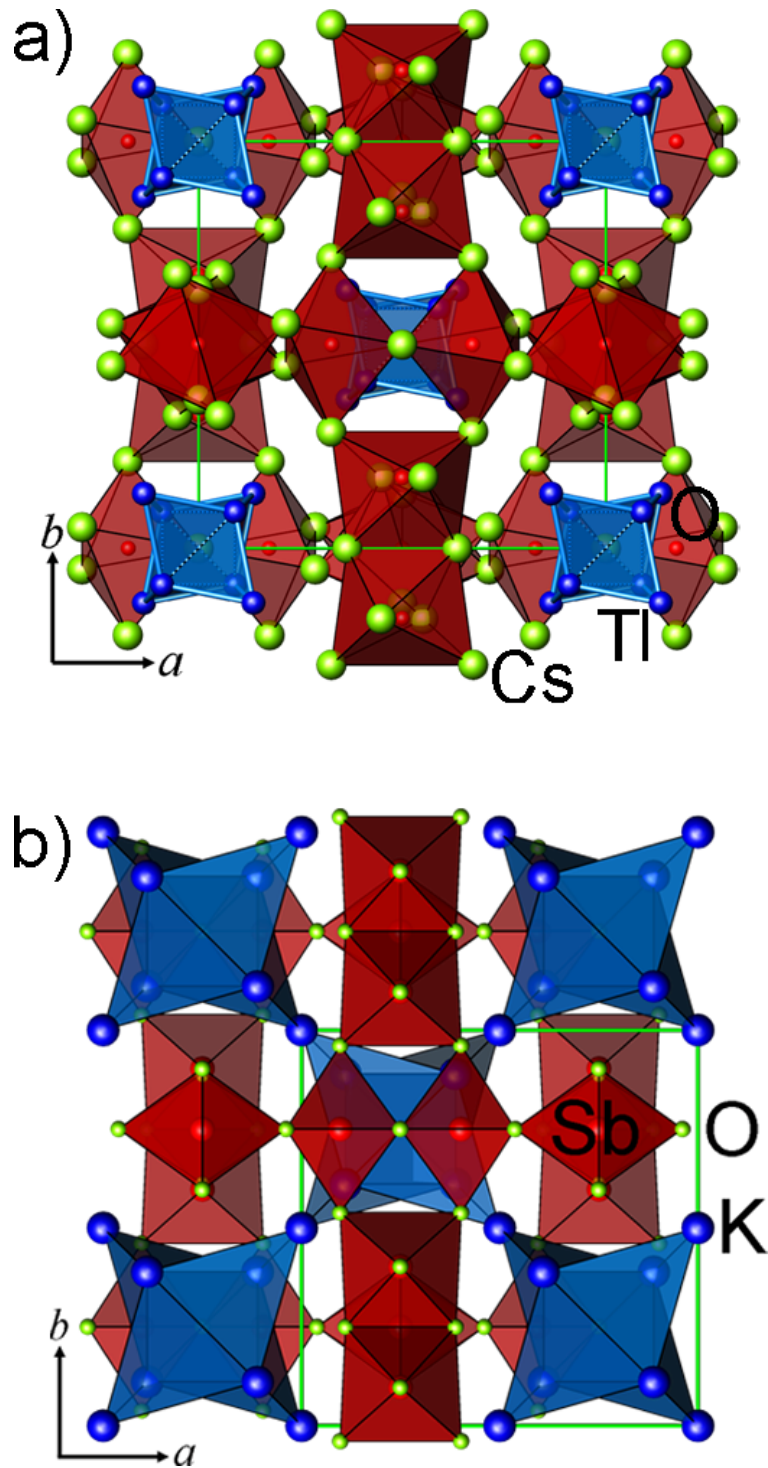


Figure 7.3. Graphical presentation of the crystal structure of $\text{Cs}_{18}\text{Tl}_8\text{O}_6$ (a , Tl_8 clusters emphasized as blue polyhedra, OCs_6 octahedra in red), and of KSbO_3 (b , SbO_6 octahedra in red, the K atoms are depicted as a corner-connected array of K_8 stella quadrangula). Green lines mark the unit cell edges.

An alternative way to represent the crystal structure of $\text{Cs}_{18}\text{Tl}_8\text{O}_6$ (Fig. 7.3a) is also commonly used for γ -brass (Cu_5Zn_8). The structure is presented in Fig. 7.4 and may be described in terms of two clusters, one of which has its center at the origin $(0, 0, 0)$ and the other is centered on $(\frac{1}{2}, \frac{1}{2}, \frac{1}{2})$. The clusters consist of a sequence of nested polyhedra: the Tl1 atoms form a tetrahedron (1st polyhedron) centered at the origin and can be denoted as inner tetrahedron (IT, *light blue edges*); an outer tetrahedron (2nd polyhedron) of Tl2 atoms caps the faces of the inner tetrahedron (OT, *red edges*); Cs1 atoms cap the edges of the OT forming an octahedron (3rd polyhedron, OH, *yellow edges*); a distorted cuboctahedron of Cs2 atoms is formed by capping the edges of the OH octahedron (4th polyhedron, CO, *blue edges*); the oxygen atoms are located on the faces of the elemental cell forming an undistorted polyhedron (5th polyhedron). These polyhedra adopt a bcc packing. Thus the structure of $\text{Cs}_{18}\text{Tl}_8\text{O}_6$ is related to the structure of γ -brass, where the cesium and thallium atoms occupy the positions of Zn and Cu ($\text{Cs}_{24}\text{Cs}_{12}\text{Tl}_8\text{Tl}_8 = \text{Zn}_{24}\text{Cu}_{12}\text{Zn}_8\text{Cu}_8$) and can be denoted as another novel “stuffed” γ -brass structure type.

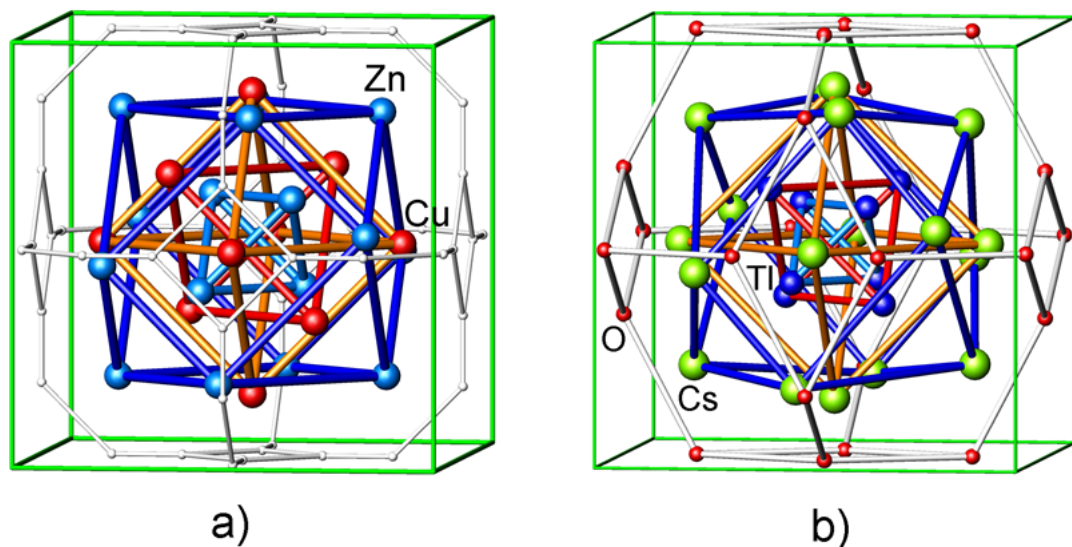


Figure 7.4. Representation of the cubic γ -brass (*a*, light blue spheres – Zn atoms, red spheres – Cu atoms, white spheres – voids located in 24-fold sites symmetry) and $\text{Cs}_{18}\text{Tl}_8\text{O}_6$ (*b*, blue spheres – thallium atoms, green spheres – cesium atoms, red spheres – oxygen atoms) structures in the form of 26-atom cluster. Green lines mark the unit cell edges.

Upon lowering the $I\bar{4}3m$ symmetry to $I23$ by the $t2$ translationengleich type transformation, the $(x, \frac{1}{2}, 0)$ site splits into two 12-fold sites $(x, \frac{1}{2}, 0)$ and $(x + \frac{1}{2}, \frac{1}{2}, 0)$. Also the (x, x, z) site occupied by Zn2 loses symmetry to become an (x, y, z) site occupied by Cs2 (Fig. 7.5). The oxygen is found to order into one of the split $(x, \frac{1}{2}, 0)$ sites due to oxygen-oxygen repulsion, which allow the 24-fold site to be only 50% occupied.

Cu_5Zn_8 $I\bar{4}3m$ (no. 217) $\downarrow t2$ $I23$ (no. 197) $\text{Cs}_{18}\text{Tl}_8\text{O}_6$	Cu₅Zn₈	Cu1:8c .3m	Zn1:8c .3m	Cu2:12e 2mm	Zn2:24g ..m	□:24f 2..
	0.828	0.110	0.355	0.313	$x \sim \frac{1}{3}$	
	x	x	0	0.313	$\frac{1}{2}$	
		x	x	0	0.036	0
	Cs₁₈Tl₈O₆	Tl1:8c .3.	Tl2:8c .3.	Cs1:12d 2..	Cs2:24f 1	O:12e 2..
	0.91059	0.13439	0.36483	0.21363	0.3271	$x \sim \frac{2}{3}$
	x	x	0	0.44826	$\frac{1}{2}$	$\frac{1}{2}$
		x	x	0	0.17401	0

Figure 7.5. Group-subgroup relation between the Cu_5Zn_8 and $\text{Cs}_{18}\text{Tl}_8\text{O}_6$ crystal structures, including the site transformations.

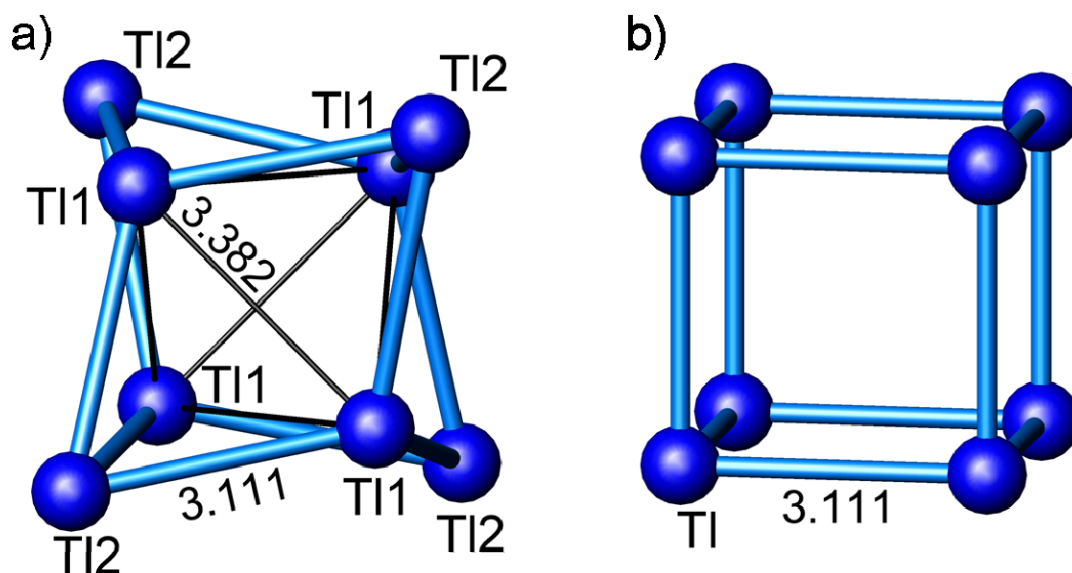


Figure 7.6. Comparison between the Tl_8 tetrahedral star (a) and ideal Tl_8 cube (b). Interatomic distances in (Å) and angles in ($^\circ$). Tl1–Tl1: $3.3816(6) \times 4$, Tl1–Tl2: $3.1113(4) \times 12$, Tl1–Tl2–Tl1: $65.84(1) \times 12$, Tl2–Tl1–Tl2: $109.548(8) \times 12$.

The presence of a structural unit such as *stella quadrangula* in both structures is clearly observed in Fig. 7.4. In contrast to γ -brass, where the corresponding unit is formed by two different types of atoms (Cu and Zn), the tetrahedral star in $\text{Cs}_{18}\text{Tl}_8\text{O}_6$ is formed by one type of atoms (thallium). Such an arrangement for a covalently bonded homo-atomic cluster, occurs for the first time in solid state compounds, to my knowledge.

Table 7.4. Selected bond distances / \AA^2 and angle / $^\circ$ of $\text{Cs}_{18}\text{Tl}_8\text{O}_6$.

		Tl1		Tl2	
Tl1–	Tl2	$3.1113(4) \times 3$	Tl2–	Tl1	$3.1113(4) \times 3$
	Tl1	$3.3816(6) \times 3$		Cs1	$3.9944(5) \times 3$
	Cs1	$4.0526(6) \times 3$		Cs2	$4.1097(5) \times 3$
	Cs2	$4.1473(5) \times 3$		Cs2	$4.3611(6) \times 3$
		Cs1			Cs2
Cs1–	O1	$2.935(6) \times 2$	Cs2–	O1	2.862(4)
	Cs1	3.615(1)		O1	2.9394(5)
	Cs2	$3.8497(5) \times 2$		Cs1	3.8498(5)
	Cs2	$3.9620(5) \times 2$		Cs1	3.9259(2)
	Tl2	3.9944(5)		Cs2	$4.0072(2) \times 2$
	Tl1	$4.0526(6) \times 2$		Tl2	4.1097(5)
	Cs2	4.4523(6)		Tl1	4.1472(5)
				Cs2	$4.1862(3) \times 2$
				Cs1	4.4523(6)
		O1			
O1–	Cs2	$2.862(4) \times 2$			
	Cs1	$2.935(6) \times 2$			
	Cs2	$2.9394(5) \times 2$			

Topologically, the Tl_8 units can be derived from an ideal cube of 8 Tl atoms by a displacive distortion resulting in a tetrahedral star, which consists of four tetrahedra, each sharing one face with a fifth, the central tetrahedron (Fig. 7.6a). The $[\text{Tl}_8]^{6-}$ tetrahedral star significantly deviates from an ideal cube as indicated in

Fig. 7.6b. Although the site symmetry of the center of the $[\text{Tl}_8]^{6-}$ cluster is T , within the limit of experimental error the higher point symmetry of T_d including the next neighboured Cs atoms is fulfilled.

The shortest Tl–Tl separation within the $[\text{Tl}_8]^{6-}$ cluster is equal to 3.111 Å, while the shortest distance between thallium atoms within the inner tetrahedron is equal to 3.382 Å. The intercluster Tl–Tl separations are clearly larger (≥ 6.4 Å). The angles between thallium atoms in both inner and outer tetrahedra $\angle \text{Tl–Tl–Tl}$ are equal to 60° , thus forming two ideal interpenetrated tetrahedrons (Fig. 7.4). The same angle inside the tetrahedra is also observed for both γ -brass and $\text{Hf}_{10}\text{Ta}_3\text{S}_3$. For better comparison, the interatomic distances in $\text{Cs}_{18}\text{Tl}_8\text{O}_6$ are given in Table 7.4.

7.1.3. Electrical Resistivity Measurements

Temperature – dependent resistivity measurements of $\text{Cs}_{18}\text{Tl}_8\text{O}_6$ were performed according to the general procedure of the *van der Pauw* method. The specific electrical resistivity increases linearly from 1.08 $\text{m}\Omega\cdot\text{cm}$ at 6 K to 3.75 $\text{m}\Omega\cdot\text{cm}$ at 290 K, which is typical for a moderate metallic conductor (Fig. 7.7).

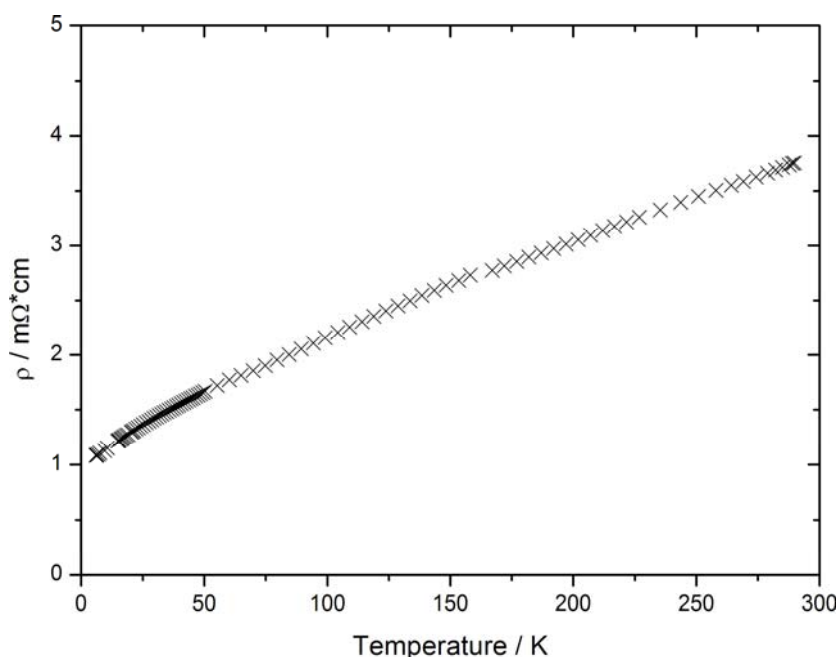


Figure 7.7. Temperature – dependent resistivity data of $\text{Cs}_{18}\text{Tl}_8\text{O}_6$.

7.1.4. Magnetic Susceptibility Measurements

The magnetization of $\text{Cs}_{18}\text{Tl}_8\text{O}_6$ was measured using a SQUID magnetometer (MPMS 5.5, Quantum Design, USA) in the temperature range 5 – 300 K at $H = 0.001, 0.1, 1, 3, 5$ and 7 T. The specimen (0.1309 g) was sealed in a quartz tube under helium. The raw data were corrected for the holder contribution.

The magnetic susceptibility is independent of temperature as well as of field strength in the range of 50 to 300 K ($-6.84 \times 10^{-4} \pm 2.5\%$ emu/mol) and approximates the sum of the diamagnetic core corrections ($18\chi(\text{Cs}^+) + 8\chi(\text{Tl}^+) + 6\chi(\text{O}^{2-}) = -9.02 \times 10^{-4}$ emu/mol) and the Larmor susceptibility [125, 126] of the cluster orbital electrons (-1.91×10^{-4} emu/mol), which was calculated assuming the shape of an ideal cube with a side length of 3.111 Å. Molar susceptibility vs. temperature plots are presented in Fig. 7.8. The presence of paramagnetic $(\text{Cs}^+)_8[\text{Tl}_{11}]^{7-}(e^-)$ in the measured sample leads to an increase of the susceptibility in the temperature range of 5 to 50 K (Fig. 7.8). Thus, the magnetic susceptibilities were described according to Curie-Weiss law in the mentioned temperature interval at 1, 3, 5, and 7T (Figs. A2.1 – A2.4) and the average amount of paramagnetic impurities in the sample was determined to be 10 wt. %.

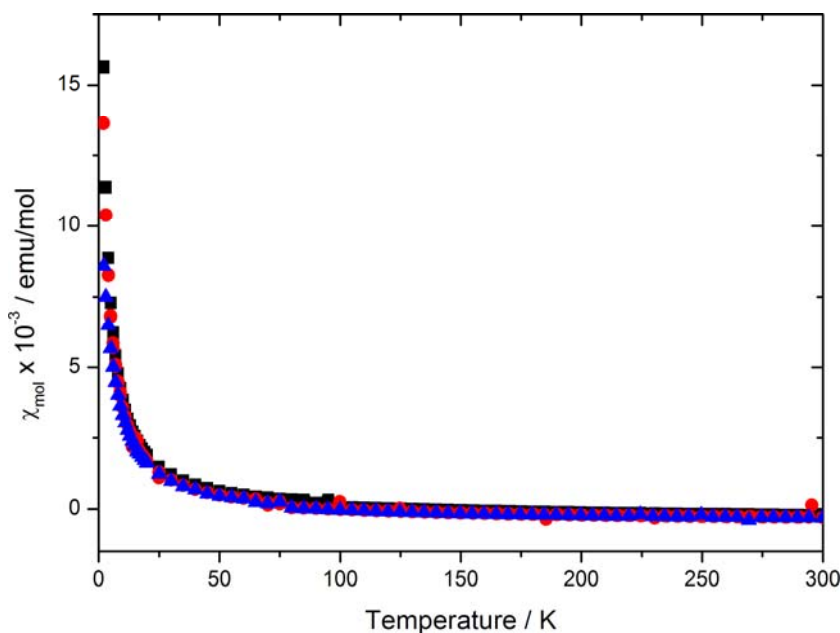


Figure 7.8. Temperature – dependent magnetic susceptibility data of $\text{Cs}_{18}\text{Tl}_8\text{O}_6$ at 0.1T (black squares), 1T (red circles) and 3T (blue triangles).

7.1.5. Electron Balance of the $[\text{Tl}_8]^{6-}$ Cluster-anion

Interestingly, $\text{Cs}_{18}\text{Tl}_8\text{O}_6$ and the previously reported $\text{Cs}_8\text{Tl}_8\text{O}$ [104] contain Tl_8 -clusters displaying the same number of valence electrons, however, develop different structures, a tetrahedral star (Fig. 7.3a) or a parallelepiped (Fig. 7.9), respectively. Both clusters can be formally described as $[\text{Tl}_8]^{6-}$ clusteranions having 30 valence electrons available. Neither of them can be understood in terms of known qualitative concepts. Within the Zintl–Klemm concept, which is based on $2e2c$ bonds, the number of valence electrons should be 40 ($12 \text{ edges} \times 2e + 8$ inert pairs) for both, the tetrahedral star and the parallelepiped. Also applying Wade's rules fails: a *closo* cluster $[\text{Tl}_8]^{6-}$ would require $34e$ ($4 \times 8 + 2$, inert-electron pairs included), which is in conflict with the $30e$ available. The $[\text{Tl}_8]^{6-}$ cluster can best be denoted as hypoelectronic [102] with $2n-2$ skeletal electrons ($14e$, disregarding $2 \times 8e$ for the lone pairs).

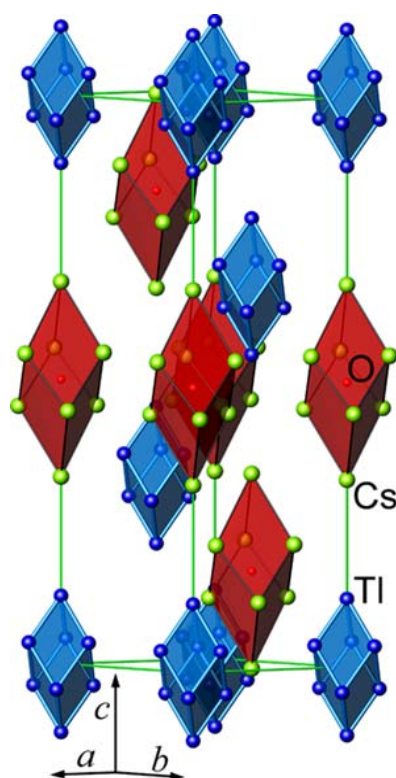


Figure 7.9. Graphical presentation of the crystal structure of $\text{Cs}_8\text{Tl}_8\text{O}$ [104]: Tl_8 clusters emphasized as blue polyhedra, Cs_8 polyhedra in red, centered by oxygen.

7.1.6. Electronic Structure Calculations and Quantum Chemical Analysis

DFT calculations using the PBE functional for exchange and correlation [138] were performed for the crystal structures as determined experimentally (band structure) as well as for isolated Cs_6Tl_8 clusters representing charge neutral cut-outs of the crystal. The band structures of the periodic systems were computed with the WIEN2k [143] code, using the following computational parameters. Radii of the atomic spheres: 2.9 Bohr (Tl), 2.7 Bohr (Cs) and 2.7 Bohr (O); cut-off parameter $\text{RKmax} = 7.0$; $\text{Gmax} = 14.0$. The Kohn-Sham equations were solved for 119 k-points in the irreducible wedge of the Brillouin zone. Increasing the number of k-points and the cutoff parameter RKmax in the periodic calculations doesn't change the density of states and the effective charges significantly. The core-valence separation was set to -6.0 Ry. Thus 13 electrons of Tl, 19 electrons of Cs and 6 electrons of O were taken as valence electrons, being treated scalar relativistic. The APW+lo basis was applied, added by local orbitals for $l = 2$ (Tl, Cs) and $l = 0$ (Cs, O). Spin-orbit interaction was included by a second-variational method [190]. The isolated Cs_6Tl_8 clusters were computed with the TURBOMOLE [145, 146] program package, applying the RI-variant. The def2-TZVP basis set was used. To check the quality of the basis sets used, selected cluster calculations (tetrahedral star, T_d , triplet, structure optimization; parallelepiped, C_1 , singlet, structure optimization) were repeated with the quadruple-zeta def2-QZVP basis set (Tl [7s6p4d4f1g], Cs [6s5p4d1f]). In both cases the maximal deviations compared to the def2-TZVP results are as follows: Tl-Tl distances < 0.005 Å, Tl-Cs distances < 0.02 Å, orbital energies < 0.02 eV. The energy difference between two states is 22 kJ/mol, compared to 24 kJ/mol obtained with the def2-TZVP basis set. The basis set quality can be regarded to be converged with respect to the investigated properties both, in the cluster and in the periodic calculations. Scalar relativistic effects were included via the choice of the proper pseudopotentials: Tl, 21 valence electrons [191]; Cs, 9 valence electrons [192]. In the two-component relativistic calculations, the spin-orbit variant of the Tl pseudopotential was used. In the scalar relativistic case the structures of the clusters were optimized with (O_h , T_d and D_{3d} symmetry) and without symmetry constraints. The energy was

converged to 10^{-9} a.u., the maximum norm of the cartesian gradient to 10^{-5} a.u.. The existence of a minimum was verified by a frequency analysis. As analytical gradients are not yet available in the two component version of TURBOMOLE [146], the fully relativistic structure optimizations were performed numerically, assuming O_h , T_d and D_{3d} symmetry respectively. Effective charges of the atoms in the crystals were calculated from the integrated electron densities within the atomic basins, obtained by a topological analysis of the electron density [147]. Details of the Cs_6Tl_8 cluster calculations at the scalar relativistic level (scalar relativistic pseudopotentials, PBE functional, def2-TZVP basis set) are presented in Table A1.1. The corresponding data of the two-component relativistic calculations (spin-orbit variant of the Tl pseudopotential) are listed in Table A1.2. For comparison, results with the B3LYP hybrid functional are given in Tables A1.2 and A1.3.

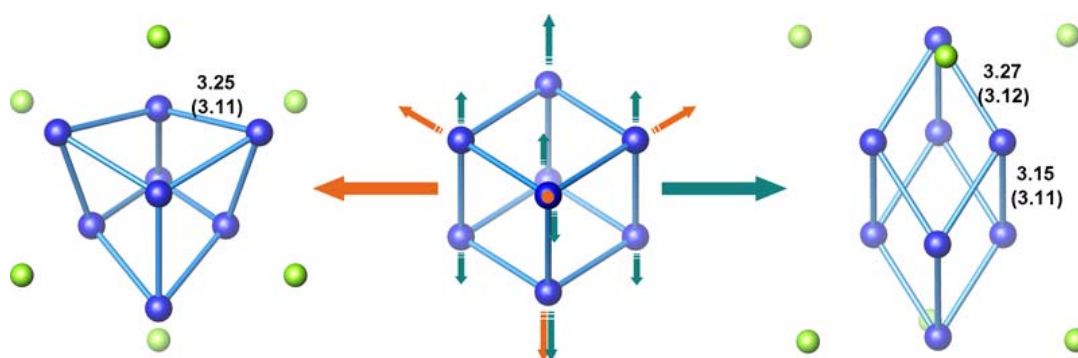


Figure 7.10. Optimized structures of Cs_6Tl_8 -Clusters. The shapes of the Tl_8 -units conform to the polyhedra found in $\text{Cs}_{18}\text{Tl}_8\text{O}_6$ (left, tetrahedral star) and in $\text{Cs}_8\text{Tl}_8\text{O}$ (right, parallelepiped). The symmetry-unique computed (two component relativistic, PBE, def2-TZVP) Tl-Tl distances are given in Å. The corresponding experimental values found for the crystal are added in parenthesis.

Topologically, both considered Tl_8 units, the tetrahedral star in $\text{Cs}_{18}\text{Tl}_8\text{O}_6$ and the parallelepiped in $\text{Cs}_8\text{Tl}_8\text{O}$, can be derived from an ideal cube by a displacive distortion as sketched in Fig. 7.10. Remarkably, in either case the lattice symmetries would allow to accommodate Tl_8 -units of cubic shape since the site symmetries are subgroups of O_h . Moreover, the nearest neighbors (Cs^+ ions) do exert but a weak crystal field, and their positions could either be easily reconciled

with a high-symmetric clusteranion by slight displacive movements ($\text{Cs}_8\text{Tl}_8\text{O}$) or already display the higher symmetry ($\text{Cs}1 \times 6: O_h$) in comparison to the tetrahedral star (T_d) in $\text{Cs}_{18}\text{Tl}_8\text{O}_6$. In order to understand the driving forces behind the distortions, and thus to resolve these puzzling inconsistencies, density functional (DFT) calculations on the periodic crystals as well as on isolated Cs_6Tl_8 clusters for both compounds have been performed. As both clusteranions derive from a cube, a hypothetical $\text{Cs}_{18}\text{Tl}_8\text{O}_6$ crystal with an ideal cubic Tl_8 -unit (side length: 3.11 \AA) was also examined.

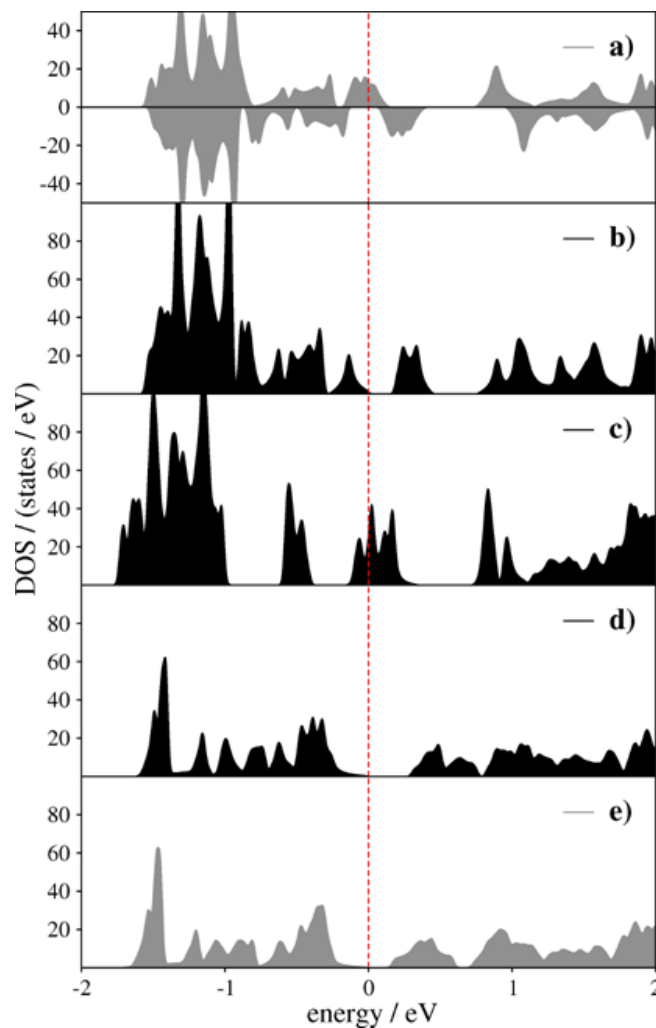


Figure 7.11. Total densities of states (DOS) near the Fermi level of $\text{Cs}_{18}\text{Tl}_8\text{O}_6$ (*a* and *b*), hypothetical $\text{Cs}_{18}\text{Tl}_8\text{O}_6$ with cubic Tl_8 -unit (*c*) and $\text{Cs}_8\text{Tl}_8\text{O}$ (*d* and *e*). Grey: without spin-orbit coupling (*a* and *e*); black: including spin-orbit coupling (*b*, *c* and *d*).

The total densities of states (DOS) near the Fermi level of $\text{Cs}_{18}\text{Tl}_8\text{O}_6$, hypothetical $\text{Cs}_{18}\text{Tl}_8\text{O}_6$ with cubic Tl_8 -unit and $\text{Cs}_8\text{Tl}_8\text{O}$ are presented in Fig. 7.11. The total DOS, obtained from a spin-polarized calculation with spin-orbit coupling, is not shown in Fig. 7.11. In this case the calculation converges to a non-spin-polarized density and the DOS for both spins is exactly one half of the DOS from the non-polarized calculation. The periodic DFT calculations for the $\text{Cs}_{18}\text{Tl}_8\text{O}_6$ crystal at the scalar relativistic level result in a spin-polarized electronic system with a finite density of states (DOS) of the majority spin component at the Fermi level (Fig. 7.11a), indicating half-metallic properties of the crystal, which is in contrast to the observed diamagnetism. This discrepancy is resolved, however, if relativistic spin-orbit coupling is included in the calculations. Thus, spin-polarization vanishes, and a gap (0.18 eV) between valence and conduction bands in the crystal opens (Fig. 7.11b and 1st column in Fig. 7.14).

The band structure of $\text{Cs}_8\text{Tl}_8\text{O}$ looks similar (Fig. 7.11). However, in contrast to $\text{Cs}_{18}\text{Tl}_8\text{O}_6$, for this compound no spin-polarization, but a band gap results already at the scalar relativistic level (Fig. 7.11e). Considering spin-orbit coupling does not change the electronic structure of $\text{Cs}_8\text{Tl}_8\text{O}$ in principle (Fig. 7.11d and columns 5 – 7 in Fig. 7.14). Calculations on the hypothetical $\text{Cs}_{18}\text{Tl}_8\text{O}_6$ crystal where the tetrahedral star is replaced by an ideal cube with side length 3.11 Å with the ideal cubic Tl_8 -unit yield a finite DOS at the Fermi level even with spin-orbit coupling (Fig. 7.11c).

The atom-projected DOS, computed with the parameters described above, are depicted for $\text{Cs}_{18}\text{Tl}_8\text{O}_6$ and $\text{Cs}_8\text{Tl}_8\text{O}$ in Figs. 7.12 and 7.13, respectively. The bands below -8.2 eV have to be attributed to the Cs ($5s$, $5p$) and Tl ($5d$) semi-core states. Thus the DOS at energies above mentioned value is considered. In the WIEN2k program the atom-projected DOS is computed inside the atomic spheres. As the condition of non-overlapping spheres leads to rather large interstitial regions in both compounds, a substantial amount of interstitial DOS contributes to the total DOS. The plane wave basis functions and thus the corresponding DOS cannot be attributed unambiguously to certain atoms. If a Kohn-Sham eigenvector is composed of plane waves and of atomic functions of only one crystallographically unique atom, however, it can be assumed that the partial DOS coming from the plane wave part is related to that atom. As this is the case for the compounds considered here, the disregard of the interstitial DOS will not impact the

conclusions drawn in the present work. The details of the atom projected DOS will be discussed below in conjunction with the MO diagrams of the Cs_6Tl_8 molecule.

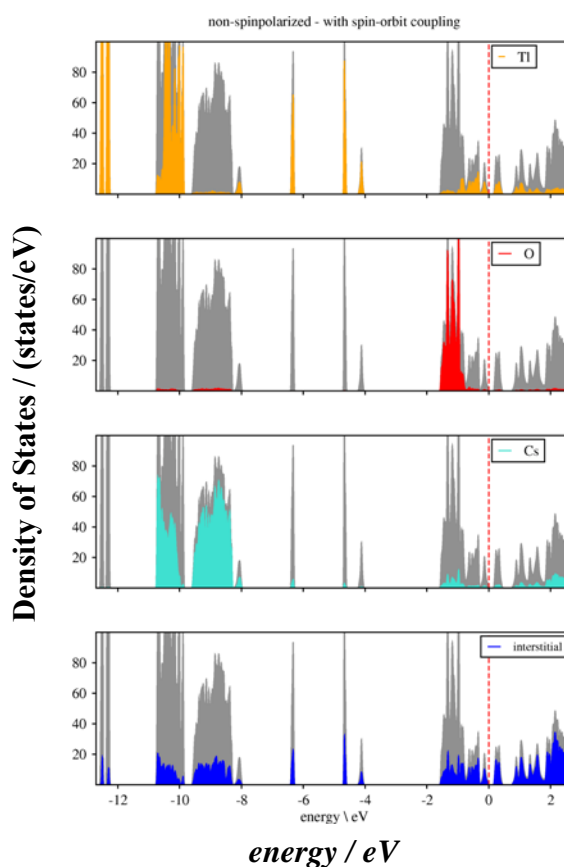


Figure 7.12. Atom-projected non-spin-polarized density of states for $\text{Cs}_{18}\text{Tl}_8\text{O}_6$, spin-orbit coupling is considered.

The energy difference between HOMO and LUMO in Cs_6Tl_8 (tetrahedral star) computed with PBE fully relativistic is 0.46 eV. Due to band dispersion, the band gap obtained in the periodic calculations is smaller (0.18 eV). The comparison of such values with measured band gaps bears uncertainties, as the treatment of the occupied and the empty eigenvalues in the Kohn-Sham equations is different. Moreover, the values strongly depend on the exchange and correlation functional (B3LYP: $\epsilon_{\text{LUMO}} - \epsilon_{\text{HOMO}} = 1.22$ eV). In the case of $\text{Cs}_{18}\text{Tl}_8\text{O}_6$ the band gap may be estimated from the spin-orbit splitting of the triply degenerate orbitals, as spin-orbit coupling is the only mechanism to lift the degeneracy. The splitting of the fully occupied t-orbitals is in the range of 0.03 and 0.05 eV. Assuming such a value as a band gap, $\text{Cs}_{18}\text{Tl}_8\text{O}_6$ can be regarded as a narrow band gap semiconductor, which explains the black color of the compound, but still not the weak metallic

behaviour observed in the resistivity measurement. If conducting surface states, as found in topological insulators, are responsible for the conductivity, then it has to be investigated in the future.

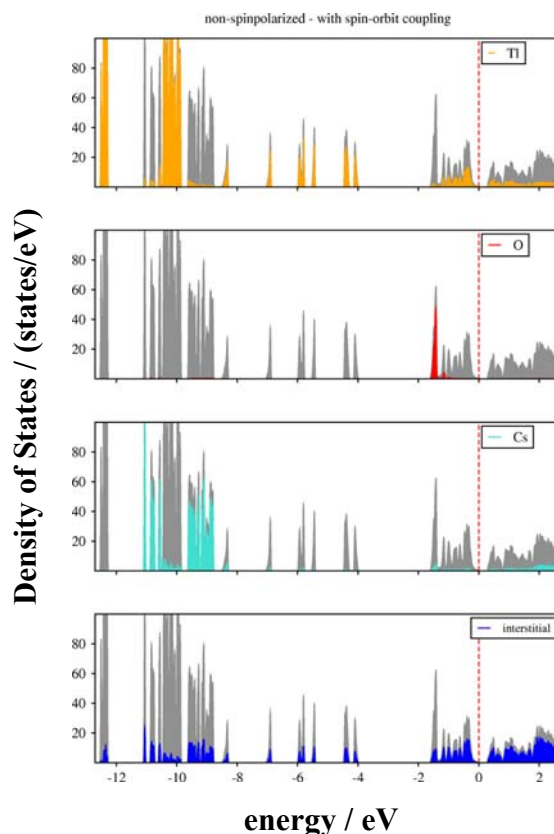


Figure 7.13. Atom-projected non-spin-polarized density of states for $\text{Cs}_8\text{Tl}_8\text{O}$, spin-orbit coupling is considered.

The analysis of the charge distribution by a topological analysis of the computed electron density [147] doesn't provide an explanation for the different shapes of the Tl_8 -units in either compounds, $\text{Cs}_{18}\text{Tl}_8\text{O}_6$ or $\text{Cs}_8\text{Tl}_8\text{O}$. The effective charges are quite similar ($\text{Cs}_{18}\text{Tl}_8\text{O}_6$: $\text{Tl1} -0.44$, $\text{Tl2} -0.49$, $\text{Cs1} +0.68$, $\text{Cs2} +0.67$, $\text{O} -1.40$; $\text{Cs}_8\text{Tl}_8\text{O}$: $\text{Tl1} -0.46$, $\text{Tl2} -0.50$, $\text{Cs1} +0.65$, $\text{Cs2} +0.64$, $\text{O} -1.39$), revealing a charge transfer of comparable size to the Tl_8 -unit ($\text{Cs}_{18}\text{Tl}_8\text{O}_6$: -3.68 ; $\text{Cs}_8\text{Tl}_8\text{O}$: -3.78). Effective charges derived from quantum chemical calculations suffer in some respect from arbitrariness [193]. Nevertheless, as effective charges tend to be lower than formal charges [194], the high cumulative negative charge in the Tl_8 -units justifies their formal description as $[\text{Tl}_8]^{6-}$. Moreover, these visually suggest to discuss the peculiarities of the clusteranions in a local picture, comparing the

electronic structures obtained on the various types of excised, charge neutral Cs_6Tl_8 molecular units (clusters) with those calculated for the extended solids.

The results for the molecular units are based on optimized structures. When spin-orbit coupling is neglected, the lowest minimum found on the potential energy surface with no symmetry restrictions corresponds to a Tl_8 -unit with the shape of a parallelepiped with D_{3d} symmetry (Fig. 7.10, right side), comparable to the Tl_8 -unit found experimentally in $\text{Cs}_8\text{Tl}_8\text{O}$. The Cs atoms take roughly the positions of Cs1 in the crystal. This minimum is a closed-shell singlet state. If the symmetry is constrained to T_d , which is the symmetry of the tetrahedral star in $\text{Cs}_{18}\text{Tl}_8\text{O}_6$, the minimum corresponds to an open-shell triplet state which is by 13 kJ/mol lower than an open-shell singlet of same symmetry. But even the triplet state is less stable by 24 kJ/mol than the parallelepiped. If, however, fully relativistic calculations including spin-orbit coupling are performed, both, the parallelepiped and the tetrahedral star configuration are closed-shell systems, and, moreover, the energetic order of both configurations is reversed: the tetrahedral star is now more stable by 13 kJ/mol than the parallelepiped. Thus the contribution of spin-orbit coupling to the stabilization of the tetrahedral star amounts to 37 kJ/mol. The optimized Tl-Tl distances in both configurations are represented in Fig. 7.10, together with the corresponding distances measured in the crystals. If the symmetry is constrained to O_h , forcing a cubic arrangement of the Tl atoms, the cluster remains an open-shell system ($\langle S_z \rangle = 0.54$) even with spin-orbit coupling. Such a cluster with an ideal Tl_8 -cube is less stable by 79 kJ/mol than the tetrahedral star. It will be worthwhile to analyze the ratio of electrostatic and relativistic forces contributing to the Jahn-Teller coupling of this cubic cluster according to the procedure as described in ref. [195]) for tetrahedral systems. This will be subject for future investigations. In order to investigate the dependence of the results on the functional, some calculations were repeated with the B3LYP [196, 197] hybrid functional (Tables A1.2 and A1.3). Total and orbital energies obtained with PBE and B3LYP, respectively, differ due to the different treatment of exchange and correlation of course. However, the relative order of the different structures, their electronic states as well as the orbital ordering remains the same. With B3LYP at the scalar relativistic level the parallelepiped is by 49 kJ/mol more stable than the tetrahedral star. As with PBE the order is reversed if spin-orbit coupling is included, the tetrahedral star being more stable by 15 kJ/mol. Thus, the relative

stabilization of the tetrahedral star due to spin–orbit coupling is even larger with B3LYP than with PBE.

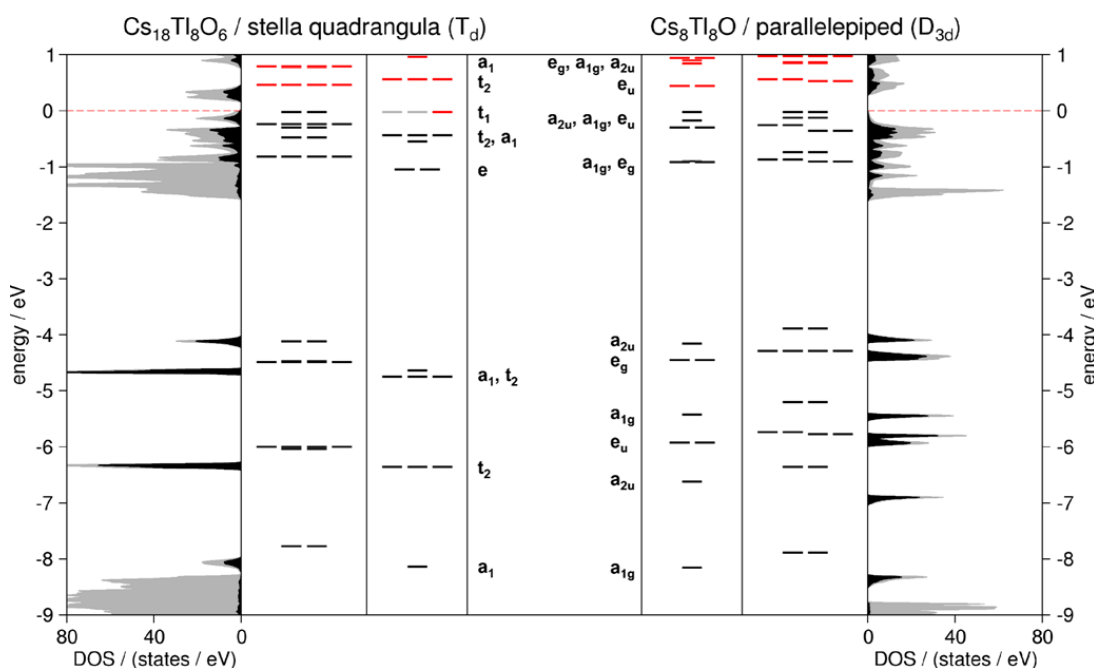


Figure 7.14. Density of states (DOS) of the crystals and MO diagrams of the Cs_6Tl_8 clusters. Left side: $\text{Cs}_{18}\text{Tl}_8\text{O}_6$ and tetrahedral star; right side: $\text{Cs}_8\text{Tl}_8\text{O}$ and parallelepiped. The diagrams show scalar relativistic MOs (majority spin, column 3 and 5; occupied: black; partially occupied: grey; unoccupied: red), fully relativistic spinors (column 2 and 6) and DOS including spin–orbit coupling (column 1 and 7; total DOS: gray; Tl-projected DOS: black). E_F and $\varepsilon_{\text{HOMO}}$ are shifted to 0 eV.

For comparison of the DOS of the extended structures with the MO diagrams calculated for the isolated cluster types (Fig. 7.14), the atom-projected DOS of the oxygen atoms (at -1 eV to -2 eV) can be disregarded. The spatial separation and the shielding by the Cs atoms render any covalent interaction with the clusteranions insignificant. Besides the O-projected DOS, only contributions of the interstitial space and of the Tl atoms are found at energies above -8.2 eV. The latter are highlighted in Fig. 7.14. The cluster MOs map very well onto the Tl-projected DOS in both cases, $\text{Cs}_{18}\text{Tl}_8\text{O}_6$ and $\text{Cs}_8\text{Tl}_8\text{O}$. The respective partial DOS in the valence region split into two parts. Below -4 eV, eight very narrow, partially

degenerate bands appear per Tl_8 -unit, which correspond to the lower MOs of the cluster in the same energy region. This part of the electronic structure can be attributed to the inert-electron pairs of the Tl atoms. The marginal dispersion of these bands points to a high localization. In the non-relativistic limit, the corresponding energy levels are shifted upwards by more than 1 eV, indicating that these bands are stabilized significantly by scalar relativistic effects. The bands between -1 eV and E_F (set to 0 eV) correspond to the 14 skeletal electrons of the n -atomic cluster ($2n-2$). The pronounced similarity of the MO patterns of the Cs_6Tl_8 clusters and the densities of states of the extended crystals as well as the analogies concerning the open- and closed-shell electronic structures support the view of covalently bonded clusteranions.

The ideal cubic arrangement leads to an open shell system at any level of theory applied in this work. Its stretching along the body diagonal leading to the parallelepiped in $\text{Cs}_8\text{Tl}_8\text{O}$ can be regarded a Jahn–Teller distortion, resulting in a closed shell electronic system. In $\text{Cs}_{18}\text{Tl}_8\text{O}_6$ the situation is more complicated. The tetrahedral star results from moving the two subsets of each four tetrahedrally arranged Tl atoms constituting the cube inwards and outwards, respectively, and still maintains a high symmetry (T_d). In a scalar relativistic MO picture, such an arrangement cannot be understood in terms of the Jahn–Teller theorem, as in this case the compound would still take a spin-polarized, open-shell electronic structure. Only in a fully relativistic treatment, which includes spin–orbit coupling, the tetrahedral star becomes a closed-shell electronic system, in accordance with the experimental findings. At this level of theory, the tetrahedral star can be regarded as a Jahn–Teller distorted cube. The stabilization of the clusteranion due to spin–orbit interaction has turned out to be much larger for the tetrahedral star than for the parallelepiped. Thus both shapes of $[\text{Tl}_8]^{6-}$ become competitive local minima on the potential energy surface, and both shapes are realized in compounds of the Cs–Tl–O system, depending on the ratio of the three constituents.

The domains (isosurfaces) of the electron-localization function (ELF) as well as a representation of the latter one on the plane for tetrahedral star, parallelepiped and cube are shown in Fig. 7.15. The ELF exhibits maxima (attractors) in the core region of Tl and Cs as well as, in the case of the tetrahedral star and the parallelepiped, in regions outside of the cage (Table 7.5). The latter can be attributed to the lone pairs of the Tl atoms. The corresponding domains merge with

the Tl(5d) domains at the values given in Table 7.5. The atomic domains are well separated, no attractor is found between two atoms. In contrast, in the cube the outer domains will be interconnected to two Tl cores (Fig. 7.15). The minimum value of ELF is observed for cluster centres ($\eta = 0.14$). According to the ELF, the Tl atoms in the tetrahedral star and in the parallelepiped are not connected by direct covalent bonds.

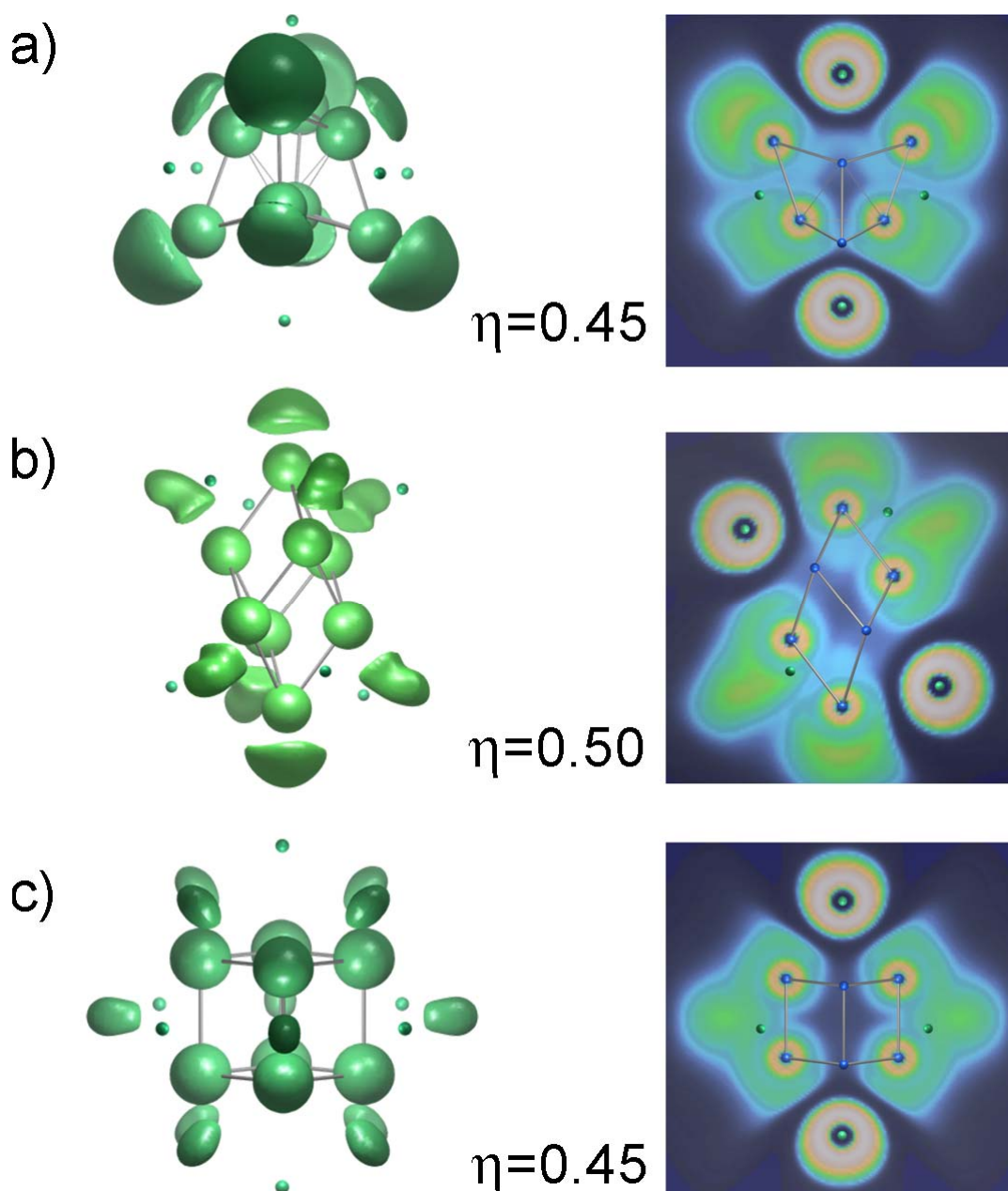


Figure 7.15. Domains (isosurfaces) of the ELF (*left*), Cs semi-core omitted as well as ELF distribution on selected planes (*right*) for Cs_6Tl_8 molecule in form of tetrahedral star (*a*), parallelepiped (*b*) and cube (*c*).

Table 7.5. The ELF distribution η in Cs_6Tl_8 neutral molecule.

	Particular ELF	Tetrahedral Star	Parallelepiped
Attractors	Cs semi-core(5s/5p)	0.90	0.90
	Tl semi-core (5d)	0.78	0.78
	Tl	0.47 – 0.58	0.56 – 0.57
Domain inter-connection	Inert pair – semi-core	0.36 – 0.38	0.37
	all Tl domains	0.25	0.28
Minimum	cluster centre	0.14	0.14

7.2. Regular $[\text{Tl}_6]^{6-}$ Cluster in $\text{Cs}_4\text{Tl}_2\text{O}$

7.2.1. Synthesis, Powder XRD and Thermal Stability

Syntheses and handlings of educts and products were performed in glovebox or using Schlenk technique. $\text{Cs}_4\text{Tl}_2\text{O}$ was prepared by reaction of the binary compounds CsTl and Cs_2O . The detailed reaction techniques for preparation of CsTl have been described in Chapter 7.1.1. The mixture of CsTl and Cs_2O in the molar ratio 1:0.95 (total amount 0.5-1 g) was placed into a tantalum tube, which was sealed under argon with an arc-welder. In order to prevent oxidation, the tantalum tube was encapsulated in a glass jacket, under argon. The reaction mixture was heated up to 573 K at a rate of 50 K/h, annealed at this temperature for one week, and then cooled to room temperature at a rate of 5 K/h. The as-synthesized products were pure, sometimes containing a small amount of $\text{Cs}_{18}\text{Tl}_8\text{O}_6$ (1-3 at.%) (Chapter 7.1), according to X-Ray powder diffraction (Fig. 7.16).

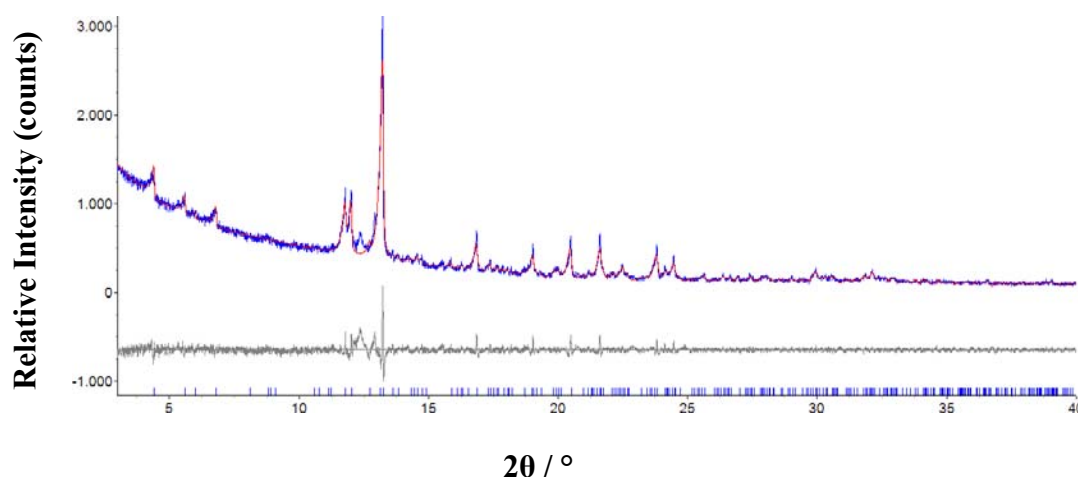


Figure 7.16. Le Bail refinement of $\text{Cs}_4\text{Tl}_2\text{O}$ (measured curve (blue line), theoretically calculated curve (red line), difference curve (grey line), Bragg reflections (blue ticks)) ($\lambda = 0.7093 \text{ \AA}$).

The purity of the product sensitively depends on purity, handling and composition of the starting mixtures, as well as on the precise control of the reaction conditions. The atom ratio of heavy elements in the product was additionally confirmed by EDX analysis, and no impurity elements were detected.

The thermal stability was studied using Differential Scanning Calorimetry. The specimen (0.0072 g) was placed in an Al crucible with a lid, cold-sealed under argon atmosphere to prevent oxidation and heated to 623 K at a rate of 10 K/min, and then cooled down to room temperature at the same rate. The whole process was run under argon. $\text{Cs}_4\text{Tl}_2\text{O}$ is extremely sensitive to moisture and air, and is stable at least up to 523 K in an argon atmosphere.

7.2.2. Crystal Structure Analysis

Single crystal X-ray structure analysis on $\text{Cs}_4\text{Tl}_2\text{O}$ was performed at room temperature. Crystallographic data, atomic coordinates and anisotropic parameters are summarized in Tables 7.6, 7.7, and 7.8, respectively.

$\text{Cs}_4\text{Tl}_2\text{O}$ crystallizes in a novel structure type (Fig. 7.17). The crystal structure contains isolated $[\text{Tl}_6]^{6-}$ octahedra and $[\text{Cs}_{12}\text{O}_3]^{6+}$ triple octahedra. The structure can be related to $\text{Cs}_8\text{Tl}_8\text{O}$ [104] by *cluster-replacement* [198], *i.e.* the general

Table 7.6. The crystallographic and structure refinement data for Cs₄Tl₂O.

Cs ₄ Tl ₂ O	
Space group (no.); <i>Z</i>	$R\bar{3}m$ (166); 9
Cell parameters / Å	$a = 11.986(1)$ $c = 20.370(2)$
Volume / Å ³	2534.3(4)
Molar weight / g·mol ⁻¹	956.38
Density (calculated) / g·cm ⁻³	5.640
Crystal form, color	Block, silver black metallic
Crystal size / mm ³	0.15 × 0.10 × 0.10
Diffractometer	Smart APEX-II CCD, Bruker AXS
Monochromator	Graphite
X-ray radiation, λ / Å	Mo-Kα, 0.71073
θ range, °	2.20 to 29.99
Index range	-16 ≤ <i>h</i> ≤ 16, -16 ≤ <i>k</i> ≤ 16, -28 ≤ <i>l</i> ≤ 28
Absorption correction	SADABS [120]
Total no. reflections <i>N</i> _{all}	15597
Independent reflections <i>N</i>	942
Reflections with <i>I</i> > 2σ(<i>I</i>) <i>N'</i>	634
Absorption coefficient, μ / mm ⁻¹	41.248
Extinction coefficient	0.000036(7)
<i>F</i> (000)	3510
Refinement method	Full-matrix least-squares on <i>F</i> ²
Weighting scheme	$w = 1/[\sigma^2(F_o^2) + (0.0180P)^2 + 113.4242P]$, where $P = (F_o^2 + 2F_c^2) / 3$
Number of free parameters	25
Goodness-on-fit on <i>F</i> ²	1.038
<i>R</i> ₁ (<i>N'</i> ; <i>N</i> _{all})	0.0367; 0.0669
<i>wR</i> ₂ (<i>N'</i> ; <i>N</i> _{all})	0.0723; 0.0836
Δρ _{min} ; Δρ _{max} / e·Å ⁻³	-2.881 / 2.945
Deposition no. [168]	CSD – 422336

arrangement of the cluster units, although of different composition and shape, is the same. The barycenters of the ionic constituents in both compounds correspond to a rhombohedral distorted NaCl type of structure. The interactions between the $(\text{Cs}/\text{O})^{\text{n}+}$ and $\text{Tl}^{\text{n}-}$ sub-structures are assumed as primarily Coulombic. The alkali metal–thallium distances $d(\text{Cs}–\text{Tl})$ are larger than 4.06 Å.

Table 7.7. Atomic coordinates and equivalent isotropic displacement parameter $U_{eq} / \text{Å}^2$ for $\text{Cs}_4\text{Tl}_2\text{O}$.

Atom	Site	x	y	z	U_{eq}
Tl1	18h	0.08985(3)	$-x$	0.56385(3)	0.0529(2)
Cs1	18h	0.56310(5)	$-x$	0.41940(5)	0.0568(3)
Cs2	18h	0.77751(5)	$-x$	0.59198(5)	0.0476(3)
O1	6c	0	0	0.8200(7)	0.036(4)
O2	3a	0	0	0	0.042(6)

Table 7.8. Atomic displacement parameters $U_{ij} / \text{Å}^2$ for $\text{Cs}_4\text{Tl}_2\text{O}$.

Atom	$U_{11} = U_{22}$	U_{33}	$U_{23} = -U_{13}$	U_{12}
Tl1	0.0489(3)	0.0536(4)	$-0.0022(2)$	0.0190(3)
Cs1	0.0772(6)	0.0437(6)	$-0.0012(2)$	0.0593(6)
Cs2	0.0532(4)	0.0458(6)	0.0051(2)	0.0335(5)
O1	0.042(6)	0.026(8)	0	0.021(3)
O2	0.051(9)	0.02(1)	0	0.025(5)

In detail, the structure is characterized by the presence of triples of face sharing $\{\text{OCs}_6\}$ octahedra extending along the c direction, which are separated by the $\{\text{Tl}_6\}$ clusters (Fig. 7.17). The oxygen atom O2 is surrounded by six Cs1 atoms, and O1 by three Cs1 and three Cs2 atoms. All Cs–O distances of 2.77 – 2.88 Å agree well with those found in Cs_2O (2.87 Å) as well as in previously reported alkali metal oxothallides [104, 199, 200]. Such Cs–O distances are indicative for a full ionization of the Cs atoms. All three octahedra in the structural unit are slightly elongated in the c direction (threefold rotation axis). The shortest Cs1–Cs1 distances of 3.725(2) Å ($\times 6$) in the central octahedron define the triangular faces, shared with the outer octahedra, while with the terminal faces

elongated edges of $4.113(2) \text{ \AA}$ ($\times 6$) are associated. The shorter Cs2–Cs2 distances of $3.986(2) \text{ \AA}$ ($\times 6$) in the outer octahedra are on the faces perpendicular to the c – axis, while the longer ones of $4.163(2) \text{ \AA}$ are between Cs2 and Cs1 atoms.

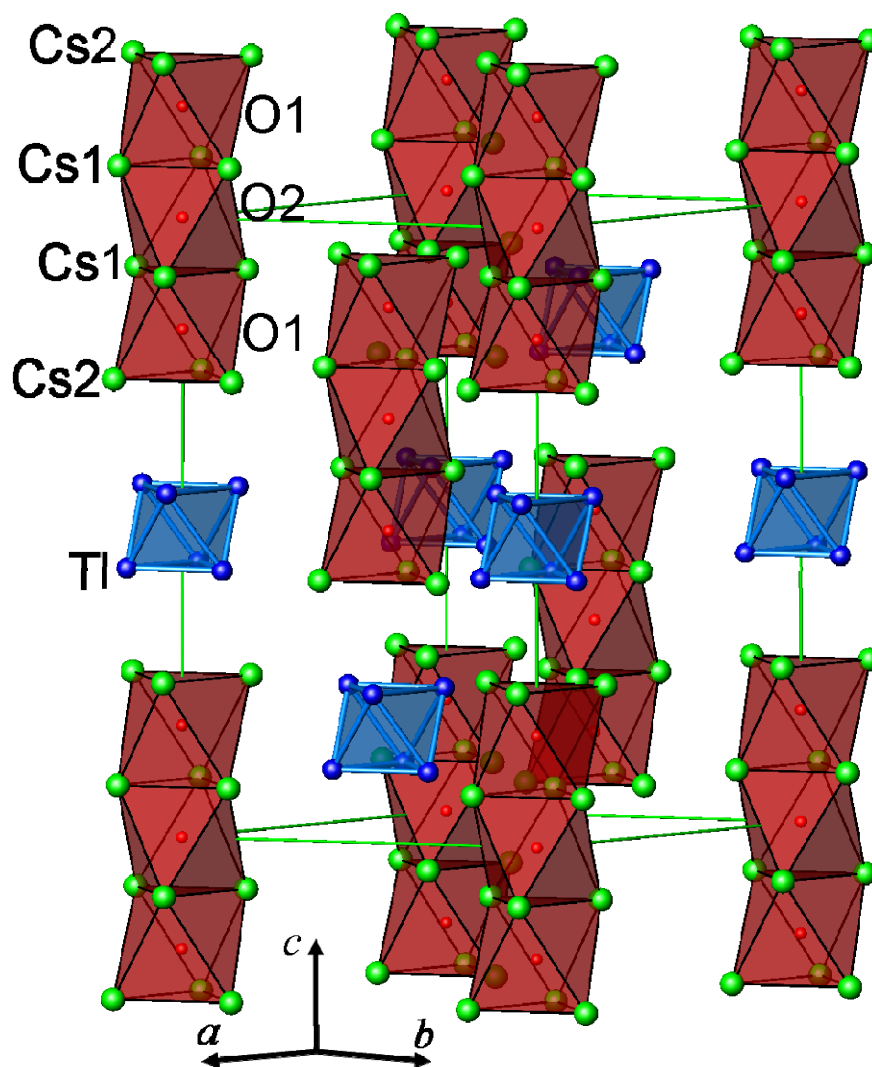


Figure 7.17. Perspective representation of the crystal structure of Cs₄Tl₂O (green line marks the unit cell edges, blue spheres – Tl atoms, green spheres – Cs atoms, red spheres – oxygen atoms).

The most interesting feature of Cs₄Tl₂O is the presence of {Tl₆} octahedra as a building unit, which can be denoted as *regular* with respect to the equality of three main diagonals ($4.546(5) \text{ \AA}$) and of the edges ($3.230(1) \text{ \AA}$ ($\times 6$) and $3.200(1) \text{ \AA}$ ($\times 6$)), see Fig. 7.18. This constitutes a striking contrast to all known compounds containing {Tl₆} octahedra [105, 182] with the same electron count, which are strongly compressed along one of their originally 4-fold axes. The corresponding

diagonals as well as the edge lengths of the $[\text{Tl}_6]^{6-}$ octahedra in the $\text{Cs}_4\text{Tl}_2\text{O}$, $\text{Rb}_{10}\text{Tl}_6\text{O}_2$, $\text{Cs}_{10}\text{Tl}_6\text{SiO}_4$ and CsTl compounds are summarized in Table 7.9. The clusters themselves are well isolated, displaying large intercluster distances of $> 7.32 \text{ \AA}$.

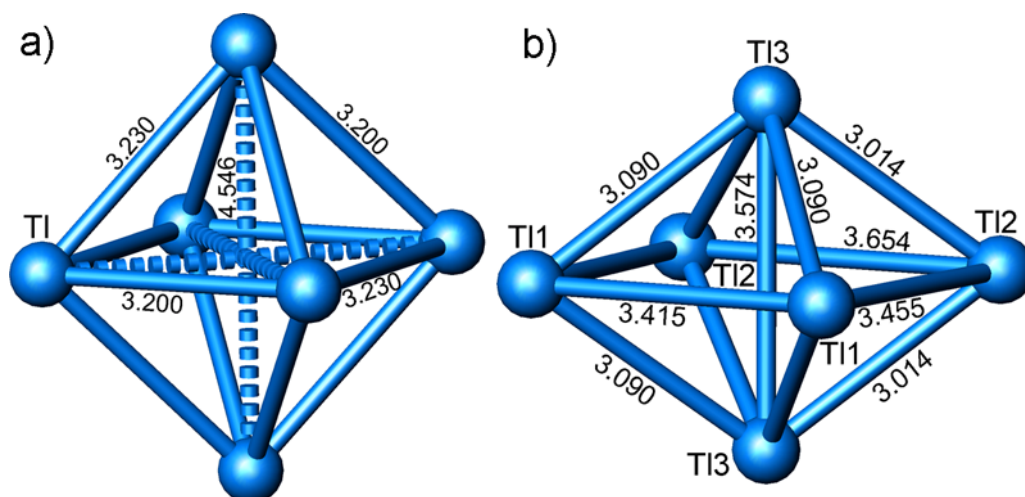


Figure 7.18. The $[\text{Tl}_6]^{6-}$ clusters in $\text{Cs}_4\text{Tl}_2\text{O}$ (a) and $\text{Rb}_{10}\text{Tl}_6\text{O}_2$ [105] (b).

Table 7.9. Bond distances / \AA of $[\text{Tl}_6]^{6-}$ clusters in various compounds.

	$\text{Cs}_4\text{Tl}_2\text{O}$	$\text{Rb}_{10}\text{Tl}_6\text{O}_2$ [105]	$\text{Cs}_{10}\text{Tl}_6\text{SiO}_4$ [Chapter 8]	CsTl [182]
$\text{Tl} - \text{Tl}^{\text{a}}$	$3.200(1) \times 6$	$3.014(1) \times 4$	$3.035(2) \times 2$	$3.026(3) \times 4$
	$3.230(1) \times 6$	$3.090(1) \times 4$	$3.061(2) \times 2$	$3.089(3) \times 4$
		$3.415(2)$	$3.068(2) \times 2$	$3.409(3) \times 2$
		$3.455(2) \times 2$	$3.117(2) \times 2$	$3.434(3) \times 2$
		$3.654(2)$	$3.407(2) \times 2$	
			$3.414(1) \times 2$	
$\text{Tl} - \text{Tl}^{\text{b}}$	$4.546(5) \times 3$	3.574	$3.800(7)$	$3.741(5)$
		4.933×2	$4.879(5)$	$4.836(3) \times 2$
			$4.765(8)$	

^{a)} – distances between thallium atoms regarding the edges of the octahedron;

^{b)} – distances between thallium atoms regarding the diagonals of the octahedron.

7.2.3. Magnetic Susceptibility Measurements

The magnetization was measured using a SQUID magnetometer (MPMS 5.5, Fa., Quantum Design, USA) in the temperature range 5–300 K at $H = 0.001, 0.1, 1, 3, 5$ and 7 T. The specimen (0.1305 g) was sealed in a quartz tube under helium. The raw data were corrected for the holder contribution. The corresponding χ_{mol} vs. temperature dependencies at 0.1, 1 and 3 T are presented in Fig. 7.19. $\text{Cs}_4\text{Tl}_2\text{O}$ is diamagnetic, showing a virtually temperature independent magnetic susceptibility in the range of 100 to 300 K (-1.25×10^{-5} to -9.37×10^{-5} emu/mol), which is of the same order of magnitude as the sum of the diamagnetic core corrections ($4\chi(\text{Cs}^+) + 2\chi(\text{Tl}^+) + \chi(\text{O}^{2-}) = -20.4 \times 10^{-5} \pm 2.5$ % emu/mol) and the Larmor susceptibility [125, 126] of the cluster orbital electrons (-8.8×10^{-5} emu/mol). At low temperatures (2–50 K) the magnetic susceptibilities increase due to presence of paramagnetic impurities. These dependences were described according to Curie-Weiss law in the temperature interval of 2–50 K at 1, 3, 5, and 7T (Figs. A2.5 – A2.8) and showed the average amount of 5 wt. % of impurities in the sample.

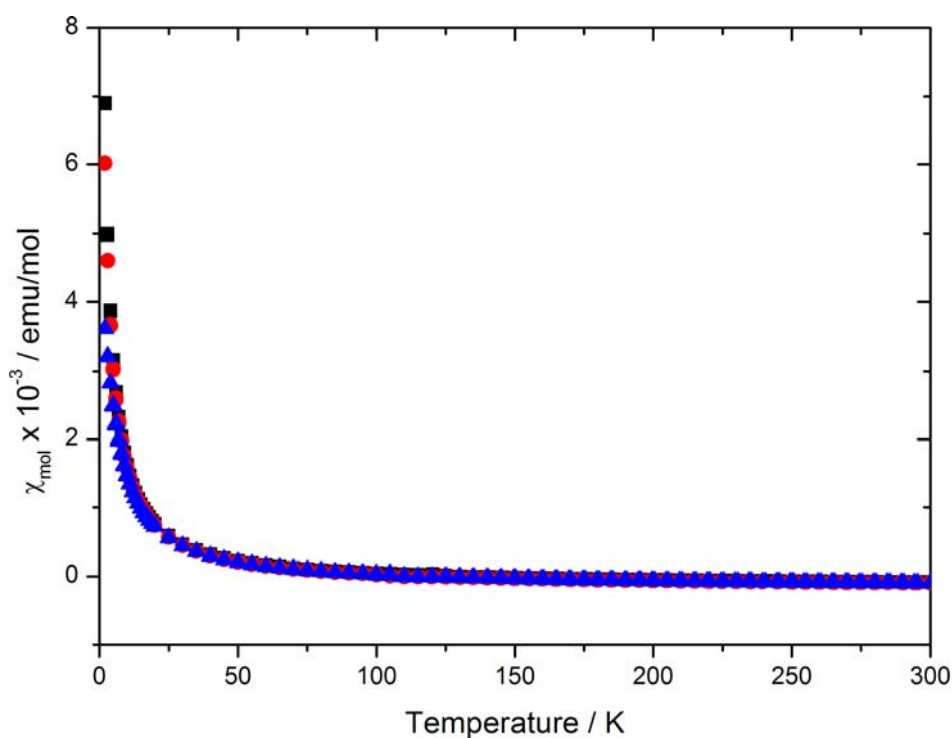


Figure 7.19. Temperature – dependent magnetic susceptibility data of $\text{Cs}_4\text{Tl}_2\text{O}$ at 0.1T (black squares), 1T (red circles) and 3T (blue triangles).

7.2.4. Electron Balance of the $[\text{Tl}_6]^{6-}$ Cluster-anion

The formal charge of the isolated $\{\text{Tl}_6\}$ unit is -6 , assuming $+1$ for Cs and -2 for O. According to Wade's rules such a *closo* cluster would require 26 valence electrons ($4 \times 6 + 2$, inert-electron pairs included), which is in conflict with the $24e$ available. Hence, the $[\text{Tl}_6]^{6-}$ cluster can be denoted as hypoelectronic [102] with $2n$ skeletal electrons ($12e$, disregarding $2 \times 6e$ for the lone pairs).

7.2.5. Electronic Structure Calculations and Quantum Chemical Analysis

DFT calculations using the PBE functional [138] were performed for the experimental crystal structures of $\text{Cs}_4\text{Tl}_2\text{O}$ as well as of the previously known $\text{Rb}_{10}\text{Tl}_6\text{O}_2$ [105]. The band structures of the periodic systems were calculated with the WIEN2k [143] code, using the following computational parameters. The radii of the atomic spheres (in Bohr) were set to: $\text{RMT}_{\text{Tl}} = 2.95$, $\text{RMT}_{\text{Cs}} = 2.70$ and $\text{RMT}_{\text{O}} = 2.50$ for $\text{Cs}_4\text{Tl}_2\text{O}$, and $\text{RMT}_{\text{Tl}} = 2.80$, $\text{RMT}_{\text{Rb}} = 2.55$ and $\text{RMT}_{\text{O}} = 2.40$ for $\text{Rb}_{10}\text{Tl}_6\text{O}_2$. In both cases the cut-off parameters $\text{RKmax} = 7.0$ and $\text{Gmax} = 14.0$ were used. The Kohn-Sham equations were solved for 231 ($\text{Cs}_4\text{Tl}_2\text{O}$) and 328 ($\text{Rb}_{10}\text{Tl}_6\text{O}_2$) k-points, respectively, in the irreducible wedge of the Brillouin zone. The core-valence separation was set to -6.0 Ry. Thus 13 electrons of Tl, 19 electrons of Cs, 9 electrons of Rb and 6 electrons of O were taken as valence electrons, being treated scalar relativistic. The APW+lo basis was applied, augmented by local orbitals for $l = 2$ (Tl, Cs), $l = 1$ (Rb) and $l = 0$ (Cs, Rb, O). Spin-orbit interaction was included by a second-variational method [190].

In contrast to all previously known compounds containing $[\text{Tl}_6]^{6-}$, the cluster in $\text{Cs}_4\text{Tl}_2\text{O}$ has an ideal octahedral shape, nevertheless maintaining a closed shell electronic structure. In order to understand the electronic reason for this peculiarity, band structure calculations in the DFT framework were performed. The total and atom-projected densities of states (DOS/PDOS) of $\text{Cs}_4\text{Tl}_2\text{O}$, taking spin-orbit coupling into account, are depicted in Fig. 7.20. The DOS is separated into

various distinct regions. Below -8 eV the bands belong to the Cs and Tl semi-core states. In the energy range between -8 eV and -4.1 eV 6 bands per $\{\text{Tl}_6\}$ unit are found. These bands show very little dispersion and are attributed to the lone pairs of the Tl atoms. Bands with predominantly O $-2p$ character are located between -2 eV and -1.5 eV. After a further gap, 6 bands per $\{\text{Tl}_6\}$ unit from -1.4 eV up to the Fermi level describe the skeletal electrons of the $[\text{Tl}_6]^{6-}$ cluster.

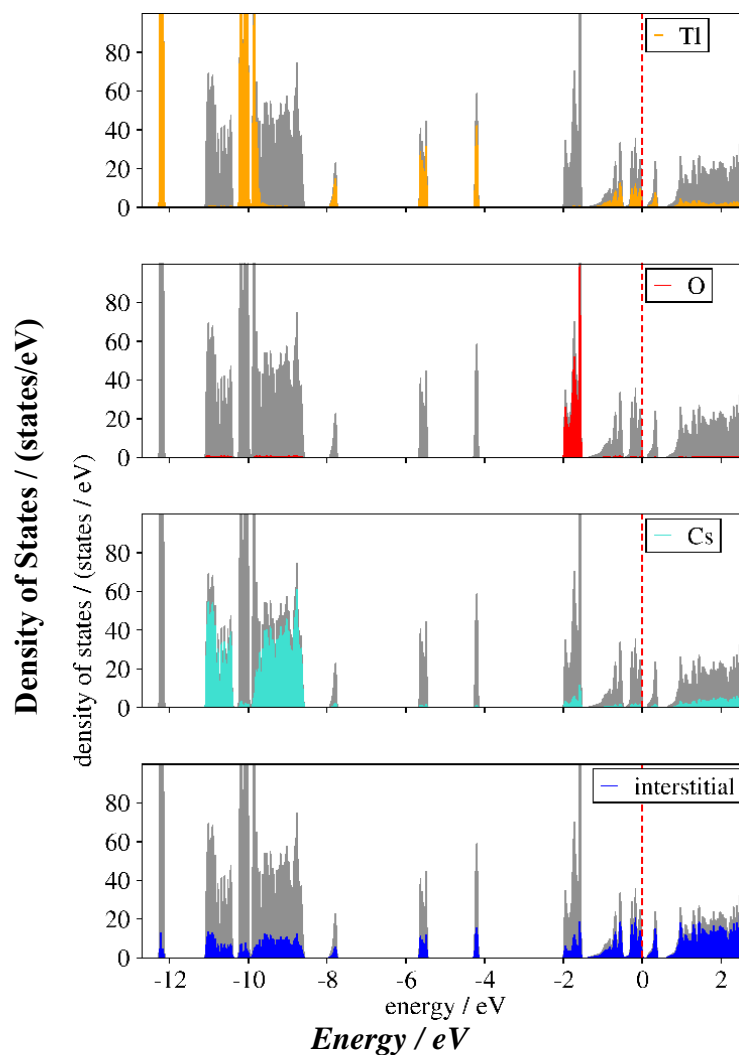


Figure 7.20. Total (grey) and atom-projected densities (colored, see legend) of states of $\text{Cs}_4\text{Tl}_2\text{O}$, from a relativistic DFT calculation including spin-orbit coupling. The Fermi level is shifted to 0 eV.

The band gap between valence and conduction bands amounts to 0.14 eV. It has to be stressed that this gap, which is in accordance with the diamagnetic properties of the compound, only opens if spin-orbit coupling is included in the

calculation. If the latter contribution is neglected, a non-zero density of states results at E_F (Fig. 7.21a). All previously reported isoelectronic clusters (see above) exhibit strongly Jahn–Teller distorted octahedra. In these cases, spin–orbit coupling does not affect the band structure significantly and a band gap is present already with the scalar relativistic approximation. As an example the DOS of $\text{Rb}_{10}\text{Tl}_6\text{O}_2$ is presented in Fig. 7.21b. In contrast, the nearly ideal octahedral shape of $[\text{Tl}_6]^{6-}$ in $\text{Cs}_4\text{Tl}_2\text{O}$ and again the opening of a band gap can only be reproduced computationally if spin–orbit coupling is considered. A similarly crucial effect of spin–orbit coupling for the correct description of the electronic structure was discussed for $\text{Cs}_{18}\text{Tl}_8\text{O}_6$, containing $[\text{Tl}_8]^{6-}$ clusters [199]. By comparing the latter cluster with an isoelectronic, but topologically different one found in $\text{Cs}_8\text{Tl}_8\text{O}$ [104] it has been revealed, that spin–orbit coupling is a mechanism alternative to the Jahn–Teller distortion to achieve a closed shell electronic system. The same scenario is now found for $[\text{Tl}_6]^{6-}$.

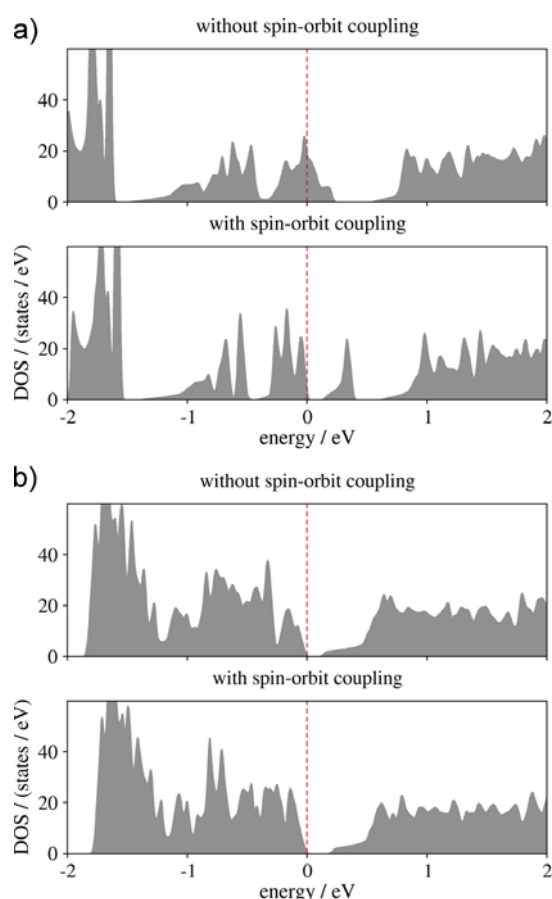


Figure 7.21. Total density of states (DOS) near the Fermi level without (*above*) and with (*below*) spin–orbit coupling of $\text{Cs}_4\text{Tl}_2\text{O}$ (a) and $\text{Rb}_{10}\text{Tl}_6\text{O}_2$ (b). E_F is shifted to 0 eV.

7.3. Two Different Tl_{11} Clusteranions in

$\text{K}_{21}\text{Tl}_{22}\text{O}_2$

7.3.1. Synthesis, Powder XRD and Thermal Stability

Since both, educts and products, are very sensitive to air and moisture, all operations were performed under dried argon (Schlenk technique or glovebox). $\text{K}_{21}\text{Tl}_{22}\text{O}_2$ was prepared by reacting potassium with thallium and K_2O in an argon atmosphere. The starting materials (total amount of 1 – 2 g) were weighed out in the molar ratios $\text{K} : \text{K}_2\text{O} : \text{Tl} = 28 : 3.2 : 22$, then placed into a tantalum tube, which was sealed under argon with an arc welder. In order to prevent oxidation, the tantalum tube was encapsulated in silica jackets, under argon. $\text{K}_{21}\text{Tl}_{22}\text{O}_2$ was synthesized by heating the reaction mixture at a rate of 50 K/h up to 773 K, annealing at this temperature for 2 days, and then cooling to room temperature at a rate of ~ 200 K/h. Unreacted elemental potassium was distilled off at 423 K in dynamic vacuum of 10^{-3} mbar. The product was obtained as black brittle crystals and must be handled under strictly inert conditions (Schlenk technique or glovebox).

According to powder diffraction X-ray analysis, the product of the reaction consists of two phases $\text{K}_{21}\text{Tl}_{22}\text{O}_2$ and KTI [201]. The chemical composition was confirmed by EDX analysis, and no impurity elements were detected. Because the $\text{K}_{21}\text{Tl}_{22}\text{O}_2$ is extremely sensitive to moisture and air, the thermal stability measurement using DSC analysis was performed in an argon atmosphere. A powder sample (~ 20 mg) was placed in an Al crucible, which was cold sealed under argon in a glovebox, heated to 673 K at a rate of 10 K/min, and then cooled down to room temperature at the same rate. According to the DSC measurements, $\text{K}_{21}\text{Tl}_{22}\text{O}_2$ is stable at least up to 513 K.

7.3.2. Crystal Structure Analysis

Single crystal X-ray structure analysis of $\text{K}_{21}\text{Tl}_{22}\text{O}_2$ was performed at room temperature. Crystallographic data, atomic coordinates and anisotropic parameters are summarized in Tables 7.10, 7.11, and 7.12, respectively.

$\text{K}_{21}\text{Tl}_{22}\text{O}_2$ crystallizes in a novel structure type (Fig. 7.22) consisting of two differently shaped isolated $[\text{Tl}_{11}]$ anionic units, OK_6 octahedra and isolated potassium cations. Selected bond distances within the anionic units as well as the OK_6 octahedra are summarized in Table 7.13. The structure contains two crystallographic different OK_6 octahedra: one, which is centered by O2 (2/3, 1/3, 0.098(2)), has diagonal distances K–K of 5.52 Å, and the second one, which is centered by O1 (0, 0, -0.466(2)), with diagonal distances K–K of 5.17 Å. All octahedra are undistorted with respect to the equality of all 3 main diagonals. The K–O distances are in the range of 2.54–2.83 Å agree well with those in other alkali metal thallide oxides (e.g. $d(\text{K–O}) = 2.59\text{--}2.74$ Å in $\text{K}_{10}\text{Tl}_6\text{O}_2$ [202]) or ternary alkali metal auride oxides (e.g. $d(\text{K–O}) = 2.62$ Å in K_3AuO [203]). Independent of such reference compounds, the bond lengths for the O2 ($d(\text{K–O}_2) = 2.70$ and 2.83 Å) atoms even agree well with the respective sums of the tabulated ionic radii for CN = 6 [204]: $r(\text{O}^{2-}) + r(\text{K}^+) = 2.78$ Å, which is indicative of a full ionization of the respective atoms. The shorter distances for O1 atoms ($d(\text{K–O}) = 2.54$ and 2.63 Å) are due to the increase in the surrounding electrostatic potential. The electrons, which are released from the K/O partial structure, are accommodated by both isolated $[\text{Tl}_{11}]$ groups.

The most interesting feature of $\text{K}_{21}\text{Tl}_{22}\text{O}_2$ is the presence of two different isolated $[\text{Tl}_{11}]$ units (Fig. 7.23). The cluster presented in Fig. 7.23a had already previously been observed in several binary and ternary thallium compounds [205–207] and has been defined as a hypoelectronic $[\text{Tl}_{11}]^{7-}$ cluster. The structure of the cluster was described as a pentacapped trigonal prismatic polyhedron, which is strongly compressed along the three fold axis. Nevertheless, according to quantum chemical calculations (ignoring relativistic effects) [205] the $[\text{Tl}_{11}]^{7-}$ cluster appears to be a very stable structural unit. Thus, one of the $[\text{Tl}_{11}]$ units in the present work will be considered as a $[\text{Tl}_{11}]^{7-}$ cluster, which is distorted from D_{3h} to D_3 symmetry.

Table 7.10. The crystallographic and structure refinement data for $K_{21}Tl_{22}O_2$.

	$K_{21}Tl_{22}O_2$
Space group (no.); Z	$P3m1$ (156); 1
Cell parameters / Å	$a = 11.0650(3)$ $c = 15.2541(4)$
Volume / Å ³	1671.41(8)
Molar weight / g·mol ⁻¹	5349.24
Density (calculated) / g·cm ⁻³	5.492
Crystal form, color	Block, silver black metallic
Crystal size / mm ³	0.22 × 0.13 × 0.13
Diffractometer	Bruker AXS, APEX SMART CCD
Monochromator	Graphite
X-ray radiation, λ / Å	Mo-K α , 0.71073
θ range, °	1.33 to 34.97
Index range	$-17 \leq h \leq 17, -17 \leq k \leq 17, -24 \leq l \leq 24$
Absorption correction	SADABS [120]
Total no. reflections N_{all}	40638
Independent reflections N	5349
Reflections with $I > 2\sigma(I)$ N'	3895
Absorption coefficient, μ / mm ⁻¹	55.911
Extinction coefficient	0.00050(5)
$F(000)$	2197
Refinement method	Full-matrix least-squares on F^2
Weighting scheme	$w = 1/[\sigma^2(F_o^2) + (0.0389P)^2 + 33.7008P]$, where $P = (F_o^2 + 2F_c^2) / 3$
Number of free parameters	102
Goodness-on-fit on F^2	1.063
R_1 (N' ; N_{all})	0.0509; 0.0816
wR_2 (N' ; N_{all})	0.1098; 0.1210
Twin volume fractions	0.943(1), 0.057(1)
$\Delta\rho_{min}; \Delta\rho_{max}$ / e·Å ⁻³	- 5.28 / 3.95

Table 7.11. Atomic coordinates and equivalent isotropic displacement parameter $U_{eq} / \text{\AA}^2$ for $\text{K}_{21}\text{Tl}_{22}\text{O}_2$.

Atom	Site	x	y	z	U_{eq}
Tl1	1 <i>b</i>	1/3	2/3	0.0304(1)	0.0289(3)
Tl2	6 <i>e</i>	0.44532(5)	0.55468(5)	0.20046(6)	0.0324(2)
Tl3	6 <i>e</i>	0.17438(5)	0.82562(5)	0.09311(6)	0.0376(2)
Tl4	6 <i>e</i>	0.17564(5)	0.3513(1)	0.30296(6)	0.0374(2)
Tl5	1 <i>b</i>	1/3	2/3	0.3678(1)	0.0369(3)
Tl6	6 <i>e</i>	-0.49244(5)	0.01512(9)	-0.28363(7)	0.0359(2)
Tl7	6 <i>e</i>	-0.53535(9)	0.23233(4)	-0.39675(6)	0.0307(2)
Tl8	1 <i>c</i>	2/3	1/3	-0.1987(1)	0.0357(3)
Tl9	3 <i>d</i>	-0.17391(5)	- x	-0.19969(7)	0.0368(2)
Tl10	1 <i>c</i>	2/3	1/3	-0.5548(2)	0.0528(5)
K1	1 <i>a</i>	0	0	-0.0606(8)	0.042(2)
K2	6 <i>e</i>	-0.2228(6)	0.8886(3)	-0.3654(4)	0.042(1)
K3	6 <i>e</i>	-0.7836(6)	0.1082(3)	-0.5622(4)	0.039(1)
K4	6 <i>e</i>	-0.5044(5)	0.991(1)	-0.5500(6)	0.064(2)
K5	6 <i>e</i>	0.2025(4)	0.7975(4)	-0.1417(4)	0.045(1)
K6	1 <i>b</i>	1/3	2/3	-0.3761(9)	0.052(3)
K7	6 <i>e</i>	0.7843(5)	0.569(1)	0.1952(7)	0.072(2)
K8	1 <i>a</i>	0	0	0.1927(9)	0.055(3)
K9	6 <i>e</i>	-0.093(1)	0.4534(5)	-0.0096(6)	0.075(3)
O1	1 <i>a</i>	0	0	-0.466(2)	0.021(4)
O2	1 <i>c</i>	2/3	1/3	0.098(2)	0.053(9)

The Tl–Tl separation within the $[\text{Tl}_{11}]^{7-}$ in $\text{K}_{21}\text{Tl}_{22}\text{O}_2$ is in the range of 3.11–3.37 Å and agree well with those in other compounds previously mentioned that contain similar clusters (e.g. $d(\text{Tl}–\text{Tl}) = 3.06–3.44$ Å in K_8Tl_{11} [205], $d(\text{Tl}–\text{Tl}) = 3.10–3.44$ Å in $\text{Rb}_{15}\text{Tl}_{27}$ [206] and $d(\text{Tl}–\text{Tl}) = 3.10–3.42$ Å in $\text{K}_{18}\text{Tl}_{20}\text{Au}_3$ [207]). The $[\text{Tl}_{11}]^{7-}$ cluster can also be described as a bipyramid of thallium atoms, where cell faces are capped by additional thallium atoms (Fig. 7.23*a*). A similar, but more distorted bipyramid can be found also in the second $[\text{Tl}_{11}]$ unit (Fig. 7.23*b*).

Table 7.12. Atomic displacement parameters $U_{ij} / \text{\AA}^2$ for $\text{K}_{21}\text{Tl}_{22}\text{O}_2$.

Atom	U_{11}	U_{22}	U_{33}	U_{23}	U_{13}	U_{12}
Tl1	0.0310(4)	U_{11}	0.0246(6)	0	0	$U_{11}/2$
Tl2	0.0288(3)	U_{11}	0.0365(4)	-0.0002(2)	0.0002(2)	0.0121(3)
Tl3	0.0443(4)	U_{11}	0.0333(4)	0.0009(2)	-0.0009(2)	0.0289(5)
Tl4	0.0425(4)	0.0300(4)	0.0354(5)	0.0101(4)	0.0051(2)	0.0150(2)
Tl5	0.0404(5)	U_{11}	0.0300(7)	0	0	$U_{11}/2$
Tl6	0.0343(3)	0.0230(4)	0.0467(5)	0.0037(4)	0.0019(2)	0.0115(2)
Tl7	0.0269(4)	0.0334(3)	0.0297(4)	-0.0020(2)	-0.0039(3)	0.0135(2)
Tl8	0.0281(4)	U_{11}	0.051(1)	0	0	$U_{11}/2$
Tl9	0.0377(4)	U_{11}	0.0398(5)	0.0027(2)	-0.0027(2)	0.0224(4)
Tl10	0.0542(7)	U_{11}	0.050(1)	0	0	$U_{11}/2$
K1	0.043(3)	U_{11}	0.040(5)	0	0	$U_{11}/2$
K2	0.042(3)	0.0371(2)	0.050(3)	0.010(1)	0.021(2)	0.021(1)
K3	0.030(2)	0.046(2)	0.035(3)	-0.001(1)	-0.001(1)	0.015(1)
K4	0.056(2)	0.086(5)	0.060(4)	-0.043(4)	-0.021(2)	0.043(3)
K5	0.045(2)	U_{11}	0.040(3)	0.007(1)	0.007(1)	0.021(3)
K6	0.047(4)	U_{11}	0.064(8)	0	0	$U_{11}/2$
K7	0.050(3)	0.091(6)	0.089(6)	-0.029(5)	-0.015(2)	0.045(3)
K8	0.058(4)	U_{11}	0.048(6)	0	0	$U_{11}/2$
K9	0.086(6)	0.073(4)	0.071(5)	-0.021(2)	-0.041(5)	0.043(3)
O1	0.022(6)	U_{11}	0.02(1)	0	0	$U_{11}/2$
O2	0.06(2)	U_{11}	0.03(2)	0	0	$U_{11}/2$

The structure of the second thallium cluster is also of the shape of a bipyramid, where the three upper faces are capped by three additional thallium atoms while the three additional Tl atoms are located on the same side, capping the three edges (Fig. 7.23b). The intercluster Tl–Tl distances are in the range of 3.06–3.35 Å, comparable to those in other known $[\text{Tl}_{11}]$ clusters. The bond distances within the anionic $[\text{Tl}_{11}]$ units are presented in Table 7.13. The clusters themselves are well isolated with large intercluster distances of > 5.65 Å.

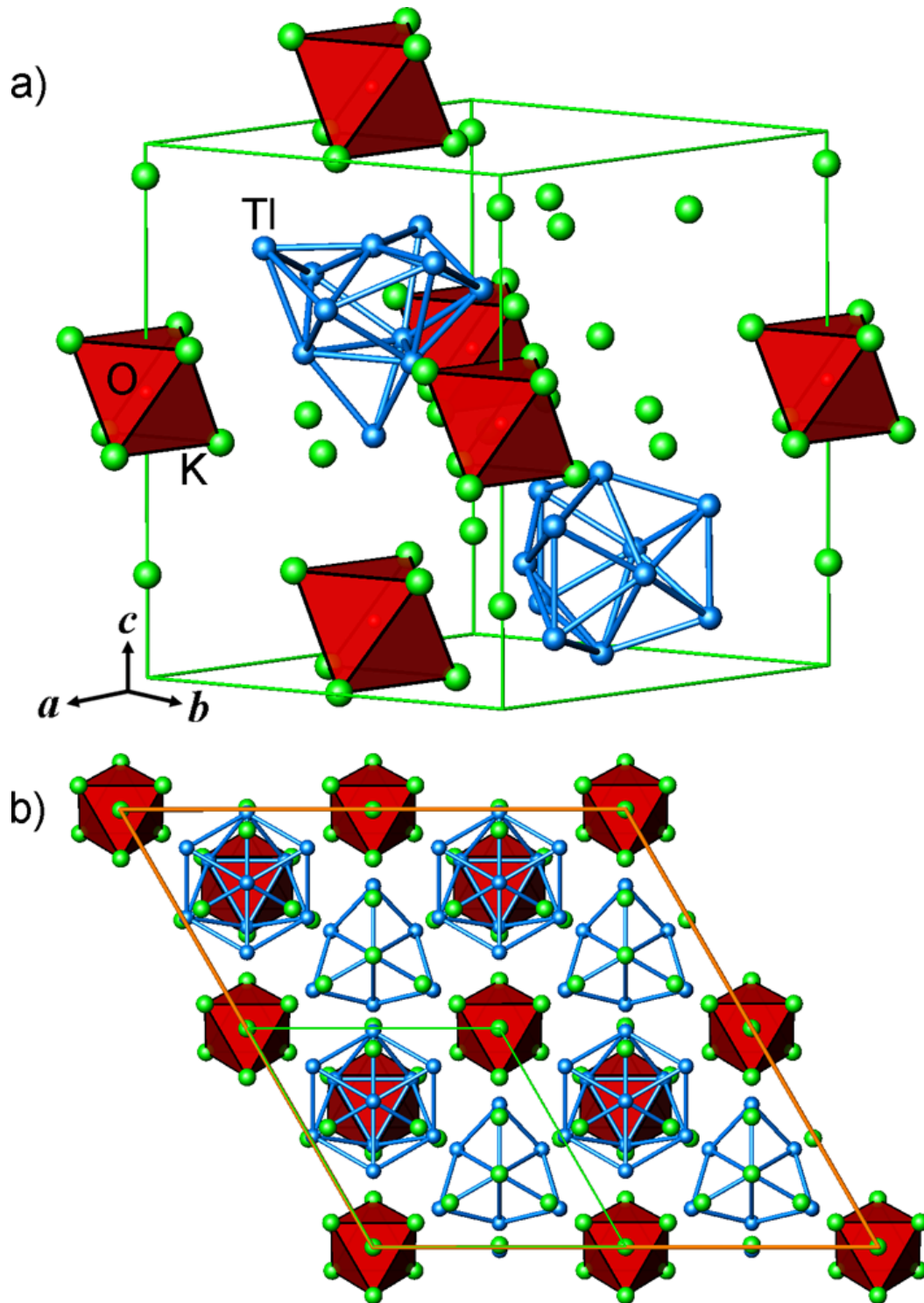


Figure 7.22. Respective graphical presentation of the crystal structure of $K_{21}Tl_{22}O_2$ (a) and the projection of latter on (001) (b): Tl_{11} clusters emphasized as blue polyhedra, OK_6 octahedra in red, green spheres – K atoms. Green lines mark the unit cell edges, orange lines mark borders of $2 \times 2 \times 2$ supercell.

Table 7.13. Selected bond distances / Å² in K₂₁Tl₂₂O₂.

		Tl1			Tl2
Tl1–	Tl3	3.193(1) × 3		Tl2–	Tl4
	Tl2	3.367(2) × 3			Tl3
	K5	3.630(6) × 3			Tl5
	K9	4.133(9) × 3			Tl1
					Tl2
					K7
					K9
					K4
		Tl3			Tl4
Tl3–	Tl2	3.1670(9) × 2		Tl4–	Tl2
	Tl1	3.193(1)			Tl5
	Tl4	3.201(1)			Tl3
	K5	3.623(7)			K3
	K8	3.671(6)			K8
	K9	3.999(7) × 2			K4
	K1	4.083(7)			K7
	K7	4.107(8) × 2			
		Tl5			Tl6
Tl5–	Tl4	3.180(1) × 3		Tl6–	Tl7
	Tl2	3.335(2) × 3			Tl9
	K4	3.354(8) × 3			Tl8
	K6	3.91(1)			K6
					K5
					K4
					K2
					K9
		Tl7			Tl8
Tl7–	Tl10	3.093(2)		Tl8–	Tl9
	Tl6	3.1812(9) × 2			Tl6
	Tl9	3.208(1)			Tl7
	Tl7	3.353(2) × 2			K9
	K3	3.468(6)			
	Tl8	3.588(2)			
	K4	3.690(7) × 2			
	K2	3.887(1) × 2			
		Tl9			Tl10
Tl9–	Tl8	3.055(2)		Tl10–	Tl7
	Tl7	3.208(1)			Tl6
	Tl6	3.310(8) × 2			K3
	K5	3.745(4) × 2			
	K2	3.865(4) × 2			
	K1	3.951(6)			
	K9	4.001(7) × 2			
		O1			O2
O1–	K3	2.54(1) × 3		O2–	K7
	K2	2.63(2) × 3			K9

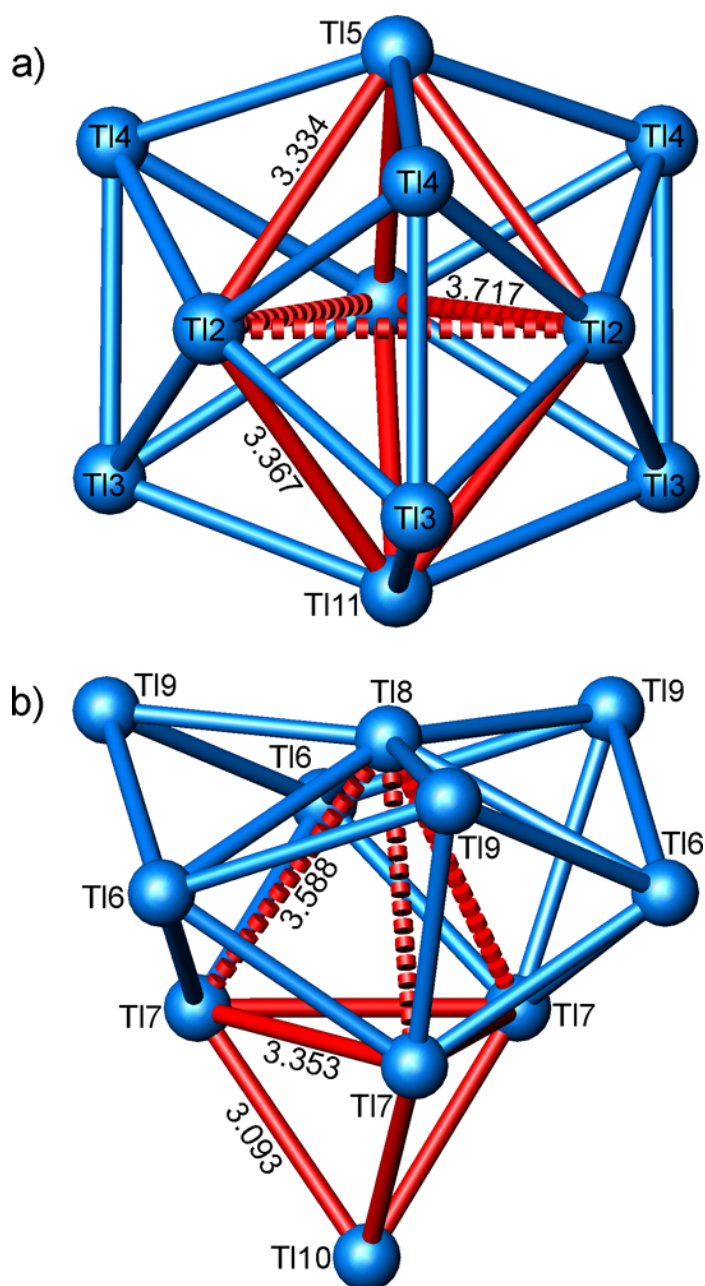


Figure 7.23. [Tl₁₁] clusters presented in K₂₁Tl₂₂O₂. Red lines are displaying arrangement of Tl atoms in the shape of trigonal bipyramid. Interatomic distances in Å. The corresponding distances are presented in Table 7.13.

In general, the discussed compound crystallizes in a trigonal structure type, which is related to both NiAs and Wurtzite (ZnS) structure types in a way that [Tl₁₁]⁷⁻ clusters occupy octahedral voids, which are formed by OK₆ octahedra (*hcp*

type packing), similar to those in NiAs while the other $[Tl_{11}]$ units are located in tetrahedral voids similar to those in the Wurtzite structure type (Fig. 7.24).

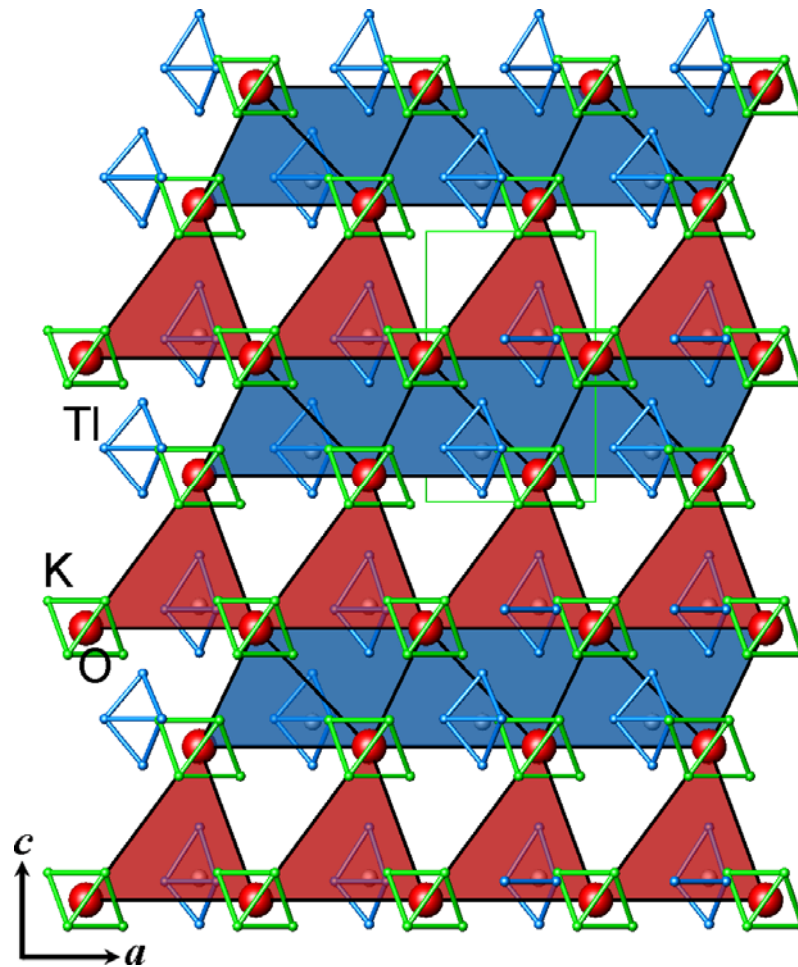


Figure 7.24. Graphical presentation of the crystal structure of $K_{21}Tl_{22}O_2$: Tl_{11} clusters emphasized as blue polyhedra (only central bipyramids are shown), red spheres – O atoms, green spheres – K atoms. Blue parallelepipeds emphasizing octahedral voids, red triangles – tetrahedral voids. Green lines mark the unit cell edges.

7.3.3. Magnetic Susceptibility Measurements

The magnetization was measured using a SQUID magnetometer (MPMS 5.5, Fa., Quantum Design, USA) in the temperature range 5–300 K at $H = 0.001, 0.1, 1, 3, 5$ and 7 T. The specimen (0.1296 g) was sealed in a quartz tube under helium. The raw data were corrected for the holder contribution. The corresponding χ_{mol} vs.

temperature dependencies at 0.1, 1 and 3 T are presented in Fig. 7.25. According to the X-ray powder diffraction measurements, the sample under investigation was a two phase product, containing KTI as an impurity. Nevertheless, because KTI is diamagnetic ($\chi_{\text{mol}} = -0.36 \times 10^{-4}$ emu/mol [201]) and the whole sample shows diamagnetic character, $\text{K}_{21}\text{Tl}_{22}\text{O}_2$ also has to be diamagnetic. The molar susceptibility of the binary phase product is virtually temperature independent in the range of 50 to 300 K (-7.03×10^{-5} to -9.15×10^{-5} emu/mol). At low temperatures (2–25 K) the magnetic susceptibilities increase due to presence of paramagnetic impurities in the sample. These dependences were described according to Curie-Weiss law in the temperature interval of 2–20 K at 1, 3, 5, and 7T (Figs. A2.9 – A2.12) and showed the average amount of 0.35 wt. % of paramagnetic impurities in the sample.

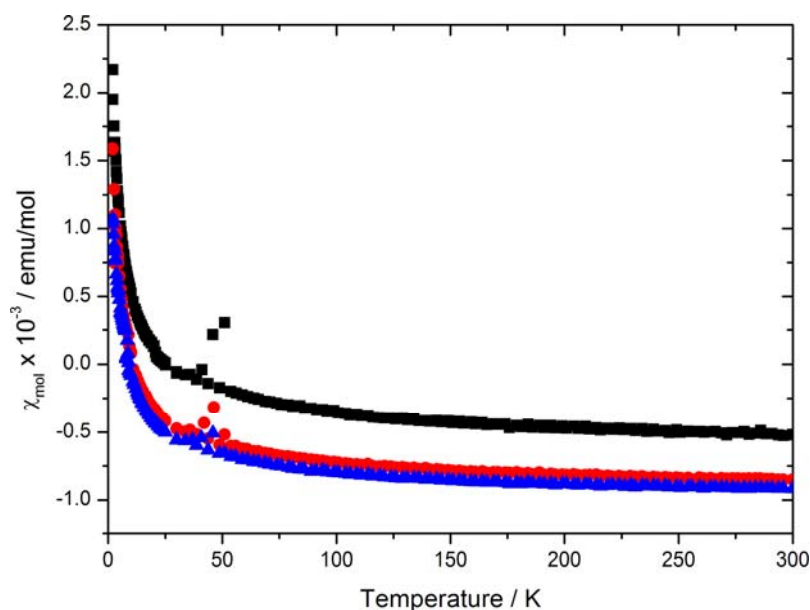


Figure 7.25. Temperature – dependent magnetic susceptibility data of $\text{K}_{21}\text{Tl}_{22}\text{O}_2$ at 0.1T (black squares), 1T (red circles) and 3T (blue triangles).

7.3.4. Electron Balance of the $[\text{Tl}_{11}]$ Cluster-anions

Interestingly, the $\text{K}_{21}\text{Tl}_{22}\text{O}_2$ contains two $[\text{Tl}_{11}]$ clusters different in shape. The phenomenon of finding different types of clusters in one compound is unusual, not

only for the thallium cluster containing compounds. Previously known $[\text{Tl}_{11}]^{7-}$ units (Fig. 7.23a) that can be formally described as clusteranions having 40 valence electrons available can not be understood in terms of known qualitative concepts. Within the Zintl–Klemm concept, which is based on $2e2c$ bonds, the number of valence electrons should be 66 ($27 \text{ edges} \times 2e + 11 \text{ inert pairs}$). Applying Wade's rules, a *closo* cluster $[\text{Tl}_{11}]^{7-}$ would require $46e$ ($4 \times 11 + 2$, inert-electron pairs included), which is in conflict with the $40e$ available. The $[\text{Tl}_{11}]^{7-}$ cluster can best be denoted as hypoelectronic [102] with $2n-4$ skeletal electrons ($18e$, disregarding $2 \times 11e$ for the lone pairs). Simple balancing of the ionic charges, results in an anionic charge of -10 for the second previously not observed $[\text{Tl}_{11}]$ clusteranion (Fig. 7.23b). Thus the latter would exhibit an open shell electronic structure, which is in conflict with the observed diamagnetism. Therefore, quantum chemical calculations have to be performed in order to reveal the mechanisms leading to a closed shell electronic structure.

7.4. Conclusions

Following a fundamental principle in chemistry, given configurations tend to stabilize by opening a gap between the highest occupied and the lowest unoccupied electronic states. As a special manifestation of this principle, highly symmetric species with degenerate frontier orbitals stabilize by geometric distortion, thus lifting electronic degeneracy and arriving at a closed shell system (Jahn–Teller or Peierls distortion). In the cluster chemistry of heavy main group elements, spin–orbit coupling is an alternative mechanism leading to a non-degenerate HOMO. Here, the first experimental evidence for such a mechanism is presented, that had previously been discussed only theoretically, e.g. for Pb clusters.

$\text{Cs}_{18}\text{Tl}_8\text{O}_6$ and $\text{Cs}_4\text{Tl}_2\text{O}$ were synthesized reacting the binary compounds CsTl and Cs_2O followed by slow cooling to room temperature, in arc-welded tantalum ampoules. According to single crystal X-ray analyses, the compounds crystallize in new structure types ($\text{Cs}_{18}\text{Tl}_8\text{O}_6$ in cubic space group $I23$ (no. 197), $a = 13.3724(3) \text{ \AA}$, $Z = 2$; and $\text{Cs}_4\text{Tl}_2\text{O}$ in the trigonal space group $R\bar{3}m$ (no. 166), $a = 11.986(1)$, $c = 20.370(2) \text{ \AA}$, $Z = 9$). $\text{Cs}_{18}\text{Tl}_8\text{O}_6$ contains isolated $[\text{Tl}_8]^{6-}$ units with the shape of a tetrahedral star, a so-called *stella quadrangula*. Furthermore, cesium

and oxygen constitute a three-dimensional network of corner and edge sharing octahedra $\infty^3[\text{OCs}_{6/2}]^+$. The crystal structure of $\text{Cs}_4\text{Tl}_2\text{O}$ consists of isolated $[\text{Tl}_6]^{6-}$ octahedra, being regular with respect to the equality of all 3 main diagonals (4.546(5) Å), and of $[\text{Cs}_{12}\text{O}_3]^{6+}$ triple octahedra extending along the *c* direction. The electronic structure of the extended solids ($\text{Cs}_{18}\text{Tl}_8\text{O}_6$ and $\text{Cs}_4\text{Tl}_2\text{O}$) as well as of excised Cs_6Tl_8 clusters has been examined by relativistic density functional calculations including spin–orbit coupling, the Jahn–Teller theorem and spin polarization. It has been shown by quantum mechanical analyses that both the tetrahedral star $[\text{Tl}_8]^{6-}$ in $\text{Cs}_{18}\text{Tl}_8\text{O}_6$ and the regular octahedra $[\text{Tl}_6]^{6-}$ in $\text{Cs}_4\text{Tl}_2\text{O}$ only exhibit a closed-shell electronic structure, in accordance with diamagnetic properties, if spin–orbit coupling is considered.

Moreover, spin–orbit interaction not only influences the electronic state, but also changes the relative energies of various cluster configurations. For the $[\text{Tl}_8]^{6-}$ cluster contained in $\text{Cs}_8\text{Tl}_8\text{O}$, which has the same number of (valence) electrons but a different structure compared to the one in $\text{Cs}_{18}\text{Tl}_8\text{O}_6$, the correct structure is already reproduced on the scalar relativistic level. Since a regular cube $[\text{Tl}_8]^{6-}$ would display an open shell degenerate ground state, the distortion encountered in $\text{Cs}_8\text{Tl}_8\text{O}$ can be completely understood in terms of the Jahn–Teller theorem. Considering spin–orbit coupling does not result in a qualitatively different ground state, but in a destabilization relative to the tetrahedral star, thus making both cluster configurations competitive. The discrimination between the kind of cluster realized depends on the boundary conditions imposed on the overall structures of the hosting extended solids. The higher content of Cs_2O in $\text{Cs}_{18}\text{Tl}_8\text{O}_6 = \text{Cs}_6\text{Tl}_8 \cdot 6 \text{Cs}_2\text{O}$ compared to $\text{Cs}_8\text{Tl}_8\text{O} = \text{Cs}_6\text{Tl}_8 \cdot \text{Cs}_2\text{O}$ alone already enforces substantially different crystal structures.

Furthermore, the analyses let appear traditional approaches admissible to qualitatively address the causal relationship between electron counts and structures of clusters, which like e.g. the Zintl–Klemm concept or Wade's rules are based on considering isolated clusters, excised from the solid. These treatments regarding the $[\text{Tl}_8]^{6-}$ clusters embedded in the solid or as charge neutral Cs_6Tl_8 units have produced rather consistent results.

The same scenario is found for distorted and regular octahedral $[\text{Tl}_6]^{6-}$ clusters. Thus, up to now all known distorted octahedral thallium clusters can be

understood in terms of the Jahn–Teller theorem featuring band gaps already within the scalar relativistic approximation. A closed shell structure of the regular $[\text{Tl}_6]^{6-}$ can be reproduced only if spin–orbit coupling is considered during calculations. Thus, the present example is one additional proof that different host structures as well as surroundings around cluster anions lead to structural stabilization of even hypoelectronic anionic species.

The third investigated compound $\text{K}_{21}\text{Tl}_{22}\text{O}_2$ was prepared by reacting potassium with thallium and K_2O in an argon atmosphere at 773 K followed by cooling to room temperature at a rate of ~ 200 K/h, sealed in a tantalum tube under argon with an arc welder. According to single crystal X-ray analysis $\text{K}_{21}\text{Tl}_{22}\text{O}_2$ crystallizes in a novel structure type (trigonal $P3m1$ (no. 156), $a = 11.0650(3)$, $c = 15.2541(4)$ Å, $Z = 1$) consisting of two differently shaped isolated $[\text{Tl}_{11}]$ anionic units, OK_6 octahedra and isolated potassium cations. One cluster had already previously been observed and has been denoted as a hypoelectronic $[\text{Tl}_{11}]^{7-}$ cluster. This cluster can be described as a bipyramid of thallium atoms, whereby all faces are capped by additional thallium atoms. The structure of the second thallium cluster is also characterized by a bipyramid, where three upper faces are capped by three additional thallium atoms while the three additional Tl atoms are located on the same side, capping the three edges. The difference in shape of both $[\text{Tl}_{11}]$ clusters as well as the anionic charge (-10) of the cluster that had previously not been observed could only be understood by performing a thorough quantum chemical analysis of the $\text{K}_{21}\text{Tl}_{22}\text{O}_2$ electronic structure.

8. Cesium Oxotetrelate-Thallides: $\text{Cs}_{10}\text{Tl}_6\text{SiO}_4$, $\text{Cs}_{10}\text{Tl}_6\text{GeO}_4$ and $\text{Cs}_{10}\text{Tl}_6\text{SnO}_3$

For the class of homoatomic clusters or network anions consisting of post-transition elements, concepts are available that allow to rationalize in an elegant and empirical manner the respective compositions, geometries and electron counts. These are the famous and popular Zintl–Klemm concept [106-108, 208] and Wade's rules [209]. Inherently, all empirical classification schemes show limited ranges of validity as well as certain exceptions [101, 102, 104, 210]. This also holds true for both of the approaches mentioned. In particular for thallium, which has shown to offer a rich and diverse chemistry of anionic clusters, neither the Zintl–Klemm concept nor Wade's rules straightforwardly apply in most of the cases encountered. Frequently, the clusters appear to be deficient in skeletal electrons, even falling below the limits as defined by Wade. They have been denoted “hypoelectronic” clusters, and the discrepancies to the qualitative bonding concepts have been tentatively attributed to a lower degree of localization of the skeletal bonds and to structural distortions that create additional bonds along body or face diagonals [102, 176, 178, 180-184].

The underlying common principle of the Zintl–Klemm concept and of Wade's rules is that structures with electron counts producing closed shell configurations, and showing a large HOMO–LUMO gap, are particularly stable. The fact, that closed shell configurations result also due to Jahn–Teller distortion or/and to spin–orbit coupling was demonstrated in Chapter 7 [199, 200]. The latter effect, stabilizing cluster geometries, is of relativistic origin exclusively, which would explain the exceptional role of thallium in cluster chemistry.

The approaches to generate new thallium ions, in particular the elusive monoatomic anion, include increasing the compositional and structural degrees of freedom by introducing additional anionic species. In extending this idea, the systems of cesium, cesium oxide and thallium with silicon dioxide, germanium dioxide and elemental tin were explored. The mixed anion phases targeted were formed indeed, and in the present work the first cesium silicate thallide, germanate thallide, and stannate thallide are discussed.

8.1. Synthesis, Powder XRD and Thermal Stability

Because both, reagents and products, are very sensitive to air and moisture, all operations were performed under dried argon (Schlenk technique or glovebox). $\text{Cs}_{10}\text{Tl}_6\text{SiO}_4$, $\text{Cs}_{10}\text{Tl}_6\text{GeO}_4$ and $\text{Cs}_{10}\text{Tl}_6\text{SnO}_3$ were prepared by reacting cesium with thallium, SiO_2 , GeO_2 , Sn and Cs_2O . The starting materials for the syntheses of $\text{Cs}_{10}\text{Tl}_6\text{SiO}_4$ and $\text{Cs}_{10}\text{Tl}_6\text{GeO}_4$ (total amount of 1 – 2 g) were weighed out in the molar ratios $\text{Cs} : \text{Cs}_2\text{O} : \text{Tl} : \text{SiO}_2(\text{GeO}_2) = 12-14 : 2.2 : 6 : 1$ and of $\text{Cs}_{10}\text{Tl}_6\text{SnO}_3 - \text{Cs} : \text{Cs}_2\text{O} : \text{Tl} : \text{Sn} = 15-20 : 4.5 : 6 : 1$, then placed into tantalum tubes, which were sealed under argon with an arc welder. In order to prevent oxidation, the tantalum tubes were encapsulated in silica jackets, under argon. $\text{Cs}_{10}\text{Tl}_6\text{SiO}_4$ was synthesized by heating the reaction mixture at a rate of 50 K/h up to 673 K, annealing at this temperature for 2 days, and then cooling to room temperature at a rate of 200 K/h. In order to obtain an as pure as possible phase (admixture of less than 2 at-% of $\text{Cs}_8\text{Tl}_{11}$), and to avoid decomposition of the sample resulting in $\text{Cs}_8\text{Tl}_{11}$, CsTl and SiO_2 phases, cooling down to room temperature with high speed was indispensable. For the synthesis of $\text{Cs}_{10}\text{Tl}_6\text{SnO}_3$, the reaction mixture of Cs, Cs_2O , Tl and Sn was heated at a rate of 50 K/h up to 773 K, annealed at this temperature for 2 days, and then cooled to room temperature at a rate of 200 K/h resulting in a pure phase with an admixture of less than 2 at-% of CsTl phase. The corresponding reactions with SnO or SnO_2 lead to the formation of samples containing at least two phases (consisting e.g. of CsTl and $\text{Cs}_{10}\text{Tl}_6\text{SnO}_3$) with CsTl (> 65%) as the main product. In contrast to the previous two compounds, $\text{Cs}_{10}\text{Tl}_6\text{GeO}_4$ was produced by quenching the quartz ampoule in an ice-water

cooling bath after applying a heating schedule at a rate of 50 K/h up to 623 K and annealing at this temperature for 3 days. In each case unreacted elemental cesium was distilled off at 373 K in a dynamic vacuum of 10^{-3} mbar. The products were obtained as black brittle crystals and handled under strictly inert conditions (Schlenk technique or glovebox).

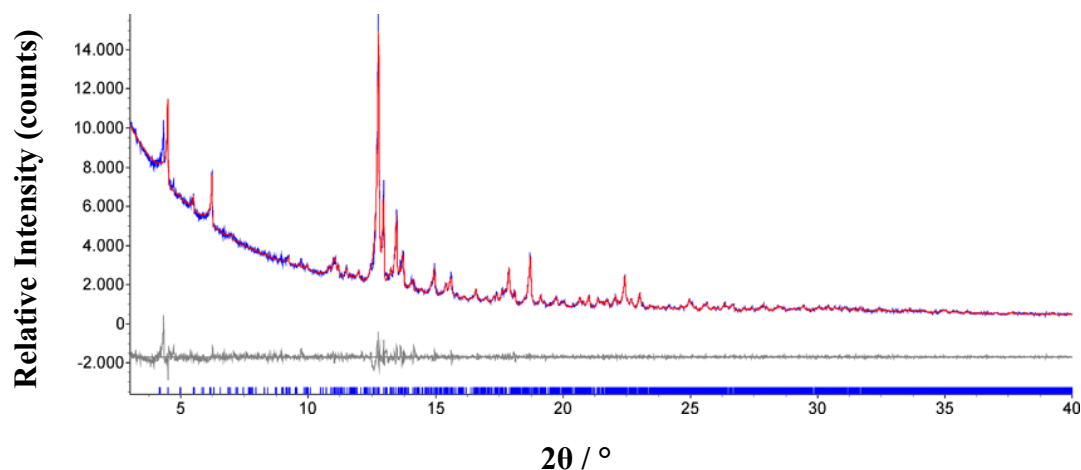


Figure 8.1. Le Bail refinement of $\text{Cs}_{10}\text{Tl}_6\text{SiO}_4$ (measured curve (blue line), theoretically calculated curve (red line), difference curve (grey line), Bragg reflections (blue ticks)) ($\lambda = 0.7093 \text{ \AA}$).

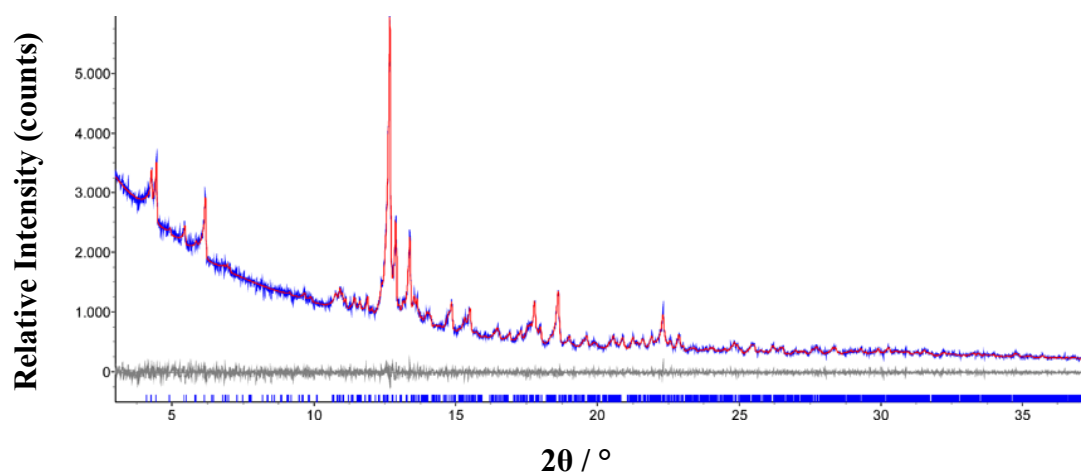


Figure 8.2. Le Bail refinement of $\text{Cs}_{10}\text{Tl}_6\text{GeO}_4$ (measured curve (blue line), theoretically calculated curve (red line), difference curve (grey line), Bragg reflections (blue ticks)) ($\lambda = 0.7093 \text{ \AA}$).

According to the powder diffraction X-ray analysis, $\text{Cs}_{10}\text{Tl}_6\text{TtO}_4$ (Tt = Si, Ge) and $\text{Cs}_{10}\text{Tl}_6\text{SnO}_3$ were obtained as single phases with less than 2 at-% admixtures

of $\text{Cs}_8\text{Tl}_{11}$ or CsTl . Refinements of measured X-ray powder patterns of $\text{Cs}_{10}\text{Tl}_6\text{SiO}_4$, $\text{Cs}_{10}\text{Tl}_6\text{GeO}_4$ and $\text{Cs}_{10}\text{Tl}_6\text{SnO}_3$ according to the Le Bail method are presented in Figs. 8.1–8.3, respectively. The chemical compositions were confirmed by EDX analysis, and no impurity elements were detected. Because the synthesized compounds are extremely sensitive to moisture and air, the thermal stability measurements using DSC analysis were performed in an argon atmosphere. The powder samples (~15 mg) were placed in Al crucibles, which were cold sealed under argon in a glovebox, heated to 623 K at a rate of 10 K/min, and then cooled down to room temperature at the same rate. According to the DSC measurements as well as high-temperature powder X-ray analysis measurements, $\text{Cs}_{10}\text{Tl}_6\text{SiO}_4$ is stable up to 573 K, $\text{Cs}_{10}\text{Tl}_6\text{GeO}_4$ up to 483 K and $\text{Cs}_{10}\text{Tl}_6\text{SnO}_3$ at least up to 623 K, respectively.

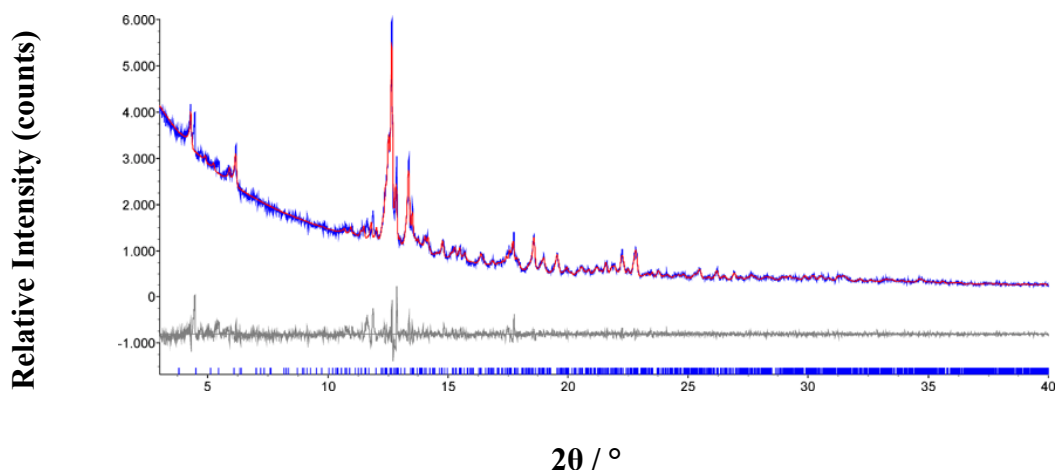


Figure 8.3. Le Bail refinement of $\text{Cs}_{10}\text{Tl}_6\text{SnO}_3$ (measured curve (blue line), theoretically calculated curve (red line), difference curve (grey line), Bragg reflections (blue ticks)) ($\lambda = 0.7093 \text{ \AA}$).

8.2. Crystal Structure Analysis

Single crystal X-ray structure analyses of $\text{Cs}_{10}\text{Tl}_6\text{SiO}_4$, $\text{Cs}_{10}\text{Tl}_6\text{GeO}_4$ and $\text{Cs}_{10}\text{Tl}_6\text{SnO}_3$ were performed at room temperature. Crystallographic data, atomic coordinates and anisotropic parameters for measurements at room temperature are summarized in Tables 8.1, 8.2, and 8.3, respectively.

The diffraction intensities of the crystals of $\text{Cs}_{10}\text{Tl}_6\text{SiO}_4$ and $\text{Cs}_{10}\text{Tl}_6\text{GeO}_4$ were first indexed and integrated assuming orthorhombic symmetry, with quite

reasonable internal R -values ($\text{Cs}_{10}\text{Tl}_6\text{SiO}_4$: $R_{\text{int}} = 0.064$, $\text{Cs}_{10}\text{Tl}_6\text{GeO}_4$: $R_{\text{int}} = 0.125$). Both structures can be refined within the space group $Pnma$ (no. 62), but with unsatisfactory reliability values ($\text{Cs}_{10}\text{Tl}_6\text{SiO}_4$: $R_1 = 0.114$, $\text{Cs}_{10}\text{Tl}_6\text{GeO}_4$: $R_1 = 0.239$) and unusual displacement parameters (mainly for the thallium atoms). Careful inspection of the reciprocal space using the Precession module of the Bruker Suite software package [211], which allows a detailed exploration of the reciprocal space without being restricted to integer hkl values [212], revealed some of the forbidden reflections $0kl$: $k + l \neq 2n$ (n glide plane) to be present, and furthermore minute splittings of reflections at higher 2θ values. The final structure refinements in the monoclinic space group $P2_1/c$ (no. 14), assuming dovetail-twinning (twinning by pseudo-merohedry, $\beta \approx 90^\circ$) has lead to significantly improved R -values and more reasonable displacement parameters (Tables 8.1 and 8.2).

The structurally related $\text{Cs}_{10}\text{Tl}_6\text{SnO}_3$ crystallizes in the orthorhombic space group ($Pnma$, no. 62), and no necessity was found to use a lower symmetry, or to even apply twin refinement (Tables 8.1 and 8.3). The group-subgroup relation [213, 214] between the aristotype $\text{Cs}_{10}\text{Tl}_6\text{SnO}_3$ and $\text{Cs}_{10}\text{Tl}_6\text{Si}(\text{Ge})\text{O}_4$ (Fig. 8.4) includes one step of symmetry reduction of type *translationengleich* ($t2$) [215]; we regard the corresponding transition that occurs when cooling down from the reaction temperature to be the reason for twinning of the silicon and germanium compounds.

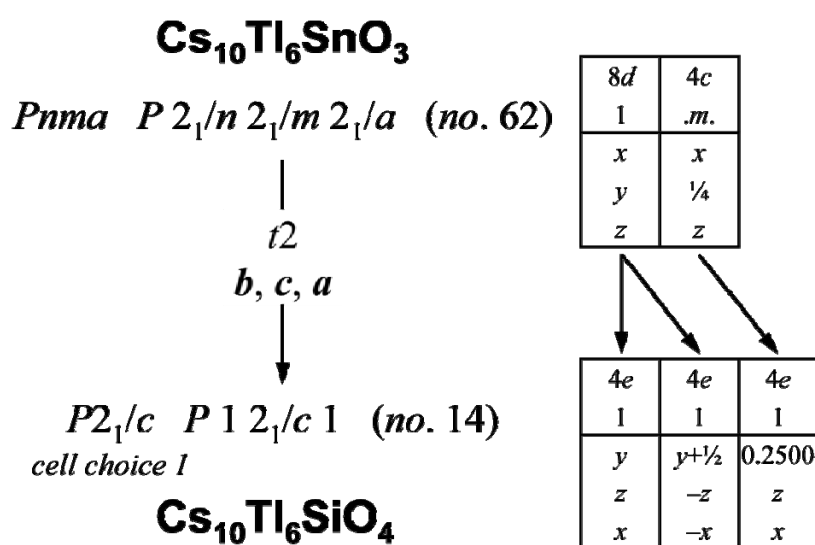


Figure 8.4. Group-subgroup relation between the $\text{Cs}_{10}\text{Tl}_6\text{SnO}_3$ and $\text{Cs}_{10}\text{Tl}_6\text{SiO}_4$ crystal structures, including the site transformations.

Table 8.1. The crystallographic and structure refinement data for Cs₁₀Tl₆SiO₄, Cs₁₀Tl₆GeO₄ and Cs₁₀Tl₆SnO₃.

	Cs ₁₀ Tl ₆ SiO ₄	Cs ₁₀ Tl ₆ GeO ₄	Cs ₁₀ Tl ₆ SnO ₃
Space group (no.); <i>Z</i>	<i>P</i> 2 ₁ / <i>c</i> (14); 4	<i>P</i> 2 ₁ / <i>c</i> (14); 4	<i>Pnma</i> (62); 4
Cell parameters / Å	<i>a</i> = 18.912(2); <i>b</i> = 11.439(1); <i>c</i> = 14.808(1) β = 90.029(2)	<i>a</i> = 19.034(2); <i>b</i> = 11.488(1); <i>c</i> = 14.863(2); β = 90.033(2)	<i>a</i> = 14.8908(8); <i>b</i> = 19.052(1); <i>c</i> = 11.5855(6)
Volume / Å ³	3203.4(5)	3250.0(6)	3286.8(3)
Molar weight / g·mol ⁻¹	2647.41	2691.91	2722.01
Density (calculated) / g·cm ⁻³	5.489	5.501	5.501
Crystal form, color	Block, metallic black	Block, metallic black	Block, metallic black
Crystal size / mm ³	0.25 × 0.18 × 0.12	0.18 × 0.12 × 0.08	0.22 × 0.14 × 0.12
Diffractometer	Bruker AXS, APEX SMART CCD		
Monochromator	Graphite		
X-Ray radiation, λ / Å	Mo-K α , 0.71073		
θ range, °	1.08 to 28.00	1.07 to 26.44	2.06 to 29.23
Index range	-24 ≤ <i>h</i> ≤ 24, -15 ≤ <i>k</i> ≤ 15, -19 ≤ <i>l</i> ≤ 19	-23 ≤ <i>h</i> ≤ 23, -14 ≤ <i>k</i> ≤ 14, -18 ≤ <i>l</i> ≤ 18	-20 ≤ <i>h</i> ≤ 20, -26 ≤ <i>k</i> ≤ 25, -15 ≤ <i>l</i> ≤ 15
Absorption correction	SADABS [120]		
Total no. reflections	34599	31064	35963
<i>N</i> _{all}			
Independent reflections <i>N</i>	7721	6694	4584
Reflections with <i>I</i> > 2 σ (<i>I</i>) <i>N</i> '	6432	5378	3620
Absorption coefficient, μ / mm ⁻¹	41.311	41.588	40.965
Extinction coefficient	–	0.000023(8)	–
<i>F</i> (000)	4328	4400	4440
Refinement method	Full-matrix least-squares on <i>F</i> ²		
Weighting scheme	$w = 1/[\sigma^2(F_o^2) + (0.0094P)^2 + 80.3945P]$, where $P = (F_o^2 + 2F_c^2) / 3$	$w = 1/[\sigma^2(F_o^2) + (0.0014P)^2 + 146.3297P]$, where $P = (F_o^2 + 2F_c^2) / 3$	$w = 1/[\sigma^2(F_o^2) + (0.0834P)^2 + 74.2922P]$, where $P = (F_o^2 + 2F_c^2) / 3$
Number of free parameters	192	192	101
Goodness-on-fit on <i>F</i> ²	1.059	1.033	1.042
<i>R</i> ₁ (<i>N</i> '; <i>N</i> _{all})	0.0500; 0.0610	0.0538; 0.0724	0.0575; 0.0742
<i>wR</i> ₂ (<i>N</i> '; <i>N</i> _{all})	0.1132; 0.1195	0.1217; 0.1321	0.1637; 0.1814
Twin volume fractions	0.505(1), 0.495(1)	0.594(1), 0.406(1)	—
$\Delta\rho_{\min}$; $\Delta\rho_{\max}$ / e·Å ⁻³	– 3.31 / 2.78	– 3.47 / 4.11	– 3.84 / 5.10
Deposition no.	CSD – 422187	CSD – 422188	CSD – 422189

Table 8.2. Atomic coordinates and equivalent isotropic displacement parameter $U_{eq} / \text{\AA}^2$ of $\text{Cs}_{10}\text{Tl}_6\text{SiO}_4$ and $\text{Cs}_{10}\text{Tl}_6\text{GeO}_4$ (*).

Atom	Site	x	y	z	U_{eq}
Tl1A	4e	0.43464(6)	0.01452(8)	0.14101(8)	0.0562(2)
		0.43917(7)*	0.02076(9)*	0.14262(8)*	0.0474(3)*
Tl1B	4e	0.93017(6)	-0.00773(8)	-0.13845(7)	0.0505(2)
		0.92967(6)*	-0.00546(9)*	-0.13760(8)*	0.0451(3)*
Tl2A	4e	0.56141(9)	-0.1645(2)	0.0562(1)	0.1142(7)
		0.5462(1)*	-0.1846(1)*	0.0427(1)*	0.0922(6)*
Tl2B	4e	0.07397(6)	0.1453(1)	-0.06604(8)	0.0644(3)
		0.07546(6)*	0.1413(1)*	-0.06587(9)*	0.0577(3)*
Tl3A	4e	0.57115(8)	0.1007(2)	0.04381(9)	0.0982(5)
		0.58030(8)*	0.0753(1)*	0.0453(1)*	0.0817(5)*
Tl3B	4e	0.06072(6)	-0.1198(1)	-0.04347(8)	0.0630(3)
		0.05822(7)*	-0.1223(1)*	-0.04344(8)*	0.0541(3)*
Cs1	4e	0.2450(1)	-0.4576(1)	0.31558(7)	0.0584(3)
		0.2387(1)*	-0.4543(2)*	0.3155(1)*	0.0489(4)*
Cs2	4e	0.74652(9)	-0.17230(9)	-0.04314(8)	0.0509(3)
		0.7415(1)*	-0.1739(1)*	-0.0359(1)*	0.0439(4)*
Cs3	4e	0.7530(1)	0.2124(1)	-0.0837(1)	0.0727(4)
		0.7553(1)*	0.2087(2)*	-0.0855(2)*	0.0722(6)*
Cs4	4e	0.2546(2)	-0.8291(1)	0.30934(9)	0.0824(5)
		0.2573(2)*	-0.8416(2)*	0.3025(1)*	0.0869(8)*
Cs5A	4e	0.4253(1)	-0.3086(2)	0.2038(2)	0.0837(6)
		0.4177(1)*	-0.2966(2)*	0.2138(2)*	0.0710(7)*
Cs5B	4e	0.93450(9)	0.3210(1)	-0.1967(1)	0.0564(4)
		0.9380(1)*	0.3217(2)*	-0.19464(1)*	0.0553(5)*
Cs6A	4e	0.40822(8)	0.3523(2)	0.1795(1)	0.0620(4)
		0.4084(1)*	0.3598(2)*	0.1895(2)*	0.0553(5)*
Cs6B	4e	0.90658(8)	-0.3423(1)	-0.1719(1)	0.0562(4)
		0.9057(1)*	-0.3386(2)*	-0.1714(1)*	0.0506(5)*
Cs7A	4e	0.6179(1)	-0.5424(2)	0.0599(2)	0.0745(5)
		0.6155(1)*	-0.5517(2)*	0.0585(2)*	0.0667(6)*
Cs7B	4e	0.1223(1)	0.5362(2)	-0.0668(2)	0.0817(6)
		0.1244(1)*	0.5424(3)*	-0.0719(2)*	0.0840(8)*
Si1	4e	0.2492(4)	-0.5254(3)	0.0983(2)	0.0331(8)
Ge1	4e	0.2504(1)*	-0.5259(2)*	0.0974(1)*	0.0250(4)*
O1	4e	0.2512(9)	-0.6386(9)	0.1701(6)	0.039(2)
		0.251(1)*	-0.646(1)*	0.174(1)*	0.036(3)*
O2A	4e	0.3187(8)	-0.444(1)	0.122(1)	0.050(4)
		0.3212(8)*	-0.436(1)*	0.122(1)*	0.038(4)*
O2B	4e	0.8232(7)	0.448(1)	-0.117(1)	0.037(3)
		0.8261(9)*	0.444(1)*	-0.118(1)*	0.035(4)*
O3	4e	0.248(1)	-0.573(1)	-0.0066(6)	0.047(3)
		0.2522(9)*	-0.572(1)*	-0.0144(9)*	0.034(3)*

Table 8.3. Atomic coordinates and equivalent isotropic displacement parameter $U_{eq} / \text{\AA}^2$ of $\text{Cs}_{10}\text{Tl}_6\text{SnO}_3$.

Atom	Site	x	y	z	U_{eq}
Tl1	8 <i>d</i>	0.14219(4)	0.43669(4)	0.00455(5)	0.0485(2)
Tl2	8 <i>d</i>	0.04390(6)	0.56153(5)	-0.17372(8)	0.0768(3)
Tl3	8 <i>d</i>	0.04762(5)	0.57249(5)	0.08929(9)	0.0740(3)
Cs1	4 <i>c</i>	0.2986(1)	¼	-0.4615(1)	0.0546(4)
Cs2	4 <i>c</i>	-0.0526(1)	¾	-0.1360(1)	0.0575(4)
Cs3	4 <i>c</i>	-0.0819(1)	¾	0.2226(1)	0.0652(5)
Cs4	4 <i>c</i>	0.3120(2)	¼	-0.8313(2)	0.110(1)
Cs5	8 <i>d</i>	0.20153(7)	0.43310(6)	-0.3173(1)	0.0554(3)
Cs6	8 <i>d</i>	0.18762(7)	0.40475(6)	0.34306(9)	0.0516(3)
Cs7	8 <i>d</i>	0.05982(9)	0.60051(8)	-0.5623(2)	0.0792(4)
Sn	4 <i>c</i>	0.07250(8)	¼	-0.5444(1)	0.0300(3)
O1	4 <i>c</i>	0.1753(9)	¼	-0.662(1)	0.039(3)
O2	8 <i>d</i>	0.1153(7)	0.3299(6)	-0.444(0)	0.042(2)

According to the group-subgroup relation, each 4*c* site in the orthorhombic space group corresponds to one 4*e* site in the monoclinic one, and each atom, located on an 8*d* site in orthorhombic $\text{Cs}_{10}\text{Tl}_6\text{SnO}_3$ splits into two 4*e* sites in monoclinic $\text{Cs}_{10}\text{Tl}_6\text{SiO}_4$, see Figure 8.4. For better comparison, corresponding atoms are labeled with the same number but with additional letters A and B, if necessary, see Tables 8.2 and 8.3.

The synthesized compounds crystallize in new structure types (Fig. 8.5), consisting of octahedral $[\text{Tl}_6]$ clusters, $[\text{SiO}_4]$, $[\text{GeO}_4]$ and $[\text{SnO}_3]$ oxoanions, respectively, and isolated cesium cations. Selected bond distances as well as the angles within the complex oxoanions are summarized in Table 8.4. The shape of the orthosilicate(IV) anion deviates only marginally from ideal tetrahedral geometry (Fig. 8.6*b*) ($106.5^\circ \leq \angle \text{O}-\text{Si}-\text{O} \leq 113.6^\circ$), with Si–O bond lengths $d(\text{Si}-\text{O})$ of 1.65 to 1.68 Å, corresponding to those in other known orthosilicates: $d(\text{Si}-\text{O}) = 1.63\text{--}1.64$ Å in K_4SiO_4 [216], $d(\text{Si}-\text{O}) = 1.60\text{--}1.65$ Å in Li_4SiO_4 [217], $d(\text{Si}-\text{O}) = 1.64\text{--}1.65$ Å in K_3LiSiO_4 [218], $d(\text{Si}-\text{O}) = 1.61\text{--}1.68$ Å in $\text{Cs}_2\text{Li}_2\text{SiO}_4$ [219] as well as recently synthesized $\text{Cs}_{20}[\text{Sn}_4]_2[\text{SiO}_4]_3$ ($d(\text{Si}-\text{O}) = 1.60\text{--}1.70$ Å) [220].

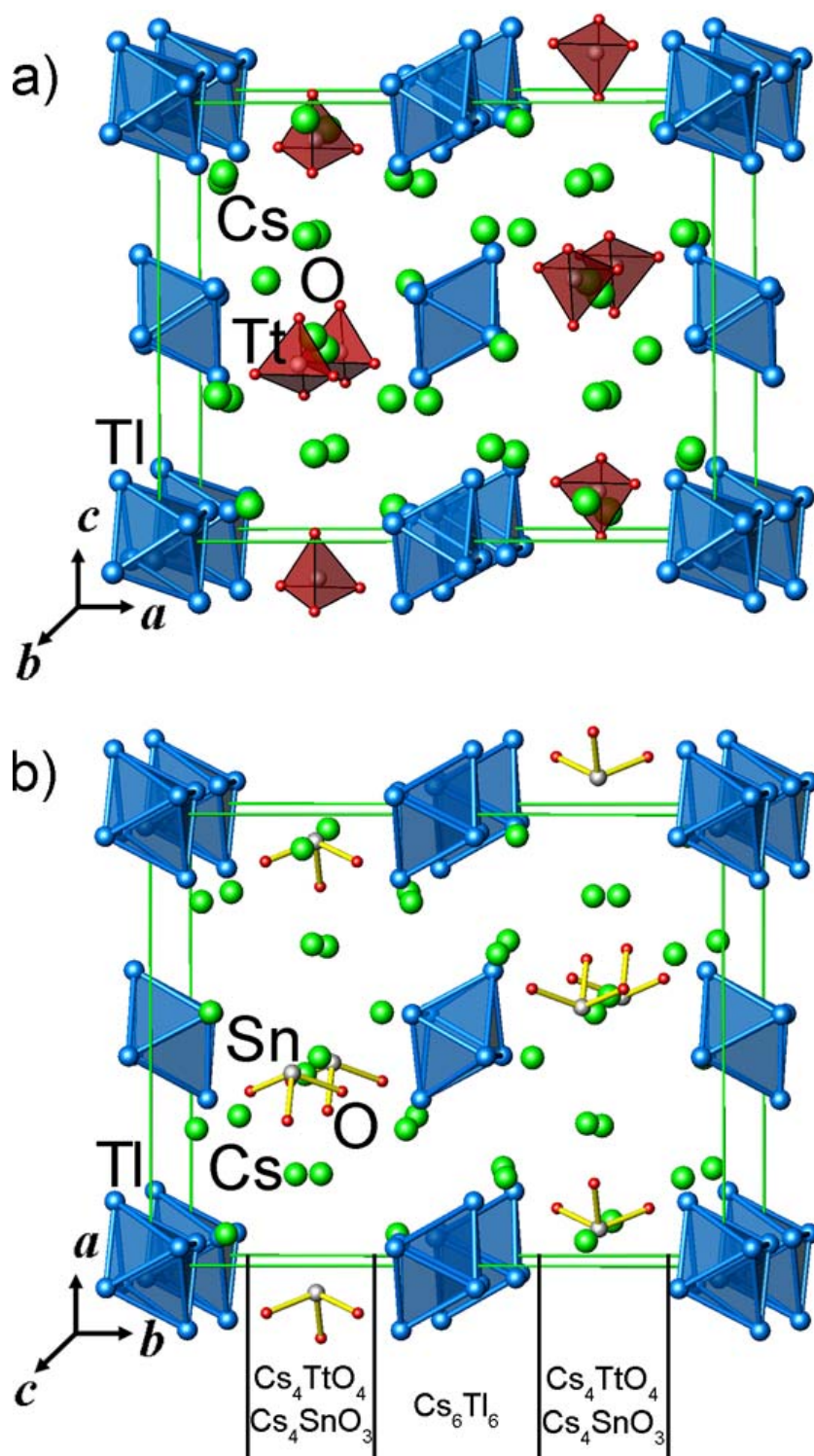


Figure 8.5. Perspective representations of the crystal structures of $\text{Cs}_{10}\text{Tl}_6\text{TtO}_4$ (Tt = Si and Ge) (a) and $\text{Cs}_{10}\text{Tl}_6\text{SnO}_3$ (b) (green lines mark the unit cell edges, blue spheres – Tl atoms, green spheres – Cs atoms, grey spheres – Si, Ge or Sn atoms, red spheres – oxygen atoms); vertical black lines at the bottom emphasize the intergrowth type of structure, consisting of Cs_6Tl_6 and Cs_4TtO_4 (Tt = Si and Ge) or Cs_4SnO_3 slabs.

The Ge–O distances in $\text{Cs}_{10}\text{Tl}_6\text{GeO}_4$ (Fig. 8.6b) range from 1.74 to 1.78 Å and are also similar to the distances in known orthogermanates with tetrahedral GeO_4 units: $d(\text{Ge–O}) = 1.75\text{--}1.78$ Å in $\text{Na}_4[\text{GeO}_4]$ [221], $d(\text{Ge–O}) = 1.75\text{--}1.78$ Å in $\text{Rb}_4[\text{GeO}_4]$ [222], $d(\text{Ge–O}) = 1.73\text{--}1.79$ Å in $\text{Rb}_{12}[\text{Sn}_4]_2[\text{GeO}_4]_3$ [220] and $d(\text{Ge–O}) = 1.72\text{--}1.77$ Å in $\text{Cs}_{12}[\text{Sn}_4]_2[\text{GeO}_4]_3$ [220].

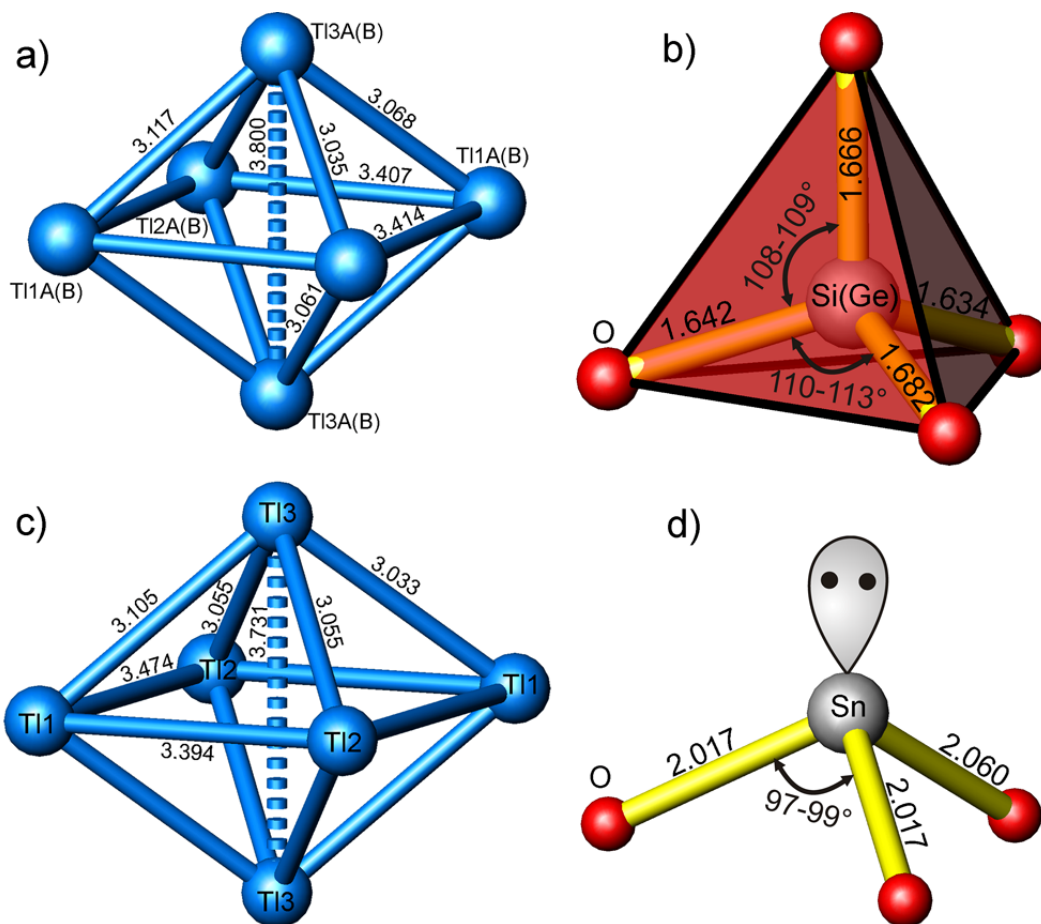


Figure 8.6. The $[\text{Tl}_6]^{6-}$ clusters in $\text{Cs}_{10}\text{Tl}_6\text{TtO}_4$ ($\text{Tt} = \text{Si}$ and Ge) (a) and $\text{Cs}_{10}\text{Tl}_6\text{SnO}_3$ (c). The tetrahedral arrangement of oxygen around Si and Ge (b) in $\text{Cs}_{10}\text{Tl}_6\text{TtO}_4$ ($\text{Tt} = \text{Si}$ and Ge) as well as triple-coordinated Sn by oxygen (d) in $\text{Cs}_{10}\text{Tl}_6\text{SnO}_3$ compound. Dotted lines emphasize the compressed diagonals of the clusters, Table 8.5.

The angles $\angle\text{O–Ge–O}$ are in the range of $107.5\text{--}112.4^\circ$; this deviation from the ideal tetrahedral arrangement is comparable to other known orthogermanates. The anionic unit $[\text{SnO}_3]^{4-}$, present in $\text{Cs}_{10}\text{Tl}_6\text{SnO}_3$, displays a ψ – tetrahedral coordination of tin by three oxygen ligands, forming an anion with approximate C_{3v} point group symmetry (Fig. 8.6d). This anion possesses a shape corresponding

Table 8.4. Selected bond distances / Å² and angles / ° of Cs₁₀Tl₆TtO₄ (Tt = Si, Ge) and Cs₁₀Tl₆SnO₃.

		Cs ₁₀ Tl ₆ SiO ₄	Cs ₁₀ Tl ₆ GeO ₄	Cs ₁₀ Tl ₆ SnO ₃		
Tl1A	–Tl3A	3.039(2)	3.026(2)	Tl1	–Tl3	3.033(1)
	–Tl3A	3.116(2)	3.114(2)		–Tl3	3.105(1)
	–Tl2A	3.388(2)	3.348(2)		–Tl2	3.394(1)
	–Tl2A	3.394(2)	3.453(2)		–Tl2	3.474(1)
Tl1B	–Tl3B	3.068(2)	3.074(2)			
	–Tl3B	3.117(2)	3.123(2)			
	–Tl2B	3.407(2)	3.405(2)			
	–Tl2B	3.414(1)	3.418(2)			
Tl2A	–Tl3A	3.001(2)	3.015(3)	Tl2	–Tl3	3.055(2)
	–Tl3A	3.044(3)	3.056(3)		–Tl3	3.055(1)
	–Tl1A	3.388(2)	3.347(2)		–Tl1	3.394(1)
	–Tl1A	3.394(2)	3.453(2)		–Tl1	3.474(1)
Tl2B	–Tl3B	3.035(2)	3.026(2)			
	–Tl3B	3.061(2)	3.064(2)			
	–Tl1B	3.407(2)	3.405(2)			
	–Tl1B	3.414(1)	3.418(2)			
Tl3A	–Tl2A	3.001(2)	3.015(3)	Tl3	–Tl1	3.033(1)
	–Tl1A	3.039(2)	3.026(2)		–Tl2	3.055(2)
	–Tl2A	3.044(3)	3.056(3)		–Tl2	3.055(1)
	–Tl1A	3.116(2)	3.114(2)		–Tl1	3.105(1)
Tl3B	–Tl2B	3.035(2)	3.026(2)			
	–Tl2B	3.061(2)	3.064(2)			
	–Tl1B	3.068(2)	3.074(2)			
	–Tl1B	3.117(2)	3.122(2)			
Tt	–O3	1.65(1)	1.74(2)	Sn	–O2	2.02(1)×2
	–O2A	1.65(2)	1.74(1)		–O1	2.05(1)
	–O2B	1.65(2)	1.76(2)			
	–O1	1.68(1)	1.78(1)			
O1	–Tt	1.68(1)	1.78(1)	O1	–Sn	2.05(1)
O2A	–Tt	1.65(2)	1.74(2)	O2	–Sn	2.02(1)
O2B	–Tt	1.65(1)	1.76(2)			
O3	–Tt	1.65(1)	1.74(1)			
O2A – Tt – O3		113.6	109.7	O2 – Sn – O2		97.6(6)
O2A – Tt – O2B		108.8	108.5	O2 – Sn – O1		98.5(4)×2
O2B – Tt – O3		108.7	110.7			
O2A – Tt – O1		106.5	107.5			
O3 – Tt – O1		110.2	112.4			
O2B – Tt – O1		109.1	107.9			

to those found in Cs_4SnO_3 [223], K_4SnO_3 [224], Na_4SnO_3 [225] as well as in the recently synthesized $\text{Cs}_{48}[\text{Sn}_4]_4[\text{SnO}_3]_4[\text{O}]_7[\text{O}_2]$ [226]. In accordance with the VSEPR model, the bond angles $\angle\text{O}-\text{Sn}-\text{O}$ are much smaller than the ideal tetrahedral angle, and range from 97.6 to 98.5°, which is comparable to other stannates(II) [223-226].

The three oxotetralide thallides presented here can be regarded as ‘double salts’. On the basis of an ionic description, Cs_6Tl_6 on one hand and the oxosilicates, -germanates and -stannates on the other hand, constitute binary and ternary, respective, partial structures, which form the quaternary structure by *inhomogeneous intergrowth* [227], c.f. Figure 8.5.

All synthesized compounds contain $[\text{Tl}_6]^{6-}$ clusters, which can be characterized as a distorted octahedron (Figs. 8.6a, c), with the Tl–Tl distances ranging from 3.03 to 3.47 Å (Table 8.4). The intercluster Tl–Tl separations are clearly larger (≥ 6.8 Å). The thallium cluster anions all display similar distortion patterns: one of the space diagonals of the octahedra is significantly compressed. The ratios of the lengths of compressed diagonals (d_1) and the averaged expanded ones (d_2) serve as a quantitative measure for the distortions encountered in various representatives (Table 8.5).

Table 8.5. Lengths of the space diagonals (Tl–Tl) of $[\text{Tl}_6]^{6-}$ octahedra / Å in various compounds.

Compound	Tl–Tl _{compressed} (d_1)	Tl–Tl _{expanded} (d_2)	d_2/d_1
CsTl [182]	3.741(5)	$4.836(3) \times 2$	1.293
KTl [181]	3.805(3)	$4.814(2) \times 2$	1.265
$\text{Rb}_{10}\text{Tl}_6\text{O}_2$ [105]	3.573(7)	$4.941(1) \times 2$	1.383
$\text{K}_{10}\text{Tl}_6\text{O}_2$ [105]	3.578(5)	$4.933(2) \times 2$	1.379
$\text{Cs}_{10}\text{Tl}_6\text{SiO}_4$	3.800(7)	4.765(8)	1.254
		4.879(5)	1.284
$\text{Cs}_{10}\text{Tl}_6\text{GeO}_4$	3.804(5)	4.757(6)	1.251
		4.889(0)	1.285
$\text{Cs}_{10}\text{Tl}_6\text{SnO}_3$	3.731(1)	4.838(3)	1.297
		4.874(7)	1.306

8.3. Electron Balance of the $[\text{Tl}_6]^{6-}$ Cluster-anion

The Tl_6 groups in the compounds under discussion provide further examples of so-called “hypo-electronic” thallium clusters (skeleton electron concentration = $24e$, which is less than $6 \times 4 + 2 = 26e$ (inert-electron pairs included), which is the polyhedral electron number required according to Wade's rule). An ideal (all diagonals of equal lengths) Tl_6 cluster obeying Wade's rule should bear a charge of $8-$, as it has been observed for $\text{Na}_{14}\text{K}_6\text{Tl}_{18}\text{M}$ ($\text{M} = \text{Mg}, \text{Zn}$) [183]. It is remarkable that in $\text{Cs}_{10}\text{Tl}_6\text{SnO}_3$ the hypo-electronic $[\text{Tl}_6]^{6-}$ cluster is found although Sn, present in the oxidation state $2+$, could easily transfer electrons to the thallium cluster. Thus one can consider $[\text{Tl}_6]^{6-}$ clusters to not require additional electrons and to be intrinsically stable. The distortion can be understood in terms of the Jahn–Teller theorem. The compression of the octahedron along one of its diagonals reduces its point group symmetry to D_{4h} , thus splitting the t_{1u} skeleton molecular orbital (MO) into e_u and a_{2u} MOs, the latter one becoming antibonding. As a result, the 24 valence electrons now occupy exclusively bonding or non-bonding MOs, thus stabilizing the cluster (Fig. 8.7) [182]. The same structural feature has been observed for all $[\text{Tl}_6]^{6-}$ cluster containing compounds, known so far [105, 181, 182].

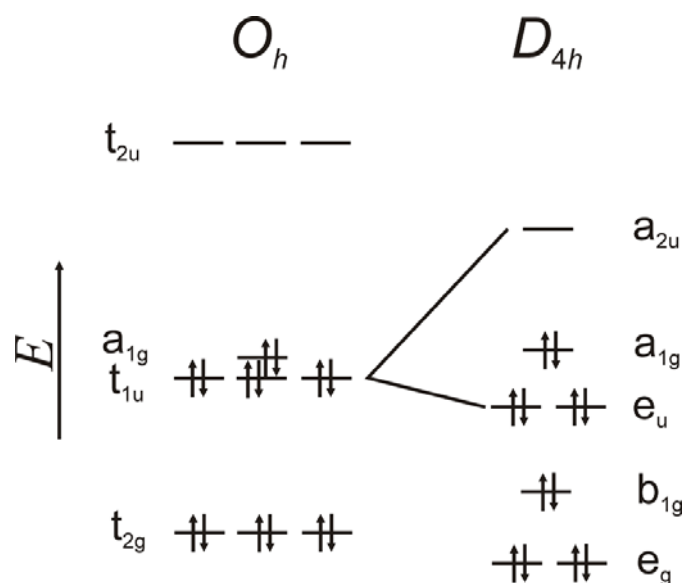


Figure 8.7. MO diagrams (qualitative sketch) of the $[\text{Tl}_6]^{8-}$ (O_h) and $[\text{Tl}_6]^{6-}$ (D_{4h}) clusters [182].

8.4. Electrical Resistivity Measurements

Temperature-dependent resistivity measurements of $\text{Cs}_{10}\text{Tl}_6\text{SiO}_4$ were performed according to the general procedure of the *van der Pauw* method. The specific electrical resistivity consists of 2 regions (Fig. 8.8). Firstly it decreases linearly from $2.99 \Omega\cdot\text{cm}$ at 7 K to $1.63 \Omega\cdot\text{cm}$ at 150 K, which is typical for semiconducting materials (Fig. 8.8). The second region from 150 to 290 K is characteristic for a moderate metallic conductor, and the resistivity slightly increases from $1.63 \Omega\cdot\text{cm}$ at 150 K to $1.67 \Omega\cdot\text{cm}$ at 290 K. The measured values are compared to other known compounds, e.g. the semiconductor CsTl ($\rho = \sim 1 \Omega\cdot\text{cm}$) [182]. To find out, whether there is a structural reason for the phase transition, single crystal structure analysis was performed at 100 K. However, no significant change in the crystallographic structure, especially compression or any other distortion of $[\text{Tl}_6]^{6-}$ octahedron, was noticeable.

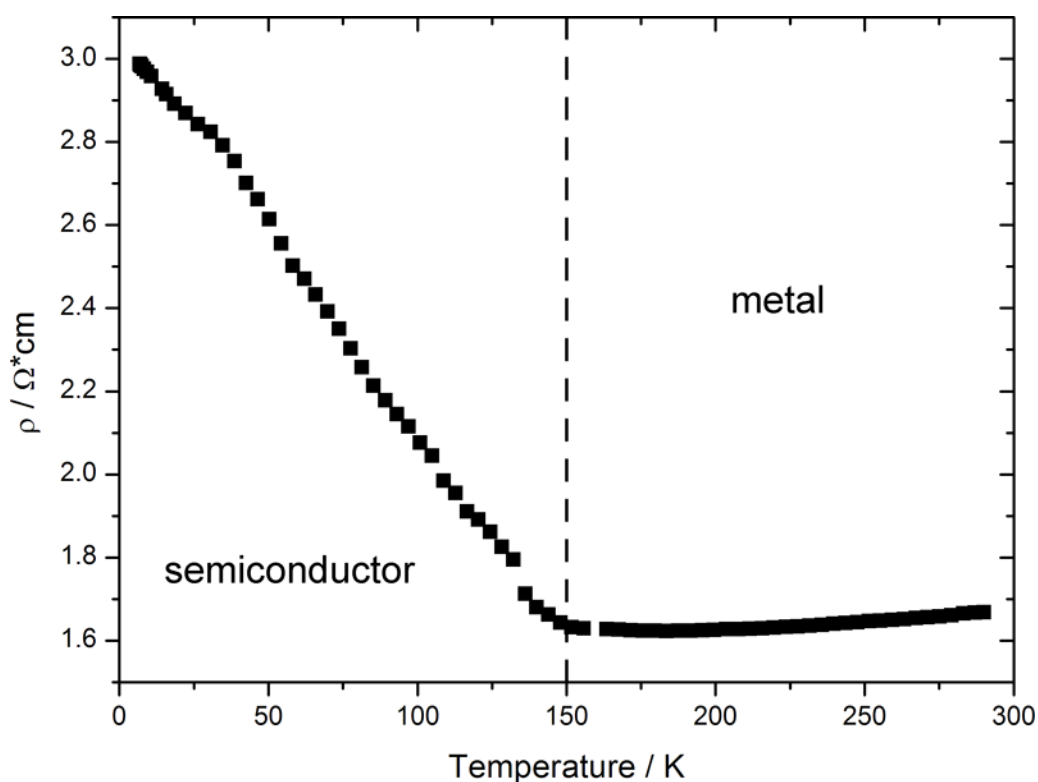


Figure 8.8. Temperature – dependent resistivity data of $\text{Cs}_{10}\text{Tl}_6\text{SiO}_4$.

8.5. Magnetic Susceptibility Measurements

The magnetization was measured using a SQUID magnetometer (MPMS 5.5, Fa., Quantum Design, USA) in the temperature range of 5–300 K at $H = 0.001, 0.1, 1, 3, 5$ and 7 T. The specimens (silicate – 0.1778 g, germanate – 0.1341 g or stannate – 0.1170 g) were sealed in quartz tubes under helium. The raw data were corrected for the holder contribution.

The magnetic susceptibility is negative and temperature independent in the range of 50–300K for all magnetic fields applied, which is indicative for diamagnetic compounds: $\chi_{\text{mol}} = -3.1 \times 10^{-4} \pm 2.5 \%$ emu/mol for $\text{Cs}_{10}\text{Tl}_6\text{SiO}_4$, $\chi_{\text{mol}} = 15 \times 10^{-4} \pm 2.5 \%$ emu/mol for $\text{Cs}_{10}\text{Tl}_6\text{GeO}_4$ and $\chi_{\text{mol}} = -6.5 \times 10^{-4} \pm 2.5 \%$ emu/mol for $\text{Cs}_{10}\text{Tl}_6\text{SnO}_3$ at field strength 3 T (Fig. 8.9) and approximates the sum of diamagnetic core corrections ($10\chi(\text{Cs}^+) + 6\chi(\text{Tl}^+) + \chi(\text{Si}^{4+}) + 4\chi(\text{O}^{2-}) = -5.628 \times 10^{-4}$ emu/mol for $\text{Cs}_{10}\text{Tl}_6\text{SiO}_4$; $10\chi(\text{Cs}^+) + 6\chi(\text{Tl}^+) + \chi(\text{Ge}^{4+}) + 4\chi(\text{O}^{2-}) = -5.692 \times 10^{-4}$ emu/mol for $\text{Cs}_{10}\text{Tl}_6\text{GeO}_4$; $10\chi(\text{Cs}^+) + 6\chi(\text{Tl}^+) + \chi(\text{Sn}^{2+}) + 4\chi(\text{O}^{2-}) = -5.7 \times 10^{-4}$ emu/mol for $\text{Cs}_{10}\text{Tl}_6\text{SnO}_3$) and the Larmor susceptibility of the cluster orbital electrons [125, 126] (-0.8×10^{-4} emu/mol – $\text{Cs}_{10}\text{Tl}_6\text{SiO}_4$, -0.8×10^{-4} emu/mol – $\text{Cs}_{10}\text{Tl}_6\text{GeO}_4$, -0.79×10^{-4} emu/mol – $\text{Cs}_{10}\text{Tl}_6\text{SnO}_3$).

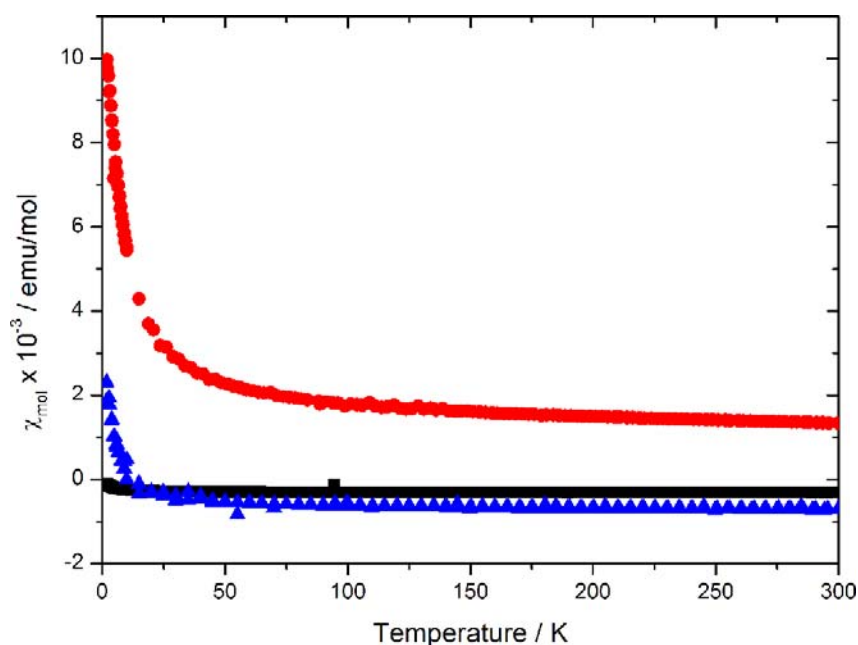


Figure 8.9. Temperature – dependent magnetic susceptibility data of $\text{Cs}_{10}\text{Tl}_6\text{SiO}_4$ (black squares), $\text{Cs}_{10}\text{Tl}_6\text{GeO}_4$ (red circles) and $\text{Cs}_{10}\text{Tl}_6\text{SnO}_3$ (blue triangles) at field strength 3T.

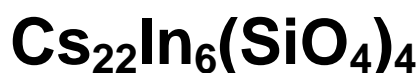
At low temperatures (2–10 K) the magnetic susceptibilities for $\text{Cs}_{10}\text{Tl}_6\text{SnO}_3$ increase due to presence in the sample of small amount of paramagnetic impurities. The dependences of magnetic susceptibility were described according to Curie-Weiss law in the temperature range of 2–10 K at 1, 3, 5, and 7T (Figs. A2.13 – A2.16) and the average amount of paramagnetic impurities in the sample was determined to be 1 wt. %.

8.6. Conclusions

Following the approach to generate new thallium ions by introducing additional anionic species with a concomitant increase in the compositional and structural degrees of freedom, new thallium cluster compounds $\text{Cs}_{10}\text{Tl}_6\text{TtO}_4$ (Tt = Si, Ge) and $\text{Cs}_{10}\text{Tl}_6\text{SnO}_3$ were synthesized and characterized. According to single-crystal X-ray analyses, the compounds crystallize in new structure types, consisting of octahedral $[\text{Tl}_6]$ clusters, $[\text{SiO}_4]$, $[\text{GeO}_4]$ and $[\text{SnO}_3]$ oxoanions, respectively, and isolated cesium cations. $[\text{Tl}_6]^{6-}$ clusters are characterized as distorted octahedra compressed along one of the 4-fold axes of an originally unperturbed octahedron, with the Tl–Tl distances ranging from 3.03 to 3.47 Å. The shape of the orthosilicate(IV) and orthogermanate (IV) anions deviates slightly from ideal tetrahedral geometry, while the bonding angles of the ψ – tetrahedral $[\text{SnO}_3]^{4-}$ anions correlate with VSEPR theory and are much smaller than the ideal tetrahedral angle.

In contrast to the Si and Ge compounds, where the oxidation state of the tetrel atom is unambiguously 4+, for the threefold coordinated Sn atom in $\text{Cs}_{10}\text{Tl}_6\text{SnO}_3$ an oxidation state of 2+ has to be assumed. Thus, the latter reveal further evidence that the so called “hypoelectronic” $[\text{Tl}_6]^{6-}$ cluster does not require additional electrons and is intrinsically stable. The distortion of $[\text{Tl}_6]^{6-}$ can be understood in terms of the Jahn–Teller theorem producing a closed-shell electronic structure, which is in agreement with the diamagnetic properties of all first oxotetrelate-thallides.

9. Cesium Silicate Indide:



One of the successful concepts in solid state chemistry, which leads to the formation of isostructural or previously unknown compounds, enabling to tune physical properties, is the substitution of similar elements in known compounds. Indium is another element, which belongs to the triel elements group like thallium and forms a remarkable diversity of cluster compounds. But indium, similar to gallium, forms preferably extended anionic cluster frameworks rather than discrete clusters, as preferably found with thallium. This process of network formation from clusters can be explained as oxidation of the ns^2 pair at each vertex followed by the generation of normal two-electron – two-center intercluster bonds. Only few examples of discrete indium clusters are known: isolated tetrahedra *nido*-[In₄]⁸⁻ [228], *nido*-[In₅]⁹⁻ [229], which can be described according to Wade's rule, and hypoelectronic [In₁₁]⁷⁻ [230-232]. Further examples of the indium clusters are *closo*-[In₆]⁴⁻ [233, 234], *closo*-[In₁₆] and *nido*-In₁₁ in Na₇In_{11.8} [126], *arachno* and *closo*-In₁₂ in A₃Na₂₆In₄₈ (A = K, Rb, Cs) [235], *closo*-[In₁₆] and *nido*-[In₁₁] units in Na₁₅In_{27.4} [228], *closo*-[In₁₂] and In-centered *closo*-[In₁₇] clusters in K₁₇In₄₁ [236], *closo*-[In₁₂] plus an In₁₅ spacer in K_{18.2}Na_{4.8}In₃₉ [198], three types of empty In₁₂, In₁₆ centered by an additional In atom (In@[In₁₆]), and open In₁₅ spacers in K₃₉In₈₀ [237]. All the latter follow either the Zintl–Klemm concept or the classical Wade's rule, also when a decrease of the nominal charge of the cluster by formation of intercluster bonds occurs. Thus, members of the isolated *closo*-Tr_n⁻ⁿ⁻² cluster family become Tr_n^{-n-2+m} when interbonded at m vertices to other clusters or Tr_n⁻². For example, *nido* clusters derived from icosahedra In₁₁ has to form the nominal isolated *nido*-[In₁₁]¹⁵⁻ (2n+4), but being reduceable to [In₁₁]⁵⁻ after linking to ten other clusters in Na₇In_{11.8} [126].

Among the big diversity of In clusters, two particular In₆ clusters have to be marked out as an illustrative example of a structure–property relationship. Such classical [In₆]⁸⁻ octahedral clusters in Rb₂In₃ [233] or isostructural Cs₂In₃ [234] can be regarded as oxidized by removing 4e⁻ and then linked into square nets by intercluster bonding at four waist vertices forming two dimensional quasi-infinite ²_∞[In₆]⁴⁻ planar sheets. Another indide anion [In₆]¹⁶⁻ [238] is presented in Ba₁₁In₆O₃ as an isolated unit in a planar tetrafluorethene shape with two short and two long In–In distances.

With respect to the concept of the element substitution mentioned above and following the aims of the present work, the investigations of the cesium indium silicate system have led to the formation of Cs₂₂In₆(SiO₄)₄ containing an isolated [In₆]⁶⁻ clusteranion, which has not been found before in compounds with covalently bonded homoatomic clusters, and which is similar to the corresponding thallium clusteranion.

9.1. Synthesis, Powder XRD and Thermal Stability

All operations during experimental procedure were performed under dried argon (Schlenk technique or glovebox). Cs₂₂In₆(SiO₄)₄ was prepared by reaction of cesium with indium, SiO₂ and Cs₂O. The starting materials for the synthesis (total amount of 1 – 2 g) were weighed out in the molar ratios Cs : Cs₂O : In : SiO₂ = 22-24 : 8 : 6 : 4, then placed into a tantalum tube, which was sealed under argon with an arc welder. In order to prevent oxidation, the tantalum tube was encapsulated in silica jacket, under argon. Cs₂₂In₆(SiO₄)₄ was synthesized by heating the reaction mixture at a rate of 50 K/h up to 673 K, annealing at this temperature for 2 days, and then cooling to room temperature at a rate of 200 K/h. The synthesized compound is extremely sensitive to moisture and air and was isolated and handled under strictly inert conditions (Schlenk technique or glovebox). According to powder diffraction X-ray analysis (refinement by Le Bail method, Fig. 9.1), Cs₂₂In₆(SiO₄)₄ was obtained as a single phase. The chemical composition was confirmed by EDX analyses, and no impurity elements were detected. According to the DSC measurements as well as high-temperature powder X-ray analysis

measurements, $\text{Cs}_{22}\text{In}_6(\text{SiO}_4)_4$ is stable at least up to 723 K. For the DSC, powder samples (~15 mg) were placed in Al crucibles, which were cold sealed under argon in a glovebox, heated to 723 K at a rate of 10 K/min, and then cooled down to room temperature at the same rate. The whole process was run under argon.

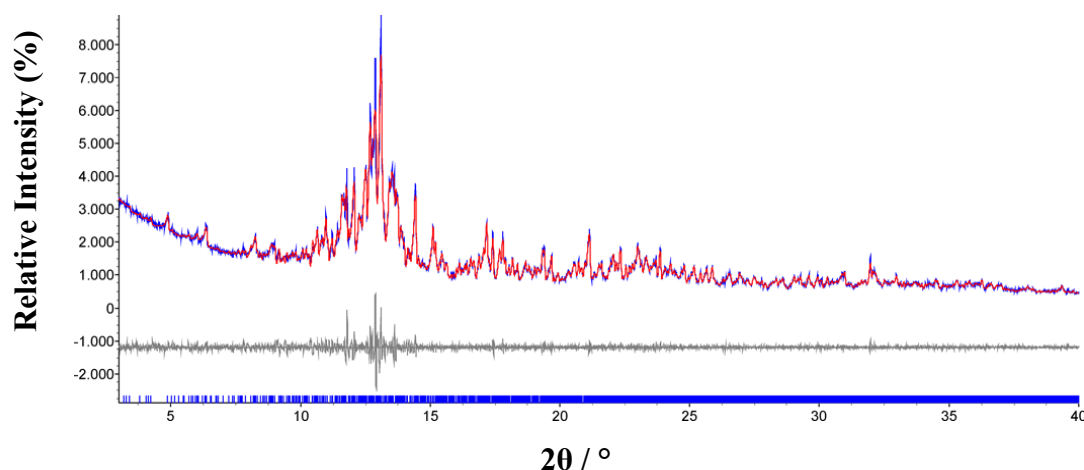


Figure 9.1. Le Bail refinement of $\text{Cs}_{22}\text{In}_6(\text{SiO}_4)_4$ (measured curve (blue line), theoretically calculated curve (red line), difference curve (grey line), Bragg reflections (blue ticks)) ($\lambda = 0.7093 \text{ \AA}$).

9.2. Crystal Structure Analysis

A single crystal X-ray structure analysis of $\text{Cs}_{22}\text{In}_6(\text{SiO}_4)_4$ was performed at room temperature. The crystallographic data, atomic coordinates and anisotropic parameters for the investigated compound are summarized in Tables 9.1–9.3, respectively.

$\text{Cs}_{22}\text{In}_6(\text{SiO}_4)_4$ crystallizes in a new structure type (Fig. 9.2a), consisting of octahedral $[\text{In}_6]$ clusters, $[\text{SiO}_4]$ oxoanions and isolated cesium cations. Selected bond distances as well as the angles within the complex oxoanions are summarized in Table 9.4. Similar to oxotetralide thallides (Chapter 8) $\text{Cs}_{22}\text{In}_6(\text{SiO}_4)_4$ can be regarded as a ‘double salt’. On the basis of an ionic description, Cs_6In_6 on one hand and the oxosilicates $4 \times \text{Cs}_4\text{SiO}_4$ on the other hand, constitute binary and ternary, respective, partial structures, which form the quaternary structure by *inhomogeneous intergrowth* [227] (Fig. 9.2a). The shape of the orthosilicate(IV)

Table 9.1. The crystallographic and structure refinement data for Cs₂₂In₆(SiO₄)₄.

	Cs ₂₂ In ₆ (SiO ₄) ₄
Space group (no.); <i>Z</i>	<i>P</i> 2 ₁ / <i>n</i> (14); 4
Cell parameters / Å	<i>a</i> = 14.3716(8) <i>b</i> = 16.144(1) <i>c</i> = 24.947(2) <i>β</i> = 94.271(1)
Volume / Å ³	5772.1(6)
Molar weight / g·mol ⁻¹	3981.30
Density (calculated) / g·cm ⁻³	4.581
Crystal form, color	Block, silver grey metallic
Crystal size / mm ³	0.23 × 0.21 × 0.11
Diffractometer	Bruker AXS, APEX SMART CCD
Monochromator	Graphite
X-ray radiation, λ / Å	Mo-Kα, 0.71073
θ range, °	0.82 to 36.45
Index range	-22 ≤ <i>h</i> ≤ 23, -26 ≤ <i>k</i> ≤ 26, -41 ≤ <i>l</i> ≤ 41
Absorption correction	SADABS [120]
Total no. reflections N _{all}	109617
Independent reflections N	28071
Reflections with I > 2σ(I) N'	20225
Absorption coefficient, μ / mm ⁻¹	16.154
Extinction coefficient	—
F(000)	6752
Refinement method	Full-matrix least-squares on F ²
Weighting scheme	$w = 1/[\sigma^2(F_o^2) + (0.1024P)^2 + 323.8895P]$, where $P = (F_o^2 + 2F_c^2) / 3$
Number of free parameters	434
Goodness-on-fit on F ²	1.039
R ₁ (N'; N _{all})	0.0841; 0.1072
wR ₂ (N'; N _{all})	0.2433; 0.2571
Twin volume fractions	0.988, 0.012
Δρ _{min} ; Δρ _{max} / e·Å ⁻³	- 7.063 / 10.648

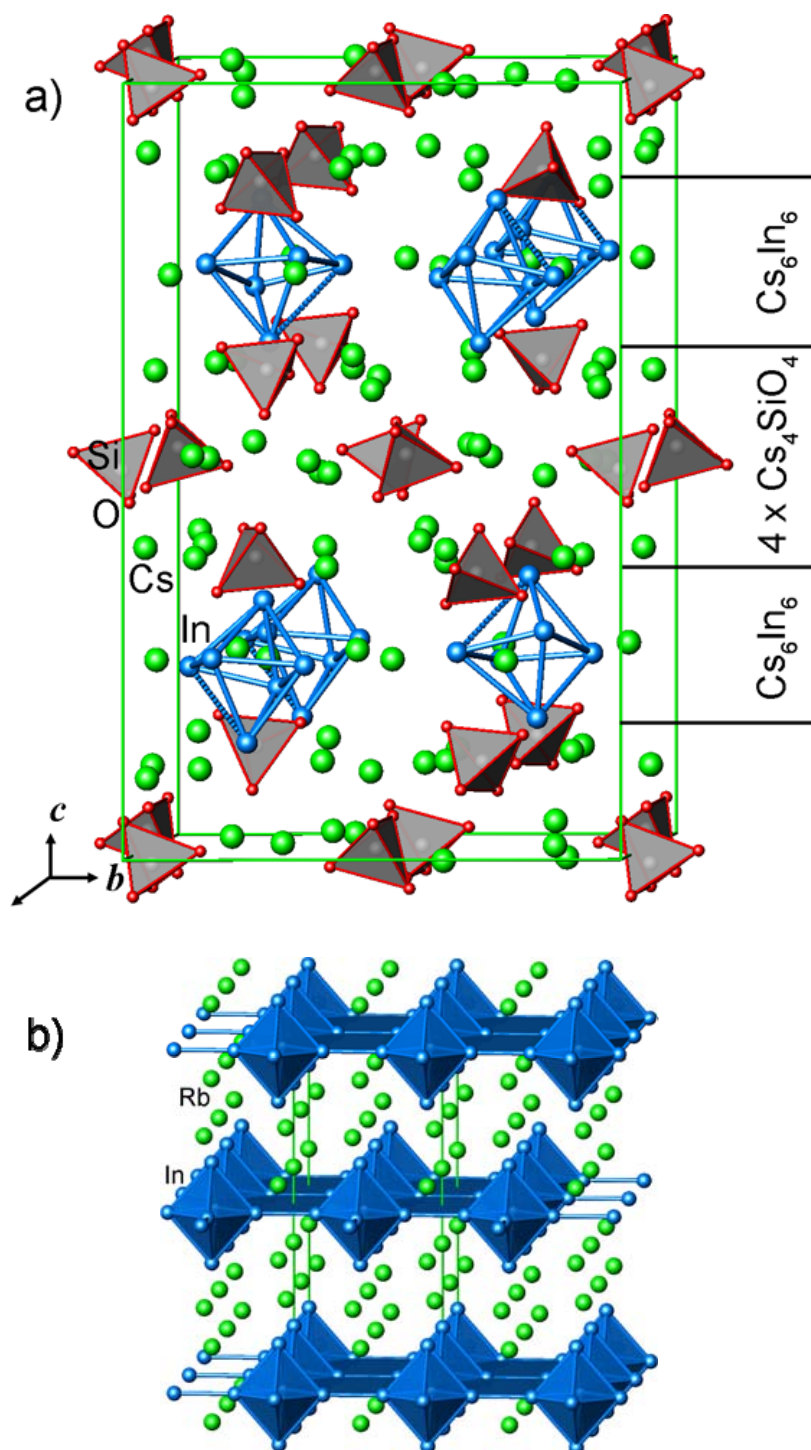


Figure 9.2. Perspective representations of the crystal structures of $\text{Cs}_{22}\text{In}_6(\text{SiO}_4)_4$ (a) and Rb_2In_3 (b) (green lines mark the unit cell edges, blue spheres – In atoms, green spheres – Cs or Rb atoms, grey spheres – Si atoms, red spheres – oxygen atoms); horizontal black lines at the right hand side emphasize the intergrowth type of structure, consisting of Cs_6In_6 and $4 \times \text{Cs}_4\text{SiO}_4$ slabs; solid blue lines represent bonding interactions between the indium atoms forming quasi-finite square planar sheets.

anion deviates from the ideal tetrahedral geometry ($106.5^\circ \leq \angle O-Si-O \leq 113.5^\circ$), similarly to other known orthosilicates. The Si–O distances range from 1.62 to 1.70 Å (Table 9.4) and are also comparable to the distances in other known orthosilicates containing tetrahedral SiO₄ units [216–220] as well as in the discussed corresponding oxosilicate compound (Cs₁₀Tl₆SiO₄: $d(\text{Si–O})$ of 1.65 to 1.68 Å, Chapter 8).

The synthesized compound contains [In₆]^{6–} clusters, which can be characterized as strongly distorted octahedra (Fig. 9.3a), with the In–In distances ($\times 11$) ranging from 2.85 to 3.35 Å and one very long In–In distance of 3.77 Å (Table 9.4). These distances are comparable to those in known In₆-units: $d(\text{In–In}) = 2.88\text{–}3.09$ Å in Rb₂In₃ [233], $d(\text{In–In}) = 2.89\text{–}3.15$ Å in Cs₂In₃ [234], $d(\text{In–In}) = 2.91\text{–}3.12$ Å in K₃Na₂₆In₄₈ [235] and $d(\text{In–In}) = 2.897\text{–}3.15$ in KNa₃In₉ [239]. The corresponding diagonals as well as the edge lengths of the In₆ octahedron of the Cs₂₂In₆(SiO₄)₄, Rb₂In₃ and Cs₂In₃ compounds are summarized in Table 9.5. In contrast to Rb₂In₃ and Cs₂In₃, where the “intercluster” In–In distances (2.808 and 2.833 Å, respectively) are even shorter than intracluster separations, the intercluster distances in Cs₂₂In₆(SiO₄)₄ are clearly larger (≥ 6.6 Å).

Table 9.2. Atomic coordinates and equivalent isotropic displacement parameter $U_{eq} / \text{Å}^2$ for Cs₂₂In₆(SiO₄)₄.

Atom	Site	<i>x</i>	<i>y</i>	<i>z</i>	U_{eq}
Cs1	4e	0.37405(6)	0.79928(5)	0.02913(3)	0.0279(2)
Cs2	4e	0.13298(6)	0.69367(5)	-0.01768(4)	0.0311(2)
Cs3	4e	0.72691(6)	0.61985(6)	0.11853(4)	0.0341(2)
Cs4	4e	0.17418(7)	0.83119(6)	0.11924(4)	0.0335(2)
Cs5	4e	0.52882(6)	0.63658(5)	-0.01986(4)	0.0321(2)
Cs6	4e	-0.12467(7)	0.62962(6)	-0.00525(4)	0.0356(2)
Cs7	4e	0.85224(7)	0.75246(7)	0.25130(4)	0.0360(2)
Cs8	4e	-0.03704(7)	0.86325(6)	0.01724(4)	0.0339(2)
Cs9	4e	0.03429(7)	0.50620(6)	-0.11306(4)	0.0353(2)
Cs10	4e	0.78462(8)	0.87738(6)	0.13266(4)	0.0381(2)
Cs11	4e	0.27552(8)	0.87592(7)	-0.10828(4)	0.0425(2)
Cs12	4e	0.09552(7)	0.66429(8)	0.24757(4)	0.0380(2)
Cs13	4e	0.32164(7)	0.63481(7)	-0.11692(5)	0.0414(2)
Cs14	4e	0.46600(7)	0.54771(8)	0.10751(4)	0.0416(2)

Table 9.2 continued

Atom	Site	x	y	z	U_{eq}
Cs15	4e	0.21356(7)	0.58567(7)	0.11660(4)	0.0392(2)
Cs16	4e	-0.23657(9)	0.93279(7)	-0.14100(4)	0.0431(2)
Cs17	4e	0.0475(1)	0.91028(7)	0.24770(5)	0.0477(3)
Cs18	4e	0.8697(1)	0.52675(7)	0.25424(4)	0.0463(3)
Cs19	4e	0.03322(8)	0.9550(1)	-0.10456(5)	0.0517(3)
Cs20	4e	0.4767(1)	0.00164(8)	0.10476(8)	0.0672(5)
Cs21	4e	0.6640(2)	0.8544(1)	-0.00828(6)	0.0715(5)
Cs22	4e	-0.29445(7)	0.66533(6)	-0.13420(4)	0.0367(2)
In1	4e	0.5287(1)	0.77940(9)	0.16664(5)	0.0422(3)
In2	4e	0.58373(9)	0.62518(8)	0.25335(5)	0.0388(2)
In3	4e	0.39333(9)	0.69078(9)	0.23686(5)	0.0429(3)
In4	4e	-0.0501(1)	0.74516(9)	-0.15291(5)	0.0427(3)
In5	4e	0.59424(9)	0.80058(9)	0.28078(6)	0.0450(3)
In6	4e	0.3973(1)	0.87593(9)	0.24565(6)	0.0452(3)
Si1	4e	0.9533(2)	0.7175(2)	0.1251(1)	0.0140(4)
O11	4e	0.9256(9)	0.6423(8)	0.1689(5)	0.037(2)
O12	4e	0.9862(9)	0.8010(9)	0.1605(5)	0.042(3)
O13	4e	0.0416(9)	0.6829(7)	0.0913(5)	0.038(2)
O14	4e	0.8604(9)	0.7367(8)	0.0847(5)	0.038(2)
Si2	4e	0.2994(2)	0.5241(2)	-0.0046(1)	0.0166(5)
O21	4e	0.3806(7)	0.5000(6)	-0.0437(4)	0.025(2)
O22	4e	0.2992(7)	0.4581(6)	0.0470(4)	0.026(2)
O23	4e	0.1980(7)	0.5197(6)	-0.0394(4)	0.026(2)
O24	4e	0.3175(7)	0.6189(6)	0.0194(4)	0.028(2)
Si3	4e	0.2029(2)	0.9636(2)	0.0117(2)	0.0178(5)
O31	4e	0.1215(8)	0.9932(6)	0.0509(4)	0.031(2)
O32	4e	0.1848(7)	0.8649(5)	-0.0053(4)	0.028(2)
O33	4e	0.1986(8)	0.0207(6)	-0.0428(4)	0.029(2)
O34	4e	0.3043(8)	0.9744(7)	0.0446(5)	0.036(2)
Si4	4e	0.4962(2)	0.2108(2)	0.1306(2)	0.0201(5)
O41	4e	0.5510(8)	0.1432(7)	0.1724(4)	0.031(2)
O42	4e	0.4982(8)	0.3013(7)	0.1601(6)	0.038(3)
O43	4e	0.3884(8)	0.1790(8)	0.1219(5)	0.040(3)
O44	4e	0.547(1)	0.2101(8)	0.0755(5)	0.047(4)

Table 9.3. Atomic displacement parameters $U_{ij} / \text{\AA}^2$ for $\text{Cs}_{22}\text{In}_6(\text{SiO}_4)_4$.

Atom	U_{11}	U_{22}	U_{33}	U_{23}	U_{13}	U_{12}
Cs1	0.0276(3)	0.0257(3)	0.0303(3)	-0.0017(3)	0.0011(3)	0.0042(3)
Cs2	0.0277(3)	0.0217(3)	0.0433(4)	-0.0051(3)	-0.0008(3)	0.0016(3)
Cs3	0.0277(4)	0.0399(4)	0.0353(4)	-0.0102(3)	0.0057(3)	-0.0081(3)
Cs4	0.0346(4)	0.0337(4)	0.0323(4)	0.0023(3)	0.0036(3)	-0.0032(3)
Cs5	0.0316(4)	0.0225(3)	0.0417(4)	0.0028(3)	0.0004(3)	0.0051(3)
Cs6	0.0408(5)	0.0348(4)	0.0315(4)	-0.0018(3)	0.0061(3)	-0.0142(3)
Cs7	0.0378(4)	0.0439(5)	0.0264(4)	0.0027(3)	0.0024(3)	0.0103(4)
Cs8	0.0337(4)	0.0246(3)	0.0434(5)	-0.0005(3)	0.0024(3)	0.0042(3)
Cs9	0.0358(4)	0.0326(4)	0.0364(4)	-0.0041(3)	-0.0049(3)	0.0020(3)
Cs10	0.0475(5)	0.0344(4)	0.0331(4)	0.0102(3)	0.0080(4)	0.0097(4)
Cs11	0.0485(6)	0.0463(5)	0.0340(4)	0.0063(4)	0.0121(4)	0.0207(4)
Cs12	0.0328(4)	0.0542(6)	0.0272(4)	-0.0008(4)	0.0039(3)	0.0052(4)
Cs13	0.0342(4)	0.0479(6)	0.0415(5)	0.0227(4)	-0.0022(4)	-0.0043(4)
Cs14	0.0282(4)	0.0619(7)	0.0350(4)	-0.0160(4)	0.0049(3)	-0.0045(4)
Cs15	0.0358(4)	0.0459(5)	0.0366(4)	-0.0045(4)	0.0073(4)	0.0103(4)
Cs16	0.0508(6)	0.0436(5)	0.0352(4)	-0.0105(4)	0.0044(4)	-0.0151(4)
Cs17	0.0716(8)	0.0341(5)	0.0368(5)	-0.0011(4)	-0.0003(5)	-0.0051(5)
Cs18	0.0678(7)	0.0375(5)	0.0337(4)	-0.0046(4)	0.0040(5)	-0.0150(5)
Cs19	0.0353(5)	0.0729(8)	0.0486(6)	-0.0290(6)	0.0136(4)	-0.0117(5)
Cs20	0.0499(7)	0.0383(6)	0.107(1)	-0.0289(7)	-0.0381(8)	0.0126(5)
Cs21	0.119(1)	0.0525(7)	0.0424(6)	0.0018(5)	0.0003(7)	-0.0498(9)
Cs22	0.0324(4)	0.0355(4)	0.0423(5)	0.0093(4)	0.0036(3)	0.0051(3)
In1	0.0479(6)	0.0443(6)	0.0346(5)	0.0085(5)	0.0044(5)	0.0034(5)
In2	0.0435(6)	0.0377(5)	0.0351(5)	0.0037(4)	0.0019(4)	0.0008(4)
In3	0.0346(5)	0.0525(7)	0.0417(6)	-0.0124(5)	0.0028(4)	-0.0138(5)
In4	0.0540(7)	0.0425(6)	0.0312(5)	0.0004(4)	0.0004(5)	-0.0008(5)
In5	0.0341(5)	0.0462(7)	0.0539(7)	-0.0127(6)	-0.0025(5)	-0.0083(5)
In6	0.0455(6)	0.0428(6)	0.0471(7)	0.0100(5)	0.0010(5)	0.0098(5)
Si1	0.016(1)	0.013(1)	0.014(1)	-0.0042(8)	0.0042(8)	-0.0027(8)
O11	0.045(6)	0.038(6)	0.027(5)	0.003(4)	-0.002(4)	-0.011(5)
O12	0.042(6)	0.046(7)	0.038(6)	-0.015(5)	-0.001(5)	-0.007(5)
O13	0.041(6)	0.025(5)	0.048(6)	-0.004(4)	0.006(5)	0.000(4)
O14	0.043(6)	0.036(6)	0.033(5)	0.005(4)	-0.002(4)	-0.006(5)
Si2	0.019(1)	0.014(1)	0.017(1)	0.0006(9)	-0.0001(9)	0.0012(9)
O21	0.028(4)	0.024(4)	0.022(4)	-0.001(3)	0.003(3)	0.001(3)
O22	0.028(4)	0.030(4)	0.020(4)	0.005(3)	0.000(3)	-0.001(3)
O23	0.023(4)	0.019(4)	0.036(5)	-0.003(3)	-0.009(3)	-0.001(3)
O24	0.029(4)	0.019(4)	0.037(5)	-0.008(3)	0.001(4)	0.000(3)
Si3	0.021(1)	0.014(1)	0.019(1)	-0.0010(9)	-0.001(1)	0.0010(9)
O31	0.033(5)	0.025(4)	0.034(5)	-0.005(4)	0.011(4)	0.005(4)
O32	0.032(5)	0.014(3)	0.036(5)	-0.001(3)	0.004(4)	0.001(3)
O33	0.038(5)	0.022(4)	0.025(4)	0.004(3)	-0.001(4)	0.002(3)
O34	0.028(5)	0.024(4)	0.052(6)	-0.005(4)	-0.016(4)	0.001(3)
Si4	0.022(1)	0.020(1)	0.019(1)	0.0001(1)	0.002(1)	0.002(1)
O41	0.039(5)	0.032(5)	0.022(4)	0.008(3)	0.001(4)	0.005(4)
O42	0.029(5)	0.028(5)	0.057(7)	-0.014(5)	-0.002(5)	0.003(4)
O43	0.028(5)	0.042(6)	0.048(7)	-0.012(5)	-0.012(4)	-0.004(4)
O44	0.069(9)	0.044(6)	0.032(5)	0.015(5)	0.028(6)	0.032(6)

Table 9.4. Selected bond distances / Å² and angles / ° of Cs₂₂In₆(SiO₄)₄.

Cs ₂₂ In ₆ (SiO ₄) ₄					
In1	– In5	2.952(2)	In2	– In5	2.914(2)
	– In3	3.067(2)		– In3	2.934(2)
	– In6	3.231(2)		– In1	3.354(2)
	– In2	3.354(2)			
In3	– In2	2.934(2)	In4	– In5	2.845(2)
	– In4	2.993(2)		– In3	2.993(2)
	– In6	2.997(2)		– In6	3.243(2)
	– In1	3.067(2)			
In5	– In4	2.845(2)	In6	– In3	2.997(2)
	– In2	2.914(2)		– In5	3.145(2)
	– In1	2.952(2)		– In1	3.231(2)
	– In6	3.145(2)		– In4	3.243(2)
Si1	– O11	1.70(1)	Si2	– O21	1.62(1)
	– O12	1.66(1)		– O22	1.67(1)
	– O13	1.67(1)		– O23	1.64(1)
	– O14	1.64(1)		– O24	1.66(1)
Si3	– O31	1.65(1)	Si4	– O41	1.67(1)
	– O32	1.66(1)		– O42	1.64(1)
	– O33	1.64(1)		– O43	1.63(1)
	– O34	1.63(1)		– O44	1.61(1)
	O – Si1 – O			O – Si2 – O	
O14 – Si1 – O12		111.1	O21 – Si2 – O23		108.7
O14 – Si1 – O13		111.5	O21 – Si2 – O24		109.7
O14 – Si1 – O11		108.1	O21 – Si2 – O22		110.7
O12 – Si1 – O13		110.0	O23 – Si2 – O24		109.9
O12 – Si1 – O11		108.0	O23 – Si2 – O22		109.1
O13 – Si1 – O11		108.0	O24 – Si2 – O22		108.7
	O – Si3 – O			O – Si4 – O	
O34 – Si3 – O32		110.4	O44 – Si4 – O42		113.5
O34 – Si3 – O33		109.5	O44 – Si4 – O43		111.9
O34 – Si3 – O31		108.6	O44 – Si4 – O41		107.8
O33 – Si3 – O32		109.3	O43 – Si4 – O42		109.0
O33 – Si3 – O31		110.1	O43 – Si4 – O41		106.1
O34 – Si3 – O32		110.4	O42 – Si4 – O41		108.2

A detailed analysis of the bond distances (Table 9.5) shows that the In₆ cluster is much more distorted than the corresponding Tl₆ polyanions [105, 182]. Thus, the [In₆]⁶⁻ cluster can be more precisely described as a condensation of three face sharing tetrahedra (Fig. 9.3a). As a consequence, In₆ polyhedra are *nido* type

clusters, according to Wade's notation [209]. Therefore, such isolated In_6 units would require $6 \times 4 + 4 = 28e$ (inert-electron pairs included), which is in conflict with the $24e$ available. In this regard, the present $[\text{In}_6]^{6-}$ cluster is very reminiscent to the well known family of $[\text{Tl}_6]^{6-}$ clusters [102, 105], where the distortion can be understood in terms of the Jahn–Teller theorem (Chapter 8.3). Thus, In_6 groups in the present compound provide a first example of so called “hypoelectronic” discrete indium clusters. Nevertheless, a thorough quantum chemical analysis has to be performed in order to understand the electronic structure of the extended solid as well as the separate cluster.

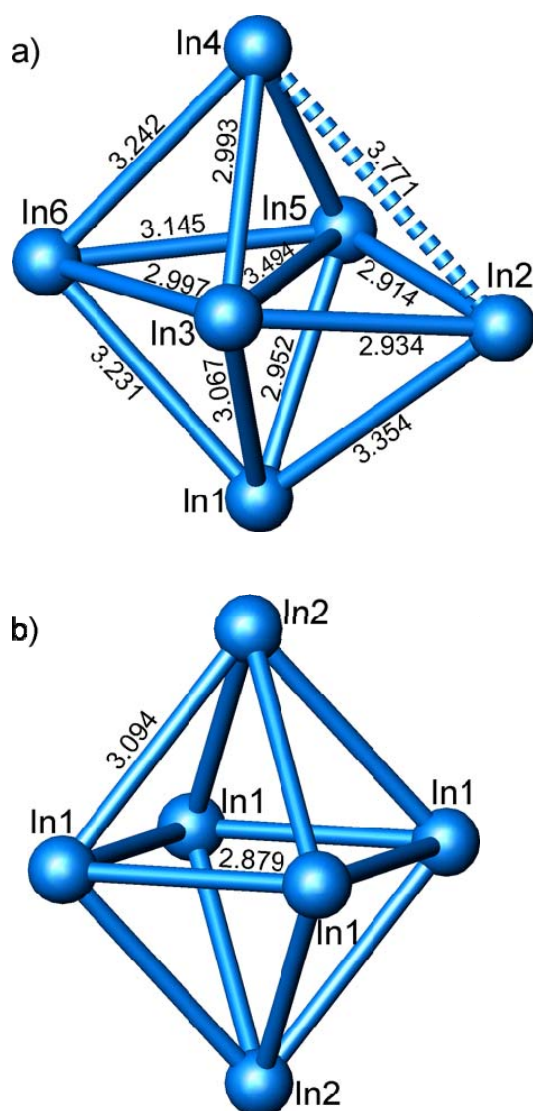


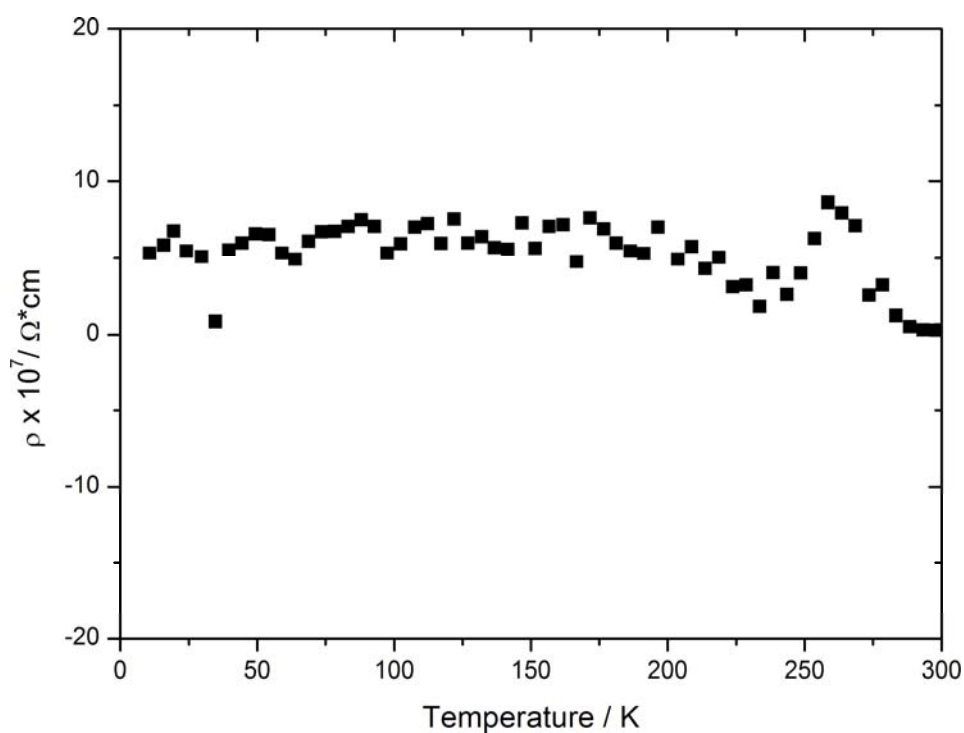
Figure 9.3. The $[\text{In}_6]^{6-}$ (a) and $[\text{In}_6]^{4-}$ (b) clusters in $\text{Cs}_{22}\text{In}_6(\text{SiO}_4)_4$ and Rb_2In_3 , respectively. Dotted line emphasizes the In–In distance, which is much too long as to be assigned to a homoatomic bond, Table 9.5.

Table 9.5. Bond distances of In₆ octahedra / Å in various compounds.

	Cs ₂₂ In ₆ (SiO ₄) ₄	Rb ₂ In ₃ [233]	Cs ₂ In ₃ [234]
In – In ^{a)}	2.998(2)	2.879(3) × 4	3.153(3) × 4
	2.994(2)	3.094(2) × 8	2.889(4) × 4
	2.934(2)		3.007(3) × 4
	3.068(2)		
	3.243(2)		
	3.231(2)		
	3.354(2)		
	2.845(2)		
	3.146(2)		
	2.952(2)		
	2.914(2)		
	“3.772(4)”		
	In – In ^{b)}	3.494(1)	4.659(3)
4.740(1)		4.072(1) × 2	4.616(8)
4.852(1)			

^{a)} – distances between indium atoms regarding the edges of the octahedron;

^{b)} – distances between indium atoms regarding the diagonals of the octahedron.

**Figure 9.4.** Temperature – dependent resistivity data of Cs₂₂In₆(SiO₄)₄.

9.3. Electrical Resistivity Measurements

Temperature-dependent resistivity measurements of $\text{Cs}_{22}\text{In}_6(\text{SiO}_4)_4$ were performed according to the general procedure of the *van der Pauw* method. The specific electrical resistivity is temperature independent and is in the range of $5\text{--}8 \times 10^7 \Omega\cdot\text{cm}$, which is typical for insulating materials (Fig. 9.4).

9.4. Conclusions

Using the successful concept in solid state chemistry of the substitution of similar elements in known compounds, a new indium cluster compound $\text{Cs}_{22}\text{In}_6(\text{SiO}_4)_4$ was synthesized and characterized. According to single crystal structure analysis the synthesized compound crystallizes in a new structure type (monoclinic $P2_1/n$ (no. 14), $a = 14.3716(8)$, $b = 16.144(1)$, $c = 24.947(2)$ Å, $\beta = 94.271(1)$, $Z = 4$), consisting of octahedral $[\text{In}_6]$ clusters, $[\text{SiO}_4]$ oxoanions and isolated cesium cations. $[\text{In}_6]^{6-}$ clusters can be described either as a strongly distorted octahedron or more precisely as a condensation of three face sharing tetrahedra, with the In–In distances ($\times 11$) ranging from 2.85 to 3.35 Å and one very long In–In distance of 3.77 Å. The shape of the orthosilicate(IV) anions deviates slightly from ideal tetrahedral geometry and are comparable to other known orthosilicates.

In contrast to Tl_6 polyhedra, which are usually referred to as *closo* clusters in shape, In_6 polyhedra in $\text{Cs}_{22}\text{In}_6(\text{SiO}_4)_4$ belong to the *nido* type of clusters. Nevertheless, similar to thallium clusters, $[\text{In}_6]^{6-}$ also cannot be described according to Wade's rules and thus provides a first example of a so-called “hypo-electronic” discrete indium cluster. A thorough quantum chemical analysis has to be performed in order to understand the electronic structure of the extended solid as well as the isolated cluster.

10. General Conclusions

During the past century many fundamental principles as well as concepts in chemistry were formulated and successfully used to understand and predict properties, in particular with their relation to the structure, of new materials. Among others, the concepts, which explain the stabilization of newly formed species, play an important role. Generally, the formation of closed shell configurations, either by opening a gap between the HOMO and LUMO electronic states (Jahn–Teller or Peierls distortion) or by following special electron counts (Zintl–Klemm concept and Wade's rules), leads to an electronic stabilization of chemical compounds. During the last decade another alternative mechanism has attracted attention, which also tends to a formation of closed shell systems, especially of heavy main group elements, namely spin–orbit coupling.

In the present work a systematic study of the quasi binary system BaAu – BaPt is reported. BaAu_{0.5}Pt_{0.5} was characterized exemplarily by single crystal X-ray diffraction analysis showing the formation of CrB type of structure. Also the homogeneity range for the CrB type of structure was established to extend from BaPt_{0.15}Au_{0.85} to BaPt_{0.90}Au_{0.10}. According to ESCA measurements, BaAu_{0.5}Pt_{0.5} can be formulated as [Ba²⁺·0.5e⁻][Au^{-0.5}·Pt²⁻_{0.5}] showing the transition of charge from electropositive barium to electronegative gold and platinum, which is in principal accordance with the Zintl–Klemm concept.

With the help of thorough quantum chemical analysis, on both, the extended solid and excised charge neutral molecular units, clearly show that a closed-shell electronic system in accordance with the magnetic properties (diamagnetic) is achieved for the highly symmetric tetrahedral star ([Tl₈]⁶⁻ cluster) in newly synthesized and characterized Cs₁₈Tl₈O₆ only if spin–orbit coupling is taken into account. For the same [Tl₈]⁶⁻ cluster contained in Cs₈Tl₈O, but crystallizing in a different structure, the correct structure is already reproduced on the scalar relativistic level and can be understood in terms of the Jahn–Teller theorem.

Furthermore, it is noteworthy, that in contrast to the known Zintl–Klemm concept or Wade's rules, where the explanation of structure stability is based on considering isolated clusters, the quantum mechanical treatments applied in present work were done regarding the $[\text{Tl}_8]^{6-}$ clusters embedded in the solid. Such a way of treatment is still unconventional, however, much more appropriate. The formation of regular octahedral $[\text{Tl}_6]^{6-}$ clusters in newly synthesized $\text{Cs}_4\text{Tl}_2\text{O}$ represents a second example of the formation of closed shell electronic structure, which can be explained only if spin–orbit coupling is considered during performing quantum mechanical analysis.

The approach to generate new thallium ions by introducing additional anionic species (e.g. SiO_4^{4-}), which increases the compositional and structural degrees of freedom, has led to formation of new thallium cluster compounds $\text{Cs}_{10}\text{Tl}_6\text{TtO}_4$ ($\text{Tt} = \text{Si}, \text{Ge}$) and $\text{Cs}_{10}\text{Tl}_6\text{SnO}_3$. The presence of Sn atom in $\text{Cs}_{10}\text{Tl}_6\text{SnO}_3$ in an oxidation state of 2+ reveal further evidence that “hypoelectronic” $[\text{Tl}_6]^{6-}$ cluster does not require additional electrons and is intrinsically stable.

Following another successful concept in solid state chemistry is the substitution of similar elements in known compounds, first steps in exploring the K–Tl–O and Cs–In–Si–O systems have been done. $\text{K}_{21}\text{Tl}_{22}\text{O}_2$ and $\text{Cs}_{22}\text{In}_6(\text{SiO}_4)_4$ were found as new compounds. The presence of two different at least in shape $[\text{Tl}_{11}]$ units in the structure of $\text{K}_{21}\text{Tl}_{22}\text{O}_2$ is quite unusual. The first isolation of covalently bonded homoatomic $[\text{In}_6]^{6-}$ clusters in $\text{Cs}_{22}\text{In}_6(\text{SiO}_4)_4$ shows the similarity of chemistry of indium to the chemistry of thallium and opens promising prospects for synthetic chemistry.

Part IV.

Summary

11. Abstract

11.1. Alkaline-Earth Metal Auride Platinides

All investigated alkaline-earth metal gold platinides have been synthesized by reaction of the corresponding mixtures of the pure elements at 1223 K in an argon atmosphere, and characterized by single-crystal X-ray analysis as well as by magnetic susceptibility and electric resistivity measurements. The new compounds ($\text{BaAu}_{0.5}\text{Pt}_{0.5}$, $\text{SrAu}_{0.5}\text{Pt}_{0.5}$, $\text{CaAu}_{0.5}\text{Pt}_{0.5}$) are isostructural and crystallize in the CrB type of structure ($\text{BaAu}_{0.5}\text{Pt}_{0.5}$: *Cmcm* (no. 63), $a = 4.3915(5)$, $b = 11.915(1)$, $c = 4.7920(5)$ Å, $Z = 4$; $\text{SrAu}_{0.5}\text{Pt}_{0.5}$: *Cmcm* (no. 63), $a = 4.262(1)$, $b = 11.435(3)$, $c = 4.632(1)$ Å, $Z = 4$; $\text{CaAu}_{0.5}\text{Pt}_{0.5}$: *Cmcm* (no. 63), $a = 3.9858(4)$, $b = 10.920(1)$, $c = 4.5249(5)$ Å, $Z = 4$), where the noble metals are randomly distributed over the centers of trigonal prisms formed by the alkaline earth metal atoms. All three intermetallics are poor metallic conductors and exhibit diamagnetic behaviour.

Phase equilibria in the quasibinary system BaAu—BaPt have been investigated by X-ray powder diffraction. Depending on composition, three structure types occur, the FeB type for BaAu, and NiAs for BaPt, while the CrB type of structure is adopted in-between. The homogeneity range for the CrB type of structure was established to extend from $\text{BaPt}_{0.15}\text{Au}_{0.85}$ to $\text{BaPt}_{0.90}\text{Au}_{0.10}$. The respective lattice parameters vary linearly, in accordance with *Vegard's law*.

The ESCA results demonstrate that the solid solution of Au and Pt with Ca or Sr is accompanied by an almost vanishing electron transfer. This is in striking contrast to findings on isostructural $\text{BaAu}_{0.5}\text{Pt}_{0.5}$. In the latter, the shifts of the $\text{Au}(4f_{7/2})$ and $\text{Pt}(4f_{7/2})$ levels as recorded with ESCA indicate a significant electron transfer from Ba to both of the noble metals which each thus adopt an anionic character. Thus, different from the alkali metal aurides, in which the anionic character of gold varies gradually with the kind of alkali metal [76], in the alkaline

earth auride platinides a discontinuity seems to occur when moving from Ba to the lighter homologues Sr and Ca. Thus $\text{BaAu}_{0.5}\text{Pt}_{0.5}$ can be formulated as $[\text{Ba}^{2+} \cdot 0.5\text{e}^-] \cdot [\text{Au}_{0.5}^- \cdot \text{Pt}_{0.5}^{2-}]$, while $\text{SrAu}_{0.5}\text{Pt}_{0.5}$ and $\text{CaAu}_{0.5}\text{Pt}_{0.5}$ both have intermetallic character, showing a negligible electron transfer from alkaline earth metals to the noble metals.

11.2. Ternary Alkali Metal Oxothallides

$\text{Cs}_{18}\text{Tl}_8\text{O}_6$

$\text{Cs}_{18}\text{Tl}_8\text{O}_6$ was synthesized reacting the binary compounds CsTl and Cs_2O at 573 K, followed by slow cooling to room temperature, in arc-welded tantalum ampoules. According to single crystal X-ray analyses, the compounds crystallize in new structure types (cubic space group $I23$ (no. 197), $a = 13.3724(3)$ Å, $Z = 2$). $\text{Cs}_{18}\text{Tl}_8\text{O}_6$ contains isolated $[\text{Tl}_8]^{6-}$ units with the shape of a tetrahedral star, a so-called *stella quadrangula*. Furthermore, cesium and oxygen constitute a three-dimensional network of corner and edge sharing octahedra $\infty^3[\text{OCs}_{6/2}]^+$. The structure of $\text{Cs}_{18}\text{Tl}_8\text{O}_6$ is related to the structure of γ -brass, where the cesium and thallium atoms occupy the positions of Zn and Cu ($\text{Cs}_{24}\text{Cs}_{12}\text{Tl}_8\text{Tl}_8 = \text{Zn}_{24}\text{Cu}_{12}\text{Zn}_8\text{Cu}_8$) and can be denoted as another novel “stuffed” γ -brass structure type.

The Tl–Tl separation within the $[\text{Tl}_8]^{6-}$ cluster is equal to 3.111 Å, while the shortest distance between thallium atoms in the inner tetrahedron of the tetrahedral star is equal to 3.382 Å. The angles between thallium atoms in both inner and outer tetrahedra $\angle \text{Tl–Tl–Tl}$ is equal to 60° , thus forming two ideal interpenetrating tetrahedra.

The electronic structure of the extended solid and of excised Cs_6Tl_8 clusters has been examined by relativistic density functional calculations including spin–orbit coupling. $\text{Cs}_{18}\text{Tl}_8\text{O}_6$ comprises a clusteranion $[\text{Tl}_8]^{6-}$ in the shape of a tetrahedral star. An isoelectronic cluster has been found previously in $\text{Cs}_8\text{Tl}_8\text{O}$, however, with the shape of a parallelepiped. Both clusteranions can be derived from a homocubane unit by displacive distortions. It has been shown by quantum

mechanical analyses that the closed-shell electronic structure of the parallelepiped is the result of a Jahn–Teller distortion, while in contrast the tetrahedral star in $\text{Cs}_{18}\text{Tl}_8\text{O}_6$ would still exhibit an open-shell degenerate HOMO within a scalar relativistic approximation. Only if spin–orbit coupling is considered, a closed-shell electronic system is obtained in accordance with the diamagnetic behavior of $\text{Cs}_{18}\text{Tl}_8\text{O}_6$.

$\text{Cs}_4\text{Tl}_2\text{O}$

$\text{Cs}_4\text{Tl}_2\text{O}$ was synthesized reacting the binary compounds CsTl and Cs_2O at 573 K, followed by slow cooling to room temperature. According to single-crystal X-ray analysis, the compound crystallizes in a new structure type (trigonal, space group $R\bar{3}m$ (no. 166), $a = 11.986(1)$, $c = 20.370(2)$ Å, $Z = 9$). It consists of isolated $[\text{Tl}_6]^{6-}$ octahedra, being *regular* with respect to the equality of all 3 main diagonals (4.546(5) Å), and of the edges (3.230(1) Å ($\times 6$) and 3.200(1) Å ($\times 6$)), and of $[\text{Cs}_{12}\text{O}_3]^{6+}$ triple octahedra extending along the c direction.

Octahedral $[\text{Tl}_6]$ clusters that have a negative charge of -8 form nearly regular octahedra and are electron precise in the sense of Wade's rules. In contrast, examples of hypoelectronic $[\text{Tl}_6]^{6-}$ known thus far all comprise octahedral clusters that are compressed along one of the fourfold axes. Surprisingly, the new compound $\text{Cs}_4\text{Tl}_2\text{O}$ contains virtually regular $[\text{Tl}_6]^{6-}$ clusters.

The electronic structure of $\text{Cs}_4\text{Tl}_2\text{O}$ has been examined by relativistic density functional calculations including spin–orbit coupling and has been compared to the one of $\text{Rb}_{10}\text{Tl}_6\text{O}_2$, which exhibits a highly distorted $[\text{Tl}_6]^{6-}$ octahedra. In the latter case the closed-shell electronic structure is the result of a Jahn–Teller distortion. In contrast, the regular octahedron in $\text{Cs}_4\text{Tl}_2\text{O}$ corresponds to a closed-shell configuration, in agreement with diamagnetic properties measured; however, this can only be explained if spin–orbit coupling is considered.

$\text{K}_{21}\text{Tl}_{22}\text{O}_2$

$\text{K}_{21}\text{Tl}_{22}\text{O}_2$ was prepared by reacting potassium with thallium and K_2O in an argon atmosphere at 773 K followed by cooling to room temperature at a rate of

~200 K/h, sealed in a tantalum tube under argon with an arc welder. According to single crystal X-ray analysis $\text{K}_{21}\text{Tl}_{22}\text{O}_2$ crystallizes in a novel structure type (trigonal $P3m1$ (no. 156), $a = 11.0650(3)$, $c = 15.2541(4)$ Å, $Z = 1$) consisting of two differently shaped isolated $[\text{Tl}_{11}]$ anionic units, OK_6 octahedra and isolated potassium cations. In general, the structure of the discussed compound is related to both NiAs and Wurtzite (ZnS) structure types in the sense that $[\text{Tl}_{11}]^{7-}$ clusters occupy octahedral voids, which are formed by OK_6 octahedra (*hcp* type packing), similar to those in NiAs while the other $[\text{Tl}_{11}]$ units are located in tetrahedral voids similar to those in the Wurtzite structure type.

One of the two, $[\text{Tl}_{11}]^{7-}$ cluster, had already been previously observed and has been denoted as hypoelectronic. This cluster can be described as a bipyramid of thallium atoms, where cell faces are capped by additional thallium atoms. The structure of the second thallium cluster is also characterized by a bipyramid, where three upper faces are capped by three additional thallium atoms while the three additional Tl atoms are located on the same side, capping the three edges. The intercluster Tl–Tl distances are in the range of 3.06–3.35 Å, comparable to those in other known $[\text{Tl}_{11}]$ clusters. The difference in shape of both $[\text{Tl}_{11}]$ clusters as well as of the formal charge one can only be understood by performing a thorough quantum chemical analysis of the electronic structure of $\text{K}_{21}\text{Tl}_{22}\text{O}_2$. According to the magnetic measurements $\text{K}_{21}\text{Tl}_{22}\text{O}_2$ is diamagnetic.

11.3. Cesium Oxotetrelate-Thallides

$\text{Cs}_{10}\text{Tl}_6\text{TtO}_4$ (Tt = Si, Ge) and $\text{Cs}_{10}\text{Tl}_6\text{SnO}_3$ have been synthesized for the first time by reacting appropriate starting materials at 623–673 K, followed by fast cooling or quenching to room temperature, in arc-welded tantalum ampoules. The synthesized compounds are extremely sensitive to moisture and air. According to the DSC measurements as well as high-temperature powder diffraction X-ray analysis measurements, $\text{Cs}_{10}\text{Tl}_6\text{SiO}_4$ is stable up to 573 K, $\text{Cs}_{10}\text{Tl}_6\text{GeO}_4$ up to 483 K and $\text{Cs}_{10}\text{Tl}_6\text{SnO}_3$ at least up to 623 K. According to single-crystal X-ray analyses, the compounds crystallize in new structure types, consisting of octahedral $[\text{Tl}_6]^{6-}$ clusters, which can be characterized as distorted octahedra compressed along one of the 4-fold axes of an originally unperturbed octahedron, $[\text{SiO}_4]^{4-}$,

$[\text{GeO}_4]^{4-}$ or $[\text{SnO}_3]^{4-}$ anions, and isolated cesium cations. The oxotetrelate thallides can be regarded as ‘double salts’, consisting of Cs_6Tl_6 on one hand and respective oxosilicates, -germanates and -stannates on the other, showing almost no any direct interaction between the two anionic moieties, as might be expressed e.g. by the formula $[\text{Cs}_6\text{Tl}_6][\text{Cs}_4\text{SiO}_4]$.

In contrast to the Si and Ge compounds, where the oxidation state of the tetrel atom is unambiguously 4+, for the threefold coordinated Sn atom in $\text{Cs}_{10}\text{Tl}_6\text{SnO}_3$ an oxidation state of 2+ has to be assumed. Thus, the latter reveal further evidence that the so called “hypoelectronic” $[\text{Tl}_6]^{6-}$ cluster does not require additional electrons and is intrinsically stable. The distortion of $[\text{Tl}_6]^{6-}$ can be understood in terms of the Jahn–Teller theorem. According to magnetic measurements all three presented oxotetrelate-thallides are diamagnetic.

11.4. Cesium Oxosilicate-Indide

$\text{Cs}_{22}\text{In}_6(\text{SiO}_4)_4$ was prepared by reacting appropriate starting materials at 673 K, followed by fast cooling at a rate of 200 K/h, in an arc-welded a tantalum ampoule. The synthesized compound is extremely sensitive to moisture and air. According to DSC as well as high-temperature powder X-ray analysis measurements, $\text{Cs}_{22}\text{In}_6(\text{SiO}_4)_4$ is stable at least up to 723 K. According to single-crystal X-ray analysis, the compound crystallizes in a novel structure type, consisting of octahedral $[\text{In}_6]$ clusters, $[\text{SiO}_4]$ oxoanions and isolated cesium cations. The cesium oxosilicate indide can be regarded as ‘double salt’, consisting of Cs_6In_6 on one side and the oxosilicate $\text{Cs}_{16}[\text{SiO}_4]_4$ ($4 \times \text{Cs}_4\text{SiO}_4$) on the other, showing almost not any direct interaction between the two anionic moieties, as might be expressed by the formula $[\text{Cs}_6\text{In}_6][\text{Cs}_{16}\text{Si}_4\text{O}_{16}]$.

The In_6 cluster is much more distorted than the known Tl_6 polyanions and can be more precisely described as a condensation of three face sharing tetrahedra, representing *nido* type clusters. Nevertheless the latter cannot be understood with known Wade's rules and thus is described as a first example of a hypoelectronic discrete indium cluster. The present $[\text{In}_6]^{6-}$ cluster is very reminiscent of the well-known family of $[\text{Tl}_6]^{6-}$ clusters, where the distortion can be understood in terms of the Jahn–Teller theorem.

Part V.

Zusammenfassung

12. Zusammenfassung

12.1. Erdalkalimetall-Auridplatinide

Alle untersuchten Erdalkalimetall-Auridplatinide wurden durch Reaktion von entsprechenden Mischungen der reinen Elemente bei 1223 K unter Argon Atmosphäre erhalten, und durch Einkristall-Röntgenstrukturanalyse sowie durch magnetische Suszeptibilitäts- und elektrische Widerstandsmessungen charakterisiert. Die neuen Verbindungen ($\text{BaAu}_{0.5}\text{Pt}_{0.5}$, $\text{SrAu}_{0.5}\text{Pt}_{0.5}$, $\text{CaAu}_{0.5}\text{Pt}_{0.5}$) sind isotruktuell und kristallisieren im CrB-Strukturtyp ($\text{BaAu}_{0.5}\text{Pt}_{0.5}$: *Cmcm* (no. 63), $a = 4.3915(5)$, $b = 11.915(1)$, $c = 4.7920(5)$ Å, $Z = 4$; $\text{SrAu}_{0.5}\text{Pt}_{0.5}$: *Cmcm* (no. 63), $a = 4.262(1)$, $b = 11.435(3)$, $c = 4.632(1)$ Å; $Z = 4$; $\text{CaAu}_{0.5}\text{Pt}_{0.5}$: *Cmcm* (no. 63), $a = 3.9858(4)$, $b = 10.920(1)$, $c = 4.5249(5)$ Å; $Z = 4$), wobei die Edelmetalle statistisch auf die Zentren der trigonalen Prismen verteilt sind, welche aus den Erdalkalimetallen gebildet werden. Alle drei intermetallischen Phasen sind schlechte metallische Leiter und weisen diamagnetisches Verhalten auf.

Die Phasengleichgewichte im quasibinären BaAu—BaPt System wurden durch Röntgenpulverdiffraktometrie untersucht. Abhängig von der Zusammensetzung kommen drei Strukturtypen vor, der FeB-Typ für BaAu und die NiAs Struktur für BaPt, während der CrB-Strukturtyp im Bereich von $\text{BaPt}_{0.15}\text{Au}_{0.85}$ bis $\text{BaPt}_{0.90}\text{Au}_{0.10}$ beobachtet wurde. Die jeweiligen Gitterparameter ändern sich linear in Übereinstimmung mit Vegards Gesetz.

ESCA-Ergebnisse zeigen, dass feste Lösungen von Au und Pt mit Ca oder Sr von einem fast verschwindenden Elektronenübergang begleitet werden. Das steht erstaunlicherweise im Gegensatz zu den Entdeckungen bei $\text{BaAu}_{0.5}\text{Pt}_{0.5}$, welches in demselben Strukturtyp kristallisiert. In letzterer Verbindung, zeigen die mit ESCA Messungen bestimmte $\text{Au}(4f_{7/2})$ und $\text{Pt}(4f_{7/2})$ Verschiebungen einen signifikanten Elektronenübergang von Ba zu den beiden Edelmetallen auf, wobei sich der

anionische Charakter von Gold stufenweise mit der Art des Erdalkalimetalls ändert. In den Erdalkalimetall-Goldplatiniden scheint eine Unstetigkeit aufzutreten, wenn man von Ba zu den leichteren Homologen Sr und Ca wechselt. Deshalb kann $\text{BaAu}_{0.5}\text{Pt}_{0.5}$ als $[\text{Ba}^{2+} \cdot 0.5\text{e}^-] \cdot [\text{Au}^-_{0.5} \cdot \text{Pt}^{2-}_{0.5}]$ formuliert werden, während die beiden Verbindungen $\text{SrAu}_{0.5}\text{Pt}_{0.5}$ und $\text{CaAu}_{0.5}\text{Pt}_{0.5}$ einen intermetallischen Charakter und einen unerheblichen Elektronenübergang vom Erdalkalimetall zum Edelmetall zeigen.

12.2. Ternäre Alkalimetalloxothallide

$\text{Cs}_{18}\text{Tl}_8\text{O}_6$

$\text{Cs}_{18}\text{Tl}_8\text{O}_6$ wurde durch Reaktion der binären Verbindungen CsTl und Cs_2O in eingeschmolzenen Tantal-Ampullen bei 573 K mit anschließendem langsamem Abkühlen auf Raumtemperatur erhalten. Nach der Einkristall-Röntgenstrukturanalyse kristallisiert die Verbindung in einem neuartigen Strukturtyp (kubisch, Raumgruppe $I23$ (no. 197), $a = 13.3724(3) \text{ \AA}$, $Z = 2$). $\text{Cs}_{18}\text{Tl}_8\text{O}_6$ besteht aus isolierten $[\text{Tl}_8]^{6-}$ -Baueinheiten in Gestalt von Tetraedersternen, sogenannten *Stella Quadrangula*, sowie einem aus Cäsium und Sauerstoff gebildeten, dreidimensionalen Netzwerk von ecken- und kantenverknüpften $\infty^3[\text{OCs}_{6/2}]^+$ -Oktaedern. Die Struktur von $\text{Cs}_{18}\text{Tl}_8\text{O}_6$ steht in Zusammenhang mit der Struktur von γ -Messing, wobei die Cäsium- und Thallium-Atome die Zn- und Cu-Lagen besetzen ($\text{Cs}_{24}\text{Cs}_{12}\text{Tl}_8\text{Tl}_8 = \text{Zn}_{24}\text{Cu}_{12}\text{Zn}_8\text{Cu}_8$) und kann als ein neuartiger "gefüllter" γ -Messing Strukturtyp bezeichnet werden. Der Tl–Tl Abstand innerhalb der $[\text{Tl}_8]^{6-}$ Cluster ist 3.111 \AA , während der kürzeste Abstand zwischen den Thallium-Atomen im innen Tetraeder des Tetraedersterns gleich 3.382 \AA ist. Der Winkel zwischen Thallium-Atomen in beiden Tetraedern $\angle \text{Tl}–\text{Tl}–\text{Tl}$ ist 60° , somit werden zwei ideale, sich gegenseitig durchdringende Tetraeder gebildet.

Die elektronische Struktur des ausgedehnten Festkörpers und des isolierten Cs_6Tl_8 -Clusters wurde mit relativistischen DFT-Rechnungen einschließlich Spin-Bahn-Kopplung untersucht. $\text{Cs}_{18}\text{Tl}_8\text{O}_6$ enthält $[\text{Tl}_8]^{6-}$ -Clusteranionen in der Gestalt eines Tetraedersterns, ein isoelektronischer Cluster wurde zuvor in $\text{Cs}_8\text{Tl}_8\text{O}$ in

Gestalt eines Parallelepipeds gefunden. Die beiden Clusteranionen können von einem idealen Würfel durch displazive Verzerrungen abgeleitet werden. Die quantenmechanische Analyse zeigt, dass die abgeschlossene elektronische Struktur des Parallelepipeds durch eine Jahn–Teller-Verzerrung erreicht wird, während im Gegensatz dazu der Tetraederstern in $\text{Cs}_{18}\text{Tl}_8\text{O}_6$ weiterhin eine offene Schale des degenerierten HOMO innerhalb relativistischer Näherung besitzt. Ein abgeschlossenes elektronisches System, in Übereinstimmung mit dem diamagnetischen Verhalten von $\text{Cs}_{18}\text{Tl}_8\text{O}_6$, kann nur dann erhalten werden, wenn eine Spin–Bahn-Kopplung berücksichtigt wird.

$\text{Cs}_4\text{Tl}_2\text{O}$

$\text{Cs}_4\text{Tl}_2\text{O}$ wurde durch Reaktion der binären Verbindungen CsTl und Cs_2O bei 573 K und anschließendem langsamen Abkühlen auf Raumtemperatur erhalten. Nach Einkristall-Röntgenanalyse kristallisiert die Verbindung in einem neuen Strukturtyp (trigonal, Raumgruppe $R\bar{3}m$ (no. 166), $a = 11.986(1)$, $c = 20.370(2)$ Å, $Z = 9$). Sie besteht aus isolierten $[\text{Tl}_6]^{6-}$ -Oktaedern, welche als regulär bezeichnet werden können, da die 3 Hauptdiagonalen gleich lang sind (4.546(5) Å), mit Kantenlängen von 3.230(1) Å ($\times 6$) und 3.200(1) Å ($\times 6$), sowie aus $[\text{Cs}_{12}\text{O}_3]^{6+}$ -Tripeloktaedern, die in Richtung der c -Achse orientiert sind.

Die oktaedrischen $[\text{Tl}_6]^{6-}$ -Cluster tragen eine achtfach negative Ladung, sind nahezu unverzerrte Oktaeder und entsprechend den Wade-Regeln elektronenpräzise. Im Gegensatz dazu sind alle bekannten Beispiele von hypoelektronischen $[\text{Tl}_6]^{6-}$ -Oktaederclustern entlang einer der vierzähligen Achsen gestaucht. Erstaunlicherweise enthält die neue Verbindung $\text{Cs}_4\text{Tl}_2\text{O}$ praktisch reguläre $[\text{Tl}_6]^{6-}$ -Cluster.

Die elektronische Struktur von $\text{Cs}_4\text{Tl}_2\text{O}$ wurde mit relativistischen DFT-Rechnungen einschließlich Spin–Bahn-Kopplung untersucht und mit $\text{Rb}_{10}\text{Tl}_6\text{O}_2$ verglichen, in letzterer Verbindung liegen sehr stark verzerrte $[\text{Tl}_6]^{6-}$ -Oktaeder vor. In $\text{Rb}_{10}\text{Tl}_6\text{O}_2$ wird die abgeschlossene elektronische Struktur durch Jahn–Teller-Verzerrung erreicht. Im Gegensatz, dazu wird in $\text{Cs}_4\text{Tl}_2\text{O}$ die geschlossenschalige Konfiguration der regulärer Oktaeder, in Übereinstimmung mit den diamagneti-

schen Eigenschaften, nur dann erreicht, wenn Spin–Bahn-Kopplung berücksichtigt wird.

$K_{21}Tl_{22}O_2$

$K_{21}Tl_{22}O_2$ wurde durch Reaktion von Kalium mit Thallium und K_2O in Tantal-Ampullen bei 773 K und anschließendem Abkühlen auf Raumtemperatur (~ 200 K/h) dargestellt. Nach Einkristall-Röntgenstrukturanalyse kristallisiert $K_{21}Tl_{22}O_2$ in einem neuen Strukturtyp (trigonal, Raumgruppe $P3m1$ (no. 156), $a = 11.0650(3)$, $c = 15.2541(4)$ Å, $Z = 1$) und besteht aus zwei anionischen $[Tl_{11}]$ -Baueinheiten unterschiedlicher Gestalt, OK_6 -Oktaedern und isolierten Kalium-Kationen. Die Struktur der diskutierten Verbindung kann sowohl auf den NiAs- als auch auf den Wurtzit(ZnS)-Strukturtyp bezogen werden, wobei die $[Tl_{11}]^{7-}$ -Cluster die oktaedrischen Lücken besetzen, während die anderen $[Tl_{11}]$ -Baueinheiten in den tetraedrischen Lücken ähnlich wie im Wurtzit Strukturtyp liegen.

Eine Cluster-Einheit wurde schon zuvor beobachtet und wurde als hypoelektronischer $[Tl_{11}]^{7-}$ -Cluster bezeichnet. Dieser Cluster kann als Bipyramide von Thallium-Atomen beschrieben werden, wobei jede Fläche durch ein zusätzliches Thallium-Atom überdacht wird. Die Struktur des zweiten Thallium-Clusters kann auch als Bipyramide beschrieben werden, wobei die drei oberen Flächen mit drei zusätzlichen Thallium-Atomen überdacht werden, während die drei anderen zusätzlichen Tl-Atome auf der gleichen Seite liegen und die drei Kanten überkappen. Die Tl–Tl-Abstände sind im Bereich von 3.06–3.35 Å und vergleichbar mit denen in anderen bekannten $[Tl_{11}]$ -Clustern. Der geometrische Unterschied von beiden $[Tl_{11}]$ -Clustern sowie die Formalladung des zuvor noch nicht beobachteten Clusters können nur mit Hilfe einer zusätzlichen vollständigen quantenchemischen Analyse der elektronischen Struktur verstanden werden. Magnetische Messungen weisen diamagnetischen Charakter von $K_{21}Tl_{22}O_2$ auf.

12.3. Cäsium Oxotetrelate-Thallide

$Cs_{10}Tl_6TtO_4$ (Tt = Si, Ge) und $Cs_{10}Tl_6SnO_3$ wurden zum ersten Mal durch Reaktion der entsprechenden Ausgangsmaterialien in, unter Argon-Atmosphäre

abgeschmolzenen, Tantal-Ampullen bei 623–673 K und anschließendem schnellen Abkühlen, bzw. Abschrecken auf Raumtemperatur erhalten. Die dargestellten Verbindungen sind extrem luft- und feuchtigkeitsempfindlich. Nach DSC sowie HT-Röntgenpulverdiffraktometrischen Messungen, ist $\text{Cs}_{10}\text{Tl}_6\text{SiO}_4$ bis 573 K, $\text{Cs}_{10}\text{Tl}_6\text{GeO}_4$ bis 483 K und $\text{Cs}_{10}\text{Tl}_6\text{SnO}_3$ mindestens bis 623 K stabil. Nach Einkristall-Röntgenstrukturanalyse kristallisieren die Verbindungen in einem neuen Strukturtyp und bestehen aus oktaedrischen $[\text{Tl}_6]^{6-}$ -Clustern, welche als verzerrte Oktaeder bezeichnet werden können, da sie entlang einer der vierzähligen Achsen gestaucht sind, sowie aus $[\text{SiO}_4]^{4-}$, $[\text{GeO}_4]^{4-}$ oder $[\text{SnO}_3]^{4-}$ Anionen und isolierten Cäsium-Kationen. Die Oxotetrelat-Thallide können als ‘Doppelsalze’ bezeichnet werden, sie bestehen aus Cs_6Tl_6 Baueinheiten einerseits und entsprechenden Oxosilicaten, -germanaten und -stannaten andererseits. Zwischen den zwei anionischen Einheiten bestehen keine direkten Wechselwirkungen, was durch die Formel $[\text{Cs}_6\text{Tl}_6][\text{Cs}_4\text{SiO}_4]$ formuliert werden kann.

Im Gegensatz zu den Si- und Ge-Verbindungen mit der Oxidationstufe 4+ für das Tetrelatom, muss für das dreifach koordinierte Sn-Atom in $\text{Cs}_{10}\text{Tl}_6\text{SnO}_3$ die Oxidationstufe 2+ vorausgesetzt werden. Die Oxidationstufe 2+ ist ein weiterer Beweis dafür, dass der sogenannte “hypoelektronische” $[\text{Tl}_6]^{6-}$ -Cluster die zusätzlichen Elektronen nicht braucht und intrinsisch stabil ist. Die Verzerrung in $[\text{Tl}_6]^{6-}$ kann im Sinne des Jahn–Teller-Theorems verstanden werden. Alle drei Oxotetrelaten-Thallide weisen diamagnetischen Charakter auf.

12.4. Cäsium Oxosilicat-Indid

$\text{Cs}_{22}\text{In}_6(\text{SiO}_4)_4$ wurde durch Reaktion der entsprechenden Ausgangsmaterialien in, unter Argon-Atmosphäre abgeschmolzenen, Tantal-Ampullen bei 673 K und anschließendem schnellen Abkühlen auf Raumtemperatur (~200 K/h) erhalten. Die dargestellte Verbindung ist extrem luft- und feuchtigkeitsempfindlich. Nach DSC sowie HT-Röntgenpulverdiffraktometrischen Messungen ist $\text{Cs}_{22}\text{In}_6(\text{SiO}_4)_4$ mindestens bis 723 K stabil. Nach Einkristall-Röntgenstrukturanalyse kristallisiert die Verbindung in einem neuen Strukturtyp und besteht aus den oktaedrischen $[\text{In}_6]$ -Clustern, den $[\text{SiO}_4]$ -Oxoanionen und isolierten

Cäsium-Kationen. Das Cäsium-Oxosilicat-Indid kann als ‘Doppelsalz’ bezeichnet werden und besteht aus Cs_6In_6 einerseits und Oxosilicat $\text{Cs}_{16}[\text{SiO}_4]_4$ ($4 \times \text{Cs}_4\text{SiO}_4$) andererseits. Es zeigen sich fast keine direkten Wechselwirkungen zwischen den beiden anionischen Baueinheiten, was durch die Formel $[\text{Cs}_6\text{In}_6][\text{Cs}_{16}\text{Si}_4\text{O}_{16}]$ ausgedrückt werden kann.

Der In_6 -Cluster ist wesentlich stärker verzerrt als die bekannten Tl_6 -Polyanionen und kann besser als drei flächenverknüpfte Tetraeder beschrieben werden, er stellt einen *nido*-Typ Cluster dar. Dennoch kann dieser Cluster nicht in Übereinstimmung mit den Wade-Regeln verstanden werden und kann somit als erster hypoelektronischer diskreter Indium-Cluster bezeichnet werden. Der dargestellte $[\text{In}_6]^{6-}$ -Cluster erinnernd an die bekannte Familie der $[\text{Tl}_6]^{6-}$ -Cluster, deren Verzerrung im Sinne des Jahn–Teller-Theorems verstanden werden kann.

13. Literature

- [1] E. Schrödinger, *Phys. Rev.* **1926**, 28, 1049 – 1070.
- [2] A. Sommerfeld, *Ann. Phys.-Berlin* **1916**, 51, 1 – 94.
- [3] A. Sommerfeld, *Ann. Phys.-Berlin* **1916**, 51, 125 – 167.
- [4] P. A. M. Dirac, *Proc. R. soc. Lond. Ser. A-Contain. Pap. Math. Phys. Character* **1928**, 118, 351 – 361.
- [5] P. A. M. Dirac, *Proc. R. soc. Lond. Ser. A-Contain. Pap. Math. Phys. Character* **1928**, 117, 610 – 624.
- [6] P. A. M. Dirac, *Proc. R. soc. Lond. Ser. A-Contain. Pap. Math. Phys. Character* **1929**, 123, 714 – 733.
- [7] P. S. Bagus, Y. S. Lee and K. S. Pitzer, *Chem. Phys. Lett.* **1975**, 33, 408 – 411.
- [8] K. S. Pitzer, *Acc. Chem. Res.* **1979**, 12, 271 – 276.
- [9] I. P. Grant, *Adv. Phys.* **1970**, 19, 747 – 811.
- [10] P. Pyykkö and J. P. Desclaux, *Acc. Chem. Res.* **1979**, 12, 276 – 281.
- [11] M. Jansen, *Solid State Sci.* **2005**, 7, 1464 – 1474.
- [12] M. Jansen, *Chem. Soc. Rev.* **2008**, 37, 1824 – 1835.
- [13] P. Pyykkö, *Adv. Quantum Chem.* **1979**, 11, 353 – 409.
- [14] P. Pyykkö, *Chem. Rev.* **1988**, 88, 563 – 594.
- [15] P. Pyykkö, *Angew. Chem.* **2002**, 114, 3723 – 3728; *Angew. Chem., Int. Ed.* **2002**, 41, 3573 – 3578.
- [16] P. Pyykkö, *Angew. Chem.* **2004**, 116, 4512 – 4557; *Angew. Chem., Int. Ed.* **2004**, 43, 4412 – 4456.
- [17] P. Pyykkö, *Inorg. Chim. Acta* **2005**, 358, 4113 – 4130.
- [18] P. Pyykkö, *Chem. Soc. Rev.* **2008**, 37, 1967 – 1997.
- [19] J.-P. Desclaux, *At. Data Nucl. Data Tables* **1973**, 12, 311 – 406.
- [20] N. Bartlett, *Gold Bull.* **1998**, 31, 22 – 25.
- [21] P. A. Christiansen, W. C. Ermler and K. S. Pitzer, *Annu. Rev. Phys. Chem.* **1985**, 36, 407 – 432.
- [22] B. A. Heß, *Ber. Bunsen-Ges. Phys. Chem. Chem. Phys.* **1997**, 101, 1 – 10.
- [23] N. Kaltsoyannis, *J. Chem. Soc., Dalton Trans.* **1997**, 1 – 11.

- [24] P. Schwerdtfeger, *Heteroat. Chem.* **2002**, *13*, 578 – 584.
- [25] G. L. Malli (Ed.), *Relativistic Effects in Atoms, Molecules, and Solids*, NATO ASI Series, New York, **1983**.
- [26] P. Pyykkö, *Relativistic Theory of Atoms and Molecules: Part 1*, Springer, Berlin, **1986**.
- [27] P. Pyykkö, *Relativistic Theory of Atoms and Molecules: Part 2*, Springer, Berlin, **1993**.
- [28] P. Pyykkö, *Relativistic Theory of Atoms and Molecules: Part 3*, Springer, Berlin, **2000**.
- [29] P. Schwerdtfeger (Ed.), *Relativistic Electronic Structure Theory, Part 1: Fundamentals*, Elsevier Science B.V., Amsterdam, **2002**.
- [30] P. Schwerdtfeger (Ed.), *Relativistic Electronic Structure Theory, Part 2: Applications*, Elsevier Science B.V., Amsterdam, **2004**.
- [31] P. Pyykkö, *Database "RTAM"*. <http://rtam.csc.fi/>.
- [32] V. Kellö, M. Urban and A. J. Sadlej, *Chem. Phys. Lett.* **1996**, *253*, 383 – 389.
- [33] C. F. Kunz, C. Hättig and B. A. Heß, *Mol. Phys.* **1996**, *89*, 139 – 156.
- [34] A. Rutkowski and W. H. E. Schwarz, *Theor. Chim. Acta* **1990**, *76*, 391 – 410.
- [35] K. M. Mackay and R. A. Mackay, *Introduction to Modern Inorganic Chemistry, 5th ed.*, Stanley Thornes (Publishers) Ltd, Cheltenham, **2000**, p. 27.
- [36] T. Andersen, H. K. Haugen and H. Hotop, *J. Phys. Chem. Ref. Data* **1999**, *28*, 1511 – 1533.
- [37] P. Villars and L. D. Calvert, *Pearson's Handbook of Crystallographic Data for Intermetallic Phases, 2ed.*, ASM International, Ohio, **1991**.
- [38] W. Biltz and F. Weibke, *Z. Anorg. Allg. Chem.* **1938**, *236*, 12 – 23.
- [39] A. Sommer, *Nature* **1943**, *152*, 215 – 215.
- [40] G. Kienast, J. Verma and W. Klemm, *Z. Anorg. Allg. Chem.* **1961**, *310*, 143 – 169.
- [41] W. E. Spicer, A. H. Sommer and J. G. White, *Phys. Rev.* **1959**, *115*, 57 – 62.
- [42] U. Zachwieja, *Z. Anorg. Allg. Chem.* **1993**, *619*, 1095 – 1097.
- [43] P. O. Nilsson, C. Norris and L. Wallden, *Phys. Kondens. Materie* **1970**, *11*, 220 – 230.
- [44] C. Norris and L. Wallden, *Phys. Lett. A* **1969**, *A 30*, 247 – 248.
- [45] C. Norris and L. Wallden, *Phys. Status Solidi A* **1970**, *2*, 381 – 390.
- [46] W. E. Spicer, *Phys. Rev.* **1962**, *125*, 1297 – 1299.

- [47] G. K. Wertheim, R. L. Cohen, G. Crecelius, K. W. West and J. H. Wernick, *Phys. Rev. B* **1979**, *20*, 860 – 866.
- [48] J. Knecht, R. Fischer, H. Overhof and F. Hensel, *J. Chem. Soc., Chem. Commun.* **1978**, 905 – 906.
- [49] R. J. Batchelor, T. Birchall and R. C. Burns, *Inorg. Chem.* **1986**, *25*, 2009 – 2015.
- [50] J. Stanek, S. S. Hafner and F. Hensel, *Phys. Rev. B* **1985**, *32*, 3129 – 3133.
- [51] C. Feldmann and M. Jansen, *Angew. Chem.* **1993**, *105*, 1107 – 1108; *Angew. Chem., Int. Ed.* **1993**, *32*, 1049 – 1050.
- [52] A. Pantelouris, G. Küper, J. Hormes, C. Feldmann and M. Jansen, *J. Am. Chem. Soc.* **1995**, *117*, 11749 – 11753.
- [53] R. Dupree, D. J. Kirby, W. Freyland and W. W. Warren, *Phys. Rev. Lett.* **1980**, *45*, 130 – 133.
- [54] R. Dupree, D. J. Kirby and W. W. Warren, *Phys. Rev. B* **1985**, *31*, 5597 – 5603.
- [55] G. A. Tinelli and D. F. Holcomb, *J. Solid State Chem.* **1978**, *25*, 157 – 168.
- [56] *Origin, Version 8.0988*, **2009**.
- [57] N. E. Christensen, *Phys. Rev. B* **1985**, *32*, 207 – 228.
- [58] O. Fossgaard, O. Gropen, E. Eliav and T. Saue, *J. Chem. Phys.* **2003**, *119*, 9355 – 9363.
- [59] G. H. Grosch and K. J. Range, *J. Alloys Compd.* **1996**, *233*, 30 – 38.
- [60] G. H. Grosch and K. J. Range, *J. Alloys Compd.* **1996**, *233*, 39 – 43.
- [61] C. Koenig, N. E. Christensen and J. Kollar, *Phys. Rev. B* **1984**, *29*, 6481 – 6488.
- [62] T. L. Liu, *Phys. Rev. B* **1975**, *12*, 3008 – 3012.
- [63] H. Overhof, R. Fischer, M. Vulli and F. Hensel, *Ber. Bunsen-Ges. Phys. Chem.* **1976**, *80*, 871 – 874.
- [64] J. Robertson, *Phys. Rev. B* **1983**, *27*, 6322 – 6330.
- [65] T. Saue, K. Faegri, T. Helgaker and O. Gropen, *Mol. Phys.* **1997**, *91*, 937 – 950.
- [66] F. Hensel, *Angew. Chem.* **1980**, *92*, 598 – 611; *Angew. Chem., Int. Ed. Engl.* **1980**, *19*, 593 – 606.
- [67] F. Hensel, *Z. Phys. Chem. (Muenchen, Ger.)* **1987**, *154*, 201 – 219.
- [68] F. Hensel and G. Schönherr, *Metall (Berlin)* **1980**, *34*, 626 – 629.

- [69] H. Hoshino, R. W. Schmutzler and F. Hensel, *Phys. Lett. A* **1975**, *51*, 7 – 8.
- [70] A. Kempf and R. W. Schmutzler, *Ber. Bunsen-Ges. Phys. Chem. Chem. Phys.* **1980**, *84*, 5 – 9.
- [71] R. W. Schmutzler, H. Hoshino, R. Fischer and F. Hensel, *Ber. Bunsen-Ges. Phys. Chem. Chem. Phys.* **1976**, *80*, 107 – 113.
- [72] F. Wooten and G. A. Condas, *Phys. Rev.* **1963**, *131*, 657 – 659.
- [73] C. Feldmann and M. Jansen, *Z. Anorg. Allg. Chem.* **1995**, *621*, 201 – 206.
- [74] C. Feldmann and M. Jansen, *Z. Naturforsch., B: Chem. Sci.* **1996**, *51*, 607 – 608.
- [75] A. Band, A. Albu-Yaron, T. Livneh, H. Cohen, Y. Feldman, L. Shimon, R. Popovitz-Biro, V. Lyahovitskaya and R. Tenne, *J. Phys. Chem. B* **2004**, *108*, 12360 – 12367.
- [76] C. Feldmann and M. Jansen, *J. Chem. Soc., Chem. Commun.* **1994**, 1045 – 1046.
- [77] R. Erdmann, R. Wormuth and R. W. Schmutzler, *Mater. Sci. Forum* **1991**, *73*, 45 – 52.
- [78] C. Feldmann and M. Jansen, *Z. Anorg. Allg. Chem.* **1995**, *621*, 1907 – 1912.
- [79] A.-V. Mudring and M. Jansen, *Angew. Chem.* **2000**, *112*, 3194 – 3196; *Angew. Chem., Int. Ed.* **2000**, *39*, 3066 – 3067.
- [80] A.-V. Mudring, J. Nuss, U. Wedig and M. Jansen, *J. Solid State Chem.* **2000**, *155*, 29 – 36.
- [81] R. Wormuth and R. W. Schmutzler, *Thermochim. Acta* **1990**, *160*, 97 – 102.
- [82] A.-V. Mudring, *Ph.D. Thesis*, Rheinische Friedrich-Wilhelms-Universität, Bonn, **2001**.
- [83] W. J. Peer and J. J. Lagowski, *J. Am. Chem. Soc.* **1978**, *100*, 6260 – 6261.
- [84] T. H. Teherani, W. J. Peer, J. J. Lagowski and A. J. Bard, *J. Am. Chem. Soc.* **1978**, *100*, 7768 – 7770.
- [85] R. Jagannathan, D. B. Wallace and J. J. Lagowski, *Inorg. Chem.* **1985**, *24*, 113 – 114.
- [86] A.-V. Mudring, M. Jansen, J. Daniels, S. Krämer, M. Mehring, J. P. Ramalho, A. H. Romero and M. Parrinello, *Angew. Chem.* **2002**, *114*, 128 – 132; *Angew. Chem., Int. Ed.* **2002**, *41*, 120 – 124.
- [87] P. D. C. Dietzel and M. Jansen, *Chem. Commun.* **2001**, 2208 – 2209.

- [88] S. Krämer, M. Mehring, A. V. Mudring and M. Jansen, *J. Phys. Chem. B* **2003**, *107*, 4922 – 4926.
- [89] H. Nuss and M. Jansen, *Z. Naturforsch., B: Chem. Sci.* **2006**, *61*, 1205 – 1208.
- [90] H. Nuss and M. Jansen, *Angew. Chem.* **2006**, *118*, 4476 – 4479; *Angew. Chem., Int. Ed.* **2006**, *45*, 4369 – 4371.
- [91] A. Karpov, J. Nuss, U. Wedig and M. Jansen, *Angew. Chem.* **2003**, *115*, 4966 – 4969; *Angew. Chem., Int. Ed.* **2003**, *42*, 4818 – 4821.
- [92] A. Karpov, U. Wedig, R. E. Dinnebier and M. Jansen, *Angew. Chem.* **2005**, *117*, 780 – 783; *Angew. Chem., Int. Ed.* **2005**, *44*, 770 – 773.
- [93] J. Köhler, J. H. Chang, *Angew. Chem.* **2000**, *112*, 2077 – 2079; *Angew. Chem., Int. Ed.* **2000**, *39*, 1998 – 2000.
- [94] J. Köhler, J. H. Chang and M. H. Whangbo, *J. Am. Chem. Soc.* **2005**, *127*, 2277 – 2284.
- [95] J. Ghilane, C. Lagrost, M. Guilloux-Viry, J. Simonet, M. Delamar, C. Mangeney and P. Hapiot, *J. Phys. Chem. C* **2007**, *111*, 5701 – 5707.
- [96] A. Karpov, J. Nuss, U. Wedig and M. Jansen, *J. Am. Chem. Soc.* **2004**, *126*, 14123 – 14128.
- [97] A. Karpov, U. Wedig and M. Jansen, *Z. Naturforsch., B: Chem. Sci.* **2004**, *59*, 1387 – 1394.
- [98] C. H. L. Goodman, *J. Phys. Chem. Solids* **1958**, *6*, 305 – 314.
- [99] A. Karpov, M. Konuma and M. Jansen, *Chem. Commun.* **2006**, 838 – 840.
- [100] R. D. Hoffmann, R. Pottgen, G. A. Landrum, R. Dronskowski, B. Kunnen and G. Kotzyba, *Z. Anorg. Allg. Chem.* **1999**, *625*, 789 – 798.
- [101] J. D. Corbett, *Structural and Electronic Paradigms in Cluster Chemistry (Structure & Bonding)*, ed. D. M. P. Mingos, Springer-Verlag, Berlin, Germany, **1997**, p. 157 – 193.
- [102] J. D. Corbett, *Angew. Chem.* **2000**, *112*, 682 – 704; *Angew. Chem., Int. Ed.* **2000**, *39*, 670 – 690.
- [103] A. Karpov, *Ph.D. Thesis*, Universität, Stuttgart, **2006**.
- [104] A. Karpov and M. Jansen, *Angew. Chem.* **2005**, *117*, 7813 – 7816; *Angew. Chem., Int. Ed.* **2005**, *44*, 7639 – 7643.
- [105] A. Karpov and M. Jansen, *Chem. Commun.* **2006**, 1706 – 1708.
- [106] E. Zintl, *Angew. Chem.* **1939**, *52*, 1 – 6.
- [107] W. Klemm, *Proc. Chem. Soc.* **1958**, 329 – 341.

- [108] W. Klemm, *Festkörperchemie, Vol. 3*, ed. F. Sauter, Braunschweig: Vieweg, **1963**, p. 233 – 251.
- [109] H. Okamoto and T. B. Massalski, *Binary Alloys Phase Diagrams (Second Edition)*, ed. T. B. Massalski, ASM International, Materials Park, Ohio, **1990**, p. 414 – 416.
- [110] W. Schlenk and A. Thal, *Ber. Dtsch. Chem. Ges.* **1913**, *46*, 2840 – 2854.
- [111] G. Stoe, *Software Package Stoe Stadi P*, **1999**.
- [112] icdd in *PCPDFWIN 2.2*, **2000**.
- [113] H. M. Rietveld, *Acta Cryst.* **1967**, *22*, 151 – 152.
- [114] H. M. Rietveld, *J. Appl. Crystallogr.* **1969**, *2*, 65 – 71.
- [115] A. Le Bail, H. Duroy and J. L. Fourquet, *Mater. Res. Bull.* **1988**, *23*, 447 – 452.
- [116] A. A. Coelho, *TOPAS Version 3.0, Graphics based profile and structure analysis software*, **2005**.
- [117] K. Brandenburg, *DIAMOND — Visual Crystal Structure Information System, Version 3.2c*, **2009**.
- [118] E. Dowty, *ATOMS — a complete program for displaying atomic structures, version 6.3.4*, **2008**.
- [119] Bruker, *Bruker Suite, Version2008/3*, **2008**.
- [120] G. M. Sheldrick in *SADABS - Bruker AXS area detector scaling and absorption, Version 2008/1, Vol.* **2008**.
- [121] G. M. Sheldrick, *Acta Crystallogr., Sect. A: Found. Crystallogr.* **2008**, *64*, 112 – 122.
- [122] L. J. van der Pauw, *Philips Res. Rep.* **1958**, *13*, 1 – 9.
- [123] J. P. Suchet, *Electrical Conduction in Solid Materials*, Pergamon, Oxford, **1975**.
- [124] H. Lueken, *Magnetochemie*, B.G. Teubner, Stuttgart, Leipzig, **1999**.
- [125] N. W. Ashcroft and N. D. Mermin, *Solid State Physics*, Holt, Rinehart and Winston, Philadelphia, **1976**.
- [126] S. C. Sevov and J. D. Corbett, *Inorg. Chem.* **1992**, *31*, 1895 – 1901.
- [127] P. Hohenberg and W. Kohn, *Phys. Rev.* **1964**, *136*, B864 – B871.
- [128] W. Kohn and L. J. Sham, *Phys. Rev.* **1965**, *140*, A1133 – A1138.
- [129] R. Hoffmann, *J. Chem. Phys.* **1963**, *39*, 1397 – 1412.
- [130] R. Hoffmann, *J. Chem. Phys.* **1964**, *40*, 2474 – 2480.

- [131] J. P. Perdew, J. A. Chevary, S. H. Vosko, K. A. Jackson, M. R. Pederson, D. J. Singh and C. Fiolhais, *Phys. Rev. B* **1992**, *46*, 6671 – 6687.
- [132] J. P. Perdew, J. A. Chevary, S. H. Vosko, K. A. Jackson, M. R. Pederson, D. J. Singh and C. Fiolhais, *Phys. Rev. B* **1993**, *48*, 4978 – 4978.
- [133] A. D. Becke, *J. Chem. Phys.* **1992**, *96*, 2155 – 2160.
- [134] B. Hammer, K. W. Jacobsen and J. K. Norskov, *Phys. Rev. Lett.* **1993**, *70*, 3971 – 3974.
- [135] A. Zupan, J. P. Perdew and K. Burke, *Int. J. Quantum Chem.* **1997**, *61*, 835 – 845.
- [136] J. P. Perdew, K. Burke and Y. Wang, *Phys. Rev. B* **1996**, *54*, 16533 – 16539.
- [137] J. P. Perdew, *Electronic Structure of Solids '91*, ed. P. Ziesche, H. Eschrig, Akademie Verlag, Berlin, **1991**, p. 11.
- [138] J. P. Perdew, K. Burke and M. Ernzerhof, *Phys. Rev. Lett.* **1996**, *77*, 3865 – 3868.
- [139] J. C. Slater, *Phys. Rev.* **1937**, *51*, 0846 – 0851.
- [140] O. K. Andersen, *Phys. Rev. B* **1975**, *12*, 3060 – 3083.
- [141] E. Sjöstedt, L. Nordström and D. J. Singh, *Solid State Commun.* **2000**, *114*, 15 – 20.
- [142] A. H. MacDonald, W. E. Pickett and D. D. Koelling, *J. Phys. C: Solid State Phys.* **1980**, *13*, 2675 – 2683.
- [143] P. Blaha, K. Schwarz, G. K. H. Madsen, D. Kvasnicka and J. Luitz, *WIEN2k, An Augmented Plane Waves + Local Orbitals Program for Calculating Crystal Properties*, Karlheinz Schwarz, Techn. Universität Wien, Austria, **2001**.
- [144] J. Kuneš, P. Novák, R. Schmid, P. Blaha and K. Schwarz, *Phys. Rev. B* **2001**, *64*, 153102.
- [145] *TURBOMOLE V6.1*, University of Karlsruhe and Forschungszentrum Karlsruhe GmbH, TURBOMOLE GmbH, <http://www.turbomole.com>, **2009**.
- [146] M. K. Armbruster, F. Weigend, C. van Wuelen and W. Klopper, *Phys. Chem. Chem. Phys.* **2008**, *10*, 1748 – 1756.
- [147] R. F. W. Bader, *Atoms in Molecules: A Quantum Theory*, Oxford University Press, Oxford, **1990**.
- [148] G. Henkelman, A. Arnaldsson and H. Jonsson, *Comput. Mater. Sci.* **2006**, *36*, 354 – 360.

- [149] E. Sanville, S. D. Kenny, R. Smith and G. Henkelman, *J. Comput. Chem.* **2007**, *28*, 899 – 908.
- [150] M. Kohout, *Program DGrid, Version 4.4*, Radebeul, **2008**.
- [151] A. Savin, A. D. Becke, J. Flad, R. Nesper, H. Preuss and H. G. von Schnering, *Angew. Chem.* **1991**, *103*, 421 – 424; *Angew. Chem., Int. Ed.* **1991**, *30*, 409 – 412.
- [152] C. Gatti, *Z. Kristallogr.* **2005**, *220*, 399 – 457.
- [153] A. Savin, R. Nesper, S. Wengert and T. F. Fässler, *Angew. Chem.* **1997**, *109*, 1892 – 1918; *Angew. Chem., Int. Ed. Engl.* **1997**, *36*, 1808 – 1832.
- [154] A. Savin, O. Jepsen, J. Flad, O. K. Andersen, H. Preuss and H. G. von Schnering, *Angew. Chem.* **1992**, *104*, 186 – 188; *Angew. Chem., Int. Ed.* **1992**, *31*, 187 – 188.
- [155] B. Silvi and A. Savin, *Nature* **1994**, *371*, 683 – 686.
- [156] G. Brauer, *Handbuch der Präparativen Anorganischen Chemie*, vol. 2, Ferdinand Enke, Stuttgart, **1978**, p. 938 – 945.
- [157] J. D. Corbett and E. A. Leon-Escamilla, *J. Alloys Compd.* **2003**, *356*, 59 – 64.
- [158] G. Brauer, *Handbuch der Präparativen Anorganischen Chemie*, vol. 2, Ferdinand Enke, Stuttgart, **1978**, p. 953 – 954.
- [159] K. R. Tsai, P. M. Harris and E. N. Lassetre, *J. Phys. Chem.* **1956**, *60*, 338 – 344.
- [160] G. S. Smith and L. E. Alexander, *Acta Cryst.* **1963**, *16*, 462 – 471.
- [161] G. S. Smith and P. B. Isaacs, *Acta Cryst.* **1964**, *17*, 842 – 846.
- [162] W. H. Baur, *Acta Cryst.* **1956**, *9*, 515 – 520.
- [163] H. E. Swanson and E. Tatge, *Nat. Bur. Stand.* **1953**, *539*, 1 – 95.
- [164] W. J. Moore and L. Pauling, *J. Am. Chem. Soc.* **1941**, *63*, 1392 – 1394.
- [165] M. L. Fornasini, *J. Solid State Chem.* **1985**, *59*, 60 – 64.
- [166] S. Andersson and B. G. Hyde, *J. Solid State Chem.* **1974**, *9*, 92 – 101.
- [167] E. Parthé, *Acta Crystallogr. Sect. B-Struct. Commun.* **1976**, *32*, 2813 – 2818.
- [168] Details may be obtained from: Fachinformationszentrum Karlsruhe, D-76344 Eggenstein-Leopoldshafen (Germany), by quoting the respective Registry Number.
- [169] L. Vegard, *Z. Phys.* **1921**, *5*, 17 – 26.
- [170] A. R. Denton and N. W. Ashcroft, *Phys. Rev. A* **1991**, *43*, 3161 – 3164.

- [171] V. Saltykov, J. Nuss, M. Konuma and M. Jansen, *Z. Anorg. Allg. Chem.* **2009**, *635*, 70 – 75.
- [172] F. Merlo, *J. Less-Common Met.* **1982**, *86*, 241 – 246.
- [173] W. Harms, F. Burggraf, M. Daub, I. Durr and C. Rohr, *Z. Anorg. Allg. Chem.* **2008**, *634*, 2255 – 2266.
- [174] D. A. Hansen and J. F. Smith, *Acta Cryst.* **1967**, *22*, 836 – 845.
- [175] Z.-C. Dong and J. D. Corbett, *J. Am. Chem. Soc.* **1994**, *116*, 3429 – 3435.
- [176] Z.-C. Dong and J. D. Corbett, *Inorg. Chem.* **1996**, *35*, 1444 – 1450.
- [177] Z.-C. Dong and J. D. Corbett, *J. Am. Chem. Soc.* **1995**, *117*, 6447 – 6455.
- [178] Z.-C. Dong and J. D. Corbett, *J. Cluster Sci.* **1995**, *6*, 187 – 201.
- [179] D. P. Huang, Z.-C. Dong and J. D. Corbett, *Inorg. Chem.* **1998**, *37*, 5881 – 5886.
- [180] S. Kaskel and J. D. Corbett, *Inorg. Chem.* **2000**, *39*, 778 – 782.
- [181] Z.-C. Dong and J. D. Corbett, *J. Am. Chem. Soc.* **1993**, *115*, 11299 – 11303.
- [182] Z.-C. Dong and J. D. Corbett, *Inorg. Chem.* **1996**, *35*, 2301 – 2306.
- [183] Z.-C. Dong and J. D. Corbett, *Angew. Chem.* **1996**, *108*, 1073 – 1076; *Angew. Chem., Int. Ed.* **1996**, *35*, 1006 – 1009.
- [184] Z.-C. Dong and J. D. Corbett, *Inorg. Chem.* **1995**, *34*, 5042 – 5048.
- [185] J. D. Corbett, *Diverse naked clusters of the heavy main-group elements. Electronic regularities and analogies*, ed. D. M. P. Mingos, Springer-Verlag Berlin, Berlin 33, **1997**, pp. 157 – 193.
- [186] B. G. Hyde and S. Andersson, *Inorganic Crystal Structures*, John Wiley & Sons, New York, **1989**, p. 342 – 344.
- [187] R. D. Shannon and C. T. Prewitt, *Acta Crystallogr., Sect. B: Struct. Sci.* **1969**, *25*, 925 – 946.
- [188] P. Spiegelberg, *Arkiv foer Kemi, Mineralogi och Geologi* **1940**, *A14*, 1 – 2.
- [189] G. A. Marking and H. F. Franzen, *J. Am. Chem. Soc.* **1993**, *115*, 6126 – 6130.
- [190] P. Novák, http://www.wien2k.at/reg_user/textbooks/novak_lecture_on_spinorbit.ps.
- [191] B. Metz, M. Schweizer, H. Stoll, M. Dolg and W. J. Liu, *Theor. Chem. Acc.* **2000**, *104*, 22 – 28.
- [192] T. Leininger, A. Nicklass, W. Küchle, H. Stoll, M. Dolg and A. Bergner, *Chem. Phys. Lett.* **1996**, *255*, 274 – 280.

- [193] M. Jansen and U. Wedig, *Angew. Chem.* **2008**, *120*, 10176 – 10180; *Angew. Chem., Int. Ed.* **2008**, *47*, 10026 – 10029.
- [194] J. Meister and W. H. E. Schwarz, *J. Phys. Chem.* **1994**, *98*, 8245 – 8252.
- [195] D. Opalka, M. Segado, L. V. Poluyanov and W. Domcke, *Phys. Rev. A* **2010**, *81*, 042501.
- [196] A. D. Becke, *J. Chem. Phys.* **1993**, *98*, 5648 – 5652.
- [197] C. T. Lee, W. T. Yang and R. G. Parr, *Phys. Rev. B* **1988**, *37*, 785 – 789.
- [198] W. Carrillo-Cabrera, N. Caroca-Canales and H. G. von Schnering, *Z. Anorg. Allg. Chem.* **1994**, *620*, 247 – 257.
- [199] U. Wedig, V. Saltykov, J. Nuss and M. Jansen, *J. Am. Chem. Soc.* **2010**, *132*, 12458 – 12463.
- [200] V. Saltykov, J. Nuss, U. Wedig and M. Jansen, *Z. Anorg. Allg. Chem.* **2010**, *636*, 2040.
- [201] Z.-C. Dong and J. D. Corbett, *J. Am. Chem. Soc.* **1993**, *115*, 11299 – 11303.
- [202] A. Karpov and M. Jansen, *Chem. Commun.* **2006**, 1706 – 1708.
- [203] C. Feldmann and M. Jansen, *Z. Anorg. Allg. Chem.* **1995**, *621*, 201 – 206.
- [204] R. D. Shannon and C. T. Prewitt, *Acta Crystallogr., Sect. B* **1969**, *25*, 925 – 946.
- [205] Z.-C. Dong and J. D. Corbett, *J. Cluster Sci.* **1995**, *6*, 187 – 201.
- [206] Z.-C. Dong and J. D. Corbett, *Inorg. Chem.* **1996**, *35*, 1444 – 1450.
- [207] Z.-C. Dong and J. D. Corbett, *Inorg. Chem.* **1995**, *34*, 5042 – 5048.
- [208] E. Zintl and W. Dullenkopf, *Z. Phys. Chem. B-Chem. Elem. Aufbau. Mater.* **1932**, *16*, 195 – 205.
- [209] K. Wade, *Adv. Inorg. Chem. Radiochem.* **1976**, *18*, 1 – 66.
- [210] J. D. Corbett, *Inorg. Chem.* **2000**, *39*, 5178 – 5191.
- [211] Bruker Suite, Version 2008/3, Bruker AXS Inc., Madison, WI, USA, **2008**.
- [212] J. Nuss, N. Z. Ali and M. Jansen, *Acta Crystallogr. Sect. B-Struct. Commun.* **2007**, *63*, 719 – 725.
- [213] H. Wondratschek and U. Müller (Ed.), *International Tables for Crystallography, Vol. A1*, Dordrecht: Kluwer Academic Publishers, **2004**.
- [214] U. Müller, *Z. Anorg. Allg. Chem.* **2004**, *630*, 1519 – 1537.
- [215] H. Bärnighausen, *MATCH, Commun. Math. Chem.* **1980**, *9*, 139 – 175.
- [216] K. Bernet and R. Hoppe, *Z. Anorg. Allg. Chem.* **1990**, *589*, 129 – 138.

- [217] H. Völlenklee, A. Wittmann and H. Nowotny, *Monatsh. Chem.* **1968**, *99*, 1360 – 1371.
- [218] R. Hofmann and R. Hoppe, *Z. Anorg. Allg. Chem.* **1988**, *560*, 35 – 46.
- [219] K. Bernet, J. Kissel and R. Hoppe, *Z. Anorg. Allg. Chem.* **1991**, *593*, 17 – 34.
- [220] C. Hoch and C. Röhr, *Z. Anorg. Allg. Chem.* **2002**, *628*, 1541 – 1547.
- [221] E. Halwax and H. Völlenklee, *Monatsh. Chem.* **1985**, *116*, 1367 – 1376.
- [222] C. Hoch and C. Röhr, *Z. Naturforsch. (B)* **2001**, *56*, 1245 – 1256.
- [223] C. Röhr and P. Zönnchen, *Z. Anorg. Allg. Chem.* **1998**, *624*, 797 – 801.
- [224] C. Röhr, *Z. Anorg. Allg. Chem.* **1995**, *621*, 757 – 760.
- [225] B. Nowitzki and R. Hoppe, *Z. Anorg. Allg. Chem.* **1984**, *515*, 114 – 126.
- [226] G. Frisch, C. Hoch, C. Röhr, P. Zönnchen, K. D. Becker and D. Niemeier, *Z. Anorg. Allg. Chem.* **2003**, *629*, 1661 – 1672.
- [227] Y. N. Grin, Y. P. Yarmolyuk and E. I. Gladyshevskii, *Sov. Phys. Crystallogr.* **1982**, *27*, 413 – 417.
- [228] S. C. Sevov and J. D. Corbett, *J. Solid State Chem.* **1993**, *103*, 114 – 130.
- [229] J. T. Zhao and J. D. Corbett, *Inorg. Chem.* **1995**, *34*, 378 – 383.
- [230] S. C. Sevov and J. D. Corbett, *Inorg. Chem.* **1991**, *30*, 4875 – 4877.
- [231] W. Blase, G. Cordier, V. Müller, U. Haussermann, R. Nesper and M. Somer, *Z. Naturforsch. (B)* **1993**, *48*, 754 – 760.
- [232] W. Blase, G. Cordier and M. Somer, *Z. Kristallogr.* **1991**, *194*, 150 – 151.
- [233] S. C. Sevov and J. D. Corbett, *Z. Anorg. Allg. Chem.* **1993**, *619*, 128 – 132.
- [234] S. P. Yatsenko, K. A. Tschuntonow, A. N. Orlov, Y. P. Yarmolyuk and Y. N. Hryn, *J. Less-Common Met.* **1985**, *108*, 339 – 343.
- [235] S. C. Sevov and J. D. Corbett, *Inorg. Chem.* **1993**, *32*, 1612 – 1615.
- [236] G. Cordier and V. Müller, *Z. Kristallogr.* **1993**, *205*, 353 – 354.
- [237] B. Li and J. D. Corbett, *Inorg. Chem.* **2003**, *42*, 8768 – 8772.
- [238] M. Wendorff and C. Röhr, *Z. Anorg. Allg. Chem.* **2006**, *632*, 1792 – 1798.
- [239] B. Li and J. D. Corbett, *Inorg. Chem.* **2002**, *41*, 3944 – 3949.

Part VI.

Appendix A

A1. Cs₆Tl₈ Cluster Calculations

Table A1.1. Scalar relativistic (column 5 non-relativistic) unrestricted open shell Kohn-Sham calculations of the Cs₆Tl₈ cluster (PBE+functional).

symmetry constraint	O_h	T_d	T_d	T_d	T_d	D_{3d}	C_1 ³⁾
shape	cube	tetrahedral star	tetrahedral star	tetrahedral star	tetrahedral star	parallelepiped	parallelepiped
opt./expt. ¹⁾	opt.	expt.	opt.	opt.	opt.	opt.	opt.
open shell configuration	triplet	triplet	triplet	singlet	triplet	singlet	singlet
$\langle S^2 \rangle$	2.00	2.01	2.01	0.667	2.01	0.0	0.0
E / Hartree	-1501.82374	-1501.82369	-1501.84320	-1501.83817	-1459.87752	-1501.85226	-1501.85226
	α/β MO / eV						
virtual	-1.07 / -1.03 t _{1u}	-1.23 / -1.19 t ₂	-1.29 / -1.21 t ₂	-1.25 / -1.25 t ₂	-1.22 / -1.14 t ₂	-1.31 / -1.31 e _u	-1.31 / -1.31 2x
open ²⁾	-1.62 / -1.38 t _{1u}	-1.70 / -1.44 t ₁	-1.86 / -1.59 t ₁	-1.73 / -1.73 t ₁	-2.06 / -1.78 t ₁		
closed	-1.78 / -1.71 t _{2u}	-1.94 / -1.85 t ₂	-2.26 / -2.17 t ₂	-2.22 / -2.22 t ₂	-2.43 / -2.33 t ₂	-1.78 / -1.78 a _{2u}	-1.78 / -1.78
	-2.85 / -2.60 a _{1g}	-2.35 / -2.30 a ₁	-2.38 / -2.35 a ₁	-2.37 / -2.37 a ₁	-2.38 / -2.36 a ₁	-1.93 / -1.93 a _{1g}	-1.93 / -1.93
	-2.80 / -2.69 e _g	-2.96 / -2.76 e	-2.89 / -2.70 e	-2.80 / -2.80 e	-3.19 / -3.00 e	-2.05 / -2.05 e _u	-2.05 / -2.05 2x
	-5.29 / -5.15 a _{2u}	-5.72 / -5.60 a ₁	-6.48 / -6.36 a ₁	-6.42 / -6.42 a ₁	-4.71 / -4.56 a ₁	-2.65 / -2.65 a _{1g}	-2.65 / -2.65
	-6.71 / -6.60 t _{2g}	-6.36 / -6.26 t ₂	-6.59 / -6.50 t ₂	-6.55 / -6.55 t ₂	-4.87 / -4.74 t ₂	-2.67 / -2.67 e _g	-2.67 / -2.67 2x
	-8.10 / -7.98 t _{1u}	-8.20 / -8.06 t ₂	-8.21 / -8.06 t ₂	-8.14 / -8.14 t ₂	-6.83 / -6.68 t ₂	-5.91 / -5.91 a _{2u}	-5.91 / -5.91
	-9.57 / -9.44 a _{1g}	-10.23 / -10.13 a ₁	-9.99 / -9.91 a ₁	-9.95 / -9.95 a ₁	-8.95 / -8.88 a ₁	-6.20 / -6.20 e _g	-6.20 / -6.20 2x
						-7.18 / -7.18 a _{1g}	-7.18 / -7.18
						-7.68 / -7.68 e _u	-7.68 / -7.68 2x
						-8.37 / -8.37 a _{2u}	-8.37 / -8.37
						-9.91 / -9.91 a _{1g}	-9.91 / -9.91

Table A1.1 continued

vib. Freq. / cm ⁻¹	1 imaginary frequency	6x0.0, 3x18.7, 3x21.3, 2x31.1, 3x31.3, 3x45.0, 3x46.4, 3x49.5, 2x51.1, 54.0, 3x58.8, 60.3, 3x63.3, 2x81.4, 85.1, 3x87.1	3 imaginary frequencies	6x0.0, 3x20.2, 3x21.6, 2x33.3, 3x34.2, 3x46.3, 3x50.2, 2x57.9, 60.4, 3x61.2, 64.8, 3x65.8, 3x68.8, 2x89.8, 3x100.1, 100.2	6x0.0, 2x2.6, 2x9.6, 17.7, 17.9, 21.4, 2x22.7, 2x26.2, 2x32.7, 2x38.3, 2x44.8, 46.0, 46.6, 2x53.1, 54.6, 2x59.6, 60.2, 61.6, 64.3, 2x72.7, 76.9, 79.1, 2x81.4, 2x84.9, 97.7	6x0.0, 2x2.7, 9.6, 9.9, 17.9, 17.9, 21.4, 2x22.6, 2x26.2, 2x32.6, 2x38.4, 2x44.9, 45.9, 46.6, 2x53.2, 54.6, 2x59.6, 60.2, 61.5, 64.3, 2x72.7, 77.0, 79.1, 2x81.4, 2x84.9, 97.8
----------------------------------	--------------------------	---	----------------------------	--	---	--

- 1) opt – Optimized structure within given symmetry; expt.: Structure as found experimentally in the Cs₁₈Tl₈O₆ crystal.
- 2) Occupation of the open shell – triplet: 2 α -electrons, 0 β -electron; singlet: 1 α -electron, 1 β -electron.
- 3) Three different starting configurations converged to the same optimized structure, which is identical to the one obtained in D_{3d} .

Table A1.2. Two-component relativistic DFT calculations of the Cs₆Tl₈ cluster, applying the PBE and the B3LYP functional.

Symmetry constraint	O_h	T_d	T_d	T_d	D_{3d}	D_{3d}
functional	PBE	PBE	PBE	B3LYP	PBE	B3LYP
shape	cube	tetrahedral	star	tetrahedral	parallelepiped	parallelepiped
opt./ expt. ¹⁾	opt.	expt.	Opt.	opt. (PBE)	opt.	Opt. (PBE)
$\langle S_z \rangle$	0.54	0.03	0.00	0.00	0.00	0.00
$N_S^{2)}$	1.09	0.05	0.00	0.00	0.00	0.00
E / Hartree	-1503.54222	-1503.55283	-1503.57244	-1502.90184	-1503.56762	-1502.89601
spinors: ϵ / eV						
virtual	-1.27	-1.28	-1.27 x4	-1.47 x4	-0.94 x4	-1.26 x2
occupied	-1.40	-1.40	-1.73 x2	-1.96 x2	-2.16 x2	-1.81 x2
	-1.88	-1.89	-1.88 x2	-2.17 x4	-2.40 x4	-1.91 x2
	-1.90	-1.91	-1.90 x4	-2.23 x2	-2.49 x2	-2.04 x2
	-2.07	-2.12	-2.26 x2	-2.41 x2	-2.62 x2	-2.14 x2
	-2.65	-2.74	-2.73 x4	-2.75 x4	-2.92 x4	-2.52 x2
	-2.75	-2.76	-5.42 x2	-6.05 x2	-6.62 x2	-2.65 x2
	-2.81	-2.84	-6.06 x2	-6.40 x2	-7.02 x2	-2.69 x2
	-5.03	-5.09	-6.09 x4	-6.42 x4	-7.05 x4	-5.67 x2
	-6.48	-6.50	-7.86 x4	-7.93 x4	-8.70 x4	-6.07 x4
	-6.51	-6.56	-7.91 x2	-7.97 x2	-8.77 x2	-6.98 x2
	-6.56	-6.57	-9.94 x2	-9.71 x2	-10.67 x2	-7.53 x2

Table A1.2 continued

-7.91	-7.91	-7.56	x2	-8.32	x2
-7.93	-7.98	-8.15	x2	-8.97	x2
-7.99	-7.99	-9.67	x2	-10.63	x2
-9.44	-9.50				

¹⁾ opt – Optimized structure within given symmetry, PBE functional;

expt. – Structure as found experimentally in the Cs₁₈Tl₈O₆ crystal.

²⁾ N_S – Number of unpaired electrons (no observable) as defined in [146].

Table A1.3. Scalar relativistic unrestricted open shell Kohn-Sham calculations of the Cs₆Tl₈ cluster, applying the B3LYP hybrid functional.

symmetry constraint	T_d	T_d	D_{3d}	C_1
shape	tetrahedral star	tetrahedral star	parallelepiped	parallelepiped
opt. ¹⁾	opt. (PBE)	opt. (B3LYP)	opt. (PBE)	opt. (B3LYP)
open shell configuration	triplet	triplet	singlet	singlet
$\langle S^2 \rangle$	2.02	2.02	0.0	0.0
E / Hartree	-1501.16798	-1501.16983	-1501.18687	-1501.18851
	α/β MO / eV			
virtual	-0.90 / -0.85 t ₂	-0.92 / -0.87 t ₂	-0.93 / -0.93 e _u	-0.95 / -0.95 2x
open ²⁾	-1.78 / -1.07 t ₁	-1.75 / -1.05 t ₁		
closed	-2.47 / -2.37 t ₂	-2.37 / -2.28 t ₂	-1.94 / -1.94 a _{2u}	-1.91 / -1.91
	-2.57 / -2.56 a ₁	-2.53 / -2.51 a ₁	-2.14 / -2.14 a _{1g}	-2.05 / -2.05
	-3.07 / -2.80 e	-3.03 / -2.77 e	-2.20 / -2.20 e _u	-2.16 / -2.16 2x
	-7.11 / -6.96 a ₁	-7.01 / -6.87 a ₁	-2.85 / -2.85 a _{1g}	-2.78 / -2.78 2x
	-7.25 / -7.13 t ₂	-7.24 / -7.12 t ₂	-2.81 / -2.81 e _g	-2.80 / -2.80
	-9.04 / -8.85 t ₂	-8.97 / -8.79 t ₂	-6.47 / -6.47 a _{2u}	-6.42 / -6.42
	-10.99/-10.90 a ₁	-10.83/-10.74 a ₁	-6.79 / -6.79 e _g	-6.82 / -6.82 2x
			-7.91 / -7.91 a _{1g}	-7.84 / -7.84
			-8.44 / -8.44 e _u	-8.43 / -8.43 2x
			-9.23 / 9.23 a _{2u}	-9.14 / -9.14
			-10.88/-10.88 a _{1g}	-10.73/10.73

Table A1.3 continued

vib. freq. / cm^{-1}	6x0.0, 3x16.4, 3x19.7, 3x27.2, 2x27.3, 3x39.6, 3x43.4, 3x45.5, 2x47.6, 51.5, 3x55.0, 58.4, 3x61.3, 2x77.0, 80.0, 3x83.2	6x0.0, 3.9, 4.3, 9.6, 9.7, 17.0, 17.2, 20.8, 21.8, 21.9, 24.7, 24.8, 31.3, 31.4, 2x35.2, 42.6, 2x43.6, 45.1, 2x50.2, 53.0, 56.7, 2x58.6, 59.7, 61.8, 2x69.9, 74.0, 77.0, 2x77.2, 2x81.7, 95.9
-------------------------------	--	---

¹⁾ opt – Optimized structure within given symmetry, obtained with the functional given in parenthesis.

²⁾ Occupation of the open shell – triplet: 2 α -electrons, 0 β -electron; singlet: 1 α -electron, 1 β -electron.

A2. Evaluation of the Magnetic Measurements

Data

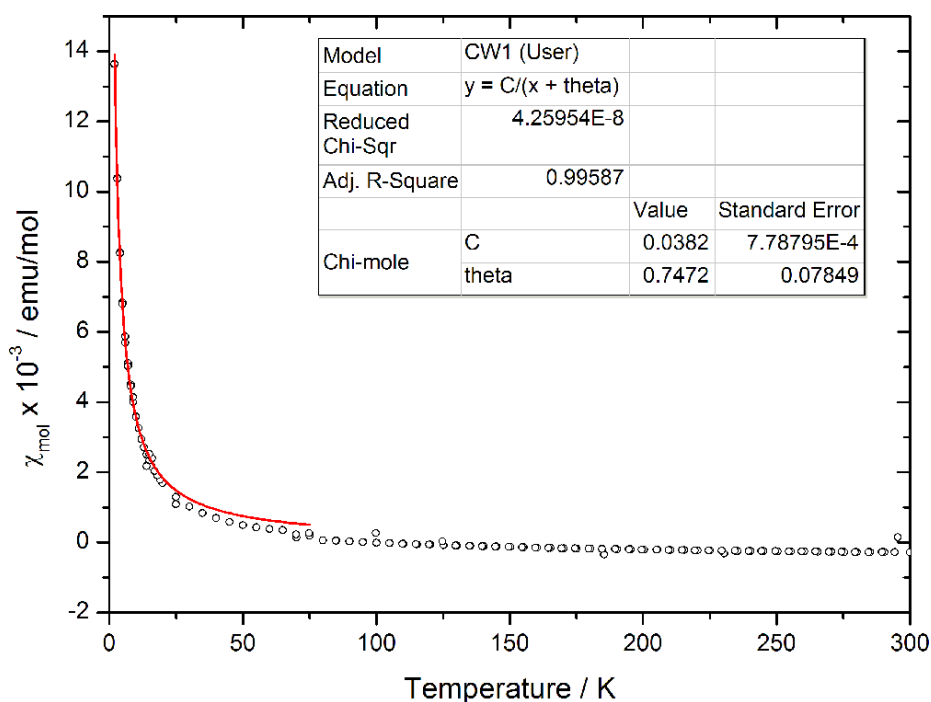


Figure A2.1. Curie-Weiss fitting (red curve) of the magnetic susceptibility data of $\text{Cs}_{18}\text{Tl}_8\text{O}_6$ at 1T (black circles).

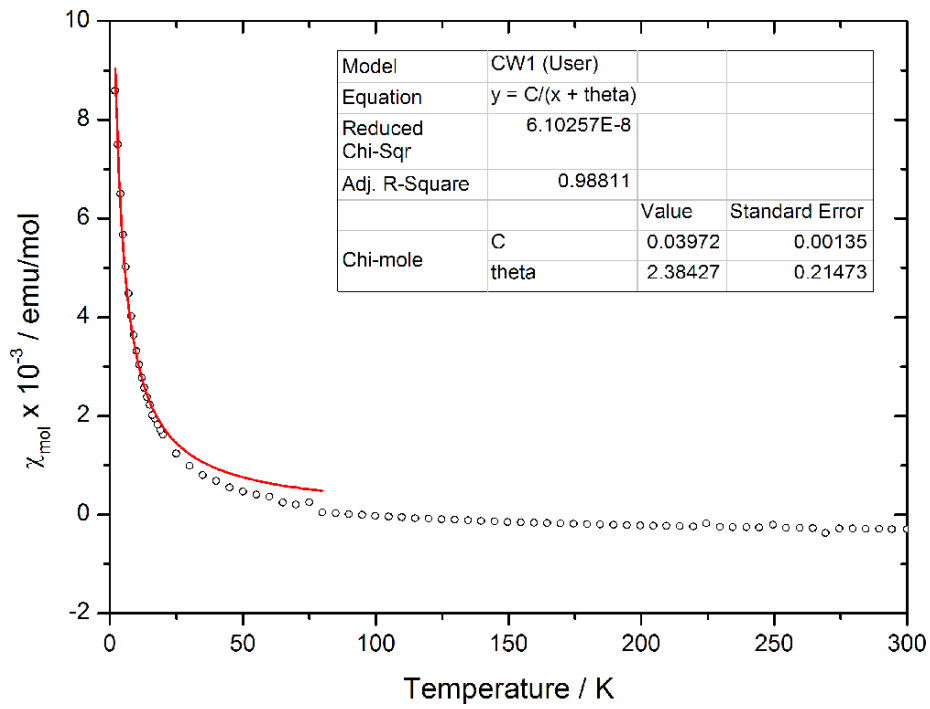


Figure A2.2. Curie-Weiss fitting (red curve) of the magnetic susceptibility data of $\text{Cs}_{18}\text{Tl}_8\text{O}_6$ at 3T (black circles).

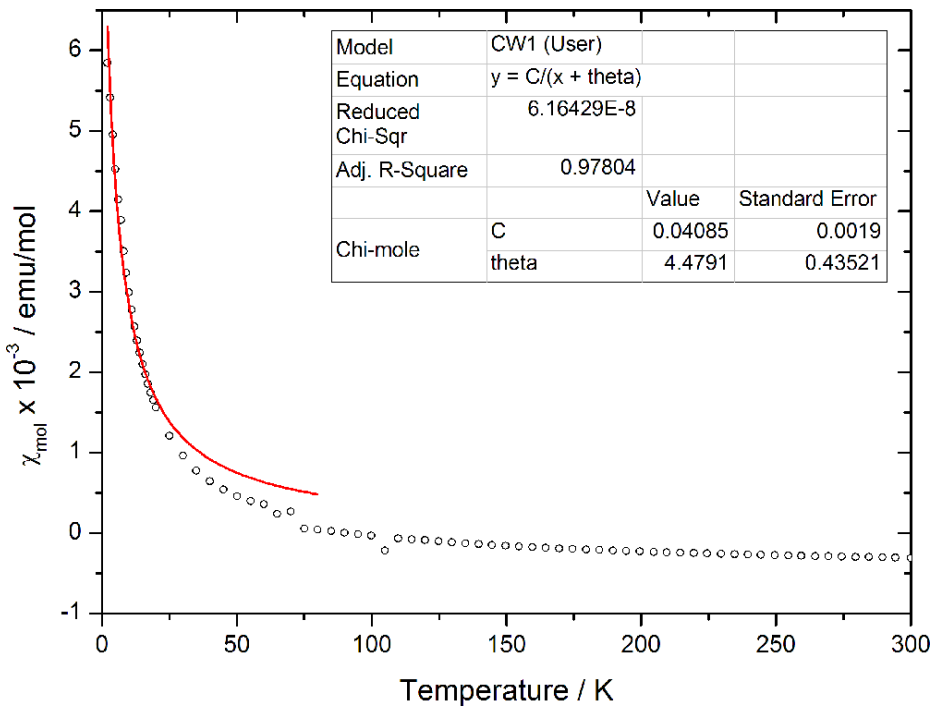


Figure A2.3. Curie-Weiss fitting (red curve) of the magnetic susceptibility data of $\text{Cs}_{18}\text{Tl}_8\text{O}_6$ at 5T (black circles).

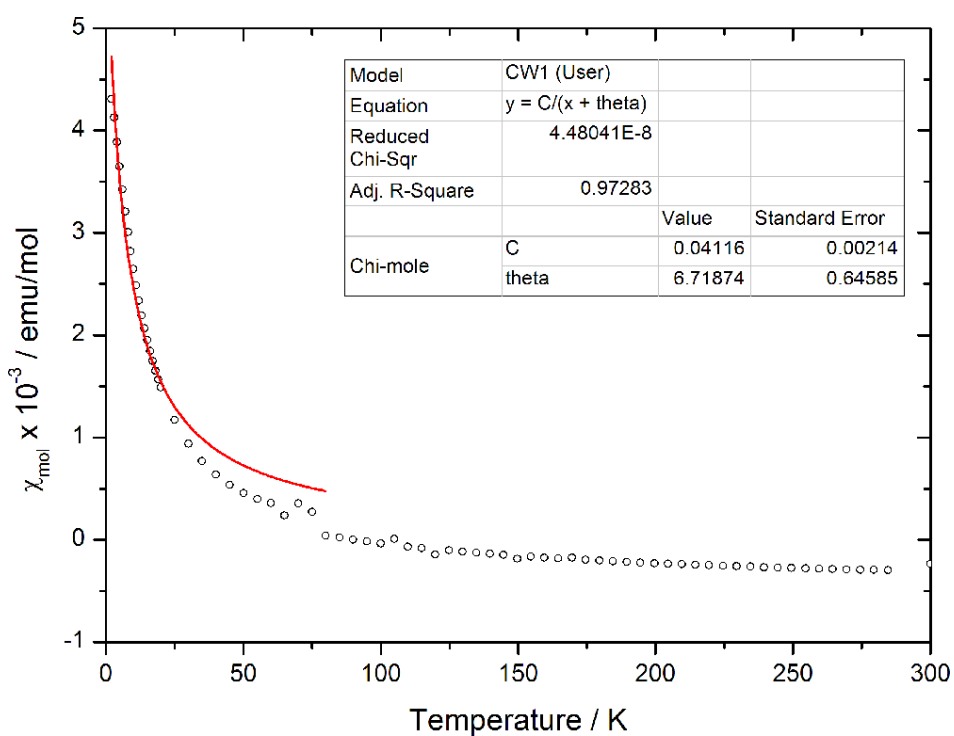


Figure A2.4. Curie-Weiss fitting (red curve) of the magnetic susceptibility data of $\text{Cs}_{18}\text{Tl}_8\text{O}_6$ at 7T (black circles).

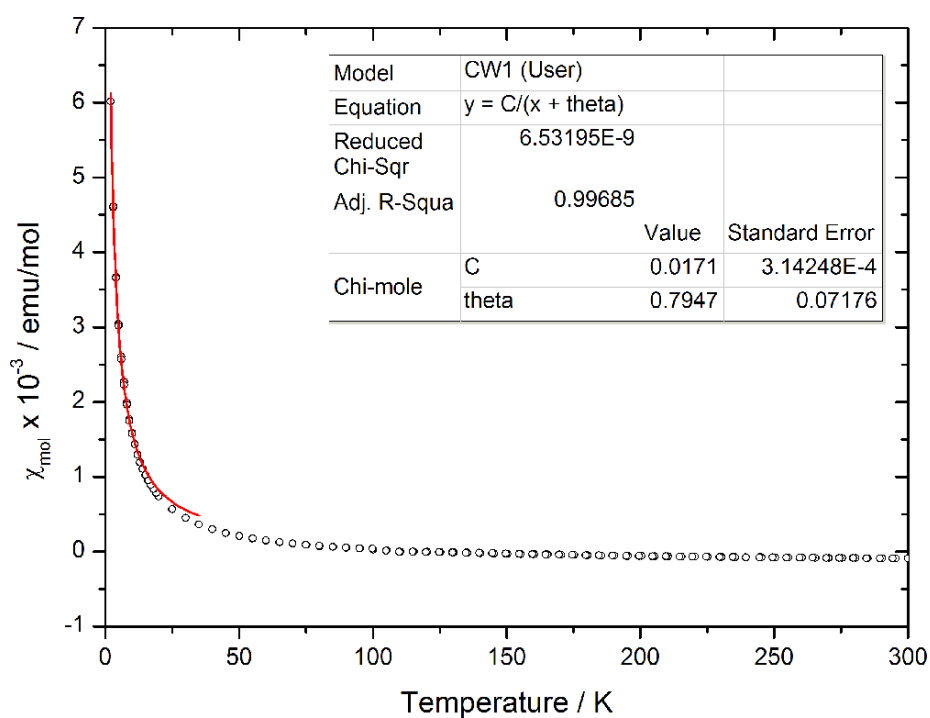


Figure A2.5. Curie-Weiss fitting (red curve) of the magnetic susceptibility data of $\text{Cs}_4\text{Tl}_2\text{O}$ at 1T (black circles).

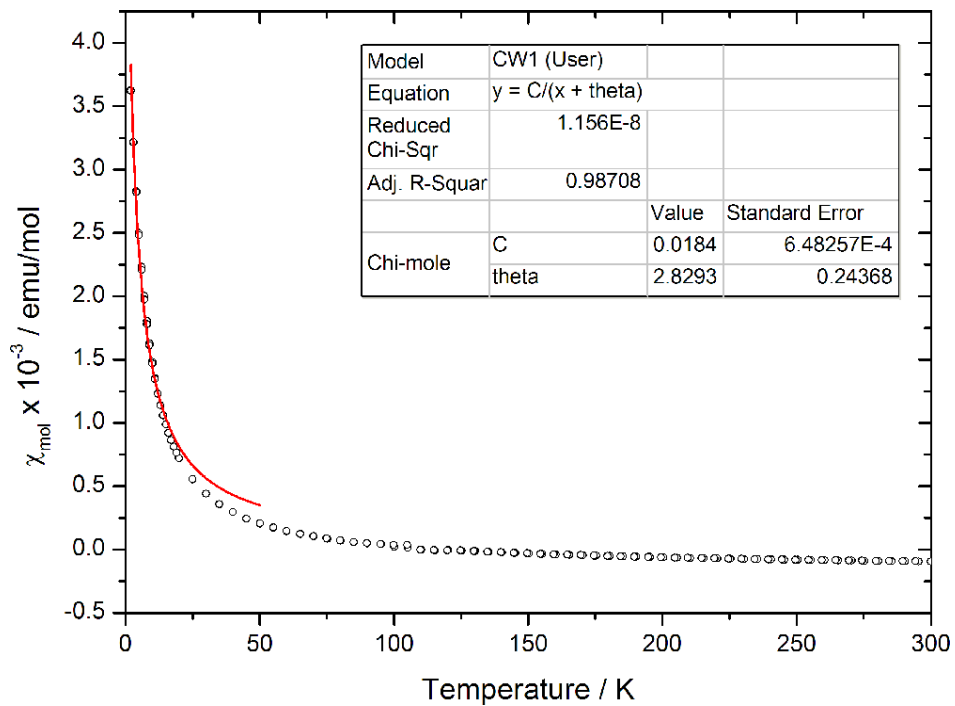


Figure A2.6. Curie-Weiss fitting (red curve) of the magnetic susceptibility data of $\text{Cs}_4\text{Tl}_2\text{O}$ at 3T (black circles).

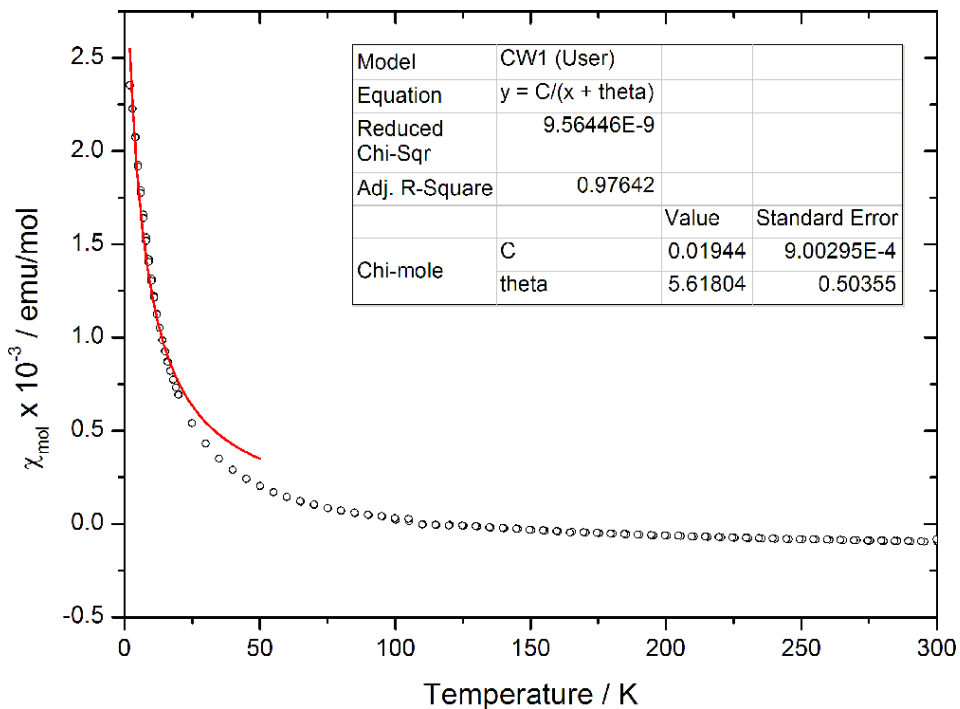


Figure A2.7. Curie-Weiss fitting (red curve) of the magnetic susceptibility data of $\text{Cs}_4\text{Tl}_2\text{O}$ at 5T (black circles).

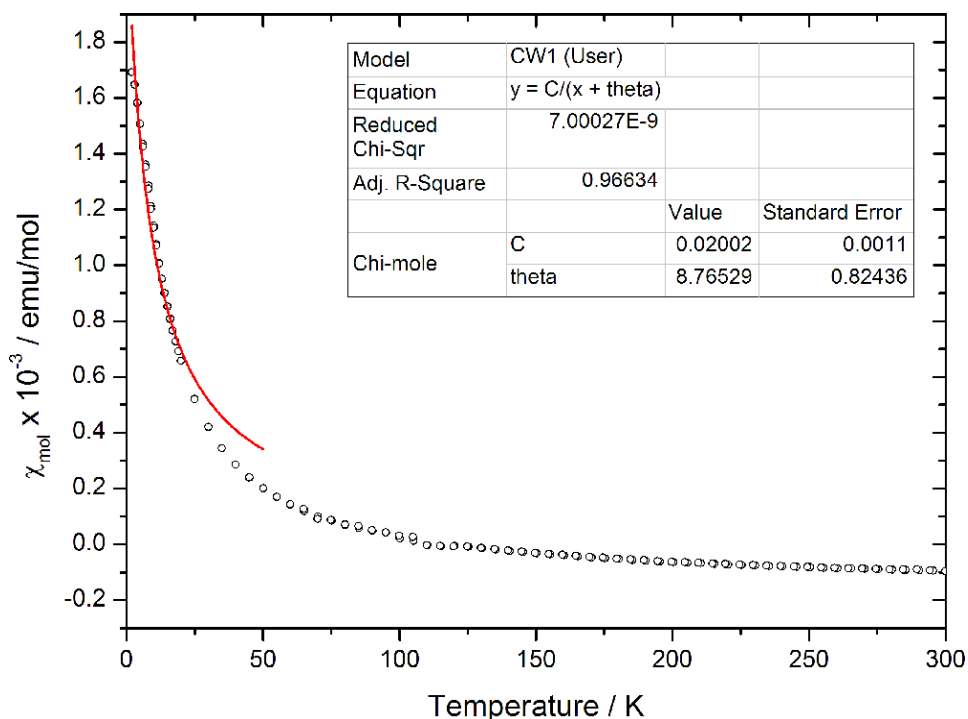


Figure A2.8. Curie-Weiss fitting (red curve) of the magnetic susceptibility data of $\text{Cs}_4\text{Tl}_2\text{O}$ at 7T (black circles).

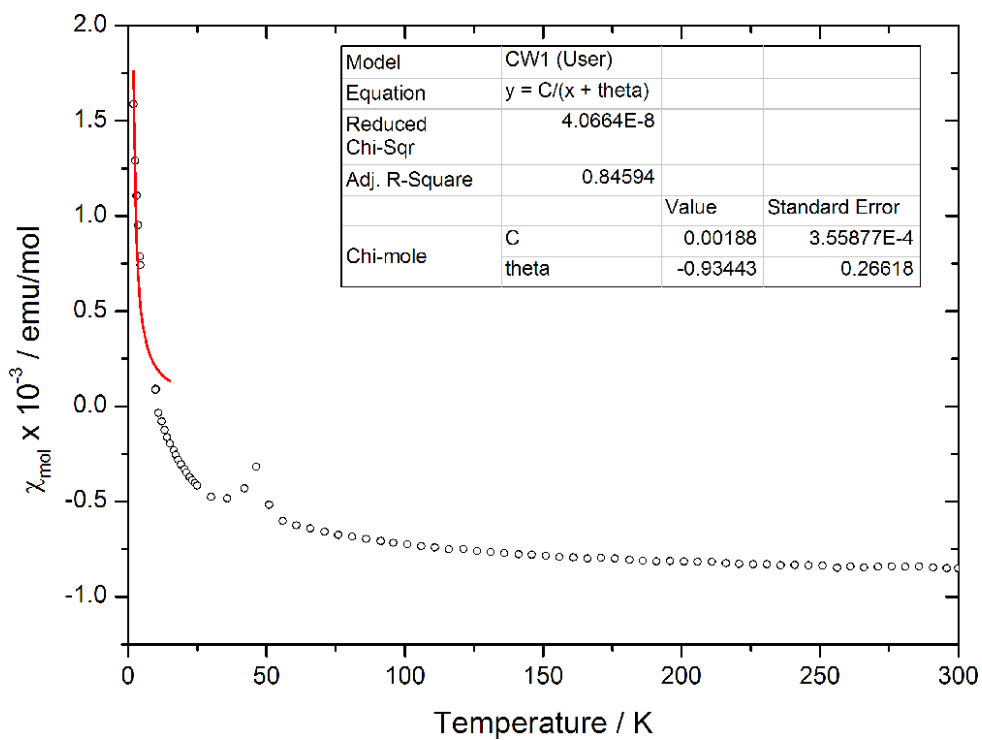


Figure A2.9. Curie-Weiss fitting (red curve) of the magnetic susceptibility data of $\text{K}_{21}\text{Tl}_{22}\text{O}_2$ at 1T (black circles).

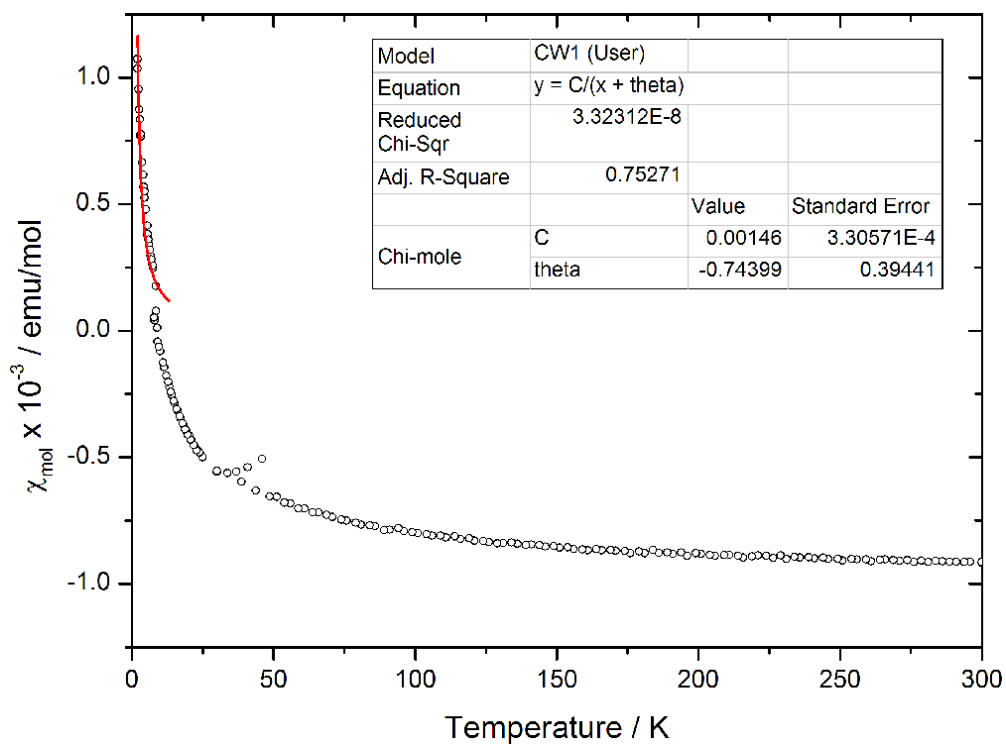


Figure A2.10. Curie-Weiss fitting (red curve) of the magnetic susceptibility data of $\text{K}_{21}\text{Tl}_{22}\text{O}_2$ at 3T (black circles).

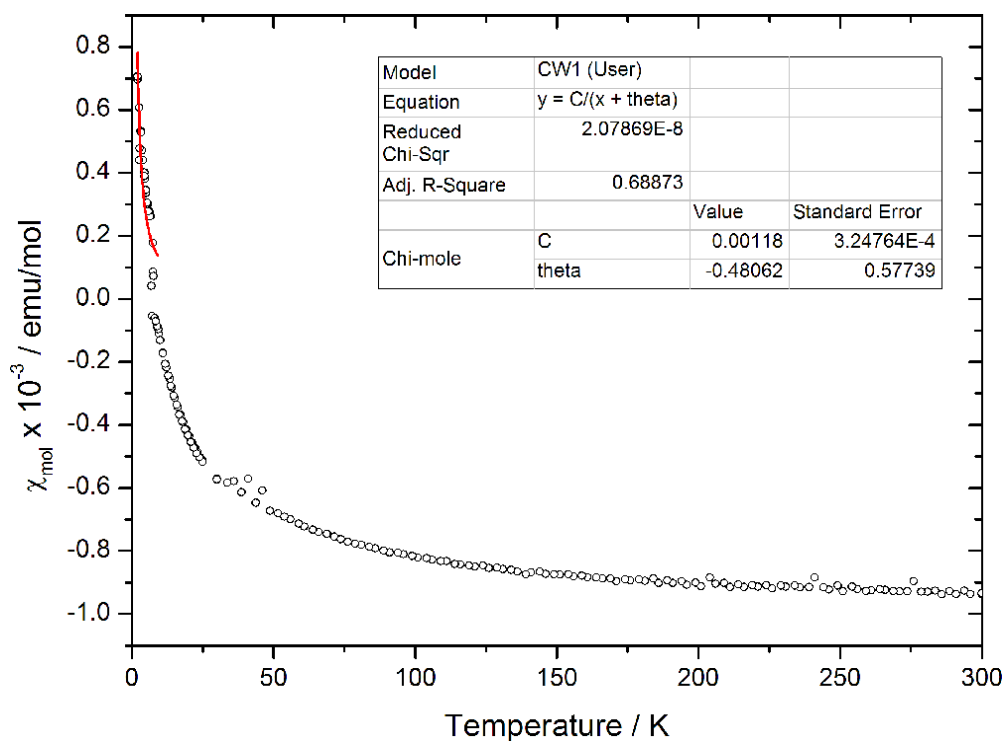


Figure A2.11. Curie-Weiss fitting (red curve) of the magnetic susceptibility data of $\text{K}_{21}\text{Tl}_{22}\text{O}_2$ at 5T (black circles).

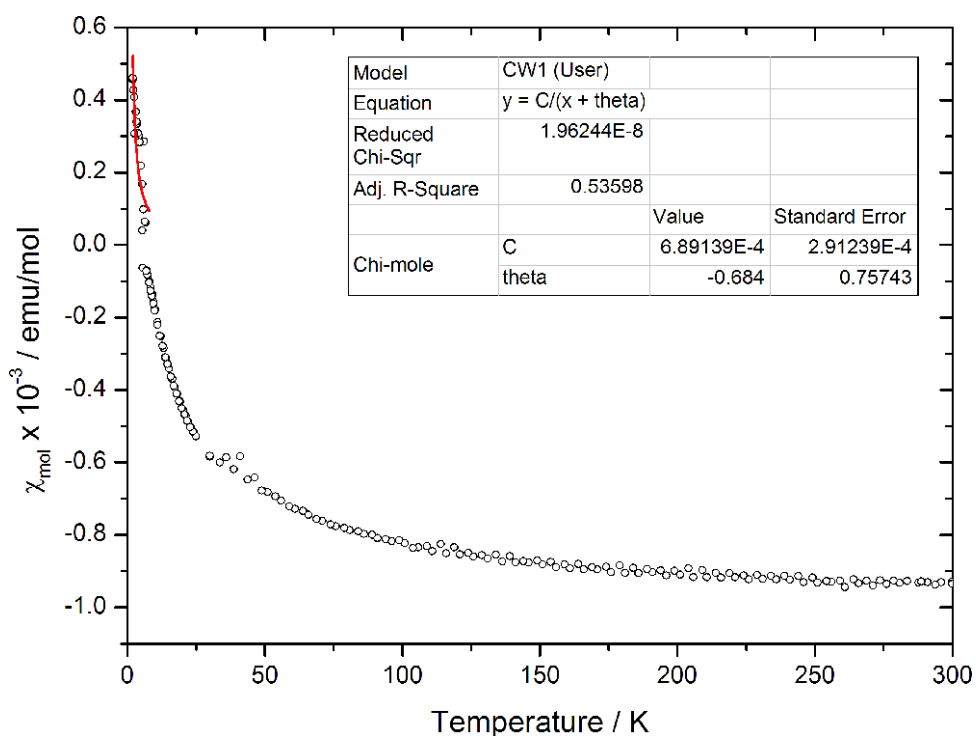


Figure A2.12. Curie-Weiss fitting (red curve) of the magnetic susceptibility data of $\text{K}_{21}\text{Tl}_{22}\text{O}_2$ at 7T (black circles).

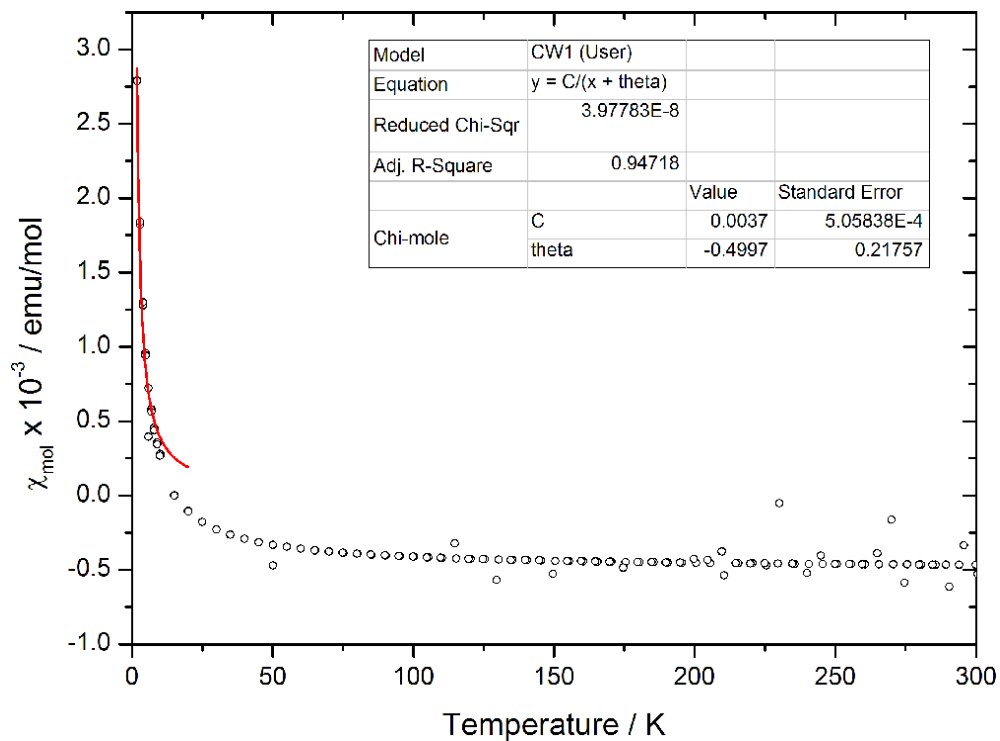


Figure A2.13. Curie-Weiss fitting (red curve) of the magnetic susceptibility data of $\text{Cs}_{10}\text{Tl}_6\text{SnO}_3$ at 1T (black circles).

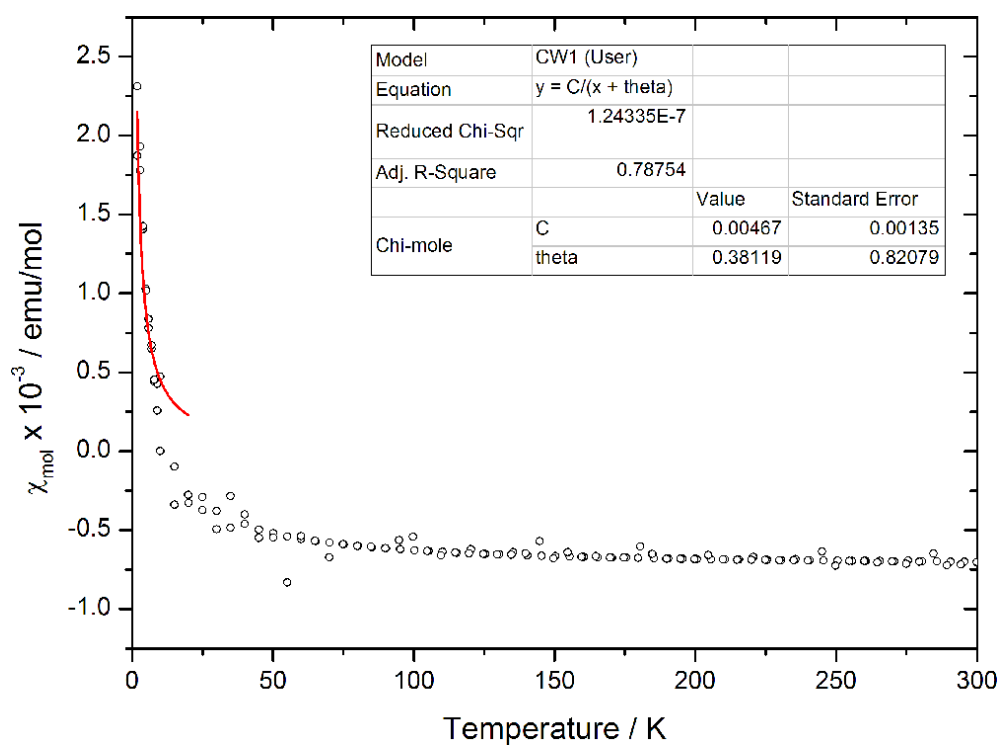


Figure A2.14. Curie-Weiss fitting (red curve) of the magnetic susceptibility data of $\text{Cs}_{10}\text{Tl}_6\text{SnO}_3$ at 3T (black circles).

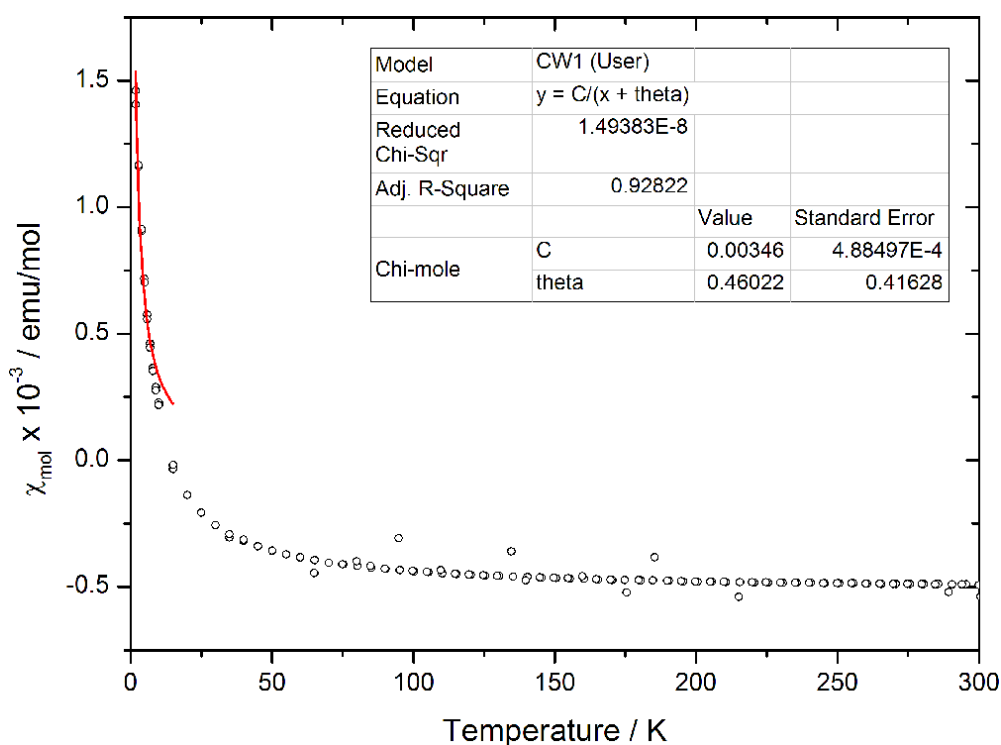


Figure A2.15. Curie-Weiss fitting (red curve) of the magnetic susceptibility data of $\text{Cs}_{10}\text{Tl}_6\text{SnO}_3$ at 5T (black circles).

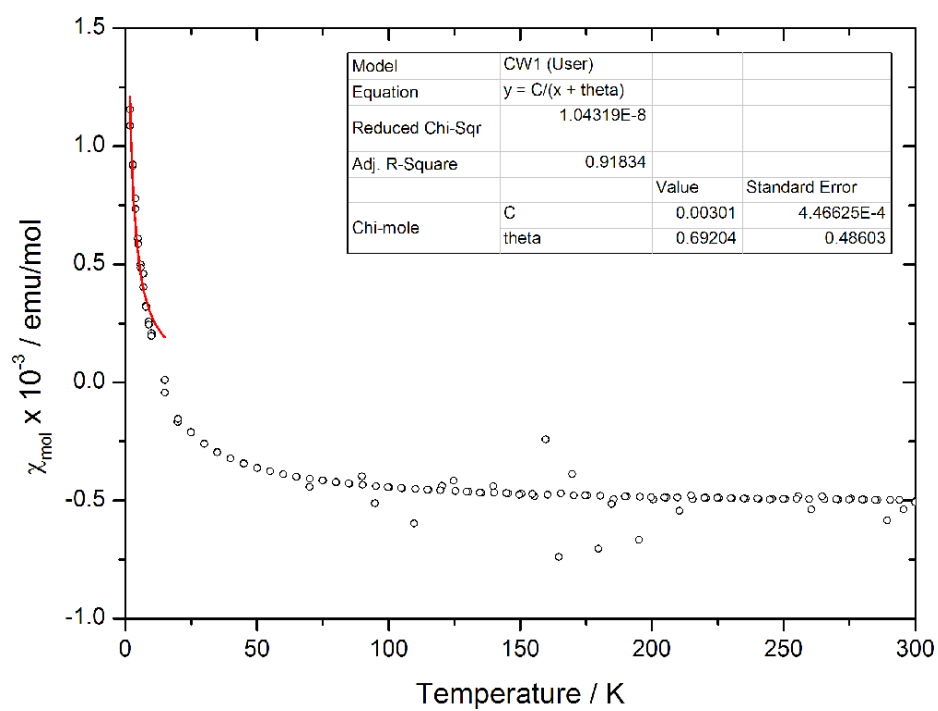


Figure A2.16. Curie-Weiss fitting (red curve) of the magnetic susceptibility data of $\text{Cs}_{10}\text{Tl}_6\text{SnO}_3$ at 7T (black circles).

Part VII.

Appendix B

14. Acknowledgements

First and foremost I would like to express sincere gratitude to my supervisor **Prof. Dr. Dr. h. c. Martin Jansen** for giving me the opportunity to make a work in his department, freedom during setting of tasks, advices and his constant interests in my research.

My sincere thanks to my Ph.D. examination committee members **Prof. Dr. Thomas Schleid** and **Prof. Dr. Robert E. Dinnebier** for their evaluation of my Ph.D. thesis.

My special thanks to leader of Solid Phase Synthesis Group **Dr. Jürgen Nuß** for the valuable discussions of the results and further suggestions, helpful answers of the questions, support in measuring all single crystals and providing their crystal structures solutions as well as for his invaluable help in proofreading of this thesis.

I am very grateful to **Dr. Ulrich Wedig** for performing theoretical calculations in the scope of the present work and thorough explanation of them.

Also I would like to thank:

Dipl. Ing. Claus Mühle for support during experiment part;

Prof. Dr. Robert E. Dinnebier for the advices and support in the refinement of crystal structures from powder diffraction data as well as for the support during daily work in the X-ray diffraction laboratory;

Prof. Dr. J. Christian Schön for the numerous discussions of public life and scientific questions, and for proofreading of the present thesis;

Ms. Marie-Luise Schreiber for quantitative elemental analysis measurements;

Mr. Mitsuharu Konuma for performing ESCA measurements;

Ms. Eva Brücher and **Ms. Gisela Siegle** for performing the magnetic and electrical resistivity measurements, respectively;

Ms. Sabine Paulsen and **Ms. Jeanette Schüller-Knapp** for invaluable assistance in general administrative matters;

My labour colleges **Ms. Sabine Prill-Diemer, Dipl. Ing. Claus Mühle, Naveed Zafar Ali** and **Katarina Djuris** for providing an enthusiastic and friendly working atmosphere.

I very much appreciated the scientific and social atmosphere within the department of Prof. Dr. Jansen.

Many thanks are to the Max Planck Society for the doctoral fellowship during my entire Ph. D. time.

Especially I would like to thank my friends **Mikhail Kabdulov** and **Dmytro Kovalenko** for the support, friendship and creating a nice environment.

Last but definitely not least, I am very thankful to my brother **Pasha, Katarina**, my **niece Sophie** and of course **my parents** for their ongoing enormous encouragement, endless support and being always with me, no matter what occurs and locations are.

15. Curriculum Vitae

Personal data

Name: Vyacheslav Saltykov
Date of birth: 08.05.1983
Place of birth: Konotop, Ukraine
Marital status: single

School education

1990-1996 School Nr.12, Konotop, Ukraine
1996-1997 Gymnasium with an advanced natural sciences training,
Konotop, Ukraine
1997-2000 Military College, Chernigov, Ukraine

Academic study

2000-2004 National Technical University of Ukraine “Kiev Polytechnic Institute”, Physical-Engineering Faculty, Chair of high-temperature composite materials and powder metallurgy, coatings.
Degree: Bachelor-diploma (State Examination passed with distinction)

2004-2006 National Technical University of Ukraine “Kiev Polytechnic Institute”, Physical-Engineering Faculty, Chair of high-temperature composite materials and powder metallurgy, coatings.
Degree: Master-diploma (passed with distinction).
Thesis topic: “Phase Equilibria and Mechanical Properties of Alloys in the Ti–Zr–Sn System”

September 2004-February 2005 Scholarship of the National Technical University of Ukraine “Kiev Polytechnic Institute” for the excellent study, scholarship of Prof. Dr. V. G. Samsonov

November 2005 Awards of Mayor of Kiev City for excellent study and the Second Student’s Prize of the National Technical University of Ukraine “Kiev Polytechnic Institute”

2006-2010 PhD work under supervision of Prof. Dr. Dr. h. c. Martin Jansen, Max Planck Institute for Solid State Research, Stuttgart, Germany.
Thesis topic: „The Relativistic Effect in Intermetallic Phases of Gold, Platinum and Thallium“

16. Publications

1. M. Bulanova, L. Tretyachenko, K. Meleshevich, V. Saltykov, V. Vereshchaka, O. Galadzhij, L. Kulak, S. Firstov, “Influence of tin on the structure and properties of as-cast Ti-rich Ti-Si alloys”, *J. Alloys Compd.* **2003**, *350*, 164 – 173.
2. M. Bulanova, L. Tretyachenko, K. Meleshevich, A. Samelyuk, V. Saltykov, L. Kulak, S. Firstov, “Structure and properties of the Ti-Zr-Si system as-cast alloys”, *Reports NASU* **2004**, *4*, 86 – 90. (in Russian)
3. O. L. Semenova, K. A. Meleshevich, V. M. Petyukh, V. A. Saltykov, A. V. Samelyuk, S. O. Firstov, “Phase equilibria in the titanium corner of hypoeutectic alloys in the Ti-Nb-Si-Al system”, *Powder Metall. Met. Ceram.* **2005**, *44*, 557 – 566.
4. V. A. Saltykov, K. A. Meleshevich, A. V. Samelyuk, O. M. Verbytska, M. V. Bulanova, “Isothermal section at 1400°C of the Ti-Zr-Sn system”, *J. Alloys Compd.* **2008**, *459*, 348 – 353.
5. V. A. Saltykov, K. A. Meleshevich, A. V. Samelyuk, M. V. Bulanova, J. C. Tedenac, “The melting diagram of the Ti-Zr-Sn system below 40 at.% Sn”, *J. Alloys Compd.* **2009**, *473*, 341 – 346.
6. V. Saltykov, J. Nuss, M. Konuma, M. Jansen, “Investigation of the Quasi Binary System BaAu – BaPt”, *Z. Anorg. Allg. Chem.* **2009**, *635*, 70 – 75.
7. V. Saltykov, J. Nuss, M. Konuma, M. Jansen, “SrAu_{0.5}Pt_{0.5} and CaAu_{0.5}Pt_{0.5}, Analogues to the Respective Ba Compound, but Featuring Purely Intermetallic Behaviour”, *Solid State Sci.* **2010**, *12*, 1615 – 1619.
8. U. Wedig, V. Saltykov, J. Nuss, M. Jansen, “Homoatomic *Stella Quadrangula* [Tl₈]⁶⁻ in Cs₁₈Tl₈O₆, Interplay of Spin–Orbit Coupling, and Jahn–Teller Distortion”, *J. Amer. Chem. Soc.* **2010**, *132*, 12458 – 12463.

9. V. Saltykov, J. Nuss, U. Wedig, M. Jansen, "Impact of Spin-orbit Coupling on the Structure of Thallium Clusters", *Z. Anorg. Allg. Chem.* **2010**, 636, 2040.
10. V. Saltykov, J. Nuss, M. Jansen, "Cs₁₀Tl₆SiO₄, Cs₁₀Tl₆GeO₄ and Cs₁₀Tl₆SnO₃ – First Oxotetrelate Thallides Containing "Hypoelectronic" [Tl₆]⁶⁻ Clusters", *Z. Anorg. Allg. Chem.*, **2010**, DOI: 10.1002/zaac.201000358.
11. V. Saltykov, J. Nuss, U. Wedig, M. Jansen, "Regular [Tl₆]⁶⁻ Cluster in Cs₄Tl₂O Exhibiting Close Shell Configuration and Energetic Stabilization due to Relativistic Spin-Orbit Coupling", *Z. Anorg. Allg. Chem.*, **2011**, 637, 357–361.
12. V. Saltykov, J. Nuss, U. Wedig, P. L. V. K. Dasari, M. Jansen, "First Isolated "Hypoelectronic" [In₆]⁶⁻ Cluster in Insulating Cs₂₂In₆(SiO₄)₄", *Z. Anorg. Allg. Chem.*, **2011**, DOI: 10.1002/zaac.201100074.

Hiermit versichere ich an Eides statt, dass ich diese Dissertation unter Verwendung der angegebenen Hilfsmittel selbständig angefertigt und bisher noch keinen Promotionsversuch unternommen habe.

Stuttgart, den

Vyacheslav Saltykov